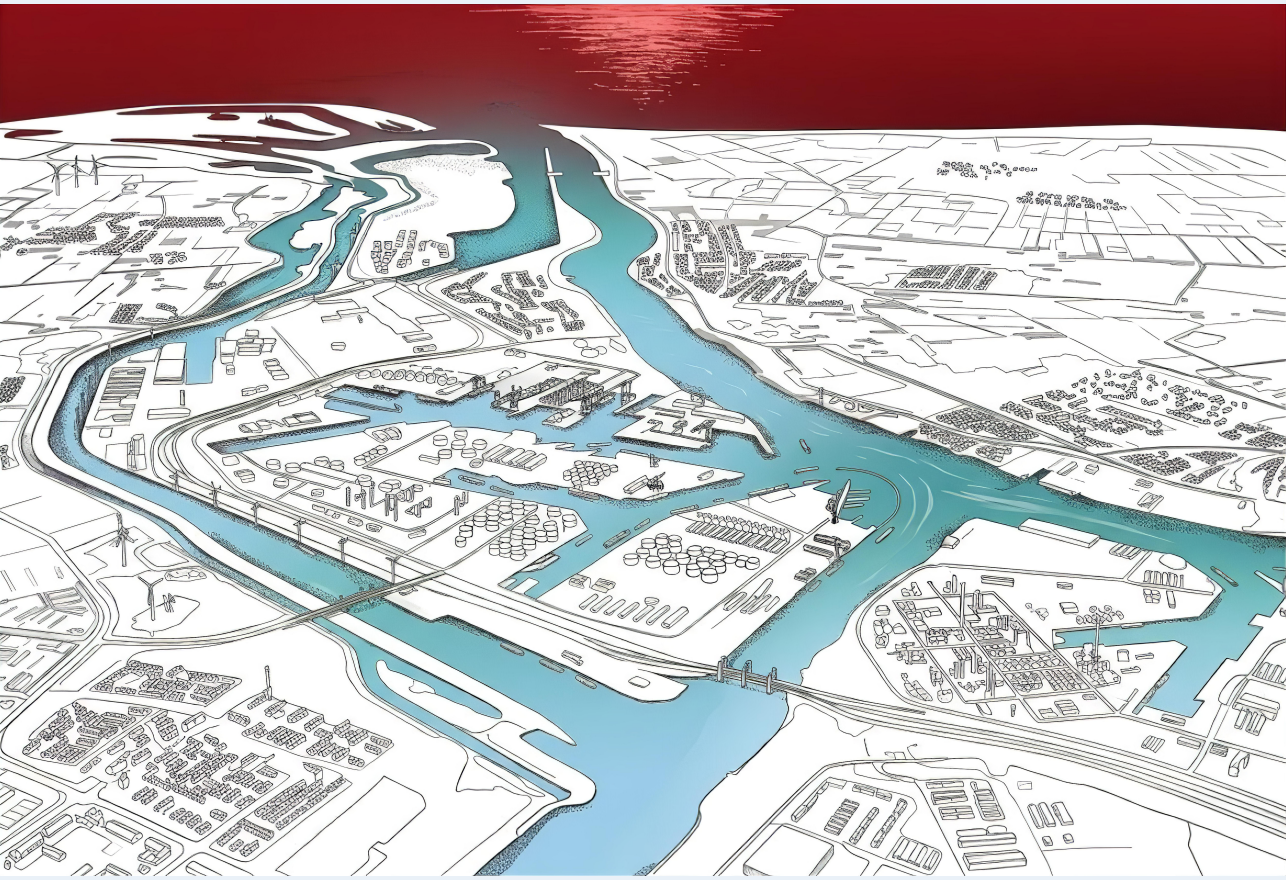
SALT INTRUSION IN CHANNELS WITH COMPLEX GEOMETRY



Daan van Keulen

2026

Propositions

1. Dispersion coefficients to quantify tidal trapping depend on the salinity gradient along the main channel.
   (this thesis)
2. Redesigning old harbours along the New Meuse into tidal parks helps mitigate salt intrusion.
   (this thesis)
3. Idealised models misrepresent system behaviour by overlooking impacts of finescale variability.
4. Scientific progress is slowed down by insufficient uptake of established knowledge.
5. Field measurements have greater scientific value than what is reflected in dissertations.
6. AI makes academia more accessible for people with dyslexia by helping them engage more fully.
7. Climate change amplifies existing regional inequalities in the Netherlands.

Propositions belonging to the thesis, entitled

Salt intrusion in channels with complex geometry

Daan van Keulen
Wageningen, 14 October 2026

SALT INTRUSION IN CHANNELS WITH COMPLEX GEOMETRY

Daan van Keulen

Thesis committee

Promotor

Prof. Dr *ir.* A.J.F. Hoitink
Professor in Hydrology and Quantitative Water Management
Wageningen University & Research

Co-promotor

Dr *ir.* W.M. Kranenburg
Assistant Professor in Hydraulic Engineering
Delft University of Technology (TU Delft)

Other Members

Prof. Dr *ir.* Florian Muijres, Wageningen University & Research,

Prof. Dr Julie Pietrzak, Delft University of Technology,

Prof. Dr Hans Burchard, Leibniz Institute for Baltic Sea Research, Germany

Dr David Ralston, Woods Hole Oceanographic Institution, United States

This research was conducted under the auspices of the Graduate School
Wageningen Institute for Environment and Climate Research (WIMEK).

SALT INTRUSION IN CHANNELS WITH COMPLEX GEOMETRY

Daan van Keulen

Thesis
submitted in fulfilment of the requirements for the degree of doctor
at Wageningen University
by the authority of the Rector Magnificus,
Prof. Dr C. Kroeze,
in the presence of the
Thesis Committee appointed by the Academic Board
to be defended in public
on Wednesday 14 October 2026
at 3.30 p.m. in the Omnia Auditorium.

Daan van Keulen
SALT INTRUSION IN CHANNELS WITH COMPLEX GEOMETRY,
188 pages

PhD thesis, Wageningen University, Wageningen, the Netherlands (2026)
With references, with summary in English

https://doi.org/10.18174/681660

Summary

This thesis advances the mechanistic understanding of salt dispersion in estuaries by examining how tidal trapping, density-driven exchange, and bathymetric discontinuities contribute to up-estuary salt transport. Through a combination of idealised numerical modelling, field observations, 3D simulations, and data analysis, the work clarifies ambiguities in existing parameterisations, provides new insights into the processes governing salt intrusion and contributes to fast predictive tools.

Chapter 1 sets out to motivate and describe the objectives of this thesis. Chapter 2 revisits classical tidal-trapping theory by isolating the additional up-estuary salt transport generated by exchange with dead-end side basins using an idealised model set-up. Building on earlier work, a conceptual framework is introduced to analyse the individual contributions of different channel–trap exchange mechanisms to the up-estuary salt transport in the main channel. It is shown that the additional up-estuary salt transport due to the advective exchange associated with the barotropic filling and emptying of traps (advective out-of-phase exchange) produces the strongest dispersive effect when the velocity phase difference between the trap and the main channel down-estuary of the trap reaches $\frac{1}{2}\pi$. This behaviour aligns with early theoretical formulations, but contradicts more recent, widely used, analytical models that neglect differences in tidal-velocity phasing between both sides of the trap, as discussed in Chapter 3. Extending the model to include both barotropic and diffusive channel-trap exchange reveals that their combined effect cannot be represented as a simple superposition, and that a Péclet number specific to tidal trapping provides an appropriate measure to evaluate the relative importance of the two mechanisms.

Chapter 4 of the thesis examines the contribution of harbour basins to the dispersion of salt in the Rhine-Meuse estuary. Observations and 3D modelling show that channel–harbour exchange is dominated by density currents rather than by barotropic filling and emptying. The strength of this exchange varies strongly between harbours due to spatial differences in the tidal salinity range (the depth-averaged salinity variation over a tidal cycle) which controls the baroclinic pressure gradient between the main channel and the harbour. The salt transport resulting from the vertically sheared exchange was found to scales with the tidal salinity range raised to the power of 3/2, consistent with analytical expressions derived from theory. Applying the tidal-trapping framework tested in Chapter 2 to individual harbours in the Rhine-Meuse estuary reveals that their net contribution to up-estuary salt transport is modest (5–10%), and that the largest harbours contribute least because they are located where the tidal salinity range is weakest. A new parameterisation for density-driven tidal trapping is proposed, showing that the resulting dispersive effect depends explicitly on the subtidal salinity gradient. This new parametrisation reflects the baroclinic nature of the exchange mechanism, unlike classical formulations for tidal trapping which are independent of the subtidal salinity gradient.

Chapter 5 investigates how the steepness of the bed slope in the transition area between maintained bed levels, which resemble a stair-case-like bathymetry, influences salt intrusion. Numerical experiments with idealised bathymetries (inspired by bathymetries such as that of the Rotterdam Waterway) show that the slope of this transition zone strongly affects the salt intrusion length. For weakly to partially stratified estuaries, milder slopes, that create an overall deeper estuary reduce salt intrusion, while steeper slopes increase it. The remarkable observation that a mild slope can reduce salt intrusion is explained by two processes: (1) enhanced tidal reflection at sharp depth transitions reduces tidal currents and vertical mixing, strengthening estuarine circulation; and (2) steep slopes promote frontal formation

near the depth transition, which locally enhances the estuarine circulation and strengthens the tidal-oscillatory salt transport upstream of the frontal region. The dynamics in the idealised bathymetric set-up resemble observations in the New Meuse, where a salinity front forms near the depth transition, a strong increase in tidal-oscillatory salt transport is observed upstream of this transition, and the limited spring–neap modulation of the salt intrusion length matches the model behaviour for sharp bed slopes.

In Chapter 6 explores whether a hybrid-harmonic regression method can be reformulated to provide fast short-to-medium-term salinity predictions at monitoring stations. The proposed model embeds a semi-empirical salinity formulation into harmonic base functions and accounts for surge-induced variability and unsteadiness in the salt balance. Applied to the well-mixed Ems and Scheldt estuaries, the method yields accurate predictions and provides physically interpretable best-fit parameters, including a new interpretation of the Van der Burgh constant. However, the approach requires sufficient training data, does not resolve the vertical salinity structure, and assumes a single dominant longitudinal axis, limiting its applicability in stratified or geometrically complex systems such as the Rhine-Meuse. For such systems, (physics informed) machine-learning models are likely more suitable for obtaining accurate salinity predictions at monitoring stations.

Overall, this dissertation resolves key ambiguities in existing parameterisations of tidal trapping, provides new analytical tools to assess the dispersive influence of density-driven tidal trapping, clarifies why larger basins do not necessarily contribute more than smaller ones, and identifies bathymetric steps as a dominant control on salt intrusion in engineered estuaries. Together, these findings advance the mechanistic understanding of tidal-dispersion processes in geometrically complex estuaries and support the development of reliable predictive tools for estuarine salinity.

Contents

Contents **vii**

1 Introduction **3**
1.1 Estuaries and Salt Intrusion: Background and Context 3
1.2 Tides in Estuaries 4
1.3 The Estuarine salt Balance 8
1.4 The Estuarine Circulation 8
1.5 Tidal dispersion 11
1.6 Predicting Estuarine Salinity and Salt Intrusion 15
1.7 Objective and Research Goals 17
1.8 Outline of thesis 19

2 Tidal trapping and its effect on salinity dispersion in well-mixed estuaries revisited **23**
2.1 Introduction 24
2.2 Methods 27
2.3 Results 34
2.4 Discussion 41
2.5 Conclusions 47

3 Critical Examination of the MacVean and Stacey (2011) formulations **49**
3.1 Introduction 50
3.2 An Initial Pulse of Solutes Subjected to Pure Out-of-Phase Tidal Trapping 50
3.3 Reproducing the solution by MacVean and Stacey (2011) 52
3.4 Concluding Remarks 56

4 Harbor-induced tidal salinity dispersion in partially stratified estuaries **57**
4.1 Introduction 58
4.2 Methods 60
4.3 Observations of Exchange Between Channel and Harbor 68
4.4 Generalization from Numerical Modeling 77
4.5 Discussion 83
4.6 Conclusions 86

5 Salinity Dynamics in Partially Deepened Estuaries With stepwise Bathymetry **89**
5.1 Introduction 90
5.2 Method and Analysis 92

5.3 Results . . . 97
5.4 Discussion . . . 108
5.5 Conclusions . . . 115

6 A new harmonic regression approach to interpret and predict estuarine salinity variation 117
6.1 Introduction . . . 118
6.2 Theoretical background . . . 120
6.3 Regression model for salinity time-series . . . 122
6.4 Application to two estuaries . . . 127
6.5 Influence of the down-stream boundary and unsteadiness . . . 139
6.6 Critical evaluation of adopted model formulation . . . 141
6.7 Discussion . . . 144
6.8 Conclusion . . . 147

7 Synthesis 149
7.1 Main findings in a broader perspective . . . 149
7.2 Implications of Our Findings for Possible Salt Intrusion Mitigation Measures . . . 151
7.3 Recommendations for Follow-Up Research . . . 153
7.4 Broader Scientific Questions . . . 155

Appendices 157

A Harbor-induced tidal salinity dispersion in partially stratified estuaries 159
A.1 The salt balance . . . 159
A.2 Expression for Tidal Trapping Driven by Gravitational Dynamics 160

B Salinity Dynamics in Partially Deepened Estuaries With stepwise Bathymetry 163
B.1 Reformulation of Dronkers (1964) Equations . . . 163

C A new harmonic regression approach to interpret and predict estuarine salinity variation 167
C.1 Details regarding the solution procedure . . . 167
C.2 Alternative base-function for the harmonic regression model . . . 170

Bibliography 173

DANKWOORD 182

PUBLICATIONS 183

Graduate School Diploma 184

Authorship statement 186

CHAPTER 1

Introduction

1.1 Estuaries and Salt Intrusion: Background and Context

Estuaries are dynamic regions that form a transition zone between rivers and oceans. The most widely used definition of an estuary is: a semi-enclosed coastal body of water, with free communication with the ocean, where saline seawater is mixed with fresh water river input (Pritchard 1952; Valle-Levinson 2010). However, defining an estuary merely as a geometrically semi-enclosed coastal body does not adequately capture the fact that estuaries represent a continuum between the alluvial and the marine environment (Savenije 2006), also see Figure 1.1.

For humans, estuaries are of great economic and ecological importance. For instance, many major seaports are located in estuaries, as they provide access to both the sea and inland waterways. In addition, the deltaic plains are typically fertile regions, making them well suited for agriculture. Unsurprisingly, a large share of the global population resides in deltaic regions (Valle-Levinson et al. 2000). In recent years, severe salt intrusion events have been reported around the world and their frequency is expected to increase (Lee et al. 2025). Severe estuarine salt intrusion events threaten freshwater resources used for drinking water supply (Mueller et al. 2024; Garcés-Vargas et al. 2020; Shammi et al. 2019), jeopardize agricultural activities, and can harm ecological systems (Saccon et al. 2025; Craft et al. 2009; Herbert et al. 2015). In addition, they pose significant risks to industries that depend on the reliable availability of freshwater. In the future, sea-level rise and reduced river discharges are projected to intensify salt intrusion and increase



Figure 1.1: Satellite picture of the Rhine-Meuse Estuary (Copernicus Sentinel-2 imagery).

the occurrence of extreme salt intrusion events in many estuaries worldwide (Lee et al. 2025).

The increase in severe salt intrusion events is driven not only by changes in the forcings (i.e., sea-level rise and reduced freshwater supply), but also by the fact that estuaries have been heavily modified for human activities. For example, in many estuaries the channel depth has greatly increased due to dredging activities to allow navigation, which typically increases salt intrusion (Rummel et al. 2025; Andrews et al. 2017; Ralston and Geyer 2019). Channel deepening also affects the tides in estuaries (Familkhalili and Talke 2016; Ralston and Talke, et al. 2019; Familkhalili and Talke and Jay 2020), which in its turn influences the salt dynamics depending on the dominant transport mechanisms. Other anthropogenic factors that can alter the extent of salt intrusion include the construction of estuarine barriers, which exert a profound influence on tidal currents (Wei and Williams, et al. 2022; Figueroa et al. 2022). Moreover, the loss of intertidal area can further increase the salinisation length in systems that are more strongly stratified (Siemes et al. 2025; Hendrickx and Pearson 2024).

The growing occurrence of severe salt intrusion events in the Rhine–Meuse estuary, together with the (predicted) reduction in freshwater availability during summer, has motivated the SALTISolutions research program. This thesis, part of Work Package 4.1 of the SALTISolutions program, aims to improve our understanding of how (human-induced) geometric-channel complexities affect salt transport mechanisms in estuaries and contribute to the development of predictive models. The role of geometric channel complexities is increasingly recognized to contribute to shaping the estuarine salt balance, particularly in short, well-mixed estuaries (Chen and Geyer, et al. 2012; Garcia and Geyer and Randall 2022; Garcia and Geyer 2022; Bo and Ralston, et al. 2024). In longer, partially stratified systems, these complexities contribute to estuarine heterogeneity (Geyer and MacCready 2014; Geyer and Ralston 2015; Corlett and Geyer 2020). It has been argued that, as a result of geometric-channel complexities, the dynamics of partially stratified estuaries deviate more strongly from the dynamics in idealized models than previously assumed (Hansen and Rattray Jr 1966a; MacCready and Geyer 2010). Furthermore, the specific role of sequential geometric channel complexities in shaping the salt dynamics in strongly human-modified partially-stratified estuaries of intermediate length, such as the Rhine–Meuse estuary, remains poorly understood. The lack of insight into how these channel complexities locally influence the dynamics and kinematics, and ultimately affect overall estuarine salt transport, poses a challenge for the design of effective countermeasures as well as the development of fast prediction tools, which typically rely on simplified geometries and simplified representations of the transport mechanisms. The following sections outline key aspects relevant to salt intrusion in estuaries. First, a brief overview of the processes governing barotropic tides is provided (Section 1.2), followed by the estuarine salinity balance (Section 1.3). After that, a short introduction to estuarine circulation (Section 1.4), tidal dispersion (Section 1.5), and finally the methods used to predict salt intrusion (Section 1.6) is given. The objectives of this thesis are described in Section 1.7.

1.2 Tides in Estuaries

At the mouth of an estuary, tidal energy enters from the adjacent marine environment. The tidal motion is primarily driven by the gravitational pull of the Moon and the Sun, while their orbit around a common centre of mass generates a resulting centrifugal force (Pugh 1987). Confined by the estuary's lateral boundaries, the tidal energy received at the mouth is transported upstream through work done by the dynamic pressure force. Due to frictional effects along the bed and banks,

the tidal energy dissipates further in the upstream direction, and beyond a certain point, tides are no longer observable.

In many estuaries the tidal range (the difference between high and low water) remains constant or even increases in the up-estuary direction, which is not expected when considering frictional losses alone. Tidal amplification is typically observed in estuaries where the cross-sectional area strongly converges or where a hard reflector is present (Savenije 2006; Friedrichs 2010; Rijn 2011; Dykstra et al. 2024). Channel convergence compresses the tidal energy into a smaller cross-sectional area, leading to an increase in tidal amplitude (often called shoaling or wave funnelling), see Figure 1.2a. This effect of channel convergence can be readily understood from the energy flux equation, known as Green's law (Green et al. 1838; Rijn 2011):

$$F = cE = \sqrt{gH} \cdot \frac{1}{8}\rho g \eta^2 B, \tag{1.1}$$

with g the gravitational acceleration, H the tide averaged depth, B the channel width, ρ the density and η the tidal elevation amplitude. In Eq. 1.1 the wave propagation speed c is assumed to be that of the classical, progressive, frictionless wave, with $c = \sqrt{gH} = \omega/k$, and $E = \frac{1}{8}\rho g \eta^2 B$ is the total energy over the estuary's width. Neglecting frictional energy losses, the tidal amplitude in the upstream direction changes according to Green's law as: $\eta_x/\eta_0 = \left(\frac{B_x}{B_0}\right)^{-1/2}\left(\frac{H_x}{H_0}\right)^{-1/4}$, where the subscript $_0$ denotes conditions at the estuary mouth, and $_x$ refers to a location further upstream. This shows that tides amplify due to the funnelling of tidal energy received at the mouth, caused by the convergence of channel depth and width. The amplification is, however, more sensitive to relative variations in width than in depth (Green et al. 1838; Jay 1991; Kästner et al. 2019).

A variety of analytical solutions have been developed to describe the propagation of tidal waves travelling in the up-estuary direction (Lanzoni and Seminara

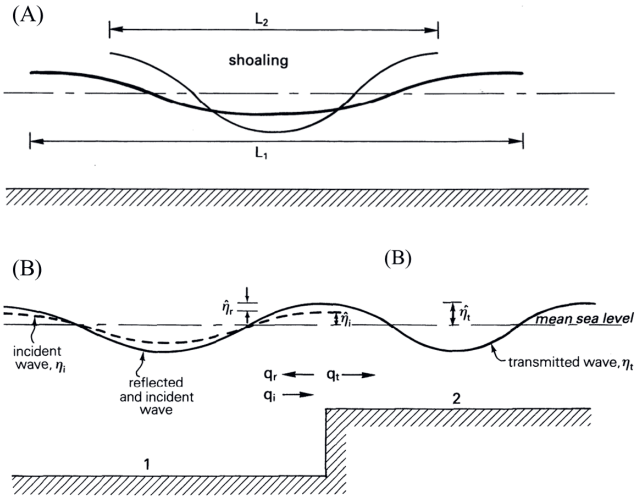


Figure 1.2: Effect of shoaling (a) and partial reflection at a step in the channel bed (b). Figure adapted from Van Rijn et al. (2010).

1998; Friedrichs 2010; Toffolon et al. 2006; Savenije et al. 2008; Rijn 2011), providing insight into the balance between frictional energy losses and channel convergence, as well as the phase difference between the tidal signals of the vertical and horizontal tide. This phase difference is a key parameter that governs the exchange between a main channel and an adjacent side basin, a process examined in detail in this thesis.

Here, a solution by Friedrichs (2010) is discussed to illustrate how several tidal characteristics vary depending on estuarine geometry and friction, with the elevation (η) and velocity (u) expressed as:

$$\eta(x,t) = \hat{\eta}_0\, e^{x/L_a}\, \mathrm{Re}\big\{e^{i(\omega t - kx)}\big\}, \tag{1.2}$$

$$u(x,t) = \hat{u}_0\, e^{x/L_a}\, \mathrm{Re}\big\{e^{i(\omega t - kx - \varphi)}\big\}. \tag{1.3}$$

where $\hat{\eta}_0$ and $\hat{u}_0$ are the elevation and current amplitude at the mouth, $L_a = \dfrac{\hat{\eta}}{\partial\hat{\eta}/\partial x}$ is the characteristic length scale over which the amplitude changes, k is the wave number, ω is the tidal angular frequency, and φ is the phase difference (or velocity phase lead) between tidal elevation and current.

For long and relatively deep systems, Friedrichs (2010) presented solutions for $\hat{u}_0$, φ, and $(kL_a)^{-1}$, where the latter represents the spatial rate of change in tidal elevation (L_a^{-1}) relative to the spatial rate of phase change (k). The tidal current amplitude at the mouth can be represented by:

$$\hat{u}_0 = g\hat{\eta}_0 \frac{k}{\omega} \left| \frac{i - (kL_a)^{-1}}{i + r/\omega} \right|, \tag{1.4}$$

where $r = \dfrac{8}{3\pi}\dfrac{c_d\hat{u}}{H}$ is the linearized friction coefficient (Dronkers 1964), with c_d the quadratic drag coefficient. The phase difference between tidal elevation and current velocity is given by:

$$\varphi = -\arctan\big((L_w k)^{-1} - (L_a k)^{-1}\big), \tag{1.5}$$

where L_w denotes the characteristic convergence length of a exponential decaying channel width. The solution for the dimensionless number $(kL_a)^{-1}$ is given by:

$$(L_a k)^{-1} = \frac{\omega}{r} + \frac{1}{2kL_w} - \sqrt{\frac{\omega^2}{r^2} + 1 + \frac{1}{4(kL_w)^2}}, \tag{1.6}$$

and its values range between -1 and 0. Equations (1.5)-(1.6) can be used to illustrate how the velocity phase lead φ (an important parameter for tidal dispersion mechanisms discussed in this thesis), and the current amplitude, u (which governs estuarine mixing dynamics), vary across different estuarine settings.

First, for a long and straight ($(kL_w)^{-1} \to 0$) and frictionless ($r/\omega \to 0$) channel(Figure 1.3a,d,g), the obtained wave characteristics correspond to those of a progressive wave: no velocity phase lead ($\varphi = 0$), and a constant current amplitude ($\hat{u} = \hat{u}_0 = \left(\frac{\hat{\eta}_0}{H}\frac{\omega}{k}\right)$). When strong friction is assumed ($r/\omega \to \infty$), Eq. (1.6) reduces to $\frac{L_a^{-1}}{k} = -1$, and the maximum phase lead of flow velocity over the surface elevation given by Eq. (1.5) becomes $\varphi = -45^\circ$ (Figure 1.3b,e,h). Hence, without channel convergence or (partial) wave reflection, the maximum phase difference is $\varphi = -45^\circ$ and is solely due to frictional effects. This phase difference, however, can reach -90°—equal to that observed for a standing wave—when

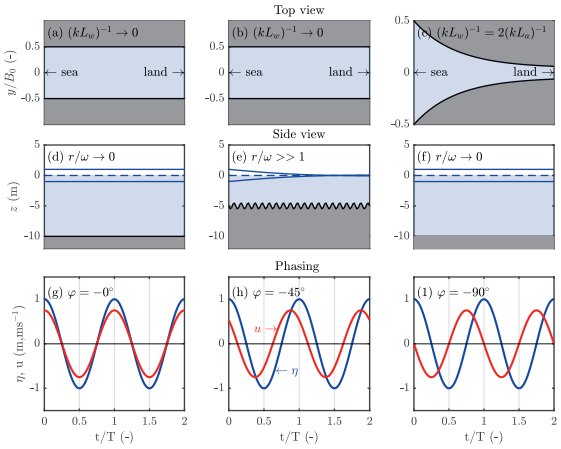


Figure 1.3: Illustration of the phase lead of tidal velocity relative to surface elevation for different geometries and frictional regimes. Panels (a–c) show the three assumed top views (straight, straight and converging). Panels (d–f): Side views for the three cases—deep with a smooth bed, shallow with a rough bed, and deep with a rough bed. The solid blue lines indicate high and low water levels, while the dashed line represents the tidally averaged surface elevation. Panels (g–i) show the tidal current u and tidal elevation η, illustrating the resulting velocity phase lead for the three different cases.

channel convergence is taken into account. In a converging estuary where the tidal amplitude remains constant ($(kL_a)^{-1} = -1$), often referred to as an equilibrium or synchronous estuary (Savenije 2006; Friedrichs 2010), Eq. (1.5) shows that $\varphi = -\arctan\left(\frac{L_w^{-1}}{k}\right)$ (Figure 1.3c,f,i). For strong convergence, the phase difference can approach $\varphi = -90°$, as in a standing wave. However, in this case, a single progressive wave is considered, yet it exhibits a phase difference of $-90°$, which corresponds to a standing wave.

The solution discussed above shows that, when the channel converges, a velocity phase lead of up to 90° is possible without reflection. In strongly converging (and highly dissipative, $r/\omega > 1$) systems, reflected waves rapidly lose energy due to widening and frictional effects during the propagation towards sea, and in practically do not exist (Friedrichs 2010). This is in contrast to deeper and non-convergent systems, where reflected waves resulting from partial wave reflection have a profound effect on tidal dynamics. Partial wave reflection is caused by discontinuities in the cross-sectional area, for instance steps in the channel bed (see Figure 1.2b). The resulting damping, velocity amplitude, and phase lead cannot be easily determined using the analytical solutions discussed above and often require a semi-analytical approach (Dronkers 1964).

The section above summarizes how the phase lead of the velocity over the tidal elevation, φ, varies depending on friction and channel (width) convergence. This velocity phase lead, or more precisely the difference in velocity phase lead between adjacent channels (see Section 1.5), is an important parameter for the dispersion of salt in estuaries characterized by a channel network. This topic is further addressed in Chapters 3 and 4 of this thesis. Furthermore, Chapter 5

investigates another aspect of geometric channel complexity, namely the influence of partial tidal reflection (the dynamics of partial-wave reflection are not fully covered here) due to steps in the channel bed and its resulting effects on salt intrusion.

1.3 The Estuarine salt Balance

In general, salt intrusion in estuaries is described as a balance between flushing by freshwater river discharge and dispersive mechanisms that act against this flushing. Assuming no lateral variations, the subtidal salt balance for the depth averaged salinity is commonly expressed as (MacCready 2004; MacCready and Geyer 2010):

$$\frac{\partial \bar{s}}{\partial t} = \frac{\partial}{\partial x}\left(- \bar{u}\bar{s} - \overline{u's'} + K_{\text{tide}} \frac{\partial \bar{s}}{\partial x}\right), \tag{1.7}$$

with $\bar{u}$ and $\bar{s}$ representing the tide- and depth-averaged current velocity and salinity, while u' and s' denote the tide-averaged vertical deviations from their depth-averaged values (see Figure 1.4 a,b and further discussed in Section 1.4). The terms on the right-hand side represent: (i) the contribution of the tide-averaged current and salinity, which is associated with flushing, predominantly due to the river-induced current; (ii) the depth-averaged product of deviations from the tidally averaged velocity and salinity, which is the result the estuarine circulation (Section 1.4); and (iii) the contribution of tidal dispersion mechanisms here parametrized using a Fickian diffusion coefficient K_{tide}. This tidal contribution results from oscillatory boundary-layer shear and from the interaction between tidal currents and local geometric-channel complexities (Fischer et al. 1979; Geyer and Signell 1992; Garcia and Geyer 2022). It is expressed in the depth-averaged, tide-varying correlation between the velocity (u_t) and salinity (s_t) signals, commonly referred to as the tidal oscillatory flux (see Figure 1.4a,b and Section 1.5 for further discussion). When the system is in equilibrium (it does not gain or lose salt in a tide-averaged perspective), a balance exists between the terms in the right hand side of the equation. The overall estuarine salt balance can be obtained by integrating over the salt intrusion length (Banas et al. 2004; Valle-Levinson 2010).

1.4 The Estuarine Circulation

Across the water column, the tide-averaged current is often seaward near the surface and directed landward near the bottom, reflecting the vertical structure of what is known as the estuarine circulation (Figure 1.4a,b). This circulation primarily results from a horizontal density gradient caused by the difference in salinity between seawater and freshwater (MacCready and Geyer 2010; Geyer and MacCready 2014). The earliest written references to the estuarine circulation date back to the first century, reported by the Romans (Valle-Levinson 2010). The precise starting point of modern estuarine dynamics is difficult to define, but early theoretical foundations were laid by Knudsen, whose classical relation connected freshwater input, salinity distribution, and exchange flow (Knudsen 1900) (see the appendix in Burchard and Bolding, et al. (2018) for the English translation). The first quantitative field evidence of estuarine circulation is widely attributed to Pritchard (1952), who documented the vertical structure of flow in the James River estuary. His measurements showed a tide-averaged seaward surface layer overlying a landward near-bed flow, confirming the two-layer exchange that theory had long suggested. These observations marked a turning point, providing the empirical basis for the modern understanding of estuarine circulation.

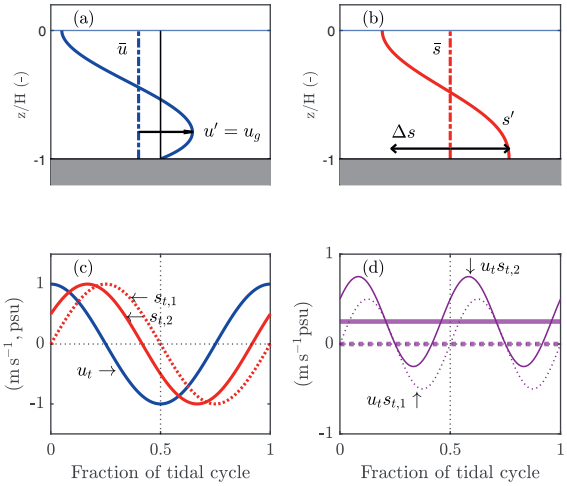


Figure 1.4: Visualization of the variables in Eq. 1.7. (a) Schematic of a typical tide-averaged velocity profile in an estuary (solid blue line). The arrow indicates the magnitude of the gravitational circulation (see Eq. 1.8). The depth- and tide-averaged velocity is shown by the dashed blue line, while the deviation from the mean is represented by the black vertical line. (b) Same as panel (a), but for the tide-averaged vertical salinity profile. The top–bottom salinity difference is indicated by Δs (see Eq. 1.9).(c) Illustration of an assumed tidal current $u_t = \cos(\omega t)$ (demeaned signal) and two assumed tidally varying salinity signals (demeaned), namely $s_{t,1} = \sin(\omega t)$ and $s_{t,2} = \sin(\omega t + \frac{1}{6}\pi)$. (d) Visualization of the correlation between $u_t s_t$, with solid lines denoting the tide-averaged values.

1.4.1 Gravitational circulation

The first classical theory of estuarine circulation in well-mixed and partially mixed estuaries was developed by Hansen and Rattray (1965). They derived a simplified analytical expression for the subtidal flow structure by assuming a balance between the pressure gradient and internal stresses. This balance leads to the classical polynomial description of the subtidal vertical velocity profile. The magnitude of the vertically sheared exchange flow, U_g, is given by (Hansen and Rattray 1965; Monismith et al. 2002; Valle-Levinson 2010) (also see Figure 1.4a):

$$U_g = \frac{1}{48} \frac{\beta g \frac{\partial \bar{s}}{\partial x} H^3}{A_v}, \tag{1.8}$$

with β the salinity expansion coefficient, A_v a constant vertical eddy viscosity, and H the water depth. This eddy viscosity A_v is commonly parametrized as $A_v \sim \hat{u}H$, with $\hat{u}$ the tidal velocity amplitude. The vertical stratification results from the competition between the straining induced by the vertically sheared flow ($U_g \frac{\partial \bar{s}}{\partial x}$) and the vertical mixing ($A_v \frac{\Delta s}{H^2}$). From this balance, the salinity difference between surface and bottom, Δs, can be approximated as (Figure 1.4b):

$$\Delta s \sim \frac{U_g \frac{\partial \bar{s}}{\partial x} H^2}{A_v}. \tag{1.9}$$

The associated depth-integrated salt flux per unit width ($F = HU_g\Delta s$), can be expressed using Eq. 1.8 and Eq. 1.9. Expressing this depth-integrated salt flux in terms of an equivalent Fickian dispersion coefficient ($F = -HK\frac{\partial \bar{s}}{\partial x}$) yields Hansen and Rattray (1965):

$$K_g \sim \frac{(\beta g)^2 \left(\frac{\partial \bar{s}}{\partial x}\right)^2 H^8}{A_v^3} \sim \frac{(\beta g)^2 \left(\frac{\partial \bar{s}}{\partial x}\right)^2 H^5}{\hat{u}^3}. \tag{1.10}$$

In Equation 1.10, the dispersion of salt due to gravitational circulations is represented by K_g. This parameter depends strongly on water depth H and decreases with increasing vertical mixing. Furthermore, the noticeable effect is its non-linear dependency on the salinity gradient itself. As the salinity field steepens, $K_g \propto \left(\frac{\partial \bar{s}}{\partial x}\right)^2$, acting as a negative feedback that counteracts further compression of the salinity field. The balance between subtidal shear by gravitation circulation and river-induced flushing is later analysed by Chatwin (1976) and further generalized by MacCready (2004).

1.4.2 Tidal Straining and Asymmetric Mixing

The classical subtidal balance for estuarine circulation discussed in the previous section explains the observed tidally averaged residual currents surprisingly well in many systems (Geyer and Trowbridge, et al. 2000; MacCready and Geyer 2010). However, analyses of the processes controlling the tidally averaged current suggest that, in many cases, factors other than the classical gravitational circulation play a more significant role in shaping the estuarine circulation (MacCready and Geyer 2010).

One of these additional mechanisms is tidal straining, first observed and analysed by Simpson and Brown, et al. (1990) and Aken (1986). During the ebb, differential advection by the vertically sheared tidal flow carries low-salinity water over denser water, enhancing stratification when mixing by the bottom boundary layer is too weak to counteract the onset of stratification. Simpson and Brown, et al. (1990) observed that during the flood, stratification breaks down rapidly due to the advection of relatively saline water over fresher water (unstable stratification). Simpson and Brown, et al. (1990) referred to this as strain-induced periodic stratification (SIPS). The balance between the strain induced stratification and mixing can be expressed based on the Horizontal Richardson number (Simpson and Brown, et al. (1990) and Stacey and Burau, et al. (2001)), nowadays often referred to as the Simpson number (Stacey and Brennan, et al. 2010; Burchard and Hetland, et al. 2011):

$$Ri_x = \frac{\beta g \frac{\partial \bar{s}}{\partial x} H^2}{c_d U_t^2}, \tag{1.11}$$

with c_d the drag coefficient. Simpson and Brown, et al. (1990) found that SIPS only occurred when $Ri_x < 0.1$, and for large values the water column remains stratified throughout the entire tide (Ralston and Stacey 2005). Tidal straining is closely related to the strain mechanism described in the previous section, but differs in that the vertical flow variations acting on the along-channel salinity gradient arise from the (vertically sheared) tidal oscillatory boundary layer instead of the gravitational circulation.

The tidal variations in stratification affect the tide-averaged momentum balance and, consequently, influence estuarine circulation. Jay and Musiak (1994) and Jay and Musiak (1996) demonstrated that stronger mixing during flood allows a more efficient transfer of high-momentum water downward, thereby strengthening the flood-averaged near-bottom current compared to the ebb-averaged current. This flood–ebb asymmetry introduces a tidally averaged current profile that has a shape similar to the profile resulting from gravitational circulation. Tidally variable mixing and its effect on the estuarine circulation has later been further analysed by various authors (Burchard and Hetland 2010; Cheng et al. 2010; Burchard and Hetland, et al. 2011; Dijkstra and Schuttelaars and Burchard 2017). This process is further complicated by the effects of lateral flow–induced strain-driven stratification (Nunes and Simpson 1985; Lerczak and Rockwell Geyer 2004; Burchard and Hetland, et al. 2011; Schulz et al. 2015).

1.5 Tidal dispersion

In many estuaries, salt transport is primarily governed by estuarine circulation, particularly in deeper and longer systems where tidal forcing is relatively weak. However, in shorter and shallower estuaries, the salt balance is generally dominated by tidal dispersion (Chen and Geyer, et al. 2012). However, even in estuaries where the estuarine circulation dominates the overall transport of salt, the upstream sections often exhibit a transition where tidal dispersion becomes the primary transport mechanism (Dijkstra and Schuttelaars and Kranenburg 2022). As noted earlier, tidal dispersion results from oscillatory boundary-layer shear and the interaction between tidal currents and local geometric-channel complexities (Geyer and Signell 1992; Fischer et al. 1979; Garcia and Geyer 2022). These channel-complexity-driven dispersion mechanisms redistribute salt over the course of a tidal cycle across distances on the order of the tidal excursion (Dronkers and Van de Kreeke 1986; Geyer and Signell 1992). This strong dependence on local geometry, combined with the relatively limited spatial extent of their influence, may explain why tidal dispersion mechanisms have historically received less attention than estuarine circulation and remain relatively poorly understood, often being represented in idealized models by a single, constant dispersion coefficient K_{tide} (MacCready 1999; Monismith et al. 2002; MacCready 2004; MacCready 2007; Ralston and Geyer and Lerczak 2008; Dijkstra and Schuttelaars 2021; Dijkstra and Schuttelaars and Kranenburg 2022; Jongbloed and Schuttelaars, et al. 2022; Biemond et al. 2025).

The impact of tidal dispersion is reflected in the correlation between the cross-sectionally averaged, tidally varying velocity and salinity signals (Fischer et al. 1979). On a tide-averaged time scale, this correlation produces a net salt flux when the two signals are less than in quadrature (MacVean and Stacey 2011), see Figure 1.4. A key insight into the tidal oscillatory flux was provided by Dronkers and Van de Kreeke (1986), who demonstrated that, within a single channel with well-defined lateral boundaries, the tidal oscillatory salt flux arises from the difference between the (laterally and/or vertically) sheared salt flux experienced along a plane moving with the tidal motion (i.e., a quasi-Lagrangian plane) and the sheared salt flux observed at a fixed Eulerian cross-section. Their analysis highlights that the tidal oscillatory flux is not purely a local phenomenon, but arises from the spatio-temporal variability of the vertically and/or laterally instantaneous sheared salt flux that occurs over the tidal excursion length during a tidal cycle. The spatial variability in lateral or vertical sheared exchange is particularly pronounced in the presence of geometric features, such as dead-end side channels, channel constrictions, or intertidal areas (Geyer and Signell 1992; Dronkers and Van de Kreeke 1986). Recent work by Garcia and Geyer (2022) further illustrates this, based on their investigation of tidal oscillatory fluxes in

the North River (USA). In the remainder of this section several geometric features that are typically associated with tidal dispersion are further discussed.

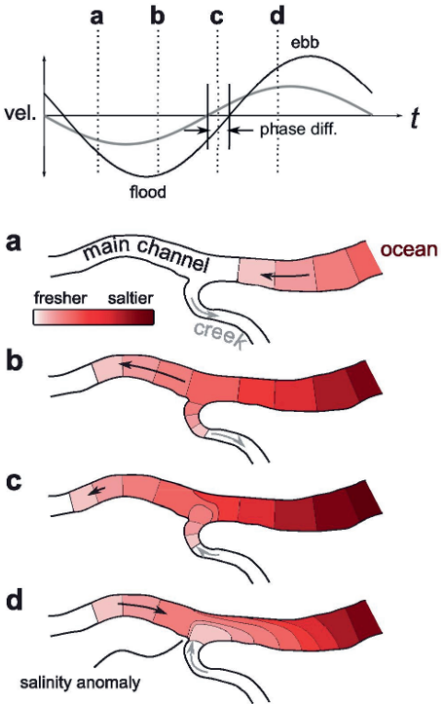


Figure 1.5: Illustration of the exchange between the main channel and a tidal creek, showing the resulting salt anomaly in the main channel due to a velocity phase difference between the two. (Figure adapted from Garcia and Geyer and Randall (2022))

1.5.1 Dead-zones and Tidal Trapping

One specific process known to contribute to the tidal-oscillatory salt flux is the temporal storage and release of saltwater in side-volumes adjacent to the main channel (often dead zones), which act as traps and give rise to the term tidal trapping (Okubo 1973; Fischer et al. 1979; Dronkers 1978; Wolanski and Ridd 1986; MacVean and Stacey 2011).

Examples of local traps include side channels such as tidal creeks or harbors (Dronkers 1978; MacVean and Stacey 2011). For these features, the length of the trap entrance, which connects them to the main channel, Δx, is much smaller than the tidal excursion length L_t (i.e., $\Delta x \ll L_t$). Besides these local features, larger-scale geometric elements such as shoals, tidal flats, marshes, and shoreline irregularities can also generate dead zones. However, these features typically extend along the estuarine axis ($\Delta x \geq L_t$). For both cases, these dead zones/traps contribute to the up-estuary salt flux by temporarily storing saltwater from the main channel and releasing it back elsewhere in the tidal cycle. Or, in other words, these dead zones introduce a redistribution of saltwater over a distance comparable to the tidal excursion.

The exchange of salt between the main channel and these dead zones can occur through different transport mechanisms, and the existing literature uses this distinction to classify various forms of tidal trapping (Okubo 1973; Dronkers 1978; MacVean and Stacey 2011). The first mechanism involves exchange driven solely by the barotropic filling and emptying of the traps. Because the cross-sectionally averaged current in the traps leads the main-channel current in phase, salt is redistributed within the main channel over the course of a tidal cycle (see Figure 1.7). As shown in Section 1.2, a phase difference often exists between the water-level signal and the flow-velocity signal, depending on friction and channel geometry. The phase lead of the velocity relative to the tidal elevation typically differs between the main channel and the side channel, resulting in a velocity-phase difference between the channel and the dead zone. This phase difference causes water entering the side channel during one part of the tide to return out of phase with the water mass that remains in the main channel, producing a net exchange (Figure 1.5). In this thesis, this process is referred to as advective out-of-phase exchange. This exchange mechanism depends on the velocity-phase difference between the main channel and the trap. However, the existing literature presents ambiguity regarding how tidal trapping depends on the difference in velocity-phase lead between the main channel and the dead zone. For example, MacVean and Stacey (2011) provide parametrizations for the associated dispersion coefficient that are inconsistent with the phase-dependence reported by Dronkers (1978).

The second exchange mechanism is referred to as diffusive exchange (Okubo 1973; MacVean and Stacey 2011). In this case, the exchange between the main channel and the trap is solely driven by processes that are, in a cross-sectionally averaged sense, diffusive of nature (strictly speaking, dispersive would be more accurate, but the term diffusive is used here to remain consistent with the relevant literature). This diffusive channel-trap exchange can, for example, be the result of eddies at the trap entrance or density currents (Dronkers 1978; Garcia and Geyer 2022). This form of tidal trapping was most notably studied by Okubo (1973), who investigated the influence of shoreline irregularities and derived an elegant expression to quantify the resulting dispersion. However, Okubo (1973)'s expression does not specify the actual mechanisms that drive the exchange. As already noted by Okubo (1973), precise knowledge of the exchange mechanisms between the main channel and the trap is required to improve our understanding of the effect of these dead zones. To date, however, only limited research has addressed this issue in relation to tidal trapping.

Research Gap: salt dispersion from a lateral tidal trap
Tidal trapping has long been recognized as an important contributor to tidal dispersion in estuaries (Schijf and Schönfled 1953; Fischer et al. 1979). However, in many 1D or 2D (idealized) models, K_{tide} is often still assumed to be constant, reflecting our limited understanding and the difficulty of providing accurate formulations to describe tidal dispersion mechanisms. This lack of understanding of how to parametrize K_{tide} is also reflected in existing parametrizations of tidal trapping through advective out-of-phase channel–trap exchange, which exhibit fundamental inconsistencies among the different proposed formulations (Schijf and Schönfled 1953; Dronkers 1978; MacVean and Stacey 2011). Chapters 2 and 3 of this thesis investigate these inconsistencies in greater detail with the aim of resolving them. Furthermore, the combined effect of simultaneous advective out-of-phase exchange and diffusive exchange has not yet been explored. This open question is addressed in Chapter 2. In addition, the processes governing diffusive exchange between channels and traps have received increasing attention (Ralston and Stacey 2005; Garcia and Geyer and Randall 2022; Garcia and Geyer 2022). Yet, their contribution to along-channel dispersion remains poorly understood and has been investigated to a much lesser extent than the exchange processes themselves. In the context of the Rhine–Meuse estuary, understanding how harbors influence salt dispersion is particularly important, as it poses challenges not only for strategic management but also for idealized modelling. Chapter 4 of this thesis addresses this gap, focusing specifically on the dynamics of channel–harbor exchange.

1.5.2 Jet-sink Exchange and the Mouth region

Jet-Sink exchange is typically associated with the mouth region of an estuary (Stommel and Farmer 1952; Chen and Geyer, et al. 2012), but is also applicable for channel constriction (Garcia and Geyer 2022) . Near the mouth of an estuary, the ebb flow typically exits as a confined jet, where inertia terms dominate the momentum balance. In contrast, the flood inflow enters more broadly around the mouth area (Figure 1.6a). As a consequence of these contrasting flood–ebb characteristics, each tidal cycle results in the exchange of non-native, relatively saline water with less saline water from inside the estuary. For this reason, the process is often described as one of the mechanisms contributing to tidal pumping, in which a net residual transport arises from flood–ebb asymmetries in current magnitude, duration, pathway, or mixing efficiency (Fischer et al. 1979). The exchange with non-native water at the estuary mouth is not solely a consequence of the jet-like characteristics of the ebb flow and the semi-circular flood inflow; it may also be influenced by the formation of bottom-lift-off fronts and other gravitational dynamics (Armi 1986; Largier 1992; MacDonald and Geyer 2005; Horner-Devine et al. 2015). These bottom-lifts typically arise from increases in depth (or width), which induce a hydraulic response that promotes front formation (MacDonald and Geyer 2005) (Figure 1.6b). Garcia and Geyer (2022) demonstrated that the vertically sheared salt flux associated with front formation at the estuary mouth significantly contributes to the tidal oscillatory salt flux observed within the estuary near the mouth, in addition to the laterally sheared exchange of salt linked to jet-like flow characteristics.

Research Gap: salt dispersion from an abrupt depth step
The mouth region of an estuary is typically associated with the dynamics of river plumes and has received considerable attention (Horner-Devine et al. 2015). Additionally, the contribution of tidal oscillatory salt flux transport near the mouth region is well recognized (Stommel and Farmer 1952; MacCready 2007; Chen and Geyer, et al. 2012; Garcia and Geyer 2022). However, the generation of bottom lift-off points—which typically develop near the estuary mouth and contribute to tidal dispersion in this region—can also develop within the estuary itself, particularly in regions with sharp changes in channel geometry (Geyer and Ralston 2015; Corlett and Geyer 2020). A key distinction between the frontal dynamics near the estuary mouth and the fronts that develop within the estuary is that the latter contribute directly to estuarine heterogeneity (Geyer and MacCready 2014; Geyer and Ralston 2015; Corlett and Geyer 2020). This estuarine heterogeneity must be reflected in the spatio-temporal variability in the contribution of exchange resulting from vertical shear. The extent to which this variability subsequently contributes to tidal dispersion (K_{tide}) by introducing flood–ebb asymmetries in the oscillatory exchange pathways remains under explored. Understanding these dynamics is particularly relevant for highly engineered estuaries, such as the Rhine–Meuse Estuary, which are characterized by stepped bathymetries that create locations where the cross-sectional area expands rapidly. In Chapter 5, we explore the dynamics of estuaries with stepped bathymetries and investigate how these sudden depth transitions influence the estuarine dynamics and may give rise to exchange mechanisms similar to those typically associated with mouth regions.

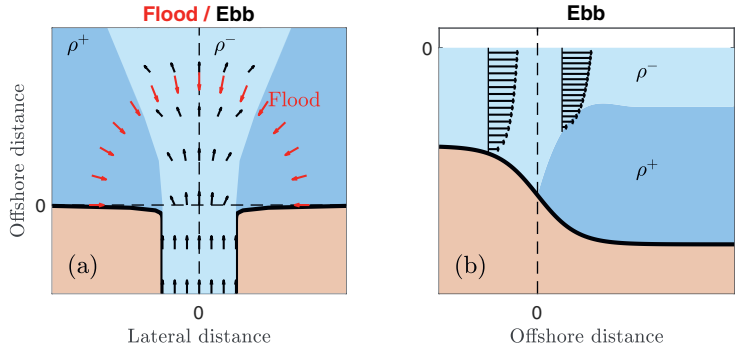


Figure 1.6: Schematic of the dynamics near the mouth region. (a) Illustration of the hypothesized flood and ebb flows at the surface of the estuary mouth. The ebb flow exits the estuary in a more confined, jet-like manner, while the flood flow approaches from all around the mouth. (b) Illustration of a bottom lift-off point that develops due to the hydraulic response caused by lateral expansion and increased depth.

1.6 Predicting Estuarine Salinity and Salt Intrusion

For accurate predictions of estuarine salinity, high-resolution hydrostatic 3D numerical models capable of resolving most of the relevant exchange mechanisms can be employed to accurately predict salt intrusion (examples are Gerritsma et al. (2025), Rummel et al. (2025), and Bo and Ralston, et al. (2024)). An alternative approach is to use 1D numeral models (Deltares 2025). Although substantially faster than full 3D models, they do not resolve the exchange mechanisms that arise from three

dimensional or at least two dimensional vertical flow and salinity structure, and therefore rely heavily on parameterisation of the dispersive processes, which limits their predictive skill. Idealised semi analytical models (MacCready 2004; Wei and Schramkowski, et al. 2016; Jongbloed and Schuttelaars, et al. 2022; Biemond et al. 2025) solve the dominant terms of the transport equation under simplified geometric and dynamical assumptions. These models provide valuable insight into salt transport mechanisms, particularly those associated with gravitational circulation, but often exhibit lower predictive skill. In recent years, machine learning approaches have also become increasingly common (Wullems et al. 2023; Zhou and Liu, et al. 2020; Rohmer and Brisset 2017).These data-driven models can provide accurate short-term salinity forecasts on time scales of a few days ahead, but their predictive skill typically deteriorates rapidly beyond this horizon. In practice, however, water managers and consultants frequently rely on simpler and more easily interpretable analytical models and semi-empirical relations to estimate salt intrusion efficiently (further discussed below) and support decision making. These relations typically predict the tidally averaged salt intrusion length, while operational decisions depend on salinity at specific intake locations and on short intra-tidal windows whose timing and duration may vary depending on surge conditions or other varying forcing conditions.

Semi-empirical predictive relations for the intrusion length are often based on the scaling of gravitational circulation (see Section 1.4). The salt intrusion length L_s can be expressed as (Hansen and Rattray Jr 1966a; Monismith et al. 2002):

$$L_s \sim \frac{(g\beta S_0)^{2/3} A^{1/3} H^{5/3}}{Q_r^{1/3} U_t}, \tag{1.12}$$

with S_0 the ocean salinity, A the cross-sectional area, H the depth, Q_r the river discharge. Based on Eq. 1.12, many authors have related the quasi-steady salt intrusion length to river discharge using a power-law relationship of the form:

$$L_s = \alpha Q_r^{\beta}, \tag{1.13}$$

to analyse intrusion dynamics and to gain insight into the underlying physics. The exponent β m may reflect the dominant transport mode, with $\beta \approx -1/3$ for gravitational circulation (Hansen and Rattray 1965; Chatwin 1976) , $\beta \approx -1$ when the intrusion length is stirred by tidal dispersion (constant dispersion coefficient) (MacCready 2007) and $\beta \approx -2$ for arrested salt-wedges systems (Schijf and Schönfled 1953). In practice, empirically obtained values for β can vary significantly due to geometry on the estuary, estuarine dynamics, and temporal variability of the river discharge (Monismith et al. 2002; Abood 1974; Ralston and Geyer and Lerczak 2008; Lerczak and Geyer and Ralston 2009). Due to unsteady effects, which arise when the estuary's response time exceeds the time scale of the dominant forcing such as discharge variations, a quasi-steady approach often fails to accurately capture the evolution of the salt intrusion length. To account for these unsteady dynamics during non-stationary discharge conditions, Eq. 1.13 is frequently extended with an autoregressive term, yielding a more predictive model for salt intrusion length (Jassby et al. 1995; Monismith et al. 2002; Reyes-Merlo et al. 2013; Guerra-Chanis et al. 2019).

Analytical models have been proposed to describe one-dimensional along-channel salinity distributions in estuaries with varying cross-sectional area. Prandle (1981), was among the first to derive an expression that accounts for both geometric variation (via an exponential decay) and different functional forms of mixing, either constant or dependent on the along-channel salinity gradient. Later, Savenije (1986) and Savenije (1993) derived a semi-empirical relation for the

along-channel dispersion coefficient and resulting salinity distribution. Despite its empirical basis, this model is widely used and cited (Nguyen and Savenije 2006; Shaha and Cho 2009; Zhang and Savenije, et al. 2011; Gisen and Savenije, et al. 2015; Gisen and Savenije 2015), with closely related models proposed by Kuijper and Van Rijn (2011) and Zhang and Savenije (2019). These models generally assume quasi-steady conditions. Extensions partially accounting for unsteady effects on one-dimensional salinity distributions have also been derived (Lewis and Uncles 2003; Gay and O'Donnell 2007), though typically under the assumption of a constant dispersion coefficient. Overall, these approaches predict tidally averaged or slack-water salinity distributions, with only a few models explicitly accounting for tidal variations (Ippen and Harleman 1961; Xu et al. 2019).

Research Gap: harmonic analysis of salt dynamics
Most of the above described formulations for one dimensional salt distributions and predictive tools for the tidally averaged salt intrusion length have limited applicability for capturing and predicting intertidal salinity variations at monitoring stations, particularly under non-stationary forcing conditions and when unsteadiness effects are important. In comparison, a related field of research focuses on forecasting non stationary estuarine tidal records (Matte and Jay, et al. 2013; Matte and Secretan, et al. 2014). To capture and predict these non-stationary water levels at monitoring stations, hybrid harmonic regression models have been developed that extend the classical harmonic analysis by incorporating analytical models for tidal propagation. These models combine analytically derived relations that link external forcing with local responses, in which empirical coefficients and exponents (similar to α and β in Eq. 1.13) are optimised within the harmonic-analysis framework, making use of the fact that tidal driving frequencies are known. This type of hybrid harmonic regression model has proven to be an effective tool for analysing non stationary water levels and for providing accurate and reliable predictions (Matte and Jay, et al. 2013; Matte and Secretan, et al. 2014). To date, this approach, which provides rapid predictions at both subtidal and intratidal time scales relevant for water management, has not been applied to estuarine salinity records. Chapter 6 investigates how this hybrid harmonic framework can be used to generate accurate salinity predictions at monitoring stations while also providing an easily interpretable synoptic description of estuarine conditions.

1.7 Objective and Research Goals

The identified research gaps show that tidal-dispersion mechanisms arising from geometric channel complexity remain insufficiently understood to effectively parameterize these processes for simplified models and/or to support decision-making for the management of estuarine systems. This lack in process understanding is particularly problematic for the Rhine–Meuse estuary, where sharp bathymetric transitions, branching channels, and extensive harbor basins create a geometric setting whose contribution to salt dispersion cannot be adequately explained using existing theory. Because this thesis is ultimately motivated by the need to better predict—and mitigate—increasingly severe salt-intrusion events, it focuses on advancing our understanding of tidal-dispersion processes generated by such geometric complexity. A further aim of this thesis is to develop fast and reliable prediction tools for salinisation at monitoring stations, which are typically located at strategically important water-management locations near freshwater intake points. Water managers rely on such predictions to support operational decision-making, ensuring that surrounding areas receive sufficient freshwater supply and are protected from further salinisation of their control zones.

With these overarching goals, and the research gaps identified in the previous section in mind, the following research objectives are addressed in this thesis:

1. **Understand salt dispersion through tidal trapping by dead-end side channels (Chapter 2 and 3).**

   The role of temporal storage and release of salt water in storage areas such as dead zones and dead-end side channels within the tidal cycle has long been recognized as a key mechanism contributing to the dispersion of salt (Okubo 1973; Fischer et al. 1979; Geyer and Signell 1992). However, the existing literature shows inconsistencies regarding how this mechanism depends on the velocity phase lead in the trap relative to the main channel velocity, when the exchange is driven by advective out-of-phase exchange. Moreover, little effort has been made to analyse and quantify the combined effects of advective out-of-phase exchange and diffusive exchange occurring simultaneously.

   - How can we quantify the additional tide-averaged up-estuary salt transport that results from channel-trap exchange?
   - What is the relation between the phase lead of the velocity signal in the trap over the velocity signal in the main channel and the resulting additional up-estuary salt transport?
   - How does the additional up-estuary salt transport depend on the relative contributions of advective out-of-phase and diffusive exchange?

2. Determine how harbor-initiated tidal trapping contributes to the dispersive transport of salt in the New Meuse (**Chapter 4).**

   Building on the knowledge gained in Chapter 2, this chapter aims to identify the dominant mechanisms of salt exchange between the main channel and adjacent harbors in the Rhine–Meuse estuary, and subsequently quantify their contribution to the overall up-estuary salt transport. Furthermore, the focus here is to develop a more thorough understanding of diffusive channel–harbor exchange and its implications for tidal dispersion.

   - To what extent do harbors contribute to salt dispersion and, ultimately, to salt intrusion in the New–Meuse estuary?
   - Through which channel–harbor exchange mechanisms do harbors influence estuarine salt dispersion?
   - What are the key geometric properties and hydrodynamic variables that determine spatial variations in the relative contribution of harbors to salt intrusion?

3. Understand how abrupt steps in the channel bed affect tidal dispersion and influence the salt intrusion (**Chapter 5).**

   To accommodate modern vessels, the lower estuary is frequently dredged, creating staircase-like bathymetries. Although such sharp bathymetric steps are widespread and are expected to affect barotropic tidal propagation (via partial reflection) and salinity structure (through rapid channel expansions that favour frontal formation), their influence on salt dispersion and salt intrusion has received surprisingly little attention.

- Do these staircase-like bottom profile significantly influence the barotropic and baroclinic tide?
- What role does the bed slope inclination of the depth transition play in shaping the resulting salt transport mechanisms?
- To what extent do staircase-like bottom profiles affect salt intrusion in estuaries?

4. **Reformulate the hybrid-harmonic regression approach developed for non-stationary tidal water level predictions to capture estuarine salinity levels at monitoring stations (Chapter 6).**

   The hybrid harmonic regression approach, which are modifications of classical harmonic analysis, have been developed to capture non-stationary estuarine water level time-series (Matte and Jay, et al. 2013; Matte and Secretan, et al. 2014; Hoitink et al. 2017). These models enable rapid predictions at monitoring stations and provide a means to interpret historical time series, with empirically determined coefficients offering a concise summary of system behaviour. So far, no attempt has been made to reformulate the hybrid harmonic regression approach to capture estuarine salinity variations at monitoring stations. Given that the dynamics of estuarine salinity differ fundamentally from those of tidal water levels, we set the following objectives:

   - Can the hybrid harmonic regression approach be reformulated to predict estuarine salinity at monitoring stations, and for what types of estuarine environments would such a model be suitable?
   - To what extent can the hybrid-harmonic regression framework deal with estuarine salinity–specific characteristics, such as prolonged periods when salinity equals that of the fresh river water and lag effects associated with unsteadiness of the salinity field?
   - Can this type of model provide a synoptic understanding of the system's functioning, enabling its use beyond purely predictive purposes?

1.8 Outline of thesis

A visual overview of the connection between the individuals chapters is given in Figure 1.7. Chapter 2 aims to understand how the temporal storage and release of salt in dead-end side channels contributes to estuarine salt dispersion, and how this additional dispersive contribution can be quantified. A numerical model with idealized geometry is used to solve the one-dimensional, cross-sectionally averaged salt balance, simulate channel–trap exchange, and quantify the resulting additional salt transport. The model results are subsequently used to verify a balance that separately quantifies the individual dispersive contributions of different channel–trap exchange mechanisms, and to explore how both advective out-of-phase exchange and exchange that is diffusive in nature shape the overall dispersive effect. Chapter 3 presents a continuation of the work in Chapter 2 (presented here as a separate chapter), and clarifies the ambiguities in the existing literature regarding advective out-of-phase exchange. Chapter 4 builds upon the understanding gained in Chapter 2 to investigate how, and through which mechanisms, channel–harbor exchange contributes to salt dispersion in the New Meuse. First, observational data from two harbors with starkly contrasting channel–harbor exchange characteristics are analysed. Subsequently, a numerical model of the system is used to simulate salinity dynamics over an extended period, enabling us to generalise the results by quantifying the contributions of individual harbors and identifying the key factors that determine their dispersive influence through tidal trapping. These new

insights are synthesised into a new parameterisation for tidal dispersion. Chapter 5 explores how sharp channel-bed variations resulting from partial channel deepening influence salt transport and the salt-intrusion length across a range of bathymetric configurations and forcing conditions, using a series of numerical simulations with idealised channel geometries. Specifically, we examine the role of partial tidal-wave reflection in shaping the salt dynamics and analyse how sharp depth transitions trigger front formation, which exerts substantial control on the tidal-dispersion mechanisms observed upstream of the depth transition. In Chapter 6, we reformulate the hybrid harmonic regression approach broadly used in tidal prediction to make it applicable to estuarine salinity records, with the aim of developing a new model type that enables fast prediction of estuarine salinity at monitoring stations. To achieve this, we investigate how to deal with clipped time series and lag effects in salinity records. We test the model by applying it to salinity records from monitoring stations. Hereafter, we evaluate the model's performance, assess the chosen model formulations, and examine the extent to which the model can be used to gain insights into estuarine dynamics, beyond the capability of providing fast prediction. Finally, Chapter 7 reflects on the insights gained throughout this thesis, briefly discusses considerations for mitigating salt intrusion, and outlines directions for future research.

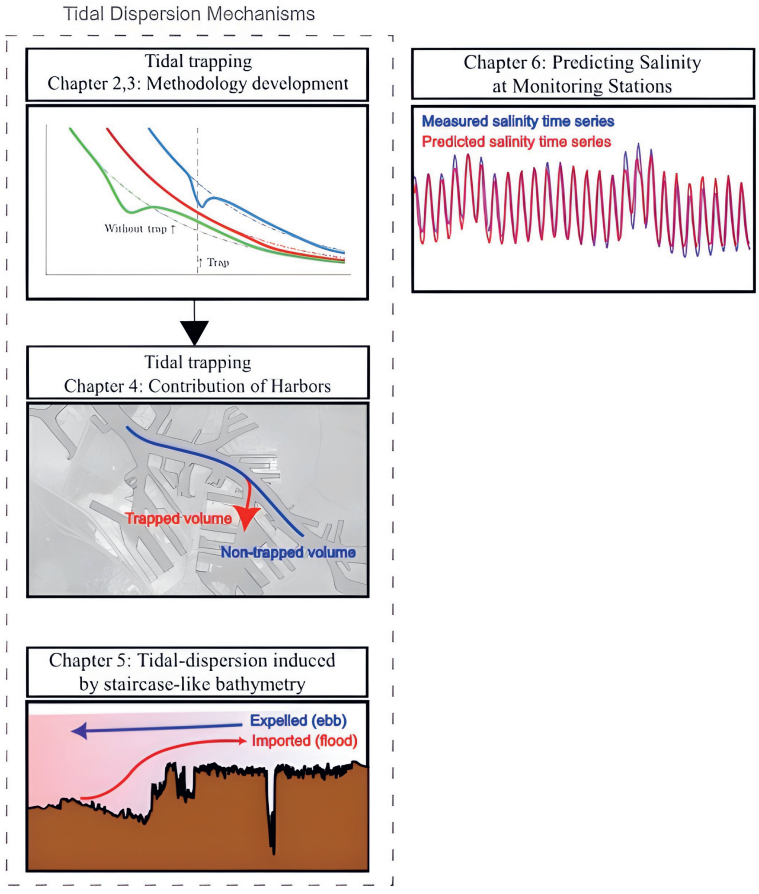


Figure 1.7: Visualization of the thematic structure of this thesis and the connections between its chapters. Chapters 2–4 investigate the role of tidal trapping induced by dead-end side channels. Chapter 2 presents the framework for quantifying the dispersive salt transport and examines tidal trapping in an idealized model representative for well-mixed estuaries. Chapter 3 presents a continuation of this work and provides a mechanistic explanation for discrepancies between existing analytical formulations for tidal trapping. Chapter 4 examines the dispersive effect of harbors using both observational data and numerical model results. In this chapter, the quantification method developed in Chapter 2 is applied to the harbors of the Rhine–Meuse system, isolating the dispersive contribution of individual basins and clarifying the mechanisms through which harbors enhance dispersion. Thereafter, Chapter 5 shifts the focus to the influence of sharp bathymetric steps on estuarine dynamics and the balance between dispersive mechanisms. Finally, Chapter 6 introduces a harmonic-regression approach for predicting estuarine salinity at monitoring stations.

CHAPTER 2

Tidal trapping and its effect on salinity dispersion in well-mixed estuaries revisited

In well-mixed estuaries, the up-estuary salt flux is often dominated by tidal dispersion mechanisms, including tidal trapping. Tidal trapping involves volumes of water being temporarily trapped in dead zones or side channels adjacent to the main channel, and released later in the tidal cycle, which causes an additional up-estuary salt flux. Tidal trapping can result from a diffusive exchange between a channel and a trap, or from filling and emptying of the trap by a tidal flow that is ahead in phase, compared to the flow in the main channel (advective out-of-phase exchange). This study revisits the dispersive contribution from tidal trapping in a single dead-end side channel using an idealized numerical model. The results indicate that advective out-of-phase exchange yields the largest additional salt flux for the largest realistic velocity phase difference of 90°. Mixing of the trapped salinity field enhances the dispersive effect for small velocity phase differences. A continuous diffusive channel-trap exchange also enhances the dispersive trap effect when the velocity phase difference is small, but can dampen it when the phase difference is large. We demonstrate that the effect of a trap is twofold: firstly, channel-trap exchange alters the salinity field and introduces an additional salt flux in the main channel over a distance equal to the tidal excursion length; secondly, the altered salinity gradients are advected in both up- and down-estuary direction, influencing the tidal salt flux over twice the excursion length.

This chapter is based on: ***van Keulen, D., W. M. Kranenburg, and A. J. F. Hoitink*** *(2025). Tidal trapping and its effect on salinity dispersion in well-mixed estuaries revisited. Estuaries and Coasts, 48(6), 153. doi:10.1007/s12237-025-01579-0.*

2.1 Introduction

In estuaries, there is a continuous competition between flushing of salt water by freshwater river discharge and up−estuary salt transporting mechanisms. In a partially or strongly stratified system, the up−estuary salt flux is predominantly driven by gravitational circulation (Hansen and Rattray Jr 1966a) which can be enhanced by asymmetry in mixing between flood and ebb (Jay and Musiak 1996; Geyer and MacCready 2014). In well-mixed and generally shorter estuaries, the up-estuary salt flux often results from tidal dispersion mechanisms. Tidal dispersion include phenomenon like jet-sink exchange (Stommel and Farmer 1952), which typically occur near the mouth of estuarine systems. Here, the outflow exhibits jet-like characteristics, while the inflow during flood is more evenly distributed, resulting in import of non-native (saline) water. Another widely studied tidal dispersion mechanism is tidal trapping, where volumes of water are temporarily trapped in dead zones or side branches, and re-discharged later in the tidal cycle (Okubo 1973; Dronkers 1978; MacVean and Stacey 2011). Often, tidal dispersion mechanisms are introduced by geometric features like channel constrictions, shoals and meanders (Garcia and Geyer 2022), though tidal dispersion can also be introduced in straight channels by a phase shift of the salinity signal due to river discharge (Dijkstra and Schuttelaars and Kranenburg 2022) .

To distinguish various transport mechanisms, the tidally averaged salt flux through a cross-section can be decomposed (Fischer et al. 1979; Lerczak and Geyer and Chant 2006). In a salt flux decomposition, tidal dispersion mechanisms are reflected in the correlation between the tidally varying demeaned velocity and salinity signals. This correlation reflects an up-estuary salt flux when the phase difference is less than in quadrature. Dronkers and Van de Kreeke (1986) demonstrated that in a Eulerian framework, the correlation related salt flux is the result of vertical or lateral exchange occurring elsewhere within the tidal excursion, and therefore termed non-local salt flux. Recently, Garcia and Geyer (2022) applied the decomposition of Dronkers and Van de Kreeke (1986) to study the origin of the tidal salt flux in the North River, linking the observed Eulerian salt flux to specific geometric features.

This study focuses on tidal trapping due to diffusive and advective exchange between a channel and a trap, and their effect on tidal dispersion. As mentioned above, tidal trapping results from the temporal storage in dead zones or side branches, referred to as traps. A net (additional) salt flux in the main channel occurs because the exchange between the channel and the trap causes volumes of water to be temporarily stored and then released at different times in the tidal cycle, introducing an up-estuary salt flux. Exchange with a trap may occur through lateral exchange mechanisms including those introduced by eddies (Dronkers 1978; Geyer and Signell 1992) or density currents set up by density differences between the channel and the trap (Abraham et al. 1986; Ralston and Stacey 2005; Giddings et al. 2012; Garcia and Geyer and Randall 2022). These processes rely on spatial variations in the flow and salinity fields at the trap entrance, which, in a cross-sectional-averaged sense, are diffusive in nature (hereafter referred to as diffusive exchange). A net salt flux can also result from the velocity phase difference between the cross-sectional averaged current in the channel and in the trap (Dronkers 1978; MacVean and Stacey 2011). This phase difference arises because the wave-type, which labels the phase relationship between variations in water level and the flow, typically differs between the channel and the trap. In the trap, which acts as a short basin, currents directly respond to water level variations, with high and low water coinciding with slack water (i.e. water level variations are in quadrature with the currents). In contrast, due to inertial effects, the main channel typically exhibits a phase difference between high or low water levels and

the corresponding moments of slack water (Friedrichs 2010). In the most extreme case of a progressive wave, this can cause the currents to be in phase with the water level variations. The velocity phase difference between the channel and the trap causes a relative displacement between the parcels that are trapped and those that remain in the main channel (Dronkers 1978). This introduces a longitudinal dispersion mechanism, referred to as advective out-of-phase exchange by Garcia and Geyer and Randall (2022) .

Several authors have derived an analytical expression to quantify the effect of tidal trapping, assuming either diffusive or advective out-of-phase exchange and evaluating a finite or continuous trap. For diffusive channel-trap exchange, Okubo (1973) derived an analytical model intended to quantify the influence of shoreline irregularities, assuming a continuous lateral trap that exchanges continuously with the main channel. Through the concentration moment analysis (Aris 1956), a solution for the effective dispersion of salt in the main channel, K_{eff}, is obtained:

$$K_{\text{eff,Okubo}} = \underbrace{\frac{r\hat{U_c}^2}{\omega}\left(\frac{\omega/k}{2(1+r)^2(1+r+\omega/k)}\right)}_{K_{\text{trp,Okubo}}} + \frac{K_b}{1+r}, \tag{2.1}$$

where $r = B_t/B_c$ is the trap to channel width ratio, k is the exchange-rate coefficient with k^{-1} being the residence time, $\hat{U_c}$ the velocity amplitude in the main channel, $\omega = 2\pi/T$ is the radian frequency (with T the tidal period), and K_b is the background dispersion coefficient (encompassing all dispersive processes other than tidal trapping). In Eq. 2.1, the effective dispersion results from the first term, $K_{\text{trap,Okubo}}$, which represents the additional dispersive effect caused by tidal trapping, and the second term, which represents a reduction of the background dispersion caused by trapped particles not being subjected to dispersion in the main channel. Although strictly speaking, Eq. 2.1 is only applicable to a continuous lateral trap and diffusive exchange, it is often used to estimate the contribution of finite traps where the exchange is driven by advective out-of-phase exchange (MacVean and Stacey 2011; Garcia and Geyer and Randall 2022).

MacVean and Stacey (2011) highlighted that Eq. 2.1 does not capture the dynamics of advective out-of-phase exchange. Assuming a source-sink term driven by advective exchange that is out-of-phase with the main channel and a salinity at the trap entrance independent of the salinity in the main channel, they used the concentration moment analysis to derive an alternative expression for the additional dispersion:

$$K_{\text{eff,MacVean}} = \underbrace{\frac{\epsilon\hat{U_c}^2}{\omega}\left(\sin\alpha\cos\alpha\left(\frac{3\cos\alpha + 32\cos\alpha}{12\pi}\right)\right)}_{K_{\text{trp,MacVean}}} + K_b, \tag{2.2}$$

with α the velocity phase difference between the flow in the trap and in the channel, and $\epsilon = (A_t\hat{U}_t\hat{S}_t)/(A_c\hat{U_c}\hat{S})$ representing the salt flux through the trap entrance relative to the salt flux in the channel, $\hat{U}_t$ the velocity amplitude in the trap, A_t is the cross-sectional area of the trap and $\hat{S}_t$ and $\hat{S}$ are the salinity amplitudes in the trap and the main channel, respectively. Again, the first term represents the additional dispersive effect caused by tidal trapping ($K_{\text{trap,MacVean}}$), and the second term represents the effect of the background dispersion. According to Eq. 2.2, the trap effect is greatest when $\alpha \approx \frac{1}{4}\pi$, and no net effect is expected for the largest physically realistic phase difference of $\frac{1}{2}\pi$. A distinct difference with Eq. 2.1 is that it is derived under the assumption of a trap existing over a limited stretch,

which is short compared to the tidal excursion length.

Dronkers (1978) derived analytical expressions for both continuous traps and finite traps. Instead of using a concentration moment analysis, he adopted a Lagrangian approach to quantify the additional salt flux due to tidal trapping. Furthermore, this work clearly outlines why the additional salt flux is variable in space for a trap that is short compared to the excursion length, but becomes constant for a continuous lateral trap. For a continuous lateral trap subject to out-of-phase exchange, Dronkers (1978) obtained the following expression:

$$K_{\mathrm{trp,Dronkers}} = \frac{2}{3}\frac{H_t B_t}{A_c}\frac{L_t^2}{T}\sin^2\alpha, \tag{2.3}$$

where L_t is the tidal excursion length and H_t the depth in the trap. In the case where the depths in the channel and trap are equal, Eq. 2.3 closely resembles Eq. 2.1. Then, the geometry ratio reduces to r, and the dimensional group is rewritten as $\frac{L_t^2}{T} \sim \frac{\hat{U}_c^2}{\omega}$. A notable difference between Eq. 2.3 from Dronkers (1978) and Eq. 2.2 from MacVean and Stacey (2011) is that in Eq. 2.3 the additional dispersion (K_{trp}) increases with the velocity phase difference, and continues to increase up to $\alpha = \frac{1}{2}\pi$, while Eq. 2.2 predicts a decrease for $\alpha > \frac{1}{4}$. Thus, the formulation by Dronkers (1978) suggests that the trap effect is strongest at the maximum physical phase difference ($\alpha = \frac{1}{2}\pi$), which stands in contrast with the findings of MacVean and Stacey (2011).

Hence, various analytical frameworks exist to quantify the dispersion resulting from tidal trapping, but these frameworks differ significantly in how the effect of the trap depends on the phase difference between the velocity in the trap and in the channel. Furthermore, the existing analytical frameworks typically assume either pure diffusive or advective out-of-phase exchange, whereas in reality, both mechanisms can occur simultaneously, an aspect that so far has not been studied. Additionally, for traps with entrance widths much smaller than the tidal excursion (e.g., side channels), insight is lacking into the spatial variability of the additional salt flux with distance from the trap resulting from the channel-trap exchange (either from diffusive or advective out-of-phase exchange).

The aims of this study are to understand the dependence of the additional salt flux on the velocity phase difference, to study and quantify the additional salt flux when the channel trap exchange occurs through both dispersive and advective out-of-phase exchange, and to establish the spatial variability of the additional salt flux for tidal trapping introduced by a dead-end side channel. To achieve this, we numerically evaluate tidal trapping induced by a dead-end side channel using an idealised 1D finite volume model incorporating local sources and sinks (Section 2.2). Subsequently, parameter dependency tests are performed to examine the impacts of alternative channel-trap exchange mechanisms on the resulting additional salt flux in the main channel over a single tidal cycle, achieved by perturbing a reference salinity field (Section 2.3). In the discussion (Section 2.4), we compare the numerical findings with the existing analytical frameworks. In addition, we discuss the validity of expressing the additional salt flux in terms of dispersion coefficients. We then examine the additional tidal salt flux under equilibrium conditions, which, at equilibrium, results not only from direct channel-trap exchange. Finally, conclusion are drawn in Section 2.5.

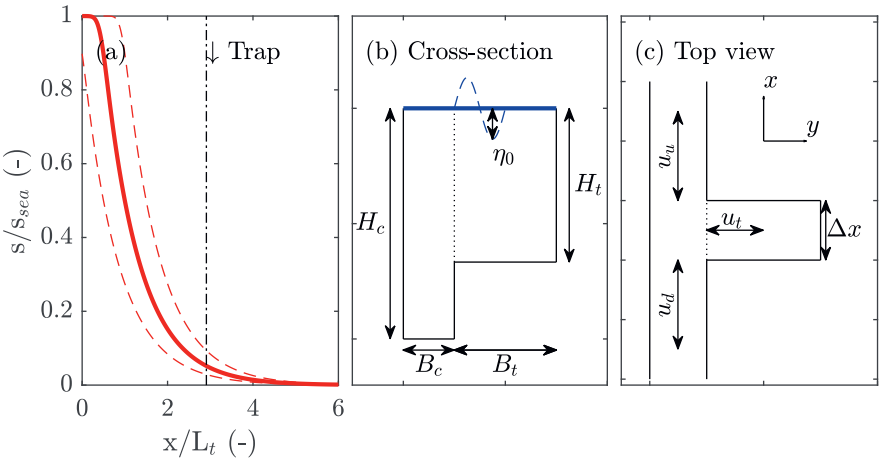


Figure 2.1: Overview of the model setup and symbols characterizing the dimensions of the trap. (a) Normalised subtidal salt curve used for the model initialisation in Section 2.3, where the distance x is normalised by the tidal excursion length L_t. Dashes lines indicate the salinity at Low Water Slack (LWS) and High Water Slack (HWS). (b) Cross-section over the trap and channel, with symbols for dimensions. Note that the horizontal and vertical dimensions are not drawn to scale. (c) Top view of the trap.

2.2 Methods

2.2.1 Model set-up

2.2.1.1 The salt balance

To investigate various scenarios and different types of channel-trap exchange, we use a simplified one-dimensional finite-volume model, which ensures mass conservation, to calculate the cross-sectional averaged salinity in the main channel. The basic salt-balance equation considered is given by:

$$\frac{\partial s}{\partial t} + \frac{\partial}{\partial x}\left(su - K_b \frac{\partial s}{\partial x}\right) = \frac{I(x)}{A_c}, \tag{2.4a}$$

$$s(0,t) = s_{sea}, \tag{2.4b}$$

$$s(L_d,t) = s_{riv}, \tag{2.4c}$$

with s representing the salinity in the main channel, u the main channel velocity (see Section 2.2.1.2), K_b a constant background diffusion coefficient for all processes other than tidal trapping, A_c a constant cross-sectional area for the main channel, and $I(x)$ a source-sink term that represents the salt flux from a local trap in the model domain (see Section 2.2.1.3). Herein, the geometry of the main channel is assumed to be straight with a rectangular cross-section, but a spatially varying cross-sectional could be described. Boundary conditions are specified at the up-estuary and down-estuary ends with constant salinity values of $s_{riv} = 0$ and $s_{sea} = 35$, respectively, where L_d denotes the length of the model domain.

For the initial salinity field an exponentially decaying profile is prescribed:

$$s(x,0) = s_{sea} e^{\left(-\frac{u_r}{K_b}x\right)}, \tag{2.5}$$

where u_r is the velocity associated with the river discharge. This profile represents the equilibrium state if u were constant and equal to u_r. The associated time-scales are defined as $T_A = L_s/u_r$ for flushing and $T_D = L_s^2/K_b$ for the dispersive time-scale, where L_s represents the salt-intrusion length. Thus, different combinations of u_r and K_b can result in identical salinity distributions, but will differ in the corresponding adjustment time-scales. Adding the tidal movement to this system introduces an additional tidal salt flux.

2.2.1.2 The current velocity in the main channel

To examine the effect of velocity phase differences between the channel and the trap on the salinity profile and tidal dispersion, we consider a simplified flow field with a constant along-channel current velocity amplitude and phasing both upstream and downstream of the trap, with their difference influenced solely by the trap to ensure mass conservation. The system's time origin ($t = 0$) is set at low water, assuming that the trap's current resembles a standing wave, so that the time origin coincides with low water slack in the trap. Tidal variations in the cross-sectional area A_c are neglected. For the downstream stretch, we impose $u = \hat{U}_{c,d}\sin(\omega t - \alpha_d)$, which is used to calculate the up-estuary velocity amplitude and phasing based on the trap properties and mass conservation. Specifically, the amplitude and phase at the up-estuary cell are calculated from the down-estuary velocity amplitude $\hat{U}_{c,d}$, phase α_d and the trap's discharge amplitude $\hat{q}_t$:

$$A_c\hat{U}_{c,d}\sin(\omega t - \alpha_d) - A_c\hat{U}_{c,u}\sin(\omega t - \alpha_u) - \Delta x\hat{q}_t\sin(\omega t) = 0. \tag{2.6}$$

Rewriting Eq. 2.6 and expressing the amplitudes and phase in Fourier coefficients and evaluating the equation at $t = 0$ and $t = \alpha_d/\omega$ allows to express the up-estuary velocity amplitude $\hat{U}_{c,u}$ and phasing α_u. The phasing downstream of the trap may vary between 0° and 90°. We acknowledge that a fixed phase with a constant current velocity amplitude is inconsistent with fully realistic estuarine tidal properties, as described by Friedrichs (2010). However, it allows for a systematic evaluation of the effect of the velocity phase difference between the main channel and the trap. Given the discharge amplitude $\hat{q}_t = B_t\eta_0\omega$ at the trap entrance, the mean current within the trap, u_t, is given by:

$$u_t = \frac{\eta_0\omega}{H_t - \eta_0\cos(wt)}(B_t - y)\sin(\omega t), \tag{2.7}$$

where y is the distance from the trap entrance, η_0 is the tidal amplitude, H_t is the mean water depth in the trap, and B_t is the width of the trap (Figure 6.1). Eq. 2.7 is used for the more complex source/sink term definitions, which require numerical evaluation of the salinity field within the trap.

2.2.1.3 Formulations for channel-trap exchange

We describe different types of channel-trap exchange by using different forms for the local source-sink term $I(x)$ in Eq. 2.4. The types of exchange are illustrated in Figure 2.2. The first two cases test theoretical forms for advective out-of-phase exchange as studied by Dronkers (1978) and MacVean and Stacey (2011). The third case evaluates pure diffusive exchange (Okubo 1973), while the final case examines the combined effect of advective out-of-phase and diffusive exchange.

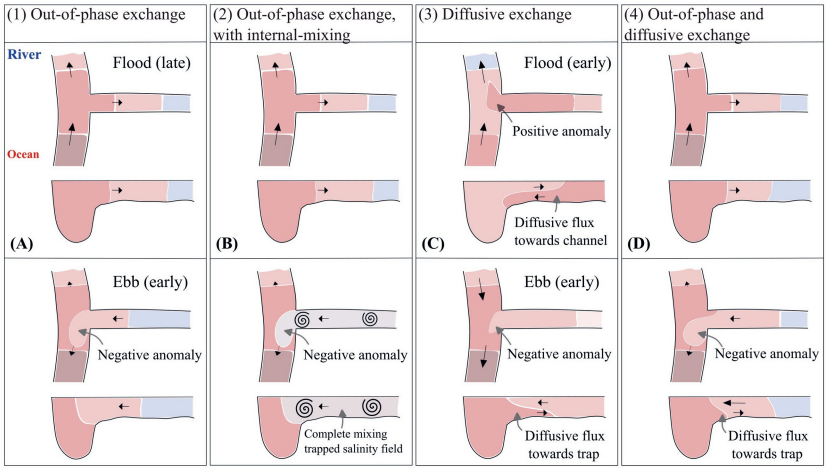


Figure 2.2: Conceptual overview of tidal trapping scenarios in a dead-end side channel. The top view shows the cross-sectionally averaged salinity, while the cross-sectional plots below further illustrate the assumed exchange mechanisms. (a) Pure advective out-of-phase exchange results in a salt anomaly that causes an up-estuary salt flux due to differences in velocity phasing between flow in the main channel and in the trap. (b) out-of-phase exchange with complete internal mixing: Similar to panel a, but the trapped salinity field exits the trap fully mixed. (c) Pure diffusive exchange: Continuous diffusive exchange causes the development of salt anomalies in the main channel and an up-estuary salt flux. The diffusive exchange is visualized here as a vertically sheared exchange flow in the cross-section plots, though the diffusive exchange flow could also result from other mechanisms . (d) out-of-phase and diffusive exchange: This situation involves channel-trap exchange driven by both types of exchange mechanisms.

Case 1: Pure advective out-of-phase channel-trap exchange
In this scenario, salt is extracted from the main channel by the trap at a rate determined by the discharge amplitude $\hat{q}_t = B_t \eta_0 \omega$, starting from $t = 0$, which is chosen to coincide with slack water in the trap. After the flow reversal in the trap at $t = T/2$, the trapped salinity field is advected back to the main channel, creating a mirrored image of the flood salinity signal:

$$I(x) = \begin{cases} \hat{q}_t \sin(\omega t) \cdot s(x,t) & 0 \leq t \leq T/2; \\ \hat{q}_t \sin(\omega t) \cdot s(x, T-t) & T/2 \leq t \leq T, \end{cases} \tag{2.8}$$

with $s(x,t)$ the salinity in the main channel. This case is most realistic for shallow systems with high cross-sectional average currents, where diffusive exchange over the trap entrance is relatively small and stratification within the trap does not occur (see Figure 2.2a).

Case 2: Advective out-of-phase channel-trap exchange with mixing
For the second case, it is assumed that the salinity field, which enters the trap during the flood phase, is fully mixed in the trap before it exits the trap (see Figure 2.2b):

$$I(x) = \begin{cases} \hat{q}_t \sin(\omega t) \cdot s(x,t) & 0 \leq t \leq T/2; \\ \hat{q}_t \sin(\omega t) \cdot s_{ebb} & T/2 \leq t \leq T, \end{cases} \tag{2.9}$$

and the salinity during ebb is given by $s_{ebb} = \frac{2}{T}\int_0^{T/2} s(x,t)dt$. This formulation mimics the effect of mixing within the trap of the salinity field that enters during the flood. It is most realistic for shallow systems where the currents in the trap are substantially reduced, allowing for internal mixing (Garcia and Geyer and Randall 2022).

Case 3: Pure diffusive channel-trap exchange
Case 3 investigates pure diffusive exchange (Figure 2.2c). A numerical sub-domain simulates the trap's salinity by solving the diffusion equation with the salinity in the main channel serving as a time-varying boundary condition. The diffusive salt flux across this boundary is determined by a lateral diffusion coefficient, K_t, specified for the trap, and the salt flux across the boundary serves as the source-sink term, $I(x)$. For the initial salinity field, the first tidal cycle is simulated repeatedly to spin up the salinity in the trap until the maximum change over one tidal cycle is less than 0.05 psu. This scenario is particularly relevant for systems where the depth-averaged current velocity in the trap is weak, and the exchange is predominantly governed by diffusive mechanisms. For example, this is generally the case for harbors or channel irregularities, where the depth-averaged current in the trap is weak due to their depth and limited length.

Case 4: advective out-of-phase & diffusive channel-trap exchange
In Case 4, the combined effect of out-of-phase and diffusive exchange is explored (see Figure 2.2d). Similar to Case 3, a numerical sub-domain is set up to simulate the salinity dynamics within the trap, but with a mean current. An adjusted version of Eq. 2.4 is used to account for the water level variations. The same spin-up procedure as described for Case 3 is used to obtain an initial salinity field.

2.2.1.4 Performed model simulations

To investigate the influence of different types of channel-trap exchange and key estuarine parameters on the dispersive effect within the main channel, we performed a systematic set of model simulations to demonstrate the effect of channel-trap exchange (Table 6.1).

In all simulations, a model domain of 200 km was discretized with variable cell sizes: 250 m near the mouth, 125 m around the trap, and 500 m in the upper estuary. A tidal period T of 12 hours is assumed and a time step of 100 seconds was used for time discretization. Furthermore, a system with a sufficiently long intrusion length is simulated to ensure the trap is not influenced by boundaries, and a long dispersive adjustment time is desired to limit the influence of background dispersion ($T_D \gg T$). To accomplish this, a cross-sectional area $A_c = 2500$ m^2 and a river velocity $u_r = -0.004$ m/s and background diffusion of $K_b = 20$ m^2/s are used to reach a salt intrusion length L_s (1 psu isohaline) of approximately 47 km. In practice, typical values K_b range from 100 to 300 m^2/s (Fischer et al. 1979), although reported values vary considerably, ranging from approximately 20 to 2000 m^2/s (Fischer et al. 1979; Savenije 2006; Kuijper and Van Rijn 2011). We use the lower limit of K_b in this study. To initialize the model with a true equilibrium salinity distribution, the model without any source/sink terms was run until an new equilibrium was reached (see Figure 6.1), which was then used to initialize the model simulations exploring the channel-trap exchange. In these simulations, a trap is located at $x_h = 40$ km with x_h indicating the center location of the trap in the main channel. The trap has an entrance width $\Delta x = 250$ m, a basin length $B_t = 12000$ m and a depth $H_t = 5$ m. There is no tidally averaged net discharge through the trap, and therefore, it can be considered a dead-end side channel. A reference simulation is performed without the trap for comparison.

Table 2.1: Overview of the assumed geometry and forcing in the channel and trap for the simulations performed in the indicated sections.

Section	Case	$\frac{B_t H_t}{A_c}$(-)	$\frac{\Delta x}{L_t}$(-)	K_b(m^2/s)	u_r (m/s)	$\hat{U}_{c,d}$(m/s)	α_d (rad)	η_0(m)	K_t(m^2/s)
2.3.1	1	24	0.04	20	0.004	1	$\frac{1}{4}\pi$	1	–
2.3.2	1	24	0.04	20	0.004	1	$0\cdots\frac{1}{2}\pi$	1	–
	2	24	0.04	20	0.004	1	$0\cdots\frac{1}{2}\pi$	1	–
	3	24	0.04	20	0.004	1	$0\cdots\frac{1}{2}\pi$	1	180
	4	24	0.04	20	0.004	1	$0\cdots\frac{1}{2}\pi$	1	180
2.3.3	4	24	0.04	20	0.004	1	$0\cdots\frac{1}{2}\pi$	$0.5\cdots2$	$1\cdots3200$
2.3.4	1	24	0.04	20, 2000	0.001, 0.1	1	$0\cdots\frac{1}{2}\pi$	1	–

Table 6.1 gives an overview of the simulations of this study. Firstly, we simulate a purely advective out-of-phase exchange between channel and trap, and report on the changes in the salinity in the main channel in Section 2.3.1. Simulations are performed using different formulations for the channel-trap exchange, while varying the velocity phase for the current in the down-estuary reach of the main channel. For simulations reported in Section 2.3.2, α_d is varied between 0 and $\frac{\pi}{2}$, such that the velocity phase difference between the downstream flow and the flow in the trap is varied between the smallest and largest physically realistic values. The simulations reported in Section 2.3.3 aim to explore the transition from advective out-of-phase to diffusive channel-trap exchange (Case 4). For these simulations, the strength of the lateral diffusion coefficient is varied between 1 m^2/s and 3200 m^2/s, and the current in the trap is varied by changing the tidal amplitude η_0 between 0.5 and 2 m. Finally, as discussed in Section 2.2.1, different combinations for u_r and K_b may yield the same salt curve, while they vary in their diffusive and advective time-scales. Altering the diffusive time-scale influences the additional salt flux. To illustrate this relationship, in Section 2.3.4, experiments are conducted assuming pure advective out-of-phase dynamics, in which K_b is set equal to 20 and 2000 m^2/s, with river induced currents of 0.1 and 0.001 m/s (Table 6.1). To allow for a meaningful comparison, both sets of experiments are initialized with the salt curve obtained from Eq. 2.5.

2.2.2 Analysis of model results

2.2.2.1 Decomposition of the tidally averaged salt fluxes

To differentiate between the various exchange mechanisms in the model and quantify the additional (tidal) salt flux introduced by the trap, the tidally averaged salt flux F through a cross-section in the main channel is decomposed. Both the flow and the salinity signal are decomposed into a subtidal mean and tidally varying component indicated with the subscripts $_0$ and $_1$, respectively. This decomposition is used to quantify the flushing by the river discharge flow ($F_0 = Q_r s_0$) and the opposing salt flux related to tidal dispersion ($F_1 = A_c\langle u_1 s_1\rangle$), with the the operator $\langle\rangle$ indicating the tidal average). In the cross-sectional averaged model, the net salt flux through a cross-section is given by:

$$F = A_c\left(u_0 s_0 + \langle u_1 s_1\rangle + K_b\frac{\partial s_0}{\partial x}\right), \tag{2.10}$$

where the third term represents the parameterized salt-flux due to background dispersion ($F_b = A_c K_b \frac{\partial s_0}{\partial x}$). The system is in (dynamic) equilibrium if the net salt flux through the cross-section equals zero throughout the entire model domain, and F_0 is balanced by F_1 and F_b. Using a Fickian diffusion coefficients, the up-estuary salt fluxes can be expressed into an effective dispersion coefficient

$K_{\text{eff}} = F_1/\left(A_c \frac{\partial s_0}{\partial x}\right) + K_b$. This effective dispersion coefficient captures all modelled dispersion mechanisms and thus does not only represent the effect of tidal trapping.

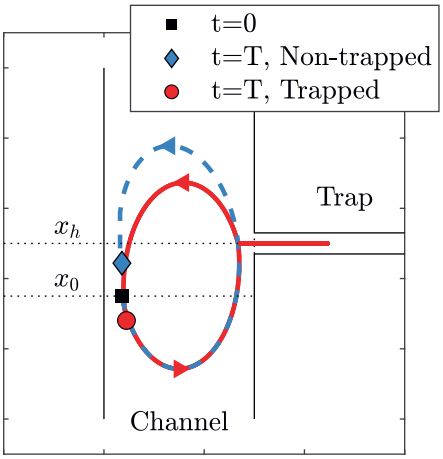


Figure 2.3: Illustration of the Lagrangian trajectory of two water parcels in a scenario where the velocity in the trap and the main channel are out-of-phase . One volume gets trapped, experiencing a displacement in the down-estuary direction, while the other remains in the main channel and is displaced in the up-estuary direction. Note that this Lagrangian displacement differs from the net up-estuary displacement δ calculated for a cross-section. The dimensions of the channel are not drawn to scale for clarity. This situation corresponds to Figure 2.4.

2.2.2.2 Quantification of the trap induced additional salt fluxes

To quantify the additional tidally averaged salt flux (directly) resulting from channel-trap exchange, two models are run for one tidal cycle: one with a trap and the other without. Both simulations start from the same initial salinity field. The increase in the tidally averaged salt flux through a cross-section near the trap in the simulation with the trap, compared to the reference simulation, is defined as the additional salt flux caused by the trap, $\tilde{F}_{\text{trp}}(x)$. This additional salt flux is used to quantify the effect of a trap under different estuarine conditions.

Analytically reproducing this additional salt flux from the observed channel-trap exchange is not straightforward. Here, we use an adjusted version of the balance proposed by Dronkers (1978) (see Eq. 20 in Dronkers (1978)) to estimate the trapping effect over the excursion length, $F_{\text{trp}}(x)$. Here we distinguish between the effects of advective out-of-phase exchange and diffusive channel–trap exchange by decomposing the instantaneous salt flux over the trap entrance f (where a positive value indicates a flux into the trap), into two component the cross-sectionally averaged advective salt flux f_A, and the diffusive salt flux f_D, parameterized by the lateral diffusion coefficient K_t. If the velocity in the main channel and trap are in phase, the additional tide averaged salt flux through a cross-section at $x = x_0$ is equal to the net salt flux over the trap entrance during the time interval between $t_{0,f}$ and $t_{0,e}$. Those instants correspond to the moments when particles, departing from x_0 at $t = 0$ in the main channel, pass by the trap during flood and ebb, respectively. If there is a velocity phase difference, a net salt flux is generated by the relative motion between the channel and the trap. A

trapped parcel experiences a down-estuary displacement from its initial location at $t = 0$, whereas a parcel remaining in the channel experiences an up-estuary displacement. This is illustrated in Figure 2.3. The balance for the additional tide averaged salt flux through a cross-section $\tilde{F}_{\mathrm{trp}}(x)$ is given by:

$$\tilde{F}_{\mathrm{trp}}(x_0) = \begin{cases} \underbrace{\int_{t_{0,f}}^{t_{0,e}} f_D dt}_{\tilde{F}_D} + \underbrace{\int_{t_{0,f}}^{t_{0,e}} f_A dt}_{\tilde{F}_A} + \underbrace{\int_{-\delta}^{0} s(x_0,0) A_c dx}_{\tilde{F}_C}, & x_1 \leq x_0 < x_h \\ \underbrace{\int_{t_{0,f}}^{t_{0,e}} -f_D dt}_{\tilde{F}_D} + \underbrace{\int_{t_{0,f}}^{t_{0,e}} -f_A dt}_{\tilde{F}_A} + \underbrace{\int_{-\delta}^{0} s(x_0,0) A_c dx}_{\tilde{F}_C}, & x_h < x_0 \leq x_2 \end{cases} \tag{2.11}$$

where $x_1 = x_h - L_t + \frac{u_c}{\omega}(1 - \cos(\alpha_d))$ and $x_2 = x_h + \frac{u_c}{\omega}(1 - \cos(\alpha_d))$ are the up- and down-estuary limits of the additional salt flux. The tilde ˜ is used to indicate that this is an analytical estimate of the additional salt flux. The first term ($\tilde{F}_D$) represents the net additional salt flux from diffusive exchange with the trap. The second term ($\tilde{F}_A$) represents the net salt flux due to advective exchange with the trap, which is typically negative when considering pure out-of-phase exchange. This negative flux results from the fact that, by definition, a larger volume leaves the trap during the evaluated period due to the effect of the relative motion between the channel and the trap. The third term ($\tilde{F}_C$) represents the salt flux resulting from the need to compensate for the net volume exiting the trap (volume conservation). This is achieved by a net displacement δ in the up-estuary direction. This displacement is calculated from the net discharge from the trap during the evaluated period: $\delta(x) = \int_{t_{0,f}}^{t_{0,e}} \Delta x \hat{q}_t \sin(\omega t) dt / A_c$, where the integral is analogous to the second term ($\tilde{F}_A$) but for the exchange of volume. Hence, if diffusive exchange is negligible, the balance between the down-estuary directed term $\tilde{F}_A$ and the compensating term $\tilde{F}_C$ describes the effect of pure advective out-of-phase exchange.

The ability of Eq. 4.5 to reproduce the additional tidally averaged salt flux and quantify the contribution of the different exchange mechanisms is demonstrated in Section 2.3.

2.2.3 Limitations

The idealized one-dimensional (1D) model adopted to explore tidal trapping has limitations. Many physical processes are either greatly simplified, represented by a single (dispersion) coefficient, or not accounted for at all. For example, the model does not capture stratification that may be generated due to the reduction in current velocity within the trap (Garcia and Geyer 2022). Additionally, the influence of lateral salinity variations in the main channel, which depend on the geometry of the system (Schulz et al. 2015), on the trapping process is neglected. Exchange at estuarine junctions is often accompanied by frontal formation (Corlett and Geyer 2020), which can significantly influence both stratification and mixing (Giddings et al. 2012; Bo and Ralston 2022). These types of processes and interactions remain unexplored. This notwithstanding, the essential mechanism of out-of-phase salinity exchange referred to as tidal trapping is captured in our 1D modelling framework.

2.3 Results

2.3.1 Changes in the along channel salinity profile (Case 1)

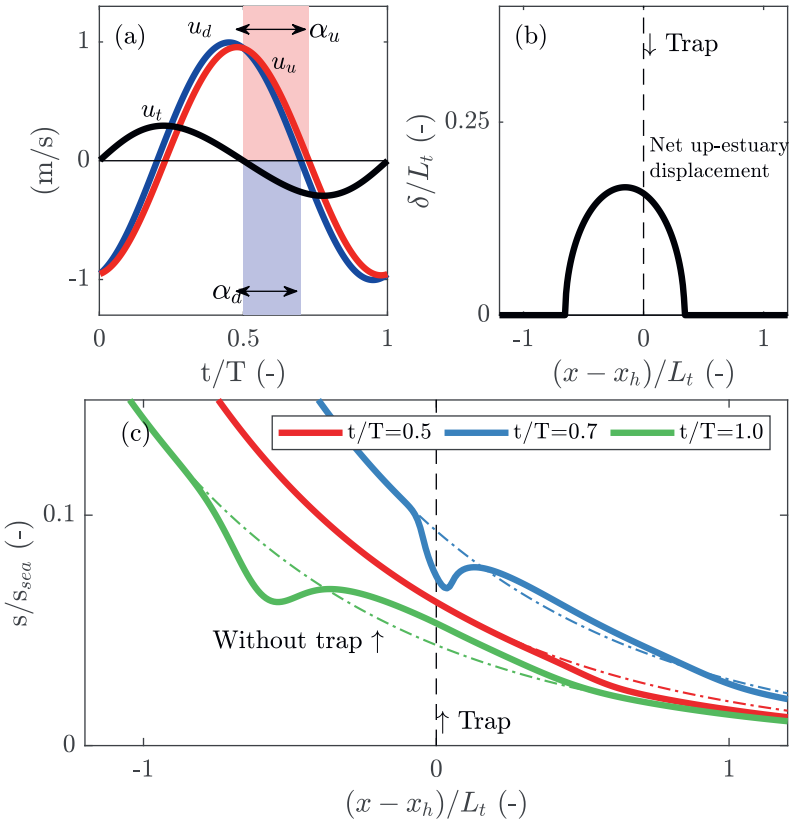


Figure 2.4: Illustration of the modelled velocities alongside intertidal salinity levels, demonstrating the development of salt anomalies driven by the net displacement of trapped and non-trapped particles, assuming pure advective out-of-phase exchange. (a) Illustration of the current velocities and resulting phase differences. The current velocity up-estuary of the trap, u_d, results from the assumed current velocity profile in the reference run and the velocity phase difference between the down-estuary section of the main channel and the trap. (b) Trap induced net up−estuary displacement δ over a tidal cycle, shown as a function of the initial location at $t/T = 0$ relative to the trap, normalised by the excursion length. (c) Simulated salinity in the reference model (dashed lines) and in the simulation with source-sink terms for out-of-phase exchange (solid lines) at various moments in time, both at and after the flow reversal in the trap (occurring at $t/T = 0.5$). In panels b and c, the x-axis shows the distance in the main channel from the trap $(x - x_h)$ is normalized by the tidal excursion L_t.

This section examines how salinity along the main channel changes under the influence of pure advective out-of-phase exchange with a trap (Case 1) and quantifies the associated additional salt flux.

Figure 2.4 presents the simulated current velocities, the calculated net displacement in up-estuary direction, and the resulting salt anomaly from the channel-trap exchange, which develops after a full tidal cycle. The adopted settings result in an up-estuary velocity amplitude $\hat{U}_{c,u} \approx 0.95$ m/s with a velocity phase $\alpha_u \approx 0.29\pi$ (Figure 2.4a). A greater velocity phase (i.e., later onsets of flood and ebb) in the up-estuary reach of the main channel causes non-trapped parcels to experience an up-estuary displacement from their initial position. In contrast, a smaller velocity phase in the trap (i.e., earlier onsets of flood and ebb) causes trapped particles to return earlier to the main channel and experience a down-estuary displacement (Figure 2.3). Figure 2.4b shows the calculated net up-estuary displacement associated with an up-estuary volume flux required to balance the down-estuary volume flux induced by the relative motion between the channel and the trap at each cross-section of the main channel. Figure 2.4c shows the development of a negative salt-anomaly which develops in the main channel when the flow in the trap reverses ($t/T > 0.5$). During the period that the trap is in flood phase, saline water is only extracted by the trap, and the trap does not generate a gradient in the along channel salinity field. Differences in the salinity field between the two simulations at $t/T = 0.5$ are solely caused by along channel gradient in the along channel velocity. However, when the flow in the trap reverses, a negative salt-anomaly develops in the main channel at x_h, caused by the re-discharge of relatively lower saline water. This negative anomaly develops because the re-discharged water re-enters the main channel down-estuary from its initial location in the tidal excursion. The non-trapped parcels experience an up-estuary displacement due to the greater velocity phase and create the observed positive salt anomaly upstream of the trap. After one tidal cycle ($t/T = 1.0$), the channel-trap exchange has resulted in a redistribution of salt over the tidal excursion length.

The effect of the developed salt anomaly on the tidally averaged salt fluxes

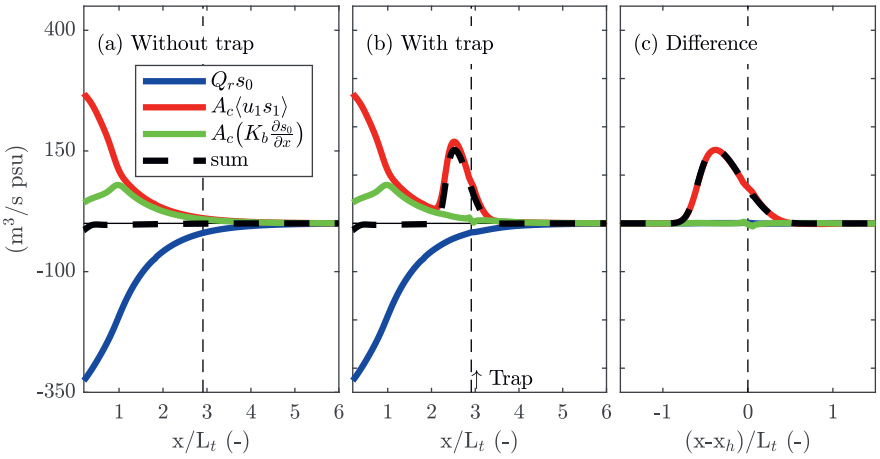


Figure 2.5: Example of the salt fluxes in the simulation with and without a trap corresponding to the situation depicted in Figure 2.4. (a) Along channel salt-fluxes for the reference simulation (no trap). The along channel coordinate is normalised by the tidal excursion length. (b) Same as panel a, but for the simulation with the trap, modelled using the source-sink terms. (c) Difference between the two simulation after one tidal cycle.

is shown in Figure 2.5. Note that both simulations start from the equilibrium

salinity distribution obtained for the situation without a trap. In both simulations, the river discharge introduces a phase shift that is smaller than in the case of quadrature, which results in an tidal salt flux over the salt intrusion length (Dijkstra and Schuttelaars and Kranenburg 2022). Furthermore, an increase in the tidal salt flux is introduced by the seaward boundary conditions and is visible near the mouth ($0 \leq x \leq L_t$), resulting from a difference in salinity during flood and ebb similar to jet-sink exchange (Stommel and Farmer 1952). In this region, the salt flux due to background dispersion is reduced, owing to a weaker subtidal salinity gradient (also see Figure 6.1a). However, in the system with a trap, an additional net salt flux is visible near the trap. Relative to the reference run, the decomposed salt fluxes are equal in both simulations, except for the additional tidal salt flux seen in the proximity of the trap which is introduced by the channel-trap exchange illustrated in Figure 2.4.

2.3.2 Results for different types of channel-trap exchange (Case 1−4)

Next, this section studies how salinity anomalies and salt fluxes in the channel differ for alternative types of channel-trap exchange (see Section 2.2.1.3). We use settings as tabulated in Table 6.1.

Figure 2.6 presents the spatio-temporal development of the salt anomaly simulated for the different cases and assumed values for α_d. The salt anomaly is defined as the difference with the reference run, $\Delta s = s - s_r$. When assuming pure advective out-of-phase exchange (Case 1), the resulting salt anomaly clearly increases with α_d and vanishes for $\alpha_d = 0$. In the latter case, the observed inter-tidal differences are solely the result of reduced flow velocities upstream of the trap. However, when the salt transported into the trap is assumed to be mixed before it flows back into the channel (Case 2), a salt anomaly develops also in absence of a phase difference (Figure 2.6a,b). Mixing in the trap causes the salinity of the rejoining water masses to differ from the water mass remaining in the main channel (Dronkers 1978; Garcia and Geyer and Randall 2022). However, the influence of mixing in the trap on the developed salt anomaly is less evident for higher velocity phase differences compared to pure advective out-of-phase exchange (Figure 2.6i,j). The salt anomaly that is observed for pure diffusive exchange (Case 3) develops in a distinctive manner. The channel-trap exchange is driven by a lateral salinity gradient, which is set-up by the tidal motion in the main channel. This results in a diffusive salt flux from the trap, that is in quadrature with the main channel velocity. A negative salt anomaly develops between the periods when the main channel current reaches peak flood and ebb (with $\alpha_d = 0$, this is between $\frac{t}{T} = \frac{1}{4}$ and $\frac{t}{T} = \frac{3}{4}$), causing the re-discharge of relatively low saline water from the trap (Figure 2.6c). For the scenario with both advective out-of-phase and diffusive exchange (Case 4), the results are similar to the scenario for advective out-of-phase exchange with mixing in the trap (Case 2), but driven by distinct processes.

Figure 2.7 presents the additional salt flux from the salt flux decomposition, the reproduced additional salt flux calculated using Eq. 4.5, and the contributions of the individual terms for the different cases. For pure advective out-of-phase exchange (Case 1), it is evident that the additional salt flux increases with the velocity phase difference (Figure 2.7a). This additional salt flux is fairly well reproduced through Eq. 4.5 (Figure 2.7e). The observed differences between the calculated salt flux and the salt flux obtained from the flux decomposition, are attributed to the fact that in the calculated salt flux, diffusion in the main channel is ignored. The reproduced salt fluxes emphasize the influence of relative displacement and show that the additional salt flux is a balance between the down-estuary

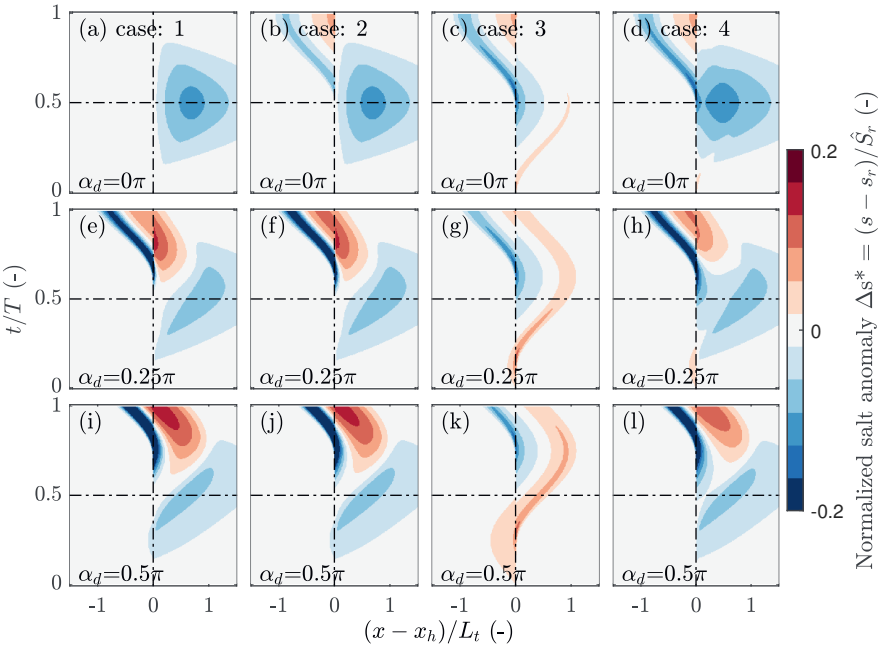


Figure 2.6: Spatio-temporal development of the normalised salt anomaly Δs^* in the main channel resulting from channel-trap exchange. Cases 1 through 4 (i.e., definition of the source-sink term) correspond to the columns and rows differ in the assumed velocity phase differences α_d. The normalised salt anomaly Δs^* is defined as the difference in the salinity in the main runs compared to the reference run normalised by the salinity amplitude: $\Delta s^* = (s - s_r)/\hat{S}_r$, with s_r the salinity in the reference simulation and $\hat{S}_r$ denoting the undisturbed the salinity amplitude in the reference run. For the x-axis, the distance in the main channel from the trap $(x - x_h)$ is normalized by the tidal excursion L_t.

directed flux from the trap $\tilde{F}_A$ and the compensating salt flux resulting from the net up-estuary displacement $\tilde{F}_C$ (Figure 2.7i). Generally, the location where the additional salt flux is largest is near the peak in the net displacement, δ, but it also depends on the shape of the along-channel salinity distribution. In our case, due to the exponentially decaying salinity field, the additional salt flux is slightly skewed, with the peak located down-estuary from the peak in displacement.

The effect of mixing in the trap (Case 2) when $\alpha_d = 0$ results in a positive contribution of $\tilde{F}_A$ (Figure 2.7j). The influence reduces at higher velocity phase differences, due to the structure of the imported salinity field. Furthermore, it is shown that the additional salt flux directly caused by the channel-trap exchange is not necessarily maximum at the location of the trap where the salt anomaly enters the channel (Garcia and Geyer and Randall 2022). Figure 2.7b shows that the additional salt flux is close to zero at the junction and peaks at $\frac{1}{2}L_t$ when α_d is small.

For the diffusive trap (Case 3), the additional salt flux is solely determined by $\tilde{F}_D$ (Figure 2.7c,g,k). Theoretically, in that case, the additional salt flux is independent of α_d. But in the performed experiments $\tilde{F}_D$ is slightly influenced by

the initial salinity field in the trap. The salt fluxes resulting from both advective out-of-phase and diffusive exchange (Case 4) show a similar development with an increase in α_d, compared to the case where mixing in the trap is assumed (Figure 2.7d). For small velocity phase differences, a net salt flux is generated through diffusive exchange, quantified by $\tilde{F}_D$. However, when the velocity phase difference is large, the resulting additional salt fluxes are lower compared to Case 1 and 2 (Figure 2.7d). For higher velocity phase differences, the reduction in the additional salt flux is caused by an increase in the magnitude of $\tilde{F}_A$, which is not compensated by $\tilde{F}_D$. The importance of advective out-of-phase versus diffusive exchange is further explored in the next section.

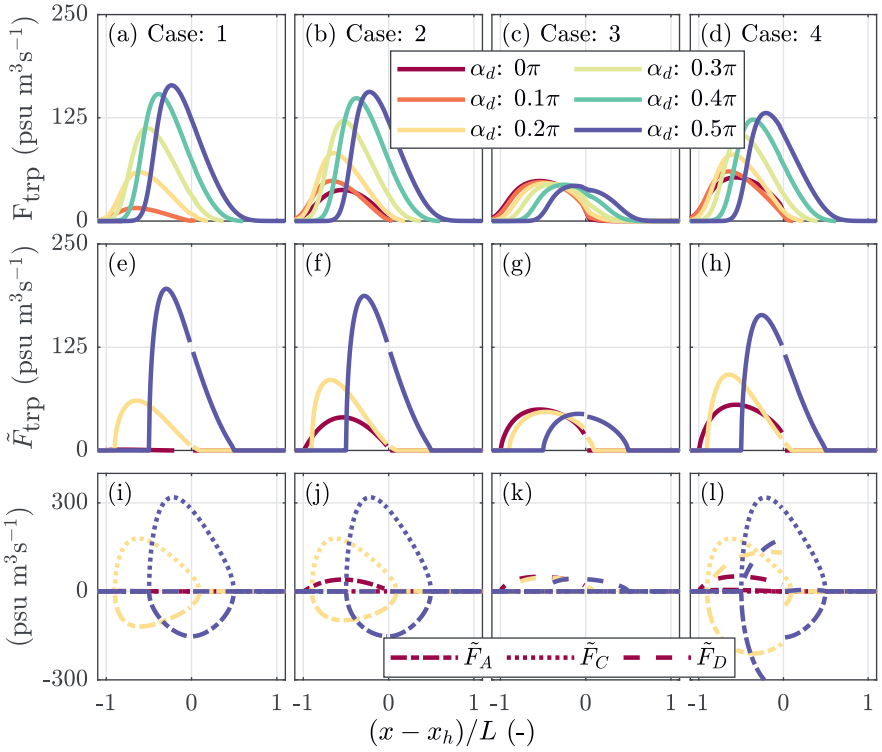


Figure 2.7: Additional salt flux in the main channel and its contributors resulting from channel-trap exchange for alternative channel-trap exchange mechanisms and assumed velocity phase differences (α_d). Panels a−d: the additional salt flux is determined by calculating the difference in salt fluxes between the simulations with and without the trap. Panels e−h: additional salt fluxes reproduced based on Eq. 4.5. Panels i−l: contribution of the individual terms of Eq. 4.5 that quantify the salt flux resulting from advective exchange over the trap entrance $\tilde{F}_A$, the salt flux resulting from the up-estuary net displacement $\tilde{F}_c$ (required to balance the relative motion between channel and trap), and the salt flux which result from the continuous diffusive channel-trap exchange, $\tilde{F}_D$. At the x-axis, the distance in the main channel from the trap ($x - x_h$) is normalized by the tidal excursion L_t.

2.3.3 Transitions between advective out-of-phase and diffusion dominated channel-trap exchange (Case 4)

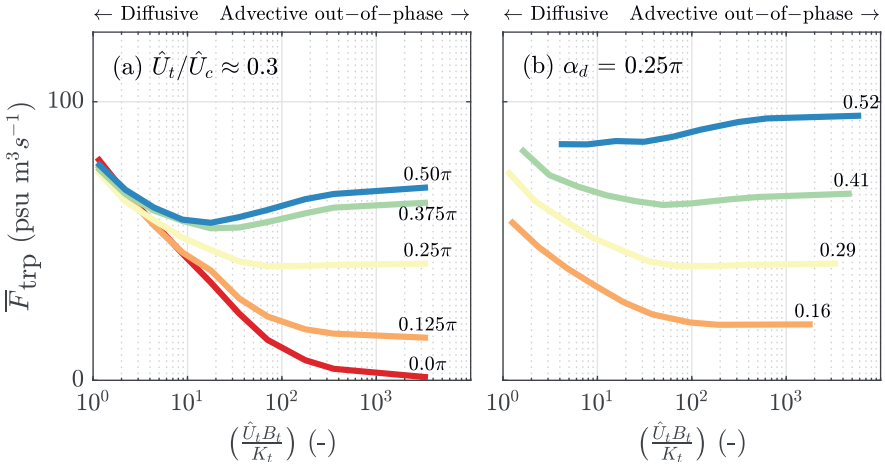


Figure 2.8: Overview of the tidal excursion-averaged additional salt flux, $\overline{F}_{\text{trp}}$, as a function of Péclet number, demonstrating the transition from diffusive to out-of-phase dominated exchange. The Péclet number is defined as $P_e = \dfrac{\hat{U}_t B_t}{K_t}$, with $\hat{U}_t$ the velocity amplitude in the trap, B_t is the length of the trap, and K_t is the assumed lateral diffusion coefficient. (a) Tidal excursion-averaged additional salt flux for alternative velocity phase differences α_d, with $\hat{U}_t/\hat{U}_c = 0.3$. (b) Same as panel (a), but with $\alpha_d = 0.25\pi$ and varying $\hat{U}_t/\hat{U}_c$.

For case 4, the channel-trap exchange occurs through a combination of advective out-of-phase and diffusive exchange. To differentiate between advective out-of-phase and diffusion−dominated exchange, we characterise the exchange using the Péclet number. The length of the basin B_t serves as the typical length scale. The advective time-scale T_A is determined from the trap's flushing time, given by $T_A = B_t/u_t$. For the diffusive time-scale, an effective migration rate within the trap is assumed, equal to $u_f = K_t/B_t$, resulting in $T_D = B_t^2/K_t$. The ratio of the two time-scales yields a Péclet number $P_e = \dfrac{T_D}{T_A} = \dfrac{\hat{U}_t B_t}{K_t}$. MacVean and Stacey (2011) used a scaled Péclet number, assuming that the characteristic time-scales of advective and diffusive exchange differ. However, both processes operate over a typical time-scale equal to T when the trap length B_t is sufficiently long. Therefore, here we consider the characteristic time-scale required to flush the trap through advective and diffusive transport. Furthermore, a tidal excursion averaged additional salt flux, $\overline{F}_{\text{trp}}$, is calculated to quantify the trap's effect:

$$\overline{F}_{\text{trp}} = \frac{1}{L_t} \int_{x_1}^{x_2} F_{\text{trp}} dx \tag{2.12}$$

where the overbar $\bar{}$ is used to indicates a tidal excursion-averaged property.

Figure 2.8 presents the tidal excursion−averaged dispersion coefficient across the tested Péclet numbers. The results indicate that the additional salt flux, $\overline{F}_{\text{trp}}$,

does not necessarily increase when transitioning from out-of-phase to diffusive dominated channel-trap exchange (i.e. from right to left in Figure 2.8a). Instead, it depends on velocity phase difference α_d. An increase in the relative importance of diffusive transport enhances the additional dispersion coefficient when α_d is small (e.g. red line in Figure 2.8a). However, for large values of α_d, where advective out-of-phase exchange significantly contributes to the additional salt flux, increasing the diffusive transport tends to diminish the trap effect, as noted in Section 2.3.2. This is more pronounced when the normalised current velocity in the trap, $\hat{U}_t/\hat{U}_c$, is high (Figure 2.8b). At low Péclet numbers, the resulting tidal excursion−averaged dispersion coefficient behaves independently of tidal characteristics and is essentially determined by the magnitude of K_t and the trap length B_t. The effectiveness of the trap diminishes at low Péclet numbers when the diffusive salt front can reach the end within half a tidal cycle, leading to reduced residence times as a consequence. So, in conclusion, the presence of a diffusive salt flux can diminish the effect of the advective out-of-phase exchange on the salt fluxes in the channel.

To explain why the presence of a diffusive salt flux can diminish the effect of the advective out-of-phase exchange, we examine the exchange over the trap entrance for two contrasting scenarios: no phase difference ($\alpha_d = 0\pi$) and the largest realistic phase difference ($\alpha_d = 0.5\pi$), as shown in Figure 2.9. Focussing on the instantaneous diffusive salt flux f_D (Figure 2.9c,d), it is evident that for $\alpha_d = 0.5\pi$, the diffusive exchange shows an asymmetry in the magnitude and duration for which f_D is directed toward the trap, even for lower K_t values, which contrasts with $\alpha_d = 0\pi$. The prolonged period during which the diffusive salt flux is directed toward the trap and increases in magnitude results from the development of a strong lateral salinity gradient near the trap entrance as the trap starts to empty. Due to the velocity phase difference, the salinity in the main channel increases, while near the trap entrance the salinity decreases as the trap empties, generating a sharp salinity gradient that promotes a diffusive flux into the trap (phase-induced diffusive salt flux). This diffusive flux increases the salinity near the trap entrance compared to the case of nearly pure advective out-of-phase exchange (Figure 2.9b). In contrast, with $\alpha_d = 0\pi$, an increase in K_t causes continuous diffusive exchange between the channel and the trap, resulting in a nearly symmetrical diffusive salt flux f_D for both flood and ebb periods. A sharp lateral salinity gradient near the trap entrance does not develop because the salinity of the rejoining water masses is nearly the same.

Panels 2.9e−j illustrate the additional salt fluxes predicted by Eq. 4.5, aiming to clarify the role of phase-induced diffusive salt fluxes. For $\alpha_d = 0\pi$, the additional salt flux is governed by diffusive exchange, $\tilde{F}_D$, which increases with K_t (see Figure 2.9g). This increase in $\tilde{F}_D$ is also observed for $\alpha_d = 0.5\pi$, but is influenced by the phase-induced diffusive salt flux (panel 2.9h). The raised salinity near the trap entrance while the trap empties (Figure 2.9b) enhances $\tilde{F}_A$ (panel 2.9f) and reduces the contribution of advective out-of-phase exchange, balancing $\tilde{F}_A$ and $\tilde{F}_C$. The increase in $\tilde{F}_A$ exceeds that of $\tilde{F}_D$, explaining why the phase-induced diffusive salt flux reduces the resulting additional salt flux. When K_t increased further, the trap's contribution increases again due to intensified diffusive exchange $\tilde{F}_D$. The magnitude of $\tilde{F}_A$ decreases slightly as salinity variations at the trap entrance diminish.

Figure 2.8b illustrates that the phase-induced diffusive reduction in the dispersive effect of the trap is more pronounced when the velocity in the trap (normalized by the main channel velocity) is relatively strong for the same Péclet number. A small current velocity in the trap leads to a shorter distance over which the salinity field is advected into the trap ($L_t \sim \hat{U}_t/\omega$) producing a stronger

gradient, since $\frac{\partial s_t}{\partial y} \sim \frac{u}{u_t}\frac{\partial s}{\partial x}$ A larger velocity in the trap increases the distance over which the salinity field is advected, and reduces lateral gradients. For smaller $\hat{U}_t/\hat{U}_c$, a diffusive salt front propagates more easily into the trap and can exceed the distance over which the salinity field is advected by the tidal motion even with a small K_t. Conversely, for larger values of $\hat{U}_t/\hat{U}_c$, the salt front propagates less easily into the trap and has to travel further to exceed the excursion limit. Hence, the structure of the salinity field remains determined by the tidal motion, and a diffusive salt flux develops during ebb, causing the phase-induced diffusive damping.

2.3.4 Influence of background dispersion in the main channel on the effect of channel-trap exchange

In previous sections, the additional salt flux was solely attributed to channel-trap exchange. Figure 6.12 illustrates how the additional salt flux due to trapping is affected by the time scale of background diffusion in the main channel. With K_b = 20 m^2/s , the additional salt flux results fully from an increase in the tidal salt flux, $\Delta F_1 = F_1 - F_{1,r}$, and the extent of the zone in the main channel where the trap effect is visible is approximately equal to L_t. In contrast, for K_b = 2000 m^2/s, the zone of influence exceeds L_t and the peak additional salt flux is reduced. Furthermore, the additional salt flux is now the result of a balance between tidal and diffusive ($\Delta F_b = F_b - F_{b,r}$) contributions, and differ substantially up- and down-estuary of the trap. Even without a velocity phase difference ($\alpha_d = 0$), the trap effect for out-of-phase exchange is not zero. This is explained by the fact that with a higher value for K_b, the system responds more rapidly to the salinity gradients that develop during the tidal cycle, influencing the resulting salt fluxes. Furthermore, an increase in the value of K_b implies an increase in the magnitude of F_b, which in turn reduces the relative importance of the trap, but also reduces the ability to reproduce F_{trp} through Eq. 4.5.

2.4 Discussion

2.4.1 Comparison with existing theory

In this study, the additional salt flux and associated dispersion coefficients resulting directly from channel-trap exchange were quantified for a single trap, much shorter than the tidal excursion length, across various scenarios. In this section, the additional salt fluxes obtained in Section 2.3.2, expressed as dispersion coefficients, are compared with existing theoretical frameworks derived for different regimes.

2.4.1.1 Pure advective out-of-phase exchange

Tidal trapping results from advective out-of-phase exchange when diffusive exchange processes are negligible, typically characterised by high Péclet numbers ($P_e > 10^3$), as illustrated in Figure 2.8. Figure 6.15 compares the tidal extent-averaged dispersion coefficient, $\overline{K}_{\mathrm{trp}}$, with analytical estimates of tidal dispersion for different velocity phase differences. The numerical results indicate that the trap effect increases with the velocity phase difference α_d and scales as $\overline{K}_{\mathrm{trp}} \sim \sin^2(\alpha_d)$. This is consistent with the expression by Dronkers (1978) for a continuous trap (see Eq. 2.3). Note that, the analytical framework by MacVean and Stacey (2011) predicts a maximum trapping effect for a channel-trap phase difference of $\frac{1}{4}\pi$, which differs

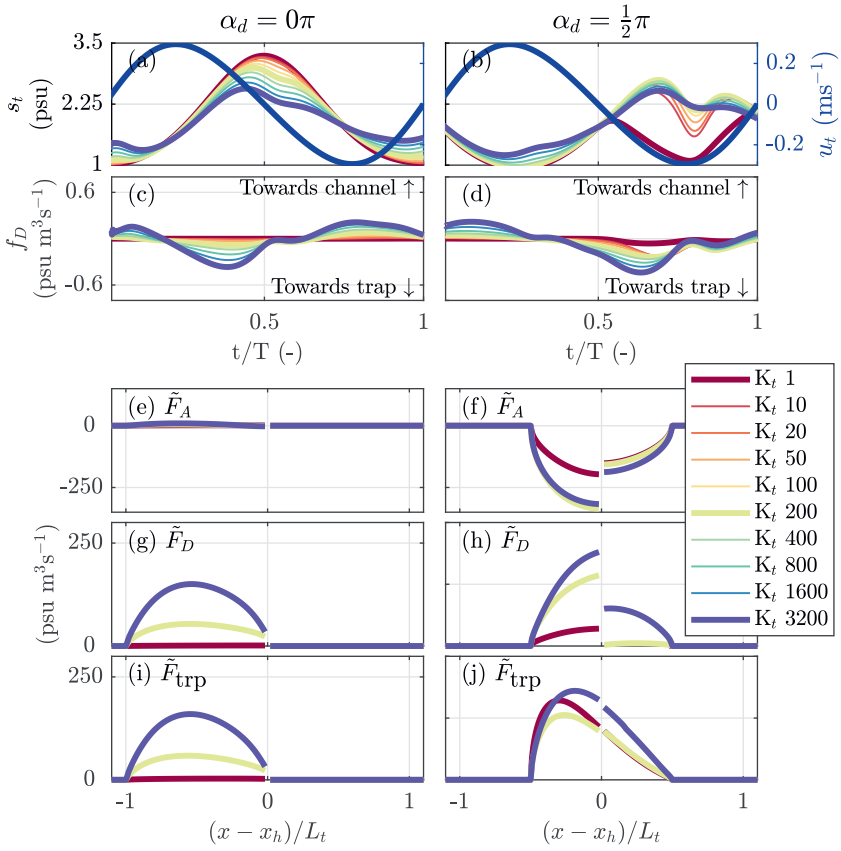


Figure 2.9: Salt fluxes at the trap entrance and resulting additional salt flux in the main channel for varying lateral diffusion coefficients, K_t, illustrating the transition from out-of-phase toward diffusive dominated channel-trap exchange. This is shown for two contrasting scenarios: (1) no velocity phase difference ($\alpha_d = 0\pi$) and (2) the largest physically realistic phase difference ($\alpha_d = 0.5\pi$). In both scenarios, $\hat{U}_t/\hat{U}_c = 0.30$ m/s. Panels a−b: salinity and current near the trap entrance. Panels c−d: instantaneous diffusive salt flux f_D at the trap entrance. Panels e−f: Predicted additional salt flux in the main channel resulting from cross-sectional average transport at the trap entrance, $\tilde{F}_A$. Panels g−h: Same as panel e−f but for diffusive exchange, $\tilde{F}_D$. Panels g−h: Predicted total additional salt flux resulting from channel trap exchange, $\tilde{F}_{\mathrm{trp}}$.

from the present results. This difference is largely explained by the fact that this study accounts for the velocity difference between the upstream and downstream regions relative to the position of the trap. However, this does not fully account for the discrepancy, and the underlying reasons are systematically investigated and discussed in Chapter 3.

2.4.1.2 Effect of mixing in the trap

Mixing in the trap causes the salinity field leaving the trap to be (partially) mixed, a phenomenon frequently observed during field studies focussed on tidal trapping

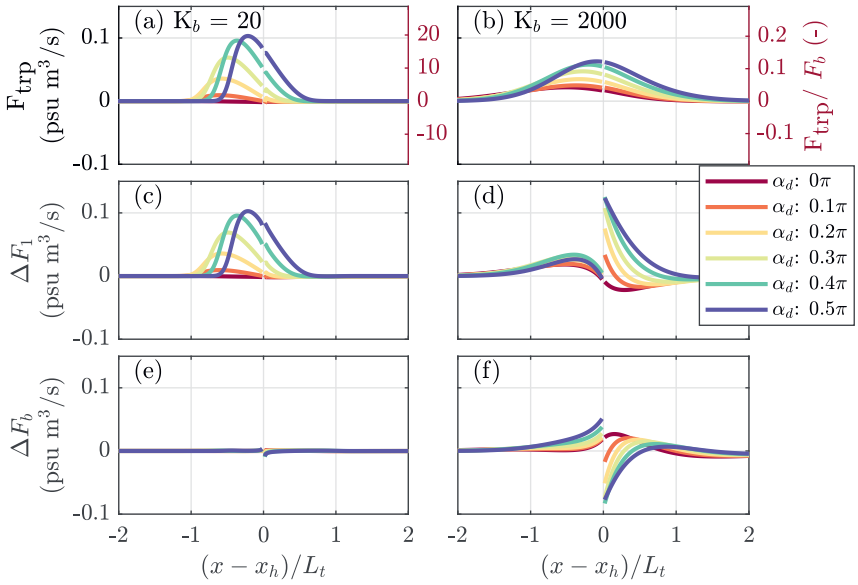


Figure 2.10: Influence of the background dispersion coefficient,K_b, on the salt flux resulting from channel-trap exchange. Shown for two scenarios with a low ($K_b = 20$ m^2/s) and ($K_b = 2000$ m^2/s) background diffusion coefficient.(a−b) Total additional salt-flux, F_{trp}. (c−d) The difference in the tidal contribution, ΔF_1. (e−f) The difference in the diffusive contribution ΔF_b.

(MacVean and Stacey 2011; Garcia and Geyer and Randall 2022). For example, Garcia and Geyer and Randall (2022) observed internal mixing in side creeks driven by a density current within the trap. By comparing their empirical estimate of tidal trapping with Eq. 2.2, they concluded that the observed internal mixing enhances the effect of tidal trapping. In the idealised model, the assumption of complete internal mixing significantly enhances the trap effect when α_d is low (see Figure 6.12). However, when $\alpha_d > \frac{1}{4}\pi$, the effect of internal mixing becomes negligible. This occurs because the maximum particle separation due to internal mixing is achieved at $\alpha_d = 0\pi$ and decreases for higher values, owing to the shape of the along-trap salinity profile.

2.4.1.3 Phase−induced diffusive damping

For values of the Péclet number between 10^1 and 10^3, both diffusive and the cross-sectional average exchange was found to be important for the trap effect. Results from the numerical model indicate that when α_d is small, the diffusive exchange tends to increase the trap effect beyond what is expected from pure advective out-of-phase exchange (Figure 6.12). However, when α_d is large and the trap is sufficiently long, a diffusive salt flux tends to diminish the trap effect. This occurs because the phase difference introduces a strong lateral gradient when the trap empties (Section 2.3.3), resulting in a diffusive salt flux into the trap, which reduces the sharpness of the resulting salt anomaly in the channel. To the authors' knowledge, the diffusive damping of the trap effect, which results from diffusive salt flux into the trap and is set up by a sharp salinity gradient at the trap entrance during the ebb phase due to the flow velocity phase difference between the trap and the main channel, has not yet been documented in the literature.

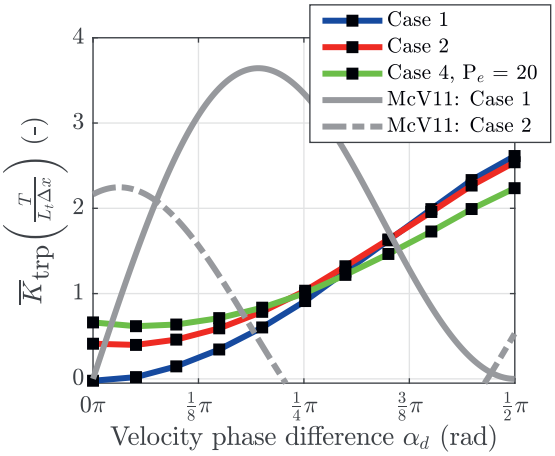


Figure 2.11: Comparison of the tidal excursion-averaged additional dispersion due to the trap, normalised by $\frac{L_t\Delta x}{T}$, plotted as a function of the phase lead of the trap velocity over the channel velocity (downstream), α_d, under different scenarios: pure advective out-of-phase exchange (case 1), advective out-of-phase exchange with mixing in the trap (case 2), and advective out-of-phase exchange with diffusive exchange (case 4, with $P_e = 20$). The numerical results are compared with the analytical framework by MacVean and Stacey (2011), indicated as McV11.

2.4.1.4 Continuous diffusive exchange

When the contribution of advective exchange decreases ($P_e < 10^1$), tidal trapping results from a continuous diffusive exchange, which arises from a lateral salinity gradient between the channel and the trap, set up by the tidal motion. This type of exchange is often observed in real estuaries (Abraham et al. 1986; Ralston and Stacey 2005; Giddings et al. 2012; De Nijs et al. 2009), especially near harbours. However, it should be noted that this type of exchange involves a density current flow, a mechanism not adequately captured within the 1D framework. The results indicate that when the trap is sufficiently long, the typical residence time matches the tidal cycle, and the trap effect is determined by the salt front's propagation length. This makes it challenging to quantify the resulting trap effect using formulations like Eq. 2.1, which require specifying the relative trap size and residence time in advance.

2.4.2 Development towards an new equilibrium

In Section 2.3, the additional salt flux was derived for a single cycle by adjusting the initial salinity field. However, as the system develops a new equilibrium, the exchange with the trap changes because of the adjusted along channel salinity field.

To explore the trap effect as the system develops towards an equilibrium, we quantified the additional salt flux over the first ten consecutive tidal cycles assuming pure advective out-of-phase exchange using Eq. 4.5, from which the excursion-averaged dispersion coefficient $\overline{\tilde{K}}_{\mathrm{trp}}$ is calculated. The calculated values for $\overline{\tilde{K}}_{\mathrm{trp}}$ show an initial decrease but stabilize after several tidal cycles (Figure 6.15a). The model suggests that $\overline{\tilde{K}}_{\mathrm{trp}}$ stabilizes when the tidally averaged salinity gradients within the tidal extent no longer show substantial deviations between consecutive tidal cycles. This suggests that the dispersion coefficient for tidal

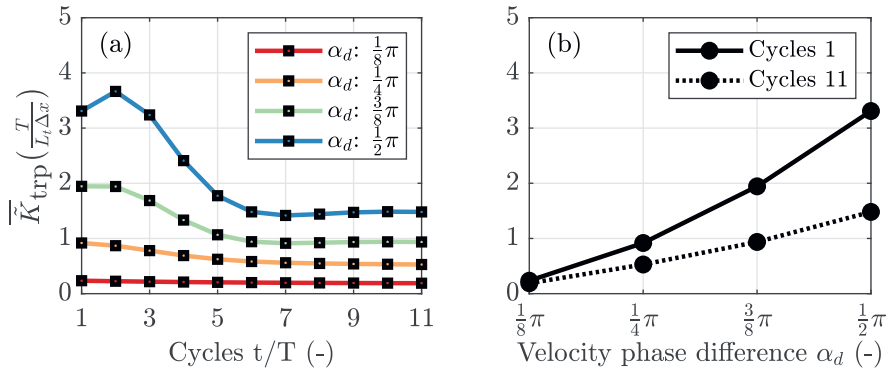


Figure 2.12: (a) Evolution of the excursion-averaged normalised dispersion coefficient $\frac{L_t \Delta x}{T}$ during the first ten tidal cycles, presented for various velocity phase differences. (b) Comparison of the excursion-averaged dispersion coefficient calculated at the start and after eleven cycles. Both are evaluated under the conditions of Case 1.

trapping depends on the salinity gradient, contrary to the common assumption that tidal trapping is independent of the salinity gradient (Okubo 1973; Dronkers 1978; Geyer and Signell 1992). However, the dispersion coefficient is derived using the local $\frac{\partial s_0}{\partial x}$, which does not necessarily correspond to the same section where channel-trap exchange occurs and gradients are adjusted. This discrepancy leads to a dependency between the trap effect and the salinity gradient. To capture tide-averaged dispersion in a coefficient, the exchange should consistently relate to the mean gradient (Geyer and Signell 1992). In the case of a local trap, the additional salt flux does not maintain a consistent relationship with the local mean gradient (Figure 6.15).

A common assumption is that the effect of a trap is limited to the additional salt flux that directly results from channel-trap exchange. However, as the system evolves towards a new equilibrium, the total tidal salt flux attributable to the presence of the trap may differ significantly from the salt flux directly resulting from channel-trap exchange. To explain this, we recall that the tidal salt flux is defined as the difference between the vertical and lateral exchange observed by a Lagrangian plane and the exchange across a specific cross-section (Dronkers and Van de Kreeke 1986). In a 1D setting, this simplifies to $A\langle u_1 s_1 \rangle = AK_b(\frac{\partial \grave{s}_0}{\partial \grave{x}} - \frac{\partial s_0}{\partial x})$, where $\grave{()}$ indicates properties observed from the Lagrangian plane. The salinity gradients resulting from channel-trap exchange are advected in both the up- and down-estuary directions, influencing the tidal salt flux within the region from -L_t to L_t relative to the trap's position x_h. This effect extends beyond the immediate location of direct exchange, affecting the overall tidal salt flux. This is further illustrated in Figure 2.13, presenting the development of the system towards a new equilibrium. For the first tidal cycle, the additional salt flux $\Delta F = F - F_r$ equals the additional salt flux that directly results from channel-trap exchange. This initial local increase in the salt flux spreads and eventually results in an overall increase of the up-estuary salt flux as the system approaches an equilibrium (see Figure 2.13b). After hundred cycles (close to a new equilibrium), the influence of the trap is evident in the tidal salt flux within the region from -L_t and L_t relative to x_h (see Figure 2.13c), exceeding the extent where the direct channel-trap exchange

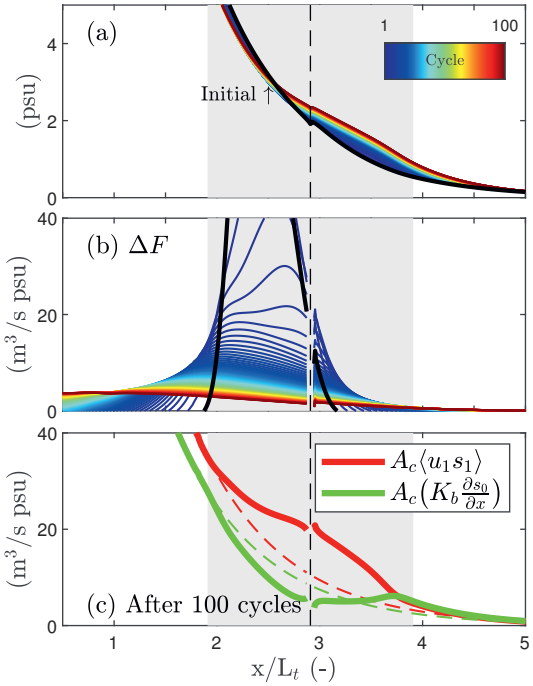


Figure 2.13: Development of the tidally averaged salinity distribution over 100 tidal cycles toward a new equilibrium, with $\alpha_d = \frac{1}{4}\pi$ and $K_b = 20$ m$^2/s$ under Case 1 channel-trap exchange conditions. The initial salt curve is shown by the solid black line. (a) Evolution of along-channel salinity distribution. In this example, the trap caused the 1 psu isohaline to migrate in up-estuary direction by $0.38L_t$. (b) Salt flux difference $\Delta F = F - F_r$ relative to the reference simulation, with ΔF being equal to F_{trp} in the first cycle. (c) The solid lines show the up-estuary salt fluxes in the new equilibrium after 100 cycles. The dashed lines show the salt fluxes for the equilibrium without the trap.

occurs.

The increase in tidal salt flux is accompanied by a reduction in the diffusive salt flux, explained by the decreased gradients in the system. To highlight the difference between the salt flux directly resulting from the channel-trap exchange (quantified through Eq. 4.5) and the resulting increase in tidal salt flux in the region from -L_t and L_t relative to x_h, referred to as the effective trap effect ($F_{\text{trp,eff}}$), we compare these two quantities. For this comparison, we assume that the decay in tidal salt flux observed both up and down estuary outside the influence zone of the trap (resulting in a constant dispersion coefficient) continues toward the trap. Figure 2.14 compares the resulting dispersion coefficients, demonstrating that the dispersion coefficient attributed to the overall increase in tidal salt flux is lower than that resulting from direct channel-trap mixing alone. The impact of the trap occurs over a larger zone. This analysis underscores the challenge of quantifying the additional tidal salt flux associated with geometric features, such as dead-end side channels. Our results warrant caution when using analytical parametrizations of channel-trap exchange to interpret observations of tidal dispersion, particularly in the presence of substantial gradients in the along-channel salinity distribution.

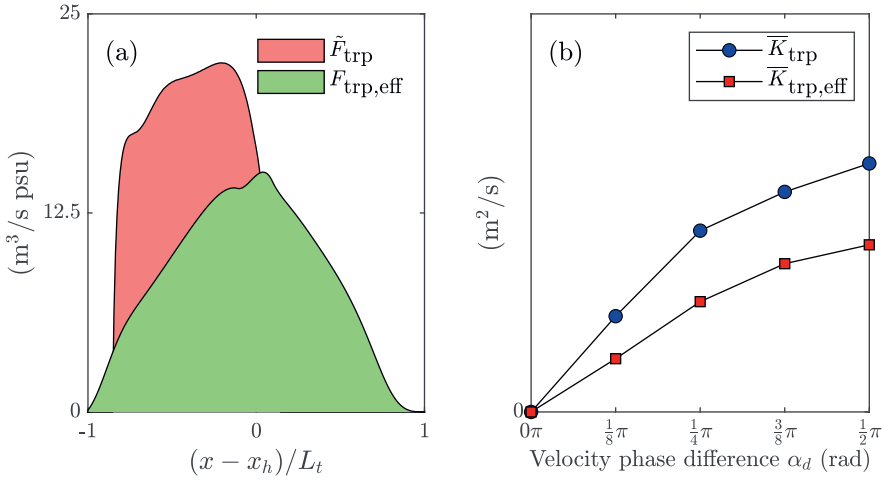


Figure 2.14: Relationship between direct mixing from channel-trap exchange and the resulting tidal salt flux associated with the trap. (a) Comparison between the salt flux directly resulting from channel-trap exchange and the overall observed increase in tidal salt flux associated with the trap, from a simulation with $\alpha_d = \frac{1}{4}\pi$ and $K_b = 20$ m$^2/s$. (b) Comparison between the excursion-averaged additional dispersion ($\overline{K}_{\text{trp}}$) and the effective increase in tidal dispersion ($\overline{K}_{\text{trp,eff}}$) for different velocity phase differences (α_d).

2.5 Conclusions

Tidal trapping, the temporal storage of water from the main channel in lateral dead zones and side channels, can increase the up-estuary salt transport. The exchange between channel and trap can occur through dispersive processes and advective out-of-phase exchange. Analytical frameworks typically assume one dominant exchange type to obtain solutions, but do not address the combined effect of both occurring simultaneously. Next, there exists an ambiguity in the literature regarding the dependence of the dispersive effect on the phase difference between the channel and the trap. This study quantifies the dispersive contribution from tidal trapping in a single dead-end side channel, accounting for both types of channel-trap exchange, using a 1D numerical model to quantify the additional salt flux resulting from different types of channel-trap exchange. The results show that pure advective out-of-phase exchange yields the largest additional salt flux for the greatest physically realistic velocity phase difference of 90°. For small velocity phase differences between flow in trap and in the main channel junction region, mixing in the trap or continuous diffusive exchange enhances the trap effect. However, diffusive exchange can reduce the trap effect compared to pure advective out-of-phase exchange when the velocity phase difference is large. This is due to an enhanced diffusive salt flux that develops when the trap empties, lowering the salinity difference between the main channel and the re-discharged water from the trap (phase-induced diffusive damping). The additional salt flux in the main channel depends on the strength of background dispersion and the associated diffusive time scales. Finally, the increase in tidal salt flux due to a trap in near-equilibrium conditions differs from the additional salt flux directly resulting from channel-trap exchange. This is because channel-trap exchange alters the salinity gradient over the region where the exchange occurs, equal to the tidal

excursion length. The altered gradients are advected in both the up- and the down-estuary directions during the subsequent tidal cycle, influencing the resulting tidal salt flux over a distance twice the tidal excursion length.

CHAPTER 3

Critical Examination of the MacVean and Stacey (2011) formulations

This chapter critically examines the widely used formulation of tidal trapping driven by advective out-of-phase exchange proposed by MacVean and Stacey (2011). Results from Chapter 2 demonstrated that advective out-of-phase exchange provides the largest additional contribution to up-estuary salt transport, consistent with the findings of Dronkers (1978) but in contrast to the conclusions drawn by MacVean and Stacey (2011). Here, we reassess the assumptions underlying their model, including the prescribed initial conditions, and verify the correctness of their derivation to identify the origin of these discrepancies. Our analysis shows that the differing results can be attributed to three key issues: (1) the along-channel velocity difference between upstream and downstream reaches of the trapping region is neglected, despite being essential for representing advective out-of-phase exchange; (2) a non-generalized source–sink formulation is adopted that acts independently of the main-channel salinity; and (3) errors occur in the derivation of the analytical solution presented by MacVean and Stacey (2011). Together, these issues explain the inconsistency between their results and earlier theoretical work

This chapter is based on: ***van Keulen, D., W. M. Kranenburg, and A. J. F. Hoitink*** *(2025). Tidal trapping and its effect on salinity dispersion in well-mixed estuaries revisited. Estuaries and Coasts, 48(6), 153. doi:10.1007/s12237-025-01579-0.*

3.1 Introduction

The dependence of salinity dispersion on the velocity phase difference between a main channel and a trap, as established in Chapter 2, aligns with the findings of Dronkers (1978), but stands in contrast to those reported by a more recent paper by MacVean and Stacey (2011). To understand the latter contrast, in this chapter we identify several key differences in the model assumptions and the methods to quantify the trap effect. We systematically assess the influence of each of these assumptions, which is supported by a series of numerical experiments.

The structure of this chapter is as follows: in Section 3.2 investigates the possible differences that proceed from assuming an initial solute pulse as assumed in the concentration moment analysis (Aris 1956; Fischer et al. 1979), which is a starting point for MacVean and Stacey (2011). Section 3.2.1 highlights the importance of the velocity difference between the upstream and downstream reaches relative to the trap in quantifying the dispersive effect of advective out-of-phase exchange. The latter is not accounted for in MacVean and Stacey (2011). The contrasting assumptions explained in Section 3.2 and 3.2.1 do not fully explain the observed differences. Even after adopting the assumptions of MacVean and Stacey (2011) regarding initial concentration, source sink term, and definition of dispersive effect, consistent agreement between analytical and numerical results was only achieved after refining the analytical derivation in MacVean and Stacey (2011), which is elaborated in the Section 3.3. A summary of our findings explaining the discrepancy is provided in Section 3.4.

3.2 An Initial Pulse of Solutes Subjected to Pure Out-of-Phase Tidal Trapping

A difference between this study and MacVean and Stacey (2011) lies in how the trap effect is determined. In this study, we adopted an initial salinity distribution that decreases monotonically in the up-estuary direction, and quantify the trap-induced additional salt flux through a cross-section (Section 2.2.2). MacVean and Stacey (2011) considered the evolution of an initial solute pulse and relate the effective dispersion to the rate of increase of the variance of the pulse. Following the approach of MacVean and Stacey (2011), we here consider the evolution of a solute pulse, and express the effective dispersion using the concentration moment analysis (Aris 1956; Fischer et al. 1979):

$$K_{\text{eff,var}} = \frac{1}{2}\frac{\partial \sigma^2}{\partial t} = \frac{\partial}{\partial t}\left(\frac{M_2}{M_0} - \mu_x^2\right), \tag{3.1}$$

where σ^2 is the variance of the solute distribution, M_0 the zeroth moment, M_2 the second moment and $\mu_x = \frac{M_1}{M_0}$ is the location of the centroid of the solute distribution. The i-th raw moment M_i of the solute concentration $s(x,t)$ is defined as:

$$M_i = \int_{-\infty}^{\infty} x^i s(x,t) dx. \tag{3.2}$$

The variance σ^2 can be expressed using the moments as follows:

$$\sigma^2 = \frac{\int_{-\infty}^{\infty}(x-\mu_x)^2 s(x,t)dx}{M_0} = \left(\frac{M_2}{M_0}\right) - \mu_x^2. \tag{3.3}$$

Since we are interested in the change in the variance after one full tidal cycle, we define $K_{\text{eff,var}} = \frac{1}{2T}\left(\sigma^2|_{t=T} - \sigma^2|_{t=0}\right)$ to express the dispersive effect of the trap.

To evaluate the evolution of an initial solute distribution, we set-up a numerical model for pure advective out-of-phase exchange, in which the initial salinity distribution in the main channel is defined as:

$$s(x-x_h,0) = \begin{cases} \frac{1}{2}\left(1-\cos(k(x-x_h)-\lambda)\right) & \text{if } \left(\frac{\lambda}{\pi T}-2\right)L_t \le \left(x-x_h\right) \le \frac{L_t\lambda}{\pi T}; \\ 0 & \text{otherwise,} \end{cases} \tag{3.4}$$

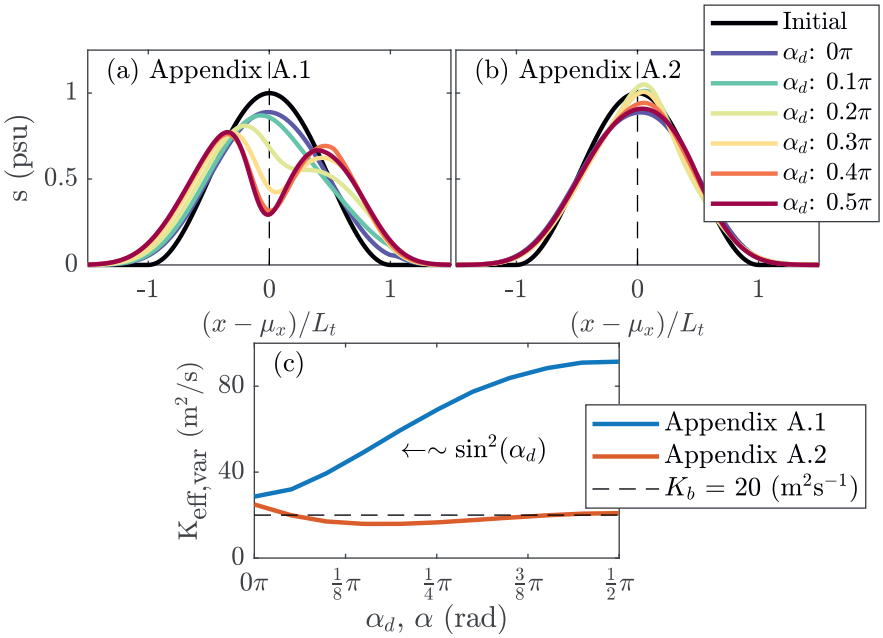


Figure 3.1: Resulting solute distributions and estimates of dispersion coefficients. (a) Initial solute distribution and the resulting distribution after one tidal cycle, for pure advective out-of-phase exchange (see Section 3.2). The x-axis shows the distance from the centre of the distribution μ_x, normalized by the tidal excursion length L_t (b) Same as (a), but under the assumption of a uniform along channel velocity (see Section 3.2.1). (c) The effective dispersion coefficient $K_{\text{eff,var}}$ for both cases, determined from the resulting solute distributions using Eq. 3.1, as a function of the velocity phase difference α_d and α.

with $k = \frac{\pi}{L_t}$ and $\lambda = \frac{\pi}{2}\big(1 - \cos(-\alpha)\big)$. This initial salinity profile enables quantification of $K_{\text{eff,var}}$ though Eq. 3.1.

Figure 3.1a presents the initial and resulting solute distributions after one tidal cycle for different values of α_d. The corresponding values of $K_{\text{eff,var}}$, quantified using Eq. 3.1, are shown in Figure 3.1c. The plot shows $K_{\text{eff,var}}$ scales with $\sin^2(\alpha_d)$, with the trap effect reaching its maximum at $\alpha_d = \frac{1}{2}\pi$. Based on this experiment, we conclude that the differences with MacVean and Stacey (2011) cannot directly be attributed to differences in the initial salinity distribution or to the method used to quantify the trapping contribution. Note that at $\alpha_d = 0$, the values of $K_{\text{eff,var}}$ are not zero. Then, it is close to the value used for K_b.

3.2.1 Assuming a Uniform Main Channel Velocity

A second key difference concerns the velocity in the main channel. MacVean and Stacey (2011) used a uniform along-channel velocity, whereas in this study, a difference between the channel velocity up-estuary and down-estuary of the trap is introduced. This difference is the result of the presence of the trap and is calculated using the continuity equation. Note that a uniform along-channel velocity was adopted by Okubo (1973) to evaluate a continuous lateral trap, where the exchange is driven by diffusive processes. However, in a trap where the exchange is driven by advective processes, a velocity phase difference is

introduced between the parts of the main channel up-estuary and down-estuary of the trap, leading to a dispersive effect as discussed in Section 2.3.1.

We conducted a second set of experiments, assuming a uniform velocity in the main channel, consistent with the approach of MacVean and Stacey (2011). The initial salinity profile is again given by Eq. 3.4, and for the source-sink term, pure advective out-of-phase exchange is assumed (see Figure 3.1b,c). In contrast to the experiment in Section 3.2, the variance of the solute distributions does not increase with an increasing velocity phase difference. Instead, it exhibits a slight decrease, and is most pronounced for $\alpha_d \approx \frac{1}{4}\pi$. This experiment emphasizes the importance of the along-channel non-uniform velocity in quantifying the effect of advective out-of-phase exchange, and clearly demonstrates that its dispersive effect cannot be accurately described unless the along-channel velocity difference introduced by the trap is taken into account.

3.3 Reproducing the solution by MacVean and Stacey (2011)

Sections 3.2 and 3.2.1 do not fully explain the differences between results presented in this paper and those by MacVean and Stacey (2011). Two key assumptions adopted by MacVean and Stacey (2011) to obtain an analytical expression remain unexplored: (1) the relationship between salinity in the main channel and the salinity level at the trap entrance, which determines the concentration of salt abstracted from (or released into) the main channel by the source-sink term and (2) the adopted definition of $K_{\text{eff,var}}$. Those assumptions are discussed in Section 3.3.1. After adopting the assumptions by MacVean and Stacey (2011), sections 3.3.2 and 3.3.3 seek to find consistent results between the analytical expressions and numerical model results, which is only achieved for an adjusted analytical expression.

3.3.1 The Adopted Source-Sink Term and Definition of the Dispersive Effect

The concentration moment analysis developed by Aris (1956), adopted by MacVean and Stacey (2011), provides a more general solution to Taylor's problem of shear dispersion (Taylor 1953), as it does not require explicit specification of the salinity distribution in the main channel (Aris 1956; Fischer et al. 1979). MacVean and Stacey (2011) assumed that this generality also applies to their model. However, their approach includes a source-sink term that removes solutes from the channel at a predefined concentration. This assumption introduces a dependency on the initial conditions, thereby reducing the generality of the results. In contrast, Okubo (1973) employed a generalized source-sink formulation in which both the source and sink terms are functions of the salinity in the main channel. This approach preserves the generality of Aris (1956) method. To illustrate that $K_{\text{eff,var}}$ depends on the initial conditions when a predefined source-sink term is used, we performed a series of model runs—assuming a uniform main channel velocity—in which the system was initialized with a solute distribution described by Eq. 3.4. Herein, α is varied between 0 and $\frac{1}{2}\pi$. We employed the source-sink term adopted by MacVean and Stacey (2011) for pure advective out-of-phase exchange (see Eq. 3.8c), but assumed that the velocity in the trap is in phase with the main channel. Figure 3.2 illustrates the resulting solute distributions and the corresponding values of $K_{\text{eff,var}}$, quantified through Eq. 3.2, which clearly vary depending on the assumed initial condition.

MacVean and Stacey (2011) do not specify an initial salinity distribution in the main channel, but prescribe a salinity at the trap entrance that fluctuates around zero to define the source–sink term. As a result, the initial concentration in the main channel can be interpreted as zero. The solute distribution that develops in the main channel after one full tidal cycle is therefore solely the outcome of the source-sink dynamics and includes both positive and negative concentration values. If there is no net salt flux from the trap (as is the case for advective out-of-phase exchange), then M_0 remains equal to zero after a

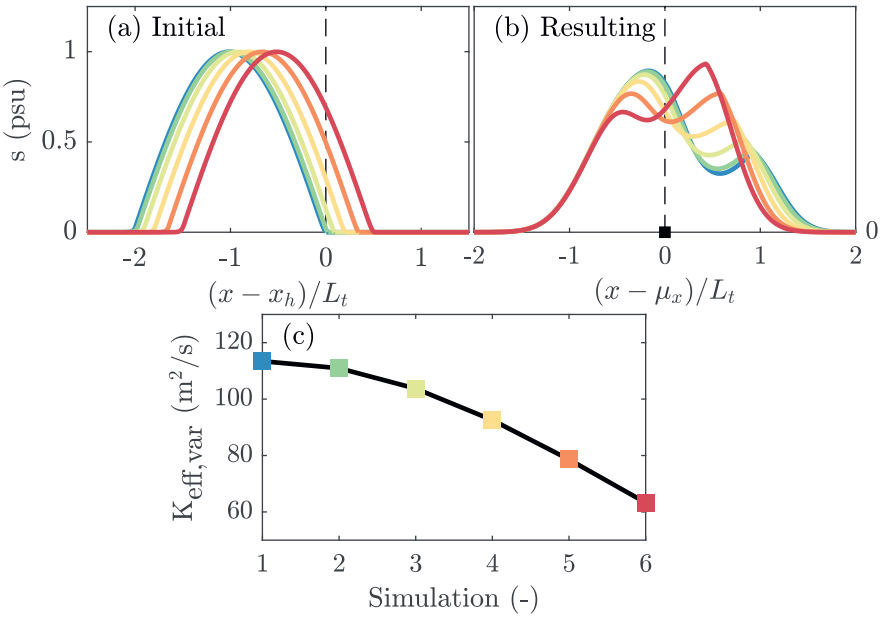


Figure 3.2: Illustration of the dependency of $K_{\text{eff,var}}$ on the initial solute distribution when adopting a non-generalized source-sink term. (a) Assumed initial solute distribution. (b) Resulting solute distribution for pure advectivive out-of-phase exchange with the velocity in trap an channel in phase ($\alpha = 0$), but assuming a non-generalized source-sink term. Here for all simulation the concentration at the trap entrance is given by 3.8a, with $\hat{S}_t = 1$ and $\alpha = 0$. (c) The effective dispersion coefficient $K_{\text{eff,var}}$ determined from the resulting solute distributions using Eq. 3.1, plotted as a function of the assumed initial condition.

full tidal cycle. This presents a problem when attempting to determine the variance of the distribution using Eq. 3.3. Instead MacVean and Stacey (2011) defined $K_{\text{eff,var}}$ as follows

$$K_{\text{eff,var}} = \frac{1}{2}\frac{\partial \sigma^2}{\partial t} = \frac{1}{2T}\frac{\Delta M_2}{\overline{M_0}}, \tag{3.5}$$

where it is assumed that $\mu_x = 0$ and M_0 is replaced by the tidal averaged $\overline{M_0}$. Setting $\mu_x = 0$ means that the centre of the distribution is always assumed to coincide with $x = 0$. In their analytical derivation, MacVean and Stacey (2011) take $x = 0$ to coincide with the position of the trap. This can be questioned, especially in cases where there is a net salt flux from the trap. Before numerically evaluating the effect of no initial concentration with a pre-defined source-sink term (Section 3.3.3), we will first re-examine the four analytical solutions presented by MacVean and Stacey (2011) in the next section.

3.3.2 Re-derivation of Analytical Expressions

The salt balance assumed by MacVean and Stacey (2011) reads:

$$\frac{\partial s}{\partial t} + \hat{U}_c \sin(\omega t - \alpha)\frac{\partial s}{\partial x} - \frac{\partial}{\partial x}\left(K_b \frac{\partial s}{\partial x}\right) = -\frac{\hat{U}_t H_t}{A_c}\sin(\omega t) \tag{3.6}$$

Differentiating Eq. 3.2.1 with respect to time, substitution of this salt balance into the obtained relation, and integration over time, yields expressions for the concentration

moments. Substituting those into Eq. 3.5 leads to a general expression for $K_{\text{eff,var}}$:

$$K_{\text{eff,var}} = -\frac{\hat{U}_c^2 \hat{Q}_T}{\overline{M_0} T A_c} \int_0^T \sin(\omega t - \alpha) \Big(\int_0^t \sin(\omega t - \alpha) \Big(\int_0^t \sin(\omega t) s_t(t) dt \Big) dt \Big) dt - \frac{l^2 \hat{Q}_T}{6 \overline{M_0} T A_c} \int_0^T \sin(\omega t) s_t(t) dt + K_b, \tag{3.7}$$

where $l = \frac{1}{2}\Delta x$ and $s_t(t)$ is the salinity at the trap entrance. The four analytical expressions presented in MacVean and Stacey (2011) are derived by adopting the following functional forms for $s_t(t)$:

$$s_t(t)_{\text{scen. 1}} = -\hat{S}_t \cos(\omega t), \tag{3.8a}$$

$$s_t(t)_{\text{scen. 2}} = -\hat{S}_t \cos(\omega t - \alpha), \tag{3.8b}$$

$$s_t(t)_{\text{scen. 3}} = \begin{cases} -\hat{S}_t \cos(\omega t - \alpha) & 0 < t < T/2; \\ \hat{S}_t \cos(\omega \left(\frac{T}{2} - t \right) - \alpha) & T/2 < t < T, \end{cases} \tag{3.8c}$$

$$s_t(t)_{\text{scen. 4}} = \begin{cases} -\hat{S}_t \cos(\omega t - \alpha) & 0 < t < T/2; \\ \frac{1}{T} \int_0^{T/2} -\hat{S}_t \cos(\omega t - \alpha) dt & T/2 < t < T, \end{cases} \tag{3.8d}$$

where $\hat{S}_t$ denotes the salinity amplitude at the trap entrance. The subscript scen., scenario, corresponds to the cases considered by MacVean and Stacey (2011). We use the term scenario instead of case here to distinguish them from the case studies introduced in main text of this paper. We are unable to reproduce the expressions presented by MacVean and Stacey (2011) when using the functional forms given in Eq. 3.8 to obtain an explicit solutions to Eq. 3.7. Instead we find the following four expressions:

$$K_{\text{eff, scen. 1}} = \hat{U}_c L_t \frac{\cos\alpha \, \sin\alpha}{4} + K_b \tag{3.9a}$$

$$K_{\text{eff, scen. 2}} = \hat{U}_c L_t \sin\alpha \frac{7 - 4\sin^2\alpha}{16 \sin\alpha \, \pi + 8\cos\alpha} - \frac{2 l^2 \pi \sin\alpha}{3T(\cos\alpha + 2\pi \sin\alpha)} + K_b \tag{3.9b}$$

$$K_{\text{eff, scen. 3}} = \hat{U}_c L_t \cos\alpha \frac{32\cos^2\alpha + 3\pi\cos\alpha\sin\alpha - 32}{12\pi(\cos\alpha + \pi\sin\alpha)} + K_b \tag{3.9c}$$

$$\begin{aligned} K_{\text{eff, scen. 4}} = \hat{U}_c L_t \Bigg[& \frac{(16 - 9\pi^2)\sin\alpha}{24\pi(3\sin\alpha\pi^2 + \cos\alpha\pi - 2\sin\alpha)} \\ & + \frac{(16 - 12\pi^2)\cos^2\alpha \, \sin\alpha}{24\pi(3\sin\alpha\pi^2 + \cos\alpha\pi - 2\sin\alpha)} \\ & + \frac{76\pi\cos\alpha - 44\pi\cos\alpha}{24\pi(3\sin\alpha\pi^2 + \cos\alpha\pi - 2\sin\alpha)} \\ & - \frac{2}{3\pi}\frac{l^2}{L^2}\sin\alpha \frac{\pi^2 - 2}{3\sin\alpha\pi^2 + \cos\alpha\pi - 2\sin\alpha} \Bigg] + K_b \end{aligned} \tag{3.9d}$$

Beyond the analytical differences, a key distinction is that Eq. 3.9a-d do not include the non-dimensional ratio $\epsilon = \frac{\hat{S}_t}{\hat{S}} \frac{\hat{Q}_t}{\hat{Q}_c} = \frac{\hat{S}_t}{\hat{S}} \frac{A_t}{A_c} \frac{\hat{U}_t}{\hat{U}_c}$, which appears in the formulations presented by MacVean and Stacey (2011). This ratio emerges when adopting the same scaling assumptions used in their analysis, specifically assuming that $\overline{M_0}$ scales as $\hat{S} L_t$. Under this scaling assumption, the parameters in front of the integral term in Eq. 3.7

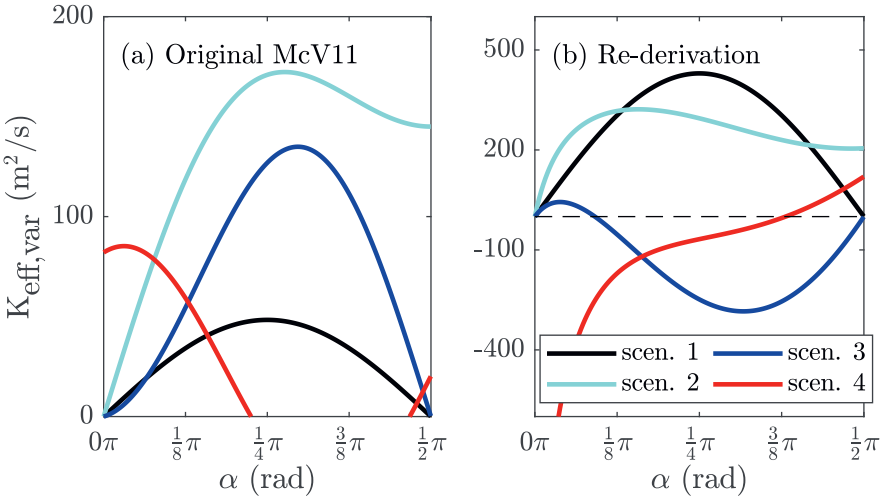


Figure 3.3: Comparison of the dispersion coefficient $K_{\text{eff,var}}$ according to the analytical solution presented by MacVean and Stacey (2011) and the results from the re-analysis. (a) The theoretical curves for the different scenarios analysed by MacVean and Stacey (2011). (b) The curves obtained after the re-derivation (see Eq. 3.9a-d).

(after taking $\hat{S}_t$ out of the integral) can be rewritten as $\frac{\hat{U}_c^2 \hat{Q}_T \hat{S}_t}{\overline{M_0} T A_c} \sim \epsilon \hat{U}_c L_t$. However, this essentially implies that we define $K_{\text{eff,var}} = \frac{1}{2T} \frac{\Delta M_2}{\overline{M_0}} \sim \frac{1}{2T} \frac{\Delta M_2}{L_t \hat{S}}$. This scaling approach introduces an inconsistency with the derivation of ΔM_2, and affects K_b in Eq. 3.7. Adopting this scaling approach leads to the following expression for scenario 3:

$$K_{\text{eff, sncr 3}} = \epsilon \hat{U}_c L_t \cos(\alpha) \frac{(32\cos(\alpha)^2 + \frac{3}{2}\pi \sin(\alpha) - 32)}{96\pi} + \epsilon K_b \frac{\cos(\alpha) + \pi \sin(\alpha)}{8}. \quad (3.10)$$

Eq. 3.10 is similar to the equation presented by MacVean and Stacey (2011) (see Eq. 2.2), especially when we express $L_t = \frac{2\hat{U}_c}{\omega}$. Figure 3.3 compares the resulting curves from Eq. 3.9 with the results presented by MacVean and Stacey (2011). The shape of the curves resulting from Case 1 and 2 are similar. For Case 3 (representing pure advective out-of-phase exchange), the new equations predict a similar shape, but result in negative dispersion coefficients. For Case 4 (complete mixing of the trapped salinity field), we obtain a curve that differs significantly from the one presented by MacVean and Stacey (2011).

3.3.3 Validation Through Numerical Experiments

To test whether we can numerically reproduce the newly derived analytical expressions Eq. 3.9a-d, we initialize the model with no solute present in the domain, i.e., $s(x, 0) = 0$, and adopt the source–sink term formulation used by MacVean and Stacey (2011). Furthermore, we assume a constant velocity in the main channel, as done in Section 3.2.1, and quantify $K_{\text{eff,var}}$ using Eq. 3.5. Figure 3.4a illustrates the resulting salinity distribution for Case 3 (advective out-of-phase exchange), and Figure 3.4b compares the numerical results for the different scenarios with Eqs. 3.9a-d. The numerical solutions confirm each of the four analytical solutions in Eqs. 3.9a-d.

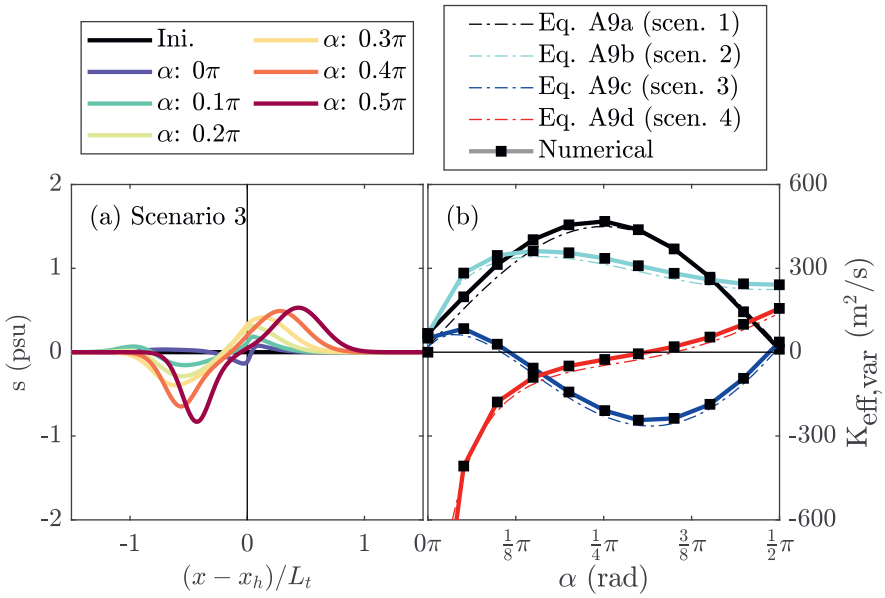


Figure 3.4: (a) Illustration of the resulting solute distribution after one tidal cycle for scenario 3 (see Section 3.3.3). (b) Comparison of the effective dispersion coefficient, $K_{\mathrm{eff,var}}$, calculated from numerically determined solute distributions (using Eq. 3.5) and the analytical expressions from Eq. 3.9, as a function of the velocity phase difference, α.

3.4 Concluding Remarks

The analytical expressions presented by MacVean and Stacey (2011) do not capture the dispersive effect of advective out-of-phase exchange. We identified the following aspects where improvements are necessary: (1) account for the difference in along-channel velocity upstream and downstream of the trap, as this is an essential feature that determines the dispersive effect of advective out-of-phase exchange. (2) Adopt a generalized source–sink term to derive an expression for the dispersive effect using concentration moment analysis, without requiring precise specification of the initial solute distribution (Aris 1956). (3) Corrections are necessary in the derivation of the analytical expressions for the different cases (see Section 3.3.2). Altogether, these aspects explain the observed differences in how the trap effect depends on the velocity phase difference between MacVean and Stacey (2011) and the present study. In this study, the model and analysis we adopt account for these aspects and therefore provide an improved and more general framework for describing dispersion due to tidal trapping by advective out-of-phase exchange.

CHAPTER 4

Harbor-induced tidal salinity dispersion in partially stratified estuaries

The contribution of traps to tidal dispersion is well-studied for well-mixed estuaries. However, the governing processes in deeper, partially stratified systems have remained under explored. Therefore, in this study, we investigate tidal trapping in such systems. Our observations and numerical model results show marked differences in the relative contribution of the instantaneous salt exchange between alternative harbor configurations relative to the main channel, associated with vertically sheared exchange flow driven by gravity dynamics. The observed variations are explained by a region in the main channel where the tidal salinity range shows a marked minimum, which limits the set-up of a baroclinic pressure gradient driving the exchange flow. Analysis of the salt flux resulting from vertical shearing between the channel and adjacent harbors, and the salinity range, suggests that this flux is proportional to the salinity range raised to the power 3/2. Quantification of the trapping-induced additional salt flux shows that it is primarily driven by this salt flux from vertical shearing between the channel and the harbor. Harbors located in regions with a smaller salinity range contributed significantly less to the net up-estuary salt flux, explained by the sensitivity of the salt flux resulting from vertical shearing to the salinity range. For the systems evaluated in this study, this resulted in the remarkable finding that the largest harbors contributed the least to the net up-estuary salt flux.

This chapter is based on: ***van Keulen, D., W. M. Kranenburg, and A. J. F. Hoitink*** *(2026). Harbor-induced tidal salinity dispersion in partially stratified estuaries. Journal of Geophysical Research: Oceans, 131, e2025JC023208. doi:10.1029/2025JC023208.*

4.1 Introduction

The intrusion of salt in estuaries is governed by a continuous interplay between freshwater flushing from river discharge and dispersive mechanisms that drive an up-estuary salt transport. The importance of different dispersive transport mechanisms differs between systems (Dijkstra and Schuttelaars 2021). When the salinity intrusion length is much longer than the the tidal excursion, the salt balance is often controlled by the estuarine circulation resulting from the gravitational circulation (Hansen and Rattray 1965; Chatwin 1976) and tidal straining (Simpson and Brown, et al. 1990). When both length scales are of similar magnitude, as in short estuaries, tidal dispersion becomes the principal mechanism of landward salt transport (Fischer et al. 1979; Geyer and Signell 1992). Nevertheless, even when estuarine circulation dominates at the system scale, tidal dispersive processes can remain locally important, particularly in the upper estuary where tidal dispersion often becomes the dominant transport mechanism (Dijkstra and Schuttelaars and Kranenburg 2022).

Geometric features, such as intertidal areas, creeks, harbors, and other channel irregularities creating dead zones adjacent to the main channel, can temporarily store volumes of saltwater within the tidal cycle and release them later. When the release occurs at a different position along the tidal excursion than where it originally comes from, a net redistribution of salt occurs over a distance equal to the tidal excursion length within a single tidal cycle (Dronkers 1978). However, the effect of this redistribution depends on the along-channel salinity structure and therefore may either enhance or reduce the net salt transport in the main channel associated with tidal dispersion. The overall impact of these geometric features is often system-dependent (Hendrickx and Pearson 2024). For example, in well-mixed estuaries, intertidal areas tend to enhance salinity intrusion by increasing tidal dispersion, whereas, in partially mixed or stratified systems, the increase in the tidal prisms and tidal currents due to these features are likely to reduce the estuarine circulation, which is the dominant transport mechanism in such environments. In this study, we investigate the exchange between channels and harbors and the associated contribution to salinity dispersion in partially stratified estuarine systems.

Salt transport decomposition techniques (Fischer et al. 1979; Lerczak and Geyer and Chant 2006) can be used to mathematically decompose the total salt transport through a cross-section and quantify the individual contributions associated with different salt transport mechanisms, based on observations or model results. Within such decompositions, tidal dispersion manifests itself in the temporal correlation between the cross-sectionally averaged tidally varying velocity and salinity signals (Fischer et al. 1979; Dronkers and Van de Kreeke 1986). However, such a transport decomposition provides limited insight into the underlying mechanisms, as the observed correlation results from exchange processes occurring elsewhere. The work by Dronkers and Van de Kreeke (1986) showed that the salt transport associated with this temporal correlation, when determined in an Eulerian reference frame, arises from shear occurring elsewhere within the tidal excursion domain and is therefore termed non-local salt transport. The Lagrangian approach of Dronkers and Van de Kreeke (1986) can be used to study the origin of the tidal salt transport through a cross-section, as was demonstrated by Garcia and Geyer (2022). An alternative approach, which focuses more directly on isolating the influence of individual geometric features and parameterizing their dispersive contribution, was proposed by Dronkers (1978) and extended in Chapter 2. This methodology quantifies the net salt transport into or out of a storage region (often called traps) over a tidal excursion, thereby directly assessing the redistribution effect of a single feature. Whereas the approach of Dronkers and Van de Kreeke (1986) provides insight into the overall resulting salt transport, the advantage of the approach of Dronkers (1978) is that it enables assessment of the relative importance of different channel–trap exchange mechanisms (see Chapter 2). This is the approach adopted in the present study.

The temporal storage in a trap can result from two types of exchange mechanisms. The first mechanism is referred to as advective out-of-phase exchange, in which a trap

is filling and emptying by the barotropic tide. When there is a velocity phase difference between the main channel and a trap, the trapped volumes will reenter the channel at a different location than where they left it, relative to the oscillating water mass in the main channel. Consequently, trapped and non-trapped parcels experience, respectively, a net down- and up-estuary displacement relative to each other (see Dronkers (1978) and Chapter 2). The resulting salinity dispersion is largest for the maximum physically realistic velocity phase difference of 90° between the channel and a trap. Mixing of the salinity field trapped during the barotropic flood can enhance the dispersive effect when the phase difference between velocity variation in the trap and in the main channel is small (see Dronkers (1978) and Chapter 2). This mechanism was also visible in the observations of Garcia and Geyer and Randall (2022), who showed that the trapped salinity field was (partially) mixed by a baroclinic circulation within the trap, causing relatively low-salinity water to leave the trap earlier during the onset of the barotropic ebb flow in the trap.

The second mechanism occurs when the exchange of salt between the channel and the trap across the trap entrance is diffusive in nature (Okubo 1973; Dronkers 1978), driven by density-driven exchange or turbulent processes. Okubo (1973) derived an elegant formulation for the dispersive effect of a continuous lateral trap undergoing diffusive exchange with the main channel. However, his formulation relies on a constant exchange rate coefficient that reflects the strength of the exchange, but does not describe a specific mechanism. Okubo (1973) noted this and suggested this to be a direction for future refinement. Both observational and modeling studies have explored the diffusive exchange processes between the channel and the trap (Ralston and Stacey 2005; Garcia and Geyer and Randall 2022), but have not proceeded to describe them in more precise formulations of the exchange and the resulting dispersion. Chapter 2 explored the combined effect of both advective out-of-phase exchange and diffusive exchange driving the transport of salt across the trap entrance. Here we show how this combined effect depends on a Péclet number for tidal trapping. In addition, their results indicated that the resulting additional up-estuary salt transport does not necessarily increase when the diffusive exchange becomes stronger, especially for larger velocity phase differences.

The specific processes of channel–harbor exchange have been studied by e.g. Roelfzema and Van Os (1978), Abraham et al. (1986), Eysink (1989), De Nijs et al. (2009), and Maren et al. (2009). These studies show that the exchange of salt results from tidal filling and emptying, eddies, and density-driven exchange. The density-driven exchange is established by the advection of the salinity field in the main channel, generating a channel–harbor density difference that drives a lock-exchange type flow. This flow reverses direction within the tidal cycle (Abraham et al. 1986; De Nijs et al. 2009; Maren et al. 2009). The characteristics of this type of exchange are influenced by the phasing and properties of the salinity field in the main channel and, on longer timescales, by hydrodynamic conditions such as storm surges (De Nijs et al. 2009). Moreover, Maren et al. (2009) found that dock length influences the phasing and strength of the exchange flow, depending on the size of the harbor basins relative to the forcing conditions. The work of both De Nijs et al. (2009) and Maren et al. (2009) focused on harbor siltation rather than salt dispersion. Early work by Roelfzema and Van Os (1978) and Abraham et al. (1986) investigated the influence of harbors on the salt intrusion length. Their results show that salt intrusion may increase due to the temporal storage and release of salt in a harbor. More specifically, Roelfzema and Van Os (1978) observed a relation between the strength of density-driven channel–harbor exchange and the salt intrusion length, but they did not quantify the actual dispersive effect of tidal trapping.

In this paper, we investigate the exchange of salt between a channel and an adjacent harbor, quantify the additional up-estuary salt transport generated by tidal trapping, and provide insights into the mechanisms by which tidal trapping governs salt dispersion in deeper, partially stratified systems. We do this based on field observations and numerical modeling of the channel-harbor salt exchange in the New Meuse, a branch of the Rhine-Meuse Estuary. The structure of this paper is as follows. Section 4.2 describes the field site, the set-up of the field measurements, the hydrodynamic model and the analysis approach. Section 4.3 presents the field observations, revealing marked

differences in channel–harbor exchange for the two harbors surveyed during the 13-hour shipboard campaigns. Section 4.4 presents numerical model results that verify the different processes observed during the shipboard measurements and provide an explanation for the observations. Subsequently, we evaluate the additional up-estuary salt transport resulting from channel-trap exchange (i.e., tidal trapping induced dispersion) for different harbors using the modeled channel-harbor exchange. In Section 4.5, we evaluate the role of tidal trapping in partially stratified systems and compare this with the classical understanding of tidal trapping in well-mixed systems. Within this comparison, we introduce a new formulation for the dispersion coefficient associated with density-driven tidal trapping. Conclusions are drawn in Section 4.6.

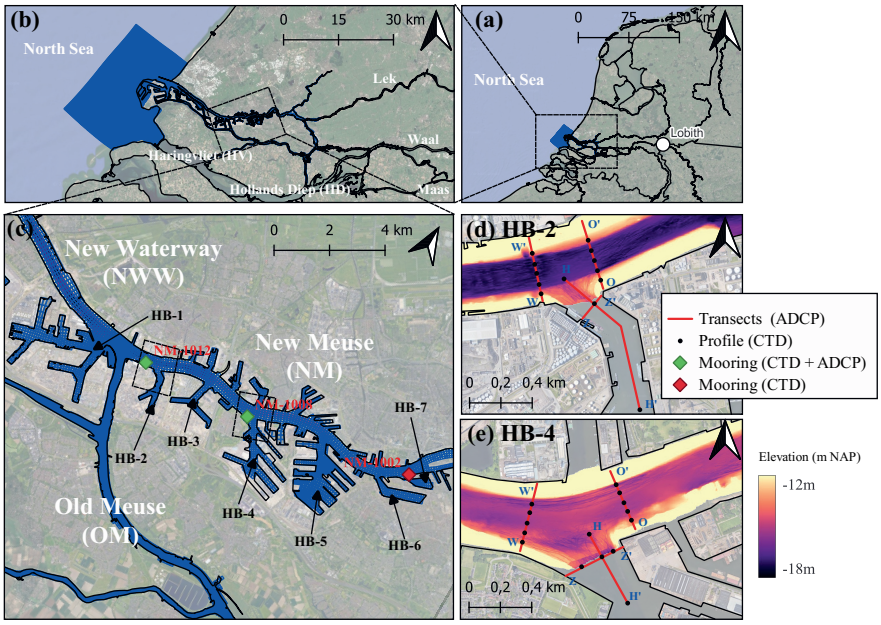


Figure 4.1: Satellite images of the Rhine–Meuse Delta, the model domain, and main branches. (a) Location of the Rhine–Meuse Estuary in the Netherlands. (b) Zoom of the lower Rhine–Meuse Estuary and extent of the model domain (dark blue colors indicate the numerical grid). (c) Overview of the New Meuse showing the studied harbors and moored measurement sites. (d) Setup of the 13-hour shipboard survey at site HB-2. (e) Setup of the 13-hour shipboard survey at site HB-4.

4.2 Methods

4.2.1 Study area

The New Meuse and the New Waterway are part of the Rhine–Meuse Estuary (Figure 4.1a–c). The Rhine-Meuse Estuary consists of a southern branch, composed of the Haringvliet (HV) and Hollands Diep (HD), and the northern branch, which includes the New Waterway (NWW) and the New Meuse (NM). The southern branch is a former estuary where discharge is regulated through sluices at the mouth. The northern and southern branches are interconnected through several smaller channels, forming a complex channel network (Figure 4.1b). The New Waterway and New Meuse channels serve as major shipping routes and host several harbors along the main channel, which are investigated in this study. The locations of the larger harbors studied here are shown in

Figure 4.1c.

Freshwater input into the Rhine-Meuse estuary is supplied by the Waal, Lek, and Maas rivers, which on average contribute 70%, 16%, and 14% of the total discharge, respectively (Leuven et al. 2023). Since the Waal and Lek are both bifurcations of the Rhine, freshwater forcing is typically expressed through the Rhine discharge measured at Lobith (Figure 4.1a). Under average discharge conditions, approximately 14% of the freshwater is transported to the North Sea through the southern estuary, while the remaining 86% exits the channel network via the northern branch (Cox et al. 2021). Because the southern branch is closed off by sluices, nearly all tidal energy enters the system through the northern branch.

4.2.2 Moored and shipboard measurements

A monitoring campaign was conducted in the New Meuse from 01-06-2022 to 24-10-2022. Two bottom-moored upward-looking ADCPs (600 kHz, manufactured by Teledyne RDI) were deployed in the New Meuse (Figure 4.1c), and two CTD arrays, each equipped with two CTD sensors, were attached to the nearby navigation buoys. A third array was installed further up-estuary. Maintenance on the CTD probes was performed every 3–4 weeks to limit the effects of biofouling. The locations of these CTD moorings are shown in Figure 4.1c. A water level gauge maintained by Rijkswaterstaat is located just upstream of NM-1012. The mooring data is used here to examine the along-channel salinity distribution in the New Meuse during the monitoring period.

A total of four 13-hour shipboard measurement campaigns were conducted at sites HB-4 and HB-2 under neap- and spring-tide conditions (Figure 4.1d,e). The data obtained is primarily used here to investigate the exchange of salt between the channel and the harbor. From a research vessel, ADCP measurements and vertical CTD profiles were collected along the transects shown in Figure 4.1d–e, providing additional insight into the flow and salinity structure. At HB-4, completing one full cycle consisting of ADCP transects and CTD profiles at all cross-sections took 60 to 70 minutes, while at HB-2 it took 45 to 55 minutes. The ADCP data were processed using ADCPTOOLS (Vermeulen et al. 2014), applying the regularization method developed by (Jongbloed and Vermeulen, et al. 2023). The processed shipboard ADCP data were projected onto a mesh with a vertical resolution of $\Delta z = 0.5$ m and a grid size of $\Delta y = 10$ m.

4.2.3 Numerical hydrodynamic modeling

The 13-hour shipboard measurements provide insight into channel–harbor exchange. However, direct comparison of the non-synchronous records across locations is challenging due to the daily inequality of the tide, fluctuating river discharge, and surge-induced variations, which all contribute to unsteadiness in the salinity field. Estimating the trapping effect (see Section 4.2.4.3) and computing tidally averaged salt fluxes from the data is challenging because of the limited time span of the 13-hour measurements.

To support the interpretation of the observations and quantify the effect of tidal trapping, a numerical hydrodynamic model of the Rhine-Meuse Estuary is used (Leuven et al. 2023). The Delft3D model solves the incompressible shallow water equations, with the eddy viscosity and diffusivity modeled using a k-ϵ scheme (Deltares 2021). The model domain covers the central and northern branches of the Rine-Meuse Estuary, as well a part of the North Sea (Leuven et al. 2023). The resolution of the computational grid varies, with the coarsest resolution applied to the offshore domain. In the region of interest, cell sizes are approximately 140 x 80 m. In the vertical, the model uses 20 equidistant σ-layers. Boundary conditions are derived from an overlapping, larger 2D hydrodynamic model.

We used model simulations from Leuven et al. (2023) covering the period 25-09-2015 to 21-10-2015. Although this period does not overlap with our measurement campaign, it was chosen because the model has been well validated for this time frame (Leuven et al. 2023). Discharge at Lobith (Q^{riv}) during this period was low, and comparable to the

Table 4.1: Overview of Rhine river discharge Q^{riv} statistics (mean, 10th and 90th percentiles) measured at Lobith, along with surge variations (standard deviation, 5th and 95th percentiles) from a nearby tide gauge. The surge variations, η^{surge}, represent water level fluctuations in the 25-hour to 14-day frequency band. The table includes data for the modeled period (25-09-2015 to 21-10-2015), a portion of the measurement campaign (01-09-2022 to 24-10-2022, shown in Figure 4.4), and a reference period 2010–2020.

Dataset	Mean(Q^{riv}) ($\mathrm{m^3\,s^{-1}}$)	Q^{riv}(10%) ($\mathrm{m^3\,s^{-1}}$)	Q^{riv}(90%) ($\mathrm{m^3\,s^{-1}}$)	Std(η^{surge}) (m)	η^{surge}(5%) (m)	η^{surge}(95%) (m)
Reference (2010–2020)	2084	1118	3258	0.13	−0.18	0.22
Modeled period (25-09 to 21-10-2015)	1116	1034	1254	0.09	−0.17	0.13
Measurement period (01-09 to 24-10-2022)	1272	887	1825	0.16	−0.24	0.33

10th percentile discharge of the measurement period ($Q^{\mathrm{riv}} \approx 1100$ m^3 s^{-1}), see Table 4.1. Moreover, discharge remained relatively constant, and storm surge induced water level variations (η^{surge}) were relatively weak. Here, η^{surge} is defined as the water level variation occurring within the 25-hour to 14-day frequency band. The combination of relatively steady discharge and relative weak surge-induced variations results in relatively stable salinity fields throughout the modeled period. In comparison, the average discharge during our measurement campaign was slightly higher ($Q^{\mathrm{riv}} \approx 1300$ m^3 s^{-1}, Table 4.1) largely due to an increase in Rhine discharge during the second half of the campaign towards average discharge conditions (see also Figure 4.4). In addition, surge-induced water level variations were more pronounced during the measurements.

The first two weeks were used to spin-up the model and are excluded from the analysis. The model simulation was initialized from a spin-up run, starting from a state in which salinity was close to equilibrium. Model output is stored at cross-sections in the main channel at 1 km intervals and at the entrances of the studied harbors, with a sampling frequency of 10 minutes.

4.2.4 Analysis

4.2.4.1 Salt Transport Decomposition Methods

The instantaneous exchange of salt between the main channel and adjacent harbors is analyzed by decomposing both measured (13-hour shipboard measurements) and modeled fluxes. The decomposed instantaneous salt transport contributions are used to quantify the contribution of different exchange mechanisms (see Section 4.3.5 and 4.4.3) and the modeled channel-harbor exchange is used to assess the contribution of tidal trapping to salinity dispersion (see Section 4.2.4.3).

4.2.4.2 Instantaneous Salt Transport Decomposition

To decompose the instantaneous salt transport, we follow the approach of Ralston and Stacey (2005), adapted to sigma-layer coordinates. We introduce a non-dimensional lateral coordinate $\gamma = y/B$, where B is the cross-sectional width. The velocity u and salinity s are decomposed as

$$\begin{aligned} s(t,\gamma,\sigma) &= s^A(t) + s^V(t,\sigma) + s^L(t,\gamma,\sigma), \\ u(t,\gamma,\sigma) &= u^A(t) + u^V(t,\sigma) + u^L(t,\gamma,\sigma), \end{aligned} \tag{4.1}$$

where the superscripts A, V, and L denote the cross-sectional mean, vertical deviation, and lateral residual, respectively. The cross-sectional means are defined as area-weighted averages. The vertical deviation of the velocity is defined as

$$u^V(t,\sigma) = \frac{\int_0^1 \left[u(t,\gamma,\sigma) - u^A(t)\right] h(\gamma,\sigma,t)\, B\, d\gamma}{\int_0^1 h(\gamma,\sigma,t)\, B\, d\gamma}, \tag{4.2}$$

where $h(\gamma,\sigma,t)$ is the physical thickness of the sigma layer at location γ and normalized vertical coordinate σ. The lateral residual is

$$u^L(t,\gamma,\sigma) = u(t,\gamma,\sigma) - u^A(t) - u^V(t,\sigma), \tag{4.3}$$

and the salinity field is decomposed analogously. Because sigma layers are terrain-following, the vertical and lateral components of the decomposition are not strictly orthogonal in physical coordinates. However, as the evaluated cross-sections are nearly rectangular, this non-orthogonality is weak and does not significantly influence the relative contributions of the vertical and lateral components to the total salt transport.

The instantaneous salt transport is then decomposed into three contributions:

$$\begin{aligned} F^T(t) &= F^A(t) + F^V(t) + F^L(t) \\ &= u^A(t)\, s^A(t)\, A + \int_0^1 \int_0^1 u^V(t,\sigma)\, s^V(t,\sigma)\, h(\gamma,\sigma,t)\, B\, d\gamma\, d\sigma \\ &\quad + \int_0^1 \int_0^1 u^L(t,\gamma,\sigma)\, s^L(t,\gamma,\sigma)\, h(\gamma,\sigma,t)\, B\, d\gamma\, d\sigma, \end{aligned} \tag{4.4}$$

where $A = \int_0^1 \int_0^1 h(\gamma,\sigma,t)\, B\, d\gamma\, d\sigma$ is the total cross-sectional area. Equation 4.4 decomposes the total instantaneous salt transport F_T into three contributions: the cross-sectional average transport F^A, and the transport associated with the vertical (F^V) and lateral (F^L) structures, respectively. To quantify tidal trapping and the contribution of alternative mechanisms, F^A represents the transport associated with advective transport (i.e., tidal filling and emptying), while F^V and F^L represent salt fluxes that, in a cross-sectionally averaged sense, act diffusively and, in the case of channel-harbor exchange, are largely associated with density-driven exchange and horizontal eddies, respectively, among other contributing processes.

Accurate quantification of the cross-sectionally averaged current at the harbor entrance u_h^A from the 13-hour boat surveys at cross-section Z-Z′ proved difficult, because the magnitude of u_h^A (1–10 cm/s) was much smaller than the vertical and lateral variations. Obtaining reliable estimates was further complicated by navigation activities and industrial discharges at HB-2. The cross-sectionally averaged velocity u_h^A is therefore estimated from water level variations, $\frac{d\eta}{dt}$, under the assumption that the harbors behave as short basins (Friedrichs 2010). In this approach, u_h^A is represented as $u_h^A = \alpha_1 + \alpha_2 \frac{d\eta}{dt}$, with the coefficients α_1 and α_2 determined by linear regression of the observations. We cross-referenced the obtained coefficient with those obtained when performing it on the numerical model, yielding differences between 15% and 30% .

In addition to decomposing the instantaneous salt transport between the channel and harbor, the subtidal salt transport in the main channel are also decomposed to provide insight into the transport mechanisms controlling up-estuary salt transport. For the decomposition of the subtidal transport, a slightly different approach is used, as shown in Appendix A.1.1. The key difference between the decomposition in Appendix A.1.1 and Eq. 4.4 is that no distinction is made between vertical and lateral variations in the cross-section. Instead, the along channel current and salinity field are decomposed into tidally averaged components, deviations from the tidally averaged and similarly into cross-sectionally averaged values and cross-sectional varying components.

4.2.4.3 Methods to Estimate the Up-Estuary Salt Transport from Tidal Trapping

To quantify the additional up-estuary salt transport resulting from channel–harbor exchange, here we adopt a salt transport balance based on Lagrangian reasoning. This balance (Eq. 4.5) was introduced by Dronkers (1978) and further analysed in Chapter 2. Using this balance, we assess the tidal trapping from the modelled salt transport.

To illustrate this balance, we consider a trap whose entrance width Δx is much smaller than the tidal excursion length L_c (i.e., $\Delta x \ll L_c$), such that the trap can be treated as a point source–sink. We first consider a deep main channel connected to a dead-end side channel in which the water is effectively stagnant (i.e., $\eta_h / H_h \ll 1$), and exchange between the main channel and the trap is primarily diffusive in nature. In this example, we assume that this diffusive salt transport into the trap is primarily driven by a density current that is 90° out of phase with the main-channel current (illustrated in Figure

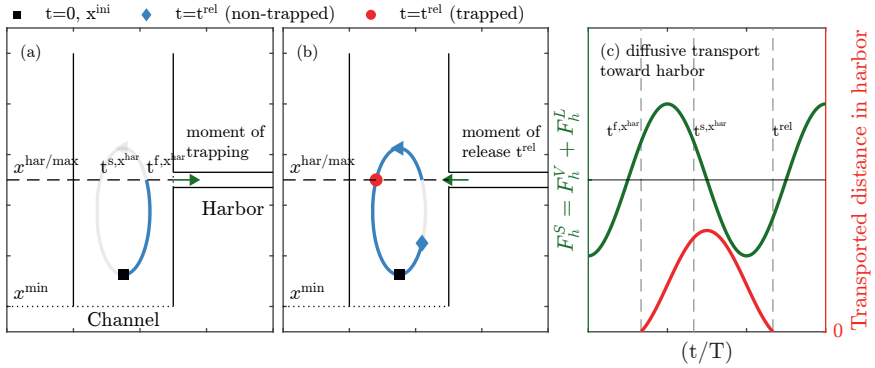


Figure 4.2: Schematic illustration and notation of tidal trapping through exchange that is diffusive in nature. The reference time (t = 0) corresponds to low-water slack in the main channel and is used to visualize trajectories originating from x^{ini}. Note that the semi-minor axes of the depicted trajectories are shown for illustrative purposes only. (a) Trajectory of a parcel from its initial position at x^{ini} to the trap location x^{har} at time $t^{\mathrm{f},x^{\mathrm{har}}}$. During this passage, exchange occurs and a fraction of the parcel is transported into the trap; its displacement is illustrated in panel (c). (b) Continuation of the trajectory of the non-trapped fraction, which passes the trap a second time at $t^{\mathrm{s},x^{\mathrm{har}}}$ and continues until the trapped volume is released back into the main channel at time t^{rel}, illustrating the dispersive effect. (c) Illustration of the assumed diffusive exchange between the channel and the harbor, together with the distance traveled by a trapped parcel within the trap.

4.2). We then introduce a control plane that moves with the flow in the main channel, starting from its initial position x^{ini} (also Figure 4.2). This plane passes the trap location at x^{har} twice during a tidal cycle. During the interval between the first ($t^{\mathrm{f},x^{\mathrm{har}}}$) and second ($t^{\mathrm{s},x^{\mathrm{har}}}$) passages, a net transport of salt into the trap occurs. The salt is therefore temporarily stored and, if the tidally averaged transport from the trap over a full cycle is zero, it must subsequently be released upstream of the control plane. Consequently, the volume that is temporarily trapped and released upstream of the control plane must have passed through the cross-section at x^{ini} where the control plane returns to $x^{\mathrm{ini}} = x^{\mathrm{har}}$ after one full cycle. Under quasi-steady-state conditions, the net salt transport through a plane originating at the trap location ($x^{\mathrm{ini}} = x^{\mathrm{har}}$) is therefore zero. If the system is not in periodic equilibrium, this net transport represents the tidally averaged salt flux from the trap into the main channel. The above described exchange mechanisms can also be visualized by tracking the displacement of trapped particles relative to non-trapped particles, illustrated in Figure 4.2. Panel (a) shows the trajectory from its initial position x^{ini} at slack water in the channel to the point where it crosses the trap ($t^{\mathrm{f},x^{\mathrm{har}}}$). During passage past the trap, exchange occurs and a portion of the volume becomes trapped. The non-trapped fraction continues to travel with the main-channel current and passes the trap again after tidal reversal (at time $t^{\mathrm{f},x^{\mathrm{har}}}$). The exchanged volume, however, continues to be transported within the trap by diffusive processes, as the assumed exchange flow is out of phase with the main-channel current (see panel c). At the moment the trapped parcel returns to the main channel, it is located upstream of the non-trapped parcel (see panel b).

In the previous example, the structure of the velocity field is such that a particle traveling with the local current in the main channel returns to its initial location after a full tidal cycle (neglecting Stokes drift and a uniform along channel current for simplicity). However, the presence of the trap, in which the current is out of phase with the main

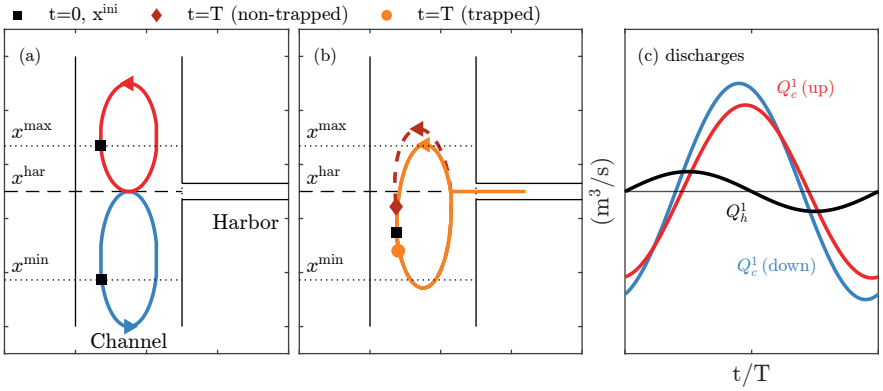


Figure 4.3: Schematic illustration and notation of tidal trapping through advective out-of-phase exchange. The reference time (t = 0) corresponds to low-water slack in the harbor and is used to visualize trajectories originating from x^{ini}. Note that the semi-minor axes of the depicted trajectories are shown for illustrative purposes only. (a) Trajectories of two water parcels that reach the harbor location at either high- or low-water slack but do not become trapped, illustrating the bounds x^{min} and x^{max}. (d) Trajectories of two water parcels initially located between x^{min} and x^{max}, where one parcel becomes trapped while the other does not, resulting in a net relative displacement from their initial positions. (e) The assumed tidally varying discharge components in the main channel down-estuary of the harbor, Q_c^1 (down), up-estuary of the harbor, Q_c^1 (up), and in the trap, Q_h^1, which introduce the relative motion between the channel and the harbor.

channel, induces a small phase difference across the length of the trap (see panel a and c in Figure 4.3). Due to the phase differences between the currents in the main channel and that in trap, the volume that becomes trapped experiences a net relative displacement in the down-estuary direction (panel b). This displacement is compensated by a net up-estuary excursion of the water volume that remains in the main channel, resulting from the phase difference within the main channel over the trap (see Chapter 2). The salt transport through the cross-section at x^{ini} therefore represents the balance between (i) the net salt transport from the trap associated with filling and emptying, and (ii) the salt transport resulting from the net up-estuary excursion of the main-channel water volume.

The additional salt transport arising from the above-described process of channel–harbor exchange, $\Delta\tilde{F}_c^{\mathrm{trp}}(x^{\mathrm{ini}})$, through the cross-section at x^{ini} in the main channel, is approximated as (see (Dronkers 1978) and Chapter 2):

$$\Delta\tilde{F}_c^{\mathrm{trp}}(x^{\mathrm{ini}}) = \underbrace{\underbrace{\int_{t^{f,x^{\mathrm{har}}}}^{t^{s,x^{\mathrm{har}}}} F_h^V\,dt}_{\tilde{F}_c^V} + \underbrace{\int_{t^{f,x^{\mathrm{har}}}}^{t^{s,x^{\mathrm{har}}}} F_h^L\,dt}_{\tilde{F}_c^L} + \underbrace{\int_{t^{f,x^{\mathrm{har}}}}^{t^{s,x^{\mathrm{har}}}} F_h^A\,dt}_{\tilde{F}_c^A} + \underbrace{\int_{-\delta}^{0} s_C(x^{\mathrm{ini}}, t^{\mathrm{LWS}})A_c^0\,dx}_{\tilde{F}_c^C}}_{\tilde{F}_c^{\mathrm{trp}}(x^{\mathrm{ini}})} \quad \begin{array}{l} x^{\min} \leqslant x^{\mathrm{ini}} < x^{\mathrm{har}} \\ \\ x^{\mathrm{har}} < x^{\mathrm{ini}} \leqslant x^{\max} \end{array} \quad . \tag{4.5}$$

$$\underbrace{\underbrace{\int_{t^{f,x^{\mathrm{har}}}}^{t^{s,x^{\mathrm{har}}}} -F_h^V\,dt}_{\tilde{F}_c^V} + \underbrace{\int_{t^{f,x^{\mathrm{har}}}}^{t^{s,x^{\mathrm{har}}}} -F_h^L\,dt}_{\tilde{F}_c^L} + \underbrace{\int_{t^{f,x^{\mathrm{har}}}}^{t^{s,x^{\mathrm{har}}}} -F_h^A\,dt}_{\tilde{F}_c^A} + \underbrace{\int_{-\delta}^{0} s_C(x^{\mathrm{ini}}, t^{\mathrm{LWS}})A_c^0\,dx}_{\tilde{F}_c^C}}_{\tilde{F}_c^{\mathrm{trp}}(x^{\mathrm{ini}})} \quad \begin{array}{l} x^{\mathrm{har}} < x^{\mathrm{ini}} \leqslant x^{\max} \end{array}$$

The tidally averaged additional along estuary salt transport at the initial position is then given by $\tilde{F}_c^{\mathrm{trp}} = \Delta\tilde{F}_c^{\mathrm{trp}}/T$, where T is the tidal period. In Eq. 4.5, $x^{\max}$ and $x^{\min}$ denote the up- and down-estuary limits of the added salt transport and and A_c^0 is the tidally averaged cross-sectional area in the main channel. The decomposed instantaneous salt transport components at the harbor entrance (Eq. 4.4) are used to distinguish between contributions to the additional salt transport from the cross-sectionally averaged exchange (F_h^A) and from exchange processes that are diffusive in nature (i.e, F_h^V and F_h^L). The first term ($\tilde{F}_c^V$) and the second term ($\tilde{F}_c^L$) represent the additional salt transport arising from the vertical and lateral structure of the channel–harbor exchange, respectively. The third term ($\tilde{F}_c^A$) represents the salt transport associated with cross-sectionally averaged

exchange over the trap entrance. This term is typically negative when flow in the channel and in the trap are out of phase, as it represents the salt flux arising from particles that are subject to a down-estuary excursion. Furthermore, $\tilde{F}_c^A$ is compensated by the salt transport arising from the up-estuary excursion of the non-trapped volumes, which is typically positive and represented by compensating term $\tilde{F}_c^C$.

To track when the control plane crosses the trap, the demeaned tidal discharge component at a cross-section just down-estuary of the evaluated harbor, Q_c^1, is used. By integrating the cumulative transport, $\int_0^t Q_c^1, \mathrm{d}t$, we determine the two moments at which the upstream volume relative to the cross-section is equal, corresponding to the times when the control plane, which has departed from x^{ini}, passes the trap. These times are denoted by $t^{\mathrm{f},x^{\mathrm{har}}}$ and $t^{\mathrm{s},x^{\mathrm{har}}}$. The relative distance from the harbor $x^{\mathrm{har}} - x^{\mathrm{ini}} \approx \frac{1}{A_c^0}\int_0^t Q_c^1, \mathrm{d}t$ is estimated from the volume that has passed through the cross-section divided by the tidally averaged cross-sectional area A_c^0. Furthermore, in our analysis, we evaluate the period between two consecutive low-water slacks in the harbor (i.e., $t = 0$ corresponds to low-water slack in the trap).

The net displacement δ in the integral in Eq. 4.5 is obtained from the net discharge from the harbor, Q_h, during the evaluated period:

$$\delta(x^{\mathrm{ini}}) = \int_{t^{\mathrm{f,x^{har}}}}^{t^{\mathrm{s,x^{har}}}} Q_h dt / A_c^0 \tag{4.6}$$

where the integral is analogous to the third term, but for the exchange of volume. Similarly, following the reasoning used to determine the crossing times of the control plane, we estimate $s_c(x^{\mathrm{ini}}, t_{\mathrm{LWS}})$ from the cross-sectionally averaged salinity signal in the main channel, immediately in front of the harbor.

Through Eq. 4.5, the additional salt transport resulting from tidal trapping can be estimated for an individual trap (see (Dronkers 1978) and Chapter 2). In essence, Eq. 4.5 quantifies the redistribution of salt water arising from the phasing and asymmetry of channel–trap exchange relative to the tidal excursion. A limitation of this approach is that it evaluates only the local balance, without explicitly accounting for variations along the tidal excursion length. Moreover, Eq. 4.5 quantifies the additional salt transport of a single harbor. In this study, Eq. 4.5 is applied to assess the potential contribution of different harbors and to identify spatial differences between them (Section 4.4.3), and to obtain a parameterization of its main effect (also see Section 4.5 and Appendix B).

4.3 Observations of Exchange Between Channel and Harbor

4.3.1 Hydrodynamics Conditions

Figure 4.4 shows the hydrodynamic conditions during the field campaign, with the 13-hour surveys highlighted in gray. The Rhine discharge was low during the first half of the campaign ($850 < Q^{\mathrm{riv}} < 1350$ m^3/s), but increased during the second half (Figure 4.4a). This increase led to an overall reduction in the measured salt concentrations in the New Meuse (Figure 4.4b). The conditions during the 13-hour surveys were characterized by a non-stationary salinity field, with subtidal salinity concentrations temporarily decreasing during the observation period. Figure 4.4c shows the observed tidal salinity range s_c^R (i.e., salinity variation over a tidal cycle) at three mooring locations. During the first half of the campaign (when Q^{riv} was relatively low), the salinity range shows a clear minimum at NM-1008, compared to NM-1012 (down-estuary) and NM-1002 (up-estuary). In Sections 4.3 and 4.4, we show that this local minimum in s_c^R strongly influences the nearby salt exchange between the channel and the harbors.

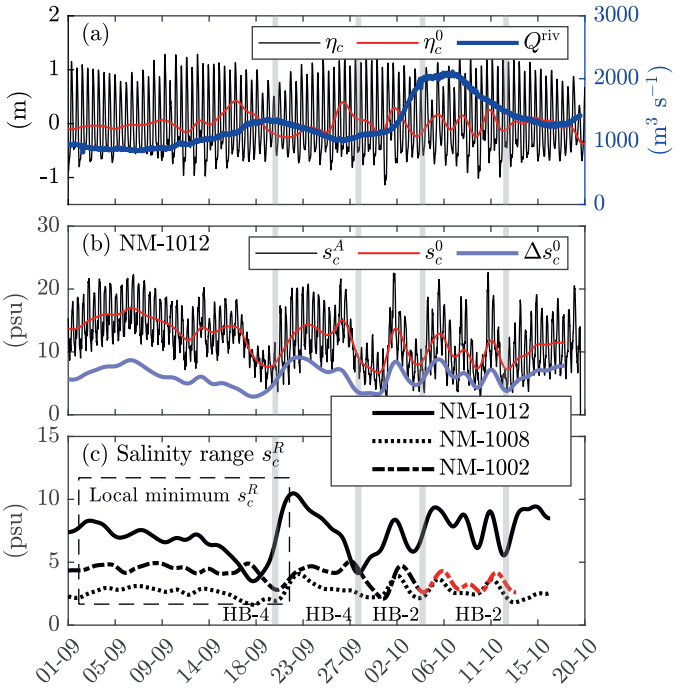


Figure 4.4: Overview of the hydrodynamic conditions during the measurement campaign. Grey lines indicate the timing of the 13-hour shipboard surveys. (a) Water levels η_c and subtidal water levels η_c^0 near mooring NM-1012, along with freshwater discharge Q^{riv} from the Rhine (the main freshwater source) measured at Lobith (see Figure 4.1a). (b) Mooring-averaged salinity s_c, subtidal salinity s_c^0, and tidally averaged top-to-bottom salinity difference Δs_c^0 at mooring NM-1012. (c) Salinity range s_c^R derived from salinity at the three moorings in the New Meuse, averaged over the corresponding mooring period (Figure 4.1). At NM-1002, the period highlighted in red indicates that the salinity signal was clipped. In this context, "clipped" means that during part of the tidal cycle, the measured salinity was equal to that of the river discharge. This influences the estimated tidal salinity range compared to stations where saline water is present throughout the entire tidal cycle.

4.3.2 Observed flow and salinity in the main channel

Figure 4.5 presents the measured along-channel velocities and salinity at transect W-W′, located down-estuary of the harbors (see Figure 4.1d,e). The barotropic tide is characterized by strong tidal distortion (see Figure 4.5a–d), which is reflected in both the large amplitude ratio $A_c^{\text{ratio}} = \hat{\eta}_c^{M_4}/\hat{\eta}_c^{M_2} \approx 0.22$ and the phase difference $\Delta\theta = 2\theta_c^{M_2} - \theta_c^{M_4} \approx 10°$ between the quarter-diurnal and semi-diurnal components. The relative large amplitude ratio (A_c^{ratio}) and the phase difference ($\Delta\theta_c$) close to zero results in nearly equal durations of flood and ebb, with the quarter-diurnal component amplifying high water and reducing low water levels.

For the semi-diurnal M_2 tidal constituent, the phasing of the horizontal tide ($\theta_c^{U_2}$) leads the vertical tide ($\theta_c^{M_2}$) by approximately 45°. The combination of the observed tidal distortion and the phase difference between the horizontal and vertical tides produces a

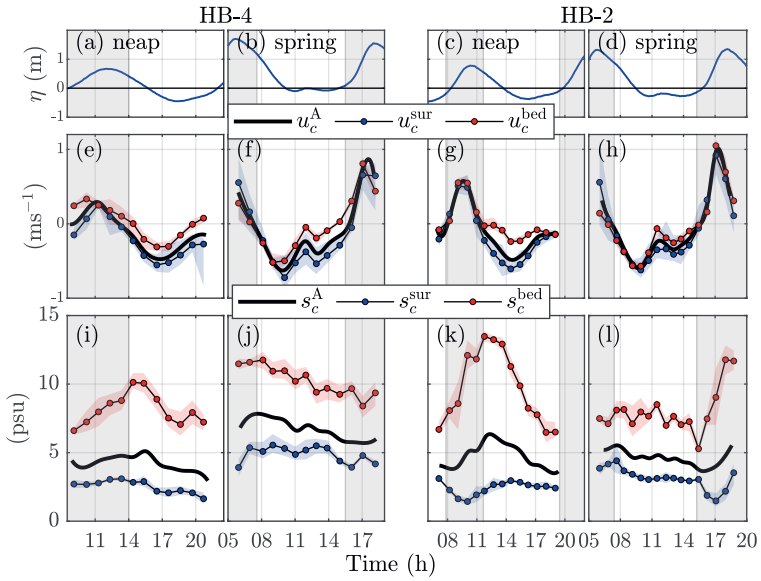


Figure 4.5: Observations in the main channel at transect W–W′ (located down-estuary of the harbors) during the 13-hour surveys. Panels (a–d) present water-level variations obtained from the nearby tide gauge. Panels (e–h) show the cross-sectionally averaged along-channel velocity (u_c^A), the near-surface velocity (u_c^{sur}), and the near-bottom velocity (u_c^{bed}). The near-surface and near-bottom properties represent the average over the near-surface 4 m and the lowermost 4 m of the water column. Panels (i–j) display the corresponding salinity fields. Lateral variations of the near-surface and near-bottom properties are indicated by red and blue shading, respectively.

relatively short and intense flood current (Figure 4.5e–h). This phase difference between the vertical and horizontal tide in the main channel is substantially smaller than the maximum velocity phase lead of 90° expected for a purely standing wave, a short basin, or a strongly convergent channel (Friedrichs 2010). Consequently, since harbors act as short basins, the velocity phase lead in the harbor to the current in the main channel, $\theta_c^{U_2} - \theta_h^{U_2}$, must be close to 45°. Because of this phase difference, there is potential for a substantial contribution of tidal trapping through advective out-of-phase exchange (see Dronkers (1978) and Chapter 2). The contribution of out-of-phase exchange is further quantified in Section 4.4.3.

Panels i through l in Figure 4.5 summarize the observed salinity dynamics. The most important observations are the weaker intertidal salinity variations at HB-4 compared to HB-2, in line with the results of the nearby moorings (Figure 4.4c). The stronger intertidal variations at the HB-2 Harbor are most pronounced in near-bed salinity, s_c^{bed}. However, direct comparisons are difficult, since conditions varied between the four surveys (Figure 4.4). Furthermore, at HB-2, the passage of relatively low-salinity water is observed during early flood, reducing the near-surface salinity (s_c^{sur}). This drop in the near-surface salinity is explained by inflow from the Old Meuse, which is at that time still in the ebb phase. The mechanism behind this type of channel interaction is discussed in detail by Warner et al. (2002).

For the monitored cross-sections during the 13-hour surveys, the salt balance has

been derived (see appendix A.1.2). Analysis of the subtidal salt transport showed that during all 13-hour surveys there was a net seaward export of salt in the main channel, as well as a net export of salt from the harbors into the main channel. We attribute this seaward export partly to subtidal water-level variations during the campaigns and partly to increased river discharge during some of the 13-hour surveys (Figure 4.4a). Up-estuary transport of salt is mostly governed by the steady shear contribution, $F_c^{\mathrm{st,shear}}$, whereas the contribution of the tidal oscillatory flux, F_c^{tide}, is small or even negative.

4.3.3 Observed flow and salinity (structure) near the harbor entrance

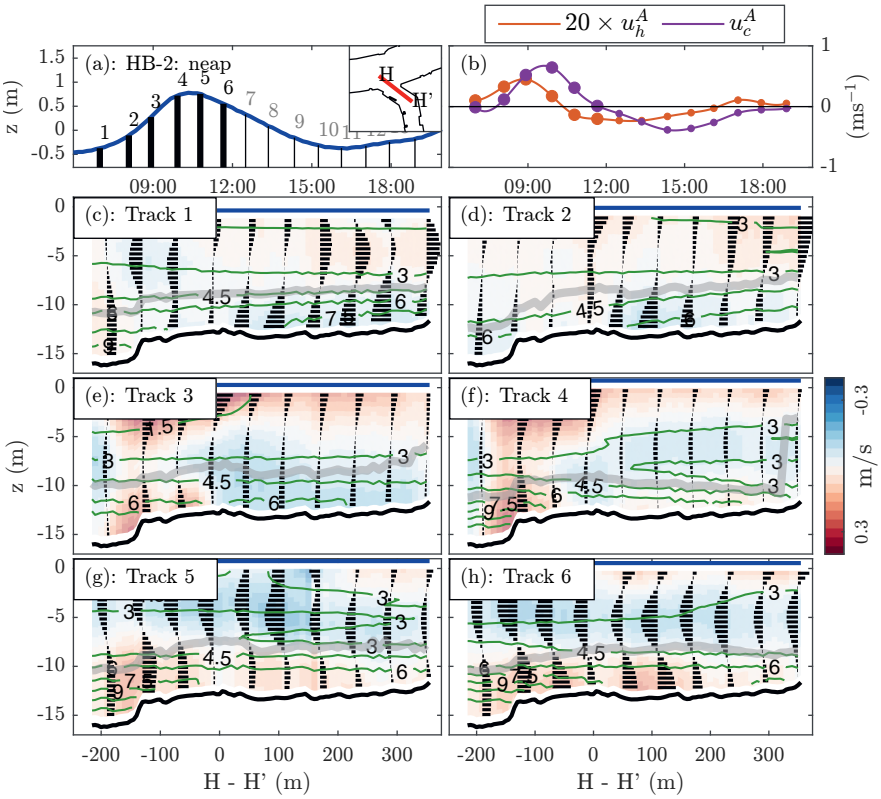


Figure 4.6: Along-harbor velocity and salinity structure at transect H–H′ at HB-2 during the neap tide (Figure 4.1c). (a) Moment within the tidal cycle at which each transect was taken. Transects shown in Panels (c–h) are indicated with a thick vertical line. (b) Along-channel (u_c^A) and along-harbor (u_c^H) velocity components. Larger scatter points are used to highlight the tracks shown in Panels (c–h). (c–h) Along-harbor velocity component indicated by color and arrows. The green contour lines indicate salinity. The thick gray line indicates the approximate height of the pycnocline, estimated by fitting a sigmoid function to the vertical salinity profiles Niesten et al. (2024).

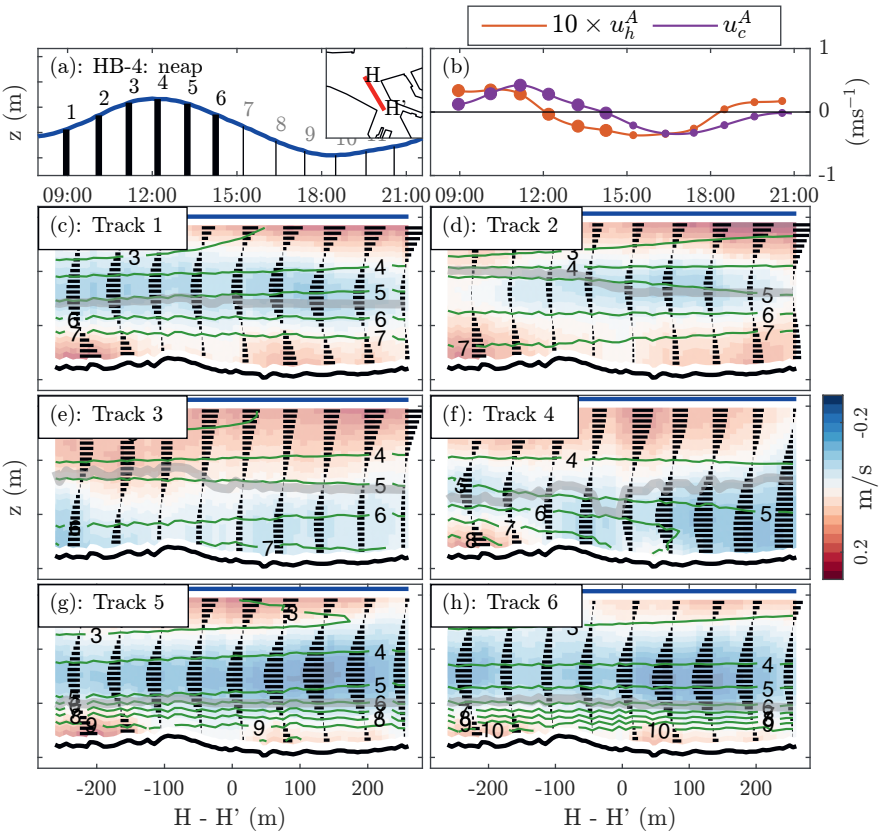


Figure 4.7: Same as Figure 4.6, but for HB-4 during the neap tide survey.

Harbors often exhibit a lock-exchange-like flow driven by density dynamics (Roelfzema and Van Os 1978; Abraham et al. 1986; De Nijs et al. 2009; Maren et al. 2009). Figures 4.6 and 4.7 show the observed along-harbor velocity structure, at HB-2 and HB-4 respectively. We focus on the transects collected around high water (HW) during the two neap-tide surveys, as they most clearly reveal the differences between the two harbors. The corresponding depth-averaged density differences between the CTD casts in the harbor and the main channel and are shown in Figure 4.8.

At HB-2 (Figure 4.6), the flow and salinity fields reveal a typical lock-exchange-like flow that reverses direction throughout the tidal cycle. At the start of the flood (tracks 1–3), the near-bed current is directed toward the main channel . This current is driven by the higher density in the harbor (panel a in Figure 4.8). Around HW (track 4), the direction of the vertically sheared flow reverses as salinity in the main channel increases with the incoming tide. This is also reflected in the fact that the depth-averaged density difference, $\Delta\overline{\rho}_{\mathrm{H-H'}}$, reverses sign during mid-flood. The vertically sheared flow, with near-bottom currents directed toward the harbor, is maintained throughout tracks 5–8 (track 8 not shown). During the main channel ebb (tracks 9–14, not shown), the vertically sheared flow reverses direction again, due to the reduction in main-channel salinity caused by the ebb current. In addition, the flow structure near the head of the harbors is locally influenced by eddies (see Figure 4.6, tracks 3–4).

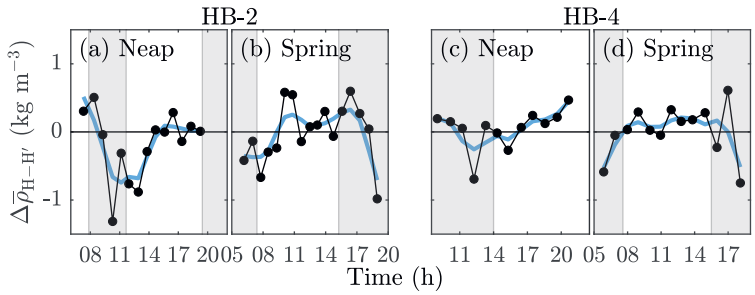


Figure 4.8: Depth-averaged density difference ($\Delta\overline{\rho}_{\mathrm{H^{\sim}H'}}$) calculated from the vertical CTD casts taken at transect H–H′. Positive values indicate a higher depth-averaged density in the harbor. The light-blue line shows the smoothed depth-averaged density difference obtained using a LOWESS filter with a span of 0.3. Gray shading indicates the duration of the horizontal flood period.

At HB-4 (Figure 4.7), a three-layered vertically sheared structure dominated the current profiles for most of the tide, deviating from the classical two-layered profile. During the early flood (tracks 1–2), both near-bottom and surface flows enter the harbor, with a mid-column outflow. This near-bed inflow contrasts with the velocity structure at HB-2 and is unexpected, given the higher depth averaged density in the harbor (Figure 4.8c). Near HW (tracks 3–4), the flow transitions to the expected two-layer structure, with the near-bed current directed toward the main channel. After HW (tracks 5–6), a near-bed current toward the harbor re-develops, accompanied by a notable increase in salinity in the lower part of the water column. However, a two-layered vertically sheared flow profile does not form, as a near-surface flow toward the harbor is maintained. The near-bed current persists up to track 7. For the remaining tracks (not shown), the flow returns to a vertical structure characterized by mid-column outflow and near-surface inflow.

4.3.4 Analysis of Observed Flow Structures in the Harbors

In the following sections, (1) the extent to which the observed vertically sheared flow is driven by density dynamics is quantified, and (2) an explanation for the mid-column outflow observed at HB-4 is provided.

4.3.4.1 Explanation of inter-tidal flow structure and density dynamics

Channel-harbor salt exchange is often assumed to be driven by gravitational dynamics. To validate this assumption and assess the role of density-driven tidal trapping, we follow the analysis of Geyer and Ralston, et al. (2024). First, the composite Froude number for a two-layer regime, G, is calculated for the flow in the harbor Armi and Farmer (1986):

$$G = \left[\frac{\left(u_h^{\mathrm{top}}\right)^2}{g' h_h^{\mathrm{top}}} + \frac{\left(u_h^{\mathrm{bot}}\right)^2}{g' h_h^{\mathrm{bot}}} \right]^{1/2}, \tag{4.7}$$

where h_h^{top} and h_h^{bot} denote the depths of the top and bottom layers, respectively. Here, the level of the interface between the two layers is based on the expected location of the pycnocline (gray lines in Figures 4.6 and 4.7), u_h^{top} and u_h^{bot} are the layer-averaged velocity in the top and bottom layer (respectively) and $g' = \left(\frac{\rho^{\mathrm{bot}} - \rho^{\mathrm{top}}}{\overline{\rho}} \right) g$ denotes reduced density. Again, the densities ρ^{top} and ρ^{bot} are layer-averaged properties. Secondly, we compare G as a function of the fractional depth of the bottom layer (the active layer)

$h'_h = \left(\frac{h_h^{\text{bot}}}{h_h^{\text{top}} + h_h^{\text{bot}}} \right)$, and compare it with the composite Froude number obtained using the Benjamin (1968) solution for density currents (G_{Ben}), as derived by Geyer and Ralston, et al. (2024):

$$G_{\text{Ben}} = \left[\frac{h'_h(2 - h'_h)}{(1 - h'_h)(1 - h'_h)^2} \right]^{1/2}. \tag{4.8}$$

This analysis allows to assess to what extent the observed flow is consistent with density-driven dynamics.

Figure 4.9 presents G against the fractional depth h'_h for the tracks in Figures 4.6 and 4.7. For HB-2, G aligns with the Benjamin (1968) analytical solution for G_{Ben} for most of the tracks. Only for tracks 3 and 4 this is not the case; these tracks cover the period during which the density current reverses direction. For HB-4, tracks 1 and 2, G deviates from G_B. These two tracks were characterized by a three-layered flow structure and a weak horizontal density gradient. For tracks 3 and 4, a two-layer flow developed and G aligns with G_{Ben}. An agreement with G_{Ben} is also obtained for tracks 5 and 6, during which a near-bed density current developed that intruded into the harbor (although the upper layer was not strictly uniform for those tracks).

The agreement between the composite Froude number and the solution by Benjamin (1968) indicates that the vertical flow structure results from density-driven dynamics. However, during the reversal of the density current at HB-2 and for the tracks at HB-4 that were characterized by a three-layered profile, the observations did not align with the theoretical solution. In the next section, the three-layered profile is further investigated.

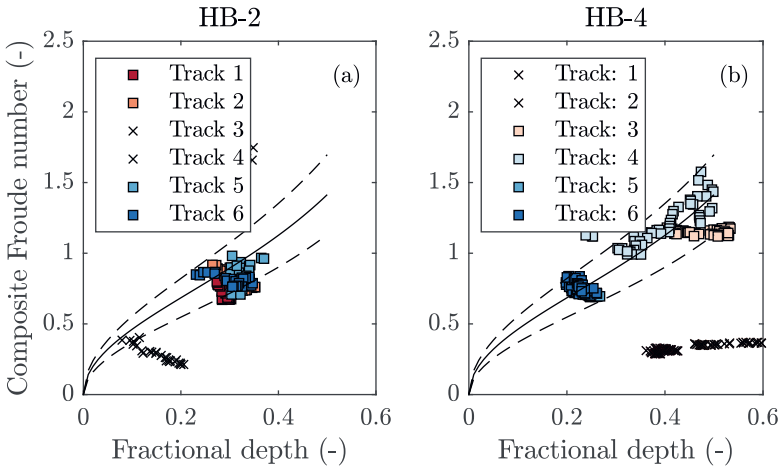


Figure 4.9: Composite Froude numbers (G) as a function of fractional depth. (a) Results for the HB-2 neap-tide survey for the tracks shown in Figure 4.6. (b) Same as (a), but for the HB-4 neap-tide survey for the tracks shown in Figure 4.7.

4.3.4.2 Explanation for the Observed Mid-Depth Outflow at HB-4

At HB-4, a persistent mid-depth flow reversal was observed (Figure 4.7). This coincided with stronger vertical stratification in the harbor compared to the main channel. We examine whether this gradient in vertical stratification can account for the observed three-layered vertically sheared flow profile. We do this by calculating the vertical profile of the residual current that would arise from the balance between the pressure gradient

and frictional forces, in a flow that is subject to a depth-varying lateral density gradient Nunes and Simpson (1985):

$$u(z) = \frac{g}{\bar{\rho} A_z}\left(\frac{3}{2H^3}\left(I_4^H + H I_3^H\right)\left(z^2 + H^2\right) - \left(I_3^z + I_3^H\right)\right), \tag{4.9}$$

Herein, g is the gravitational acceleration, $\bar{\rho}$ the depth averaged density (denoted by the over-bar $\bar{\cdot}$), A_z is the vertical eddy viscosity, H is the water depth, and z is the vertical coordinate (positive upwards). In Eq. 4.9, I_n^z is defined as:

$$I_n^z = \int_0^z \int_0^z .. \int_0^z \frac{\partial \rho}{\partial y} dz_1 .. dz_{n-1} dz_n, \tag{4.10}$$

where I^H indicates that the integral is evaluated up to $z = -H$, and y indicates the direction perpendicular to the main channel (or along the channel in the harbor). For a depth-uniform horizontal density gradient, Eq. 4.9 reduces to the classical expression for gravitational circulation (Hansen and Rattray 1965) or transverse velocity (Nunes and Simpson 1985). To investigate the influence of horizontal differences in the vertical stratification, we decompose the tidal-mean horizontal density gradient into a component that is both tidally and depth averaged, $\langle \overline{\rho}_y \rangle$, and a component that is tidally averaged but varies with depth, $\langle \rho'_y \rangle$. Here, the operator $\langle \cdot \rangle$ denotes a tidal average. Subsequently, these properties are used to obtain a current profile, Eq. 4.9, which is governed by $\langle \overline{\rho}_y \rangle$ and $\langle \rho'_y \rangle$. Here, the horizontal stratification gradient is expressed through the gradient in the potential energy anomaly Φ_y, with the potential energy anomaly defined as $\Phi = -g \int_{-H}^{\eta} \rho'_y z dz$ Simpson and Brown, et al. (1990).

Figure 4.10 illustrates the baroclinic pressure–induced acceleration and the corresponding current profiles driven by Φ_y in panels a and b, alongside the well-known profiles resulting from $\langle \overline{\rho}_y \rangle$. The results are obtained for idealized density configurations with either a depth-averaged horizontal density gradient or a density gradient that varies linearly with depth, reverses sign, and has a depth-average equal to zero. Panel c shows the baroclinic pressure–induced acceleration calculated from the observed tidally averaged density gradient, $\langle \rho_{\mathrm{H-H'}} \rangle$, obtained from the CTD profiles at transect H–H′ during the neap-tide survey at HB-4. The tidally and depth-averaged contribution $\langle \overline{\rho}_{\mathrm{H-H'}} \rangle$ was nearly zero, but, as indicated, stratification of the water column was significantly stronger in the channel, resulting in $\Phi_{\mathrm{H-H'}}$ being positive. In the absence of a depth-averaged density gradient, but in the presence of a horizontal stratification gradient, the baroclinic acceleration peaks at mid-depth and vanishes near the bottom. Panel d of Figure 4.10 compares the observed tidally averaged residual current profile with that predicted by Eq. 4.9, using the observed profiles of $\langle \rho_{\mathrm{H-H'}} \rangle$. To match the observed current magnitude, A_z was set to 0.003 m^2/s, which is similar to the value found by Biemond et al. (2025). The current profile resulting from $\langle \Phi_{\mathrm{H-H'}} \rangle$ exhibits a pronounced outflow at mid-depth and inflow near the surface, as observed. Therefore, we attribute the observed mid-depth outflow and surface inflow—present throughout nearly the entire tidal cycle—to stronger stratification in the main channel compared to the harbor.

4.3.5 Analysis of Instantaneous Channel–Harbor Salt Exchange

To investigate whether the mechanisms of salt exchange differ between the two harbors, we quantify the instantaneous channel–harbor salt exchange and the contributions of different exchange processes. Specifically, we decompose the instantaneous salt transport observed at transect Z–Z′ using Eq. 4.4 to quantify the contributions from tidal filling and emptying, as well as the exchange of salt that is diffusive in nature (Figure 4.11).

The instantaneous salt transport resulting from the cross-sectionally averaged current and salinity (F_h^A), which reflects the salt transport due to filling and emptying of the harbor, dominates the total instantaneous salt transport for both harbors (compare Figure 4.11 e-h with 4.11 a-d). This transport can be further decomposed into two components: the instantaneous cross-sectionally averaged salt transport associated with

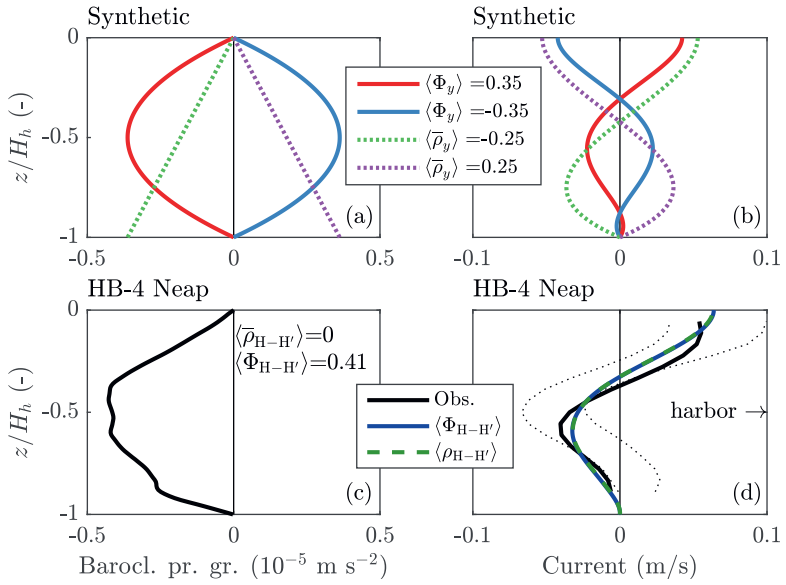


Figure 4.10: Influence of the difference in stratification between the main channel and the harbor on the residual currents observed near the harbor entrance of HB-4 during the neap-tide survey. (a) Synthetical profiles of depth-averaged density ($\overline{\rho}_y$) and stratification (Φ_y), based on either a constant horizontal density gradient or a linearly varying horizontal density gradient over depth, with a zero depth-averaged mean. (b) Flow velocity profiles calculated corresponding to conditions in panel (a) using Eq. 4.9. (c) Profile of the baroclinic pressure gradient calculated from the tidally averaged density gradient ($\langle\rho_{\mathrm{H-H'}}\rangle$) at the along-harbor transect H–H' at HB-4. (d) Observed tidally averaged velocity profile, compared with velocity profiles calculated using Eq. 4.9 with the measured density gradient $\langle\rho_{\mathrm{H-H'}}\rangle$ or the stratification gradient ($\langle\Phi_{\mathrm{H-H'}}\rangle$). A vertical eddy viscosity of $A_z = 0.003$ m^2/s is used for the calculations. Dashed lines indicate the velocity profiles around peak flood and ebb.

the tidally averaged salinity, and the transport associated with the deviation from the tidal mean. This yields

$$F_h^A = F_h^{\mathrm{st,A}} + F_h^{\mathrm{var,A}} = u_h^A \langle s_h^A \rangle + u_h^A \left(s_h^A - \langle s_h^A \rangle \right), \tag{4.11}$$

where $\langle\cdot\rangle$ denotes a tidal average. Evaluating both terms shows that the contribution of F_h^A is predominantly determined by the exchange of water with salinity equal to the tidal average ($F_h^{\mathrm{st,A}}$), whereas the contribution from inter-tidal salinity variations ($F_h^{\mathrm{var,A}}$) is an orders of magnitude smaller (compare panels e-h in Figure 4.11 with panels a-d). This implies that the change in salt concentration due to filling and emptying is small.

For the salt transport that is diffusive in nature, the contribution of the laterally sheared salt flux in the along-channel direction of the harbor, F_h^L, was found to be small. Note that F_h^L was assessed from the CTD casts taken at transect Z–Z′ only for HB-4 (Figure 4.1e). This limited contribution arises because the observed lateral salinity differences were small, despite the presence of lateral variation in the current field (mostly in near-surface currents). In contrast, the exchange associated with the instantaneous vertically sheared salt transport (F_h^V) is substantially larger compared to F_h^L and $F_h^{\mathrm{var,A}}$.

At HB-2, F_h^V is directed into the harbor (positive) from approximately HWS–2h to HWS+2h, consistent with the observed density current dynamics (Figure 4.6). Compared to HB-4, the observed variations in F_h^V at HB-2 are larger, particularly during the neap-tide surveys. At HB-4, the contribution from the vertical structure (F_h^V) is on average directed seawards (negative) during both surveys and exhibits relatively weak inter-tidal variability, which we attribute to the smaller salinity range (Figures 4.4 and 4.5). The net seaward salt transport toward the main channel at HB-4 is consistent with the salt balance being unsteady during the 13-hour measurement (see Appendix A.1.2). Its more pronounced influence on the dynamics at HB-4 aligns with the analysis of the relative importance of subtidal exchange compared to tidal trapping (this is further discussed in Section 4.4.4).

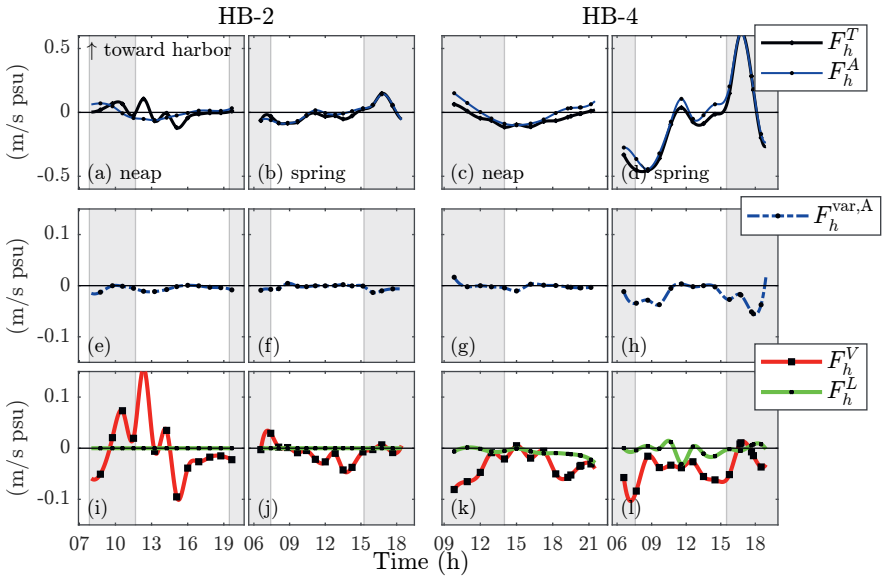


Figure 4.11: Instantaneous salt transport observed at the harbor entrance (transect Z–Z′) during the 13-hour surveys at HB-2 and HB-4. Positive values denote transport directed into the harbor. (a–d) Total instantaneous salt transport (F_h^T) and the salt transport associated with barotropic filling and emptying (F_h^A). (e–h) Contribution to the salt transport associated with the cross-sectionally averaged current and tidally varying salinity ($F_h^{\mathrm{var,A}}$). (i–l) Instantaneous salt transport associated with vertically (F_h^V) and laterally (F_h^L) sheared salt transport, both considered diffusive in nature. Gray shading indicates horizontal flood in the main channel.

4.4 Generalization from Numerical Modeling

We further investigate the harbor-channel exchange and its effect on salinity dispersion with the numerical model. Section 4.4.1 is mainly focused on the salinity range variation along the estuary, which plays a key role in the harbor contribution to salt dispersion. In Section 4.4.2, we examine the channel-harbor salt exchange for the larger harbors (Figure 4.1) and relate differences in exchange to the local minimum in salinity range. This is followed by the quantification of the effect of tidal trapping on the dispersion of salt in the main channel (Section 4.4.3). In Section 4.4.4, we compare the additional salt transport

from tidal trapping to that associated with subtidal exchange between the channel and the harbor.

4.4.1 Subtidal Salt Transport and the Minimum in Salinity Range

Figure 4.12a presents the subtidal salt fluxes in the main channel, as determined from the simulations mentioned in Section 4.2.3, following the decomposition outlined in Appendix A.1.1. The up-estuary directed transport contributions are shown as a fraction of the salt transport associated with flushing by the river discharge (F_c^i/F_c^{res}). This fraction is known as the diffusive salt fraction (Hansen and Rattray Jr 1966b). Flushing by the river discharge (F_c^{res}) is primarily balanced by the transport related to the steady shear flux, $F_c^{\mathrm{st,shear}}$, throughout most of the domain. The transport due to the tidal oscillatory flux, F_c^{tide}, which incorporates the effects of tidal trapping, becomes the dominant term upstream of km 1005. This transition is consistent with findings by Kranenburg et al. (2022), Dijkstra and Schuttelaars and Kranenburg (2022) and Biemond et al. (2025). Note that upstream of the junction (indicated by the thick grey dashed line), the tidal oscillatory contribution is negative, consistent with the subtidal salt transport derived from the 13-hour shipboard survey (Appendix A.1.2). This is partly due to the import of relatively low-salinity water from the Old Meuse (see Figure 4.5), but it is expected to also be strongly influenced by changes in channel depth further up-estuary (km 1002), which we address in a follow-up paper.

Consistent with the field observations during lower discharge conditions (Figure 4.4), the model results show a local minimum in the tidal salinity range, s_c^R, with the lowest values occurring near HB-4 and HB-5. How this minium influences the instantaneous channel-harbor salt exchange is explored in the next section. Furthermore, this minimum is not caused by the harbors themselves, as confirmed by exploratory model experiments in which the harbors were removed (data not shown). A potential explanation for the increase in s_c^R in the upper part of the New-Meuse to a sharp increase in channel depth occurring down-estuary of km 1002, allowing the formations of fronts and the creation of sharp gradient in the along channel salinity structure (Geyer and Ralston 2015; Corlett and Geyer 2020).

Panel c in Figure 4.12 shows the phasing of the M_2 constituent for both the vertical tide ($\theta_c^{M_2}$) and the horizontal tide ($\theta_c^{U_2}$) in the main channel. The potential up-estuary salt transport due to advective out-of-phase exchange depends on the velocity phase difference between the currents in the main channel and the harbor (see Dronkers (1978) and Chapter 2). This velocity phase difference is close to $\theta_c^{U_2} - \theta_h^{U_2} \approx \theta_c^{U_2} - (\theta_c^{M_2} - 90°)$, since the current in the trap is approximately 90° out of phase with the surface elevation due to the short basin length (Friedrichs 2010). Just up-estuary of the junction, the phase difference between the horizontal and vertical tides is largest (about 42°), implying a smaller channel-harbor velocity phase difference for the adjacent harbors. Further up-estuary, $\theta_c^{U_2} - \theta_h^{U_2}$ decreases (to about 20° at HB-7), leading to an increased channel-harbor velocity phase difference. Hence, a significant contribution from advective out-of-phase exchange is possible based on the phase difference, especially for the more up-estuary harbors; this is further examined in Section 4.4.3.

4.4.2 Relation Between Instantaneous Channel-Harbor Salt Exchange and the Salinity Range

The relationship between the instantaneous channel-harbor exchange from vertical shearing and the salinity range in the main channel is further explored in Figure 4.13.

We first examine the instantaneous salt transport, decomposed through Eq. 4.4, for the

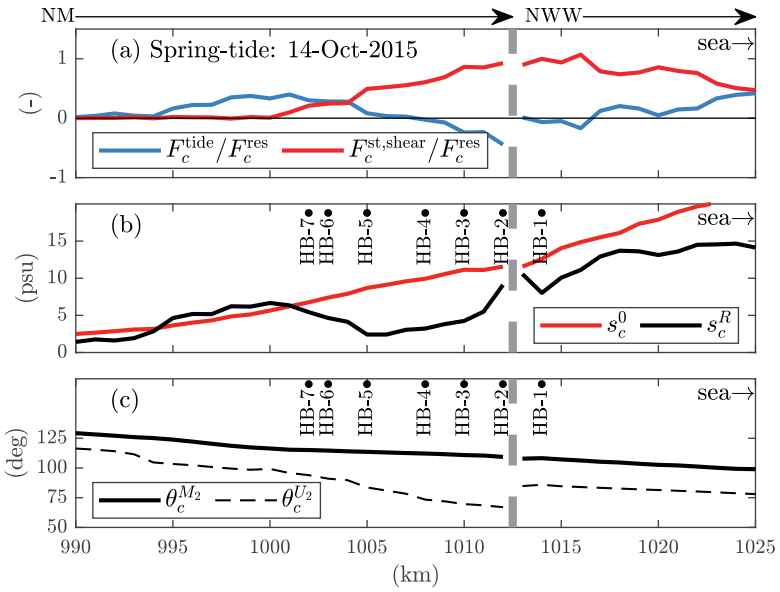


Figure 4.12: Overview of the modeled estuarine conditions near spring tide (14-10-2015). (a) Dominant components of the subtidal salt transport: the tidal oscillatory salt contribution (F_c^{tide}) and the contribution from steady shear ($F_c^{\text{st,shear}}$). Along-channel salt transport contributions are expressed as a diffusive salt fraction, F_c^i/F_c^{res}, where F_c^{res} represents flushing driven by river discharge. (b) Subtidal salinity s_c^0 and the tidal salinity range s_c^R. The tidal salinity range exhibits a local minimum between HB-4 and HB-5. (c) Phasing of the vertical tide ($\theta_c^{M_2}$) and horizontal tide ($\theta_c^{U_2}$) based on the dominant M_2 tidal constituent. The thick grey dashed line marks the location of the junction between the New Waterway (NWW), the New Meuse (NM), and the Old Meuse (OM).

different harbors, normalized by the absolute maximum value of total instantaneous salt transport F_h^T (Figure 4.13 a-f). The relative contribution of the transport F_h^V due to the vertically sheared flow is clearly the smallest at HB-4 and HB-5, where s_c^R is small (see Figure 4.12). This local reduction in the transport contributions thar are diffusive in nature is further highlighted by an increase in the ratio $R = \langle|F_h^A|\rangle/(\langle|F_h^V|\rangle + \langle|F_h^L|\rangle)$ (Figure 4.13h).

To understand the relationship between F_h^V and s_c^R, we consider a first-order approximation of the maximum salt transport associated with a salt flux resulting from a density-driven, two-layer sheared flow (Benjamin 1968; Kranenburg 1996). For the case of an arrested front, where the flow in the passive (lower) layer has reduced to zero, Benjamin (1968) obtained the solution $\frac{U_u}{g'H} = \frac{1}{4}$, where U_u is the velocity upstream of the front and H is the depth. When we assume equal depths for the top and bottom layers and approximate the density difference from s_c^R as $\Delta\rho = \rho_0\beta s_c^R$ (Maren et al. 2009), we can define the following properties to assess the instantaneous salt transport associated with

vertically sheared flow resulting from fronts in the harbors:

$$\begin{aligned} u^{\text{top}} &= -\tfrac{1}{2}\sqrt{\tfrac{\rho_0 \beta s_c^R}{\overline{\rho}}\, g H_h}, & u^{\text{bot}} &= \tfrac{1}{2}\sqrt{\tfrac{\rho_0 \beta s_c^R}{\overline{\rho}}\, g H_h}, \\ q^{\text{top}} &= -\tfrac{1}{4} H_h \sqrt{\tfrac{\rho_0 \beta s_c^R}{\overline{\rho}}\, g H_h}, & q^{\text{bot}} &= \tfrac{1}{4} H_h \sqrt{\tfrac{\rho_0 \beta s_c^R}{\overline{\rho}}\, g H_h}, \\ s^{\text{top}} &= s_h^A - \tfrac{1}{2} s_c^R, & s^{\text{bot}} &= s_h^A + \tfrac{1}{2} s_c^R. \end{aligned} \tag{4.12}$$

where H_h is the depth of the harbor and the superscripts $^{\text{top}}$ and $^{\text{bot}}$ indicate the upper and lower layers, respectively. The magnitude of the salt transport for this two-layer flow, based on Eq. 4.12, is given by:

$$\hat{F}_h^V = q^{\text{top}} s^{\text{top}} + q^{\text{bot}} s^{\text{bot}} = \frac{1}{4} (\beta g)^{1/2} \left(s_c^R H_h\right)^{3/2} B_h, \tag{4.13}$$

with B_h the width of the harbor entrance and $\frac{\rho_0}{\overline{\rho}} \approx 1$. Note that the positive x-direction is defined as pointing into the harbor. Eq. 4.13 indicates that the salt transport from the exchange caused by vertical shearing scales with the salinity range as $\hat{F}_h^V \propto \left(s_c^R\right)^{3/2}$.

Equation 4.13 assumes that the instantaneous salt transport associated with vertical variations is driven solely by density differences, and neglects the contribution from the depth-averaged current generated by the periodic filling and emptying of the basins. Since the depth-averaged currents are typically an order of magnitude smaller due to the large depth of the basin, this contribution is expected to be small.

In panel i of Figure 4.13, the root of the tide-averaged squared salt transport from vertical shearing per unit width $\sqrt{\langle \left(\overline{u_h^V s_h^V}\right)^2 \rangle}$ as computed from the model results, is plotted against the tidal salinity range s_c^R in front of the harbors. A power-law fit to the data ($y = \alpha x^\beta$) yielded a skill (r^2) of 0.83 and an exponent of 1.58±0.41 (solid curve in Figure 4.13, panel i). The obtained power from the fitted function closely matches the exponent predicted by Eq. 4.13, which suggests that $\hat{F}_h^V \propto \left(s_c^R\right)^{3/2}$. The findings on how the transport F_h^V depends on the tidal salinity range s_c^R explain the relatively weak contribution at HB-4 and HB-5, which are located in regions where s_c^R exhibits a local minimum (panel b in Figure 4.12).

4.4.3 Quantifying the Additional Salt Transport induced by Tidal Trapping

We quantify the additional up-estuary directed salt transport resulting from tidal trapping and isolate the contributions of both advective out-of-phase exchange and diffusive processes (arising from the instantaneous vertically and laterally sheared salt flux), using Eq. 4.5. For the diffusive contribution, we do not distinguish between vertically and laterally sheared salt flux but instead assess their combined effect, denoted as $\tilde{F}_S$. Moreover, we use the tidal varying part of F_h^A and $F_h^S = F_h^L + F_h^V$ (i.e., we subtracted the subtidal average) to ensure that our estimates are not influenced by subtidal salt transport into or out of the harbor basins.

Figure 4.14 shows the additional salt transport in the main channel resulting from channel-harbor exchange for HB-2 and HB-4 for a single tidal cycle. For both harbors, the additional up-estuary salt transport, $\tilde{F}_c^{\text{trp}}$, is predominantly due to $\tilde{F}_c^S$, which arises from vertically and laterally sheared exchange flows (see panels c and f in Figure 4.14). The additional salt transport varies over a distance approximately equal to the tidal excursion length, L_c, since this is the distance over which a redistribution of saltwater occurs due to tidal trapping (see Dronkers (1978) and Chapter 2). Within this range, the additional salt

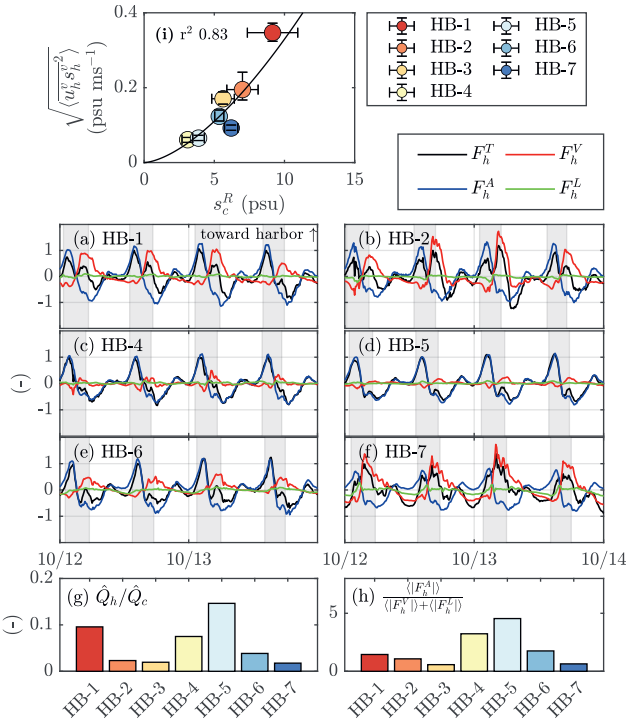


Figure 4.13: Overview of the modeled instantaneous exchange of salt between the channel and the harbors. (a-c). Normalized instantaneous decomposed salt transport contributions for different harbors, derived from Eq. 4.4. The salt transport contributions are normalized by the absolute maximum value for the period shown ($F_h^i/\max(|F_h^T|)$). The gray shaded background shows the cross-sectionally averaged flood associated with the horizontal tide in the main channel. (g) Relative size of the harbor, based on the ratio between the discharge amplitude at the harbor entrance $\hat{Q}_h$ and the discharge amplitude in the main channel $\hat{Q}_c$. (h) Ratio between the absolute tide-averaged advective exchange $\langle|F_h^A|\rangle$ and the absolute tide-averaged diffusive exchange $\langle|F_h^V|\rangle+\langle|F_h^L|\rangle$. (i) Relation between the salinity range s_c^R and the squared, tide-averaged salt flux from vertical shearing per unit width $\sqrt{\langle\overline{u_c^V s_c^V})^2\rangle}$. The black line represents a power-law fit to the data of the form $y = \alpha x^\beta$.

transport reaches a maximum near the down-estuary end of the tidal excursion relative to the position of the harbor. This downstream peak is explained by the asymmetry in F_h^S, which results in a more intense exchange near high water slack (shown in panels b and e in Figure 4.14).

To summarize the trapping effect over time, panels a and f in Figure 4.15 present the excursion-averaged additional salt transport over a spring–neap cycle for the different harbors, where the tidal excursion-averaged salt transport is defined as:

$$\overline{\tilde{F}_c^i} = \frac{1}{L_c}\int \tilde{F}_c^i dL_c, \tag{4.14}$$

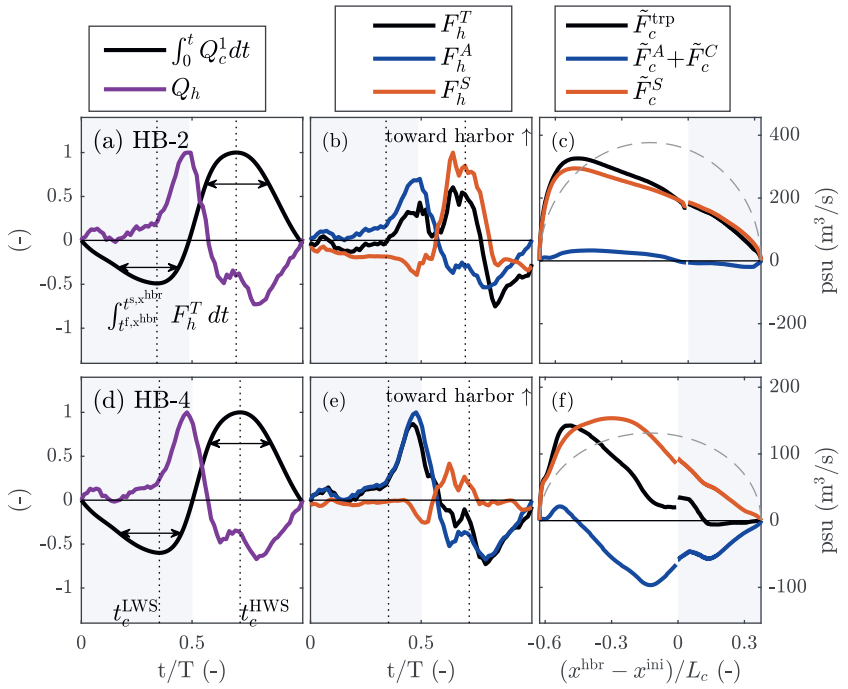


Figure 4.14: Illustration of the additional up-estuary salt flux $\tilde{F}_c^{\mathrm{trp}}$ quantified through Eq. 4.5, shown for HB-2 and HB-4. (a,d) Periods over which the integral in Eq. 4.5 is evaluated. The double-headed arrows indicate the interval between the first and second moments when a plane moving along the main channel passes the harbor location (x^{har}). (b,e) Instantaneous salt fluxes over the harbor entrance. (c,f) The additional salt transport $\tilde{F}_c^{\mathrm{trp}}$, decomposed into contributions from advective out-of-phase exchange ($\tilde{F}_c^A + \tilde{F}_c^C$) and from exchange that is diffusive in nature ($\tilde{F}_c^S$). The gray dashed line shows the additional salt transport predicted by Eq. A.10, where s_c^R is attributed 7.5 and 2 psu, H_h is taken 15 and 14 m, and the ratio A_h/A_c is 0.5 and 0.6, for HB-2 and HB-4 (respectively). For all panels, blue shading indicates that the initial locations of parcels traveling with the cross-sectionally averaged discharge at $t = 0$ are situated up-estuary of x^{har}, whereas the white background indicates they are located down-estuary of x^{har}.

where L_c is the tidal excursion length in the main channel, and the superscript ^{i} denotes the specific transport component. From Figure 4.15, it is clear that the additional salt transport resulting from tidal trapping is primarily due to $\overline{\tilde{F}_c^S}$, which is mainly driven by the vertically sheared salt flux resulting from density dynamics (see Section 4.4.2). The effect of out-of-phase exchange ($\overline{\tilde{F}_c^A} + \overline{\tilde{F}_c^C}$), represented by the joint effect of the net down-estuary directed salt transport from the harbor ($\tilde{F}_c^A$) and the compensating up-estuary salt transport ($\tilde{F}_c^C$), is small and, for several harbors, even negative. This negative contribution has two causes. First, $\tilde{F}_c^A$ tends to become increasingly negative as the relative strength of diffusive channel–trap exchange increases. This is because the diffusive exchange causes the salinity in the harbor to rise as the basin begins to empty, making $\tilde{F}_c^A$ more negative compared to its value in the absence of diffusive exchange. Secondly, due to the import of low-salinity water from the Old Meuse channel (see Figure 4.5), the volume experiencing an up-estuary excursion has low salinity. This second effect

is the primary source of the negative contribution to the advective out-of-phase exchange for harbors located near the junction (i.e., HB-1 to HB-4). Furthermore, the time series shows that the excursion-length-averaged additional salt transport exhibits little to no spring–neap variability at most locations. However, the influence of the diurnal tidal inequality is clearly present.

Panel g in Figure 4.15 shows the additional salt transport from tidal trapping, averaged over a spring-neap cycle, expressed relative to the tidally averaged salt transport associated with flushing by the river discharge in the main channel, $\frac{\overline{\tilde{F}_c^i}}{F_c^{\text{res}}}$, also referred to as the diffusive salt fraction (Hansen and Rattray Jr 1966b). This ratio quantifies the importance of tidal trapping to the overall up-estuary salt transport. It shows that the estimated contribution of tidal trapping in the individual harbors is 2 to 10% of the up-estuary directed salt transport. Furthermore, the contributions of HB-4 and HB-5 are the weakest, despite being the largest harbors. This is a noteworthy results, as in expressions for tidal trapping in literature, tidal trapping generally increases with an increase in relative trap size. Their small contribution is further emphasized in panel h in Figure 4.15, which shows the diffusive salt fraction scaled by $\epsilon = \frac{\hat{Q}_c}{\hat{Q}_h}$. Their relatively small contribution is related to the limited contribution of $\overline{\tilde{F}_c^S}$. The two largest harbors (HB-4 and Hb-5) are located in a region where the tidal salinity range is small (Figure 4.12), which results in a small vertical shear related salt transport (see Section 4.4.2).

Overall, our analysis of the additional salt transport due to tidal trapping indicates that the relative contribution of harbors to salt dispersion is primarily determined by conditions in the main channel. Specifically, the salinity range s_c^R controls the strength of the exchange flow from vertically sheared salt flux between the channel and the harbors.

4.4.4 Relative Importance of Subtidal Exchange compared to Tidal Trapping

Section 4.4.3 showed that larger harbors do not necessarily produce a greater additional salt transport through tidal trapping. This is due to the locally reduced diffusive channel–harbor exchange on intratidal time scales, which results from the local minimum in the tidal salinity range. In contrast, the net subtidal salt transport into or out of the harbors reflecting changes in salt storage related to spring–neap variability, river discharge change and storm surges, tends to increase with harbor size (Figure 4.16). This emphasizes that the influence of harbors can vary significantly depending on their size and their location within the system (i.e., in regions characterized by strong subtidal and/or intertidal salinity dynamics). In this context, the largest harbors act as sources or sinks of salt on a subtidal timescale, thereby contributing to the unsteadiness of the system and likely increasing its adjustment timescales. This notwithstanding, their contribution to the up-estuary salt transport through tidal trapping is minimal. Vice versa, in this particular case, the smaller basins contribute substantially to the additional salt transport via tidal trapping, but their role in salt storage on a subtidal timescale is limited.

4.5 Discussion

In this paper, we analyzed channel-harbor salt exchange and quantified the additional up-estuary salt transport resulting from tidal trapping in harbors along the partially-stratified New Meuse and New Waterway. The additional up-estuary salt transport resulting from tidal trapping is primarily caused by a vertically sheared channel–harbor exchange flow driven by gravitational dynamics, while the contribution from tidal trapping through advective out-of-phase exchange is small. The conditions under which tidal trapping transitions from being dominated by advective out-of-phase exchange to being governed by diffusive processes from for example turbulence and density currents have

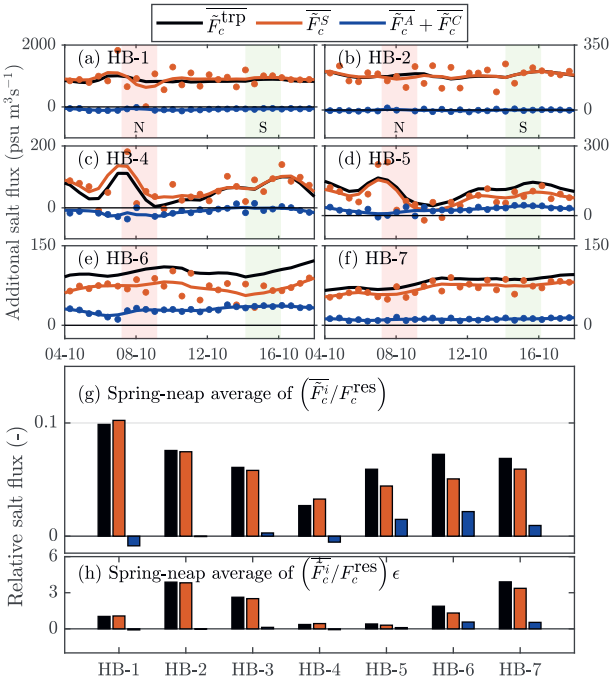


Figure 4.15: Overview of the additional (up-estuary) salt transport resulting from tidal trapping for the different harbors. (a-f) Tidal-excursion-averaged value of the additional salt transport resulting from tidal trapping, $\overline{\tilde{F}_c^{\mathrm{trp}}}$, and the individual contributions of advective out-of-phase exchange ($\overline{\tilde{F}_c^{A}} + \overline{\tilde{F}_c^{C}}$) and diffusive exchange ($\overline{\tilde{F}_c^{S}}$). Scatter points represent values obtained for individual tidal cycles, while the solid line indicates the smoothed response (running average over 5 tidal cycles). (g) The additional salt transport contributions ($\overline{\tilde{F}_c^{i}}$), relative to F_c^{res} (i.e., expressed as a diffusive salt fraction), averaged over a spring–neap cycle.(h) Same as panel (g), but scaled by the relative discharge amplitude from the main channel to the harbor, $\epsilon = \hat{Q}_c/\hat{Q}_h$, to partially eliminate the influence of harbor size.

been explored in Chapter 2. Here we evaluated the transition based on the tidal trapping Péclet number $P_{e,\mathrm{trapping}} = (\hat{U}_h \ell_h)/K_h$, where $\hat{U}_h$ is the velocity amplitude in the harbor, ℓ_h is the harbor or trap length, and K_h is a dispersion coefficient that parameterizes the instantaneous diffusive exchange. In Chapter 2 we found that for small tidal trapping Péclet numbers ($P_{e,\mathrm{trapping}} < 10^1$), the contribution of advective out-of-phase exchange to the resulting up-estuary salt transport becomes negligible, and tidal trapping is then governed by diffusive exchange. From this, the dominance of diffusive exchange in relatively deep harbors can be readily understood. The current amplitude at the harbor entrance is inversely related to the depth of the harbor $\hat{U}_h \approx (2\hat{\eta}\ell_h)/(TH_h)$. Assuming that the diffusive exchange results from the vertically sheared salt transport driven by gravitational dynamics (see Section 4.4.2), the dispersion coefficient based on Eq. 4.13 is expected to increase with harbor depth, following $K_h \propto H_h^{1/2}$. Using these relations, the tidal trapping Péclet number decreases rapidly with increasing basin depth, since $P_{e,\mathrm{trapping}} \propto H_h^{-3/2}$.

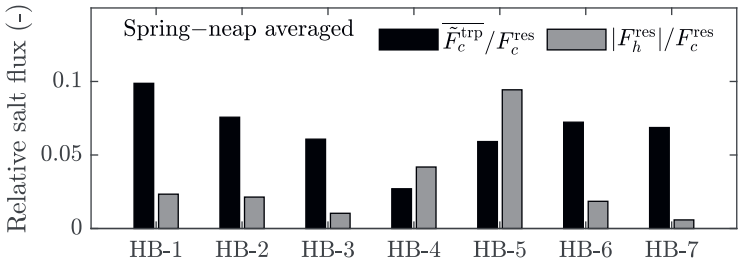


Figure 4.16: Comparison of the spring–neap averaged additional salt transport due to tidal trapping, $\overline{\tilde{F}_c^{\mathrm{trp}}}$, with the absolute subtidal salt transport into/out of the harbors, $|F_h^{\mathrm{res}}|$, both normalized by F_c^{res}. The comparison highlights the relative importance of channel–harbor exchange on intertidal versus subtidal time scales across the different harbors.

Based on the observed vertically shear related fluxes at the HB-2 and HB-4, we estimated K_h to be 30 and 10 $\mathrm{m^2 s^{-1}}$ for the two harbors, using a dock length of $\ell_h = 2000$ m, with $\hat{U}_h = 0.02$ and 0.05 m/s. The resulting Péclet numbers are 1.33 and 10 for HB-2 and HB-4, respectively. These values indeed align with conditions where the additional salt transport mainly results from exchange that is diffusive in nature.

Tidal dispersion is often considered to be independent of the subtidal along-channel salinity gradient, in contrast to the parameterization of dispersion driven by the gravitational circulation (Hansen and Rattray 1965; Monismith et al. 2002). Parameterizations of dispersion coefficients for tidal trapping driven by advective out-of-phase exchange (see Schijf and Schönfled (1953) and Dronkers (1978) and Chapter 2) are independent of the salinity gradient, as demonstrated by Dronkers (1978). For tidal trapping driven by exchange that is diffusive in nature, Okubo (1973) derived an elegant expression, which, similar to the expression for advective out-of-phase exchange, is independent of the subtidal along-channel salinity gradient. In cases where tidal trapping results from a channel-harbor exchange driven by density dynamics, the resulting vertically sheared salt transport is found to be proportional to the tidal salinity range, according to: $\hat{F}_h^V \propto \left(s_c^R\right)^{3/2}$ (see Section 4.4.2). Under the assumption that s_c^R is solely the result of advection of a stationary salinity field, then $s_c^R \approx L_c \frac{\partial s_c^0}{\partial x}$. Assuming that the density-driven exchange in/out of the harbor varies sinusoidally in time and is in quadrature with the velocity in the main channel, a relation for the dispersion coefficients resulting from tidal trapping via channel-harbor exchange driven by density dynamics can be derived (see Appendix A.2 for details):

$$K_c^{\mathrm{trp}}(x^{\mathrm{ini}}) = \frac{1}{8\pi}\sqrt{\frac{1}{2}}\left(\frac{B_h H_h}{A_c}\right)\left(\beta L_c \frac{\partial s_c^0}{\partial x} g H_h\right)^{1/2} L_c \cdot \left(1 - \left(2\frac{x^{\mathrm{ini}}}{L_c} - 1\right)^2\right)^{1/2}. \quad (4.15)$$

Eq. 4.15 shows the dependence of dispersion on the ratio between harbor and channel cross-sectional area. The correct dimensions are determined by the propagation speed of the density current into the harbor $\sqrt{\beta L_c \frac{\partial s_c^0}{\partial x} g H_h}$ times the tidal excursion length in the main channel L_c, which provides an intuitive measure of the dispersive effect of tidal trapping driven by density dynamics. A noticeable difference with the formulations by Okubo (1973) and Dronkers (1978) is that Eq. 4.15 depends on the salinity gradient according to $K_c^{\mathrm{trp}} \propto \sqrt{\frac{\partial s_c^0}{\partial x}}$. This difference can be explained from the fact that Okubo (1973) assumes an exchange-rate coefficient that represents the flux without specifying its

driving processes. In contrast, for Eq. 4.15, it is assumed that the channel-harbor exchange results from density dynamics, which introduces a dependence on the subtidal salinity gradient. Finally, although Eq. 4.15 is derived under (highly) simplified conditions, it predicts our quantification of the additional salt transport reasonably well (see Figure 4.14).

The analysis of channel–harbor exchange reveals regions where the instantaneous vertically sheared salt flux exhibits a local minimum (Figure 4.13), which strongly reduces the net effect of tidal trapping (Figure 4.15). This minimum in the tidal salinity range s_c^R is not caused by the harbors themselves, but rather by differences in branch characteristics and sharp depth transitions within the New Meuse. This is consistent with the overall limited role of harbor-induced tidal trapping, which contributes only about 5% of the up-estuary salt transport. The existence of this minimum in the tidal salinity range demonstrates that the contribution of harbors varies significantly between locations, depending on the nature of the exchange (as discussed above). However, to obtain a more complete understanding of the influence of harbors in a system like the Rhine–Meuse estuary, it is necessary to better resolve the interactions between individual branches and to determine how harbor effects combine or counteract one another. Moreover, the exchange between the main channel and side basins also affects main-channel dynamics, for instance through the formation of fronts Giddings et al. (2012), Corlett and Geyer (2020), and Bo and Ralston (2020). These processes can influence stratification and vertical mixing, while introducing additional shear that modifies dispersive mechanisms. To further advance understanding of trapping dynamics in side channels, it would be valuable to compare the additional salt transport resulting from the temporal storage studied herein with a decomposition of the tidal salt flux as derived by Dronkers and Van de Kreeke (1986) and more recently applied by Garcia and Geyer (2022) and Garcia and Bo, et al. (2025). Such a comparison could help to relate the effect of trapping to shear-driven processes in the main channel. However, applying this type of analysis in a channel-network system remains challenging.

The main channel response to the additional salt transport from a trap differs between deep and shallow systems as follows. In a simplified 1D setting, an additional salt transport resulting from trapping will locally decrease the along-channel subtidal salinity gradient. This (local) reduction in the salinity gradient dampens the up-estuary salt transport driven by background dispersion. In deeper systems, the background dispersion is generally driven by the gravitation circulation, whereas in shallower systems, it is the result of tidal dispersion mechanisms. The dispersion coefficient for gravitational circulation has been derived as $K_G(x) \sim \frac{(\beta g)^2 H_c^8}{A_v^3}\left(\frac{\partial s_c^0}{\partial x}\right)^2$ (Hansen and Rattray 1965; Monismith et al. 2002) and depends on the subtidal salinity gradient, whereas tidal dispersion is independent, or, as we discussed above, is weakly dependent on the subtidal salinity gradient. As a consequence, additional local dispersion will increase salinity levels up-estuary of the trap faster in well-mixed systems compared to systems where background dispersion is determined by the gravitation circulation. This is accompanied by a stronger decrease in the subtidal salinity gradient.

How harbors, or traps in general, influence the salt intrusion length depends on multiple aspects and is not easily estimated a priory. Exploratory model experiments were performed in which harbors were closed. The closure of HB-1, and the combined closrue of HB-4 and HB-5 both resulted in a reduction of the salt intrusion length. In particular, the closure of HB-4 and HB-5 reduced up-estuary salinity levels. In contrast, the closure of HB-6 and HB-7 cause an increase in the salt intrusion length. Roelfzema and Van Os (1978) and Abraham et al. (1986) concluded that the harbor effect on salt intrusion in the Rhine-Meuse depends on two main counteracting mechanisms: additional mixing by temporal storage and release causing an increase, versus enhanced vertical mixing and an increase of the tidal prism causing a reduction. Scale models showed that closing harbors in the New Meuse predominantly caused a reduction in the intrusion length. The latter agrees with our results for the HB-4 and HB-5, which contribute little to the additional salt-transport, but increase the tidal prism because of their size. Similar conclusions were drawn by Hendrickx and Pearson (2024), who explored the role of intertidal areas and

found that in partially stratified systems, intertidal areas reduce the estuarine circulation. Vice versa, in well-mixed systems, they found increasing salt intrusion. They did not quantify the relative contribution of individual mechanisms.

4.6 Conclusions

In this study, we investigate the exchange of salt between a partially stratified channel and its adjacent harbors, and examine how this exchange influences up-estuary salt transport along the New Meuse within the Rhine-Meuse Estuary. During a field campaign, four shipboard surveys were conducted at two harbor basins. Analysis of the field observations indicates that the instantaneous salt exchange between the channel and a harbor is dominated by a vertically sheared, density-driven flow, which prevails over the contribution from barotropic filling and emptying of the harbors. The observed vertically sheared density-driven salt flux is less strong for the harbor where the tidal salinity range in the main channel was weaker, which limits the setup of the baroclinic pressure gradient driving this exchange flow. At one harbor, the observations revealed a current profile with a persistent mid-column outflow, which we attribute to a gradient in stratification driving a baroclinically induced acceleration that peaks in the core of the water column.

Numerical modeling results generalized the observations from the field, showing a marked reduction in the contribution of the vertically sheared salt flux for the harbors located in the region where the tidal salinity range is small. The salt transport by the vertically sheared exchange flow into and out of the harbor is empirically found to scale with the tidal salinity range to the 3/2, which is in agreement with theory for density dynamics. Evaluation of the harbor-induced additional up-estuary salt transport (i.e. trapping-induced dispersion) showed that the additional salt transport is primarily induced by the channel-harbor salt flux component from the vertically sheared exchange flow. Due to the sensitivity of this exchange to the tidal salinity range, harbors located in regions with a smaller salinity range contributed significantly less to the net up-estuary salt transport. This explains the at first instance somewhat surprising observation that the largest harbors in the New Meuse contributed the least to the up-estuary salt transport through tidal trapping.

Finally, we show that when channel–trap exchange is governed by density dynamics, the resulting tidal-trapping contribution to along-channel salt dispersion scales with the square root of the along-channel salinity gradient. This contrasts with classical parameterizations of advective out-of-phase exchange, which are independent of that gradient. This scaling follows from expressing tidal trapping as a dispersion coefficient under the assumption that the tidal salinity range arises from advection of the subtidal along estuary salinity profile.

CHAPTER 5

Salinity Dynamics in Partially Deepened Estuaries With stepwise Bathymetry

Many present-day estuaries exhibit steps in the bathymetry due to deepening of the lower estuary for port accessibility. In this study, we examine how the slope inclination of the depth transitions between steps with fixed bed levels affects estuarine salinity dynamics and the resulting salt intrusion length (SIL). Using numerical experiments, we show that in strain-induced periodic stratification and partially stratified estuary classes, steeper bed slopes can increase the salt-intrusion length, even though the estuary on average becomes shallower. We explain this increase from two mechanisms. (1) A steeper bed slope enhances reflection of the barotropic tide, which reduces the currents down-estuary when the depth transition is located within a quarter-wavelength of the forcing. This leads to decreased vertical mixing and enhancing gravitational circulation driven salt transport. (2) Reduced depth up-estuary of the depth transition restricts this gravitationally driven salt transport, producing a sharp along-channel salinity gradient near the depth transition. Barotropic forcing acting on this salinity field on an intertidal timescale causes the development of a lift-off point during late ebb, which transitions into a tidal intrusion front during the subsequent flood. The steeper the bed slopes, the stronger these frontal dynamics. The associated vertically sheared salt transport amplifies the tidal oscillatory transport up-estuary, contributing to increased SIL for steeper bed slopes. These findings highlight the critical role of bed slope inclination of the depth transitions in controlling salinity dynamics and exchange processes, and show that partial shallowing does not necessarily reduce the SIL under all forcing and bathymetric conditions.

This chapter is based on the manuscript: ***van Keulen, D., W. M. Kranenburg, and A. J. F. Hoitink*** *(2026). Salinity Dynamics in Partially Deepened Estuaries With Stepwise Bathymetry. Manuscript in preparation for submission.*

5.1 Introduction

In many estuaries, the navigation channel is dredged to its greatest depth in the lower reaches to ensure access to seaports. As a result, present-day estuarine bathymetries often exhibit a stepped longitudinal profile, reflecting the stepwise increase in dredging depth from the lower toward the upper estuary (Figure 5.1). In this study, we investigate how the bed-slope inclination of the transition between the lower and upper estuary influences estuarine salinity dynamics.

A uniformly dredged channel is typically associated with tidal amplification and enhanced wave propagation (Familkhalili and Talke 2016; Ralston and Talke, et al. 2019; Winterwerp and Wang, et al. 2013; Vellinga et al. 2014). In most cases, dredging-induced tidal amplification can be explained from the changing balance between amplification due to channel convergence and attenuation due to frictional energy losses (Friedrichs 2010; Rijn 2011; Savenije et al. 2008; Jay 1991). Channel convergence compresses tidal energy into a progressively smaller cross-sectional area, leading to amplification of the tidal range, following Green's law (Jay 1991; Rijn 2011; Kästner et al. 2019). Friction, by contrast, dissipates tidal energy through bottom stress, causing attenuation of the tidal wave as it propagates landward. Increasing channel depth reduces frictional energy dissipation, thereby modifying the balance between convergence-caused amplification and frictional damping. This balance is particularly relevant when the characteristic geometric length scales of the channel are comparable to the tidal wavelength. However, when depth variations occur over spatial scales much shorter than the tidal wavelength, the tidal wave can no longer adjust smoothly to the changing geometry. In such cases, the local wavenumber changes abruptly rather than gradually along the channel. Because both the tidal discharge and the water-level amplitude must remain continuous across the depth transition, the incoming wave cannot satisfy these conditions with a single progressive component. Instead, part of the wave energy is redirected seaward, producing a reflected wave. This mechanism has been described in classical tidal-wave theory and confirmed in recent studies (Dronkers 1964; Talke et al. 2021; Dykstra et al. 2024). Sharp bed steps, such as those shown in Figure 5.1, are typical locations where partial tidal reflection can occur.

Channel deepening not only alters barotropic tidal characteristics but also tends to increase the estuarine salt intrusion length (SIL) (Rummel et al. 2025; Andrews et al. 2017; Chant et al. 2018; Ralston and Geyer 2019). This increase in SIL due to deepening can often be explained using classical theory on gravitational circulation (Hansen and Rattray Jr 1966a; Chatwin 1976; Monismith et al. 2002), which states that the intrusion length scales with channel depth as $H^{5/3}$. For the Hudson Estuary (US), Ralston and Geyer (2019) found that the present-day SIL, relative to that obtained for the pre-dredging bathymetry, is broadly consistent with this scaling. Furthermore, due to the relatively uniform depth of the Hudson, salt can intrude largely unimpededly, relaxing some of the theoretical constraints on gravitationally driven exchange flow (Ralston and Geyer 2019; Chant et al. 2018; MacCready and Geyer 2010). Such behaviour is less likely in partially deepened channels, where the SIL cannot freely adjust but is instead constrained by depth transitions. Observations by Chant et al. (2018) in Newark Bay—a system in which salinity intrusion is geometrically constrained—support this interpretation and show that channel deepening led to a doubling of the exchange flow.

In partially deepened systems, the overall salt transport tends to be increasingly dominated by estuarine circulation within the deepened reach (Kranenburg et al. 2022; Dijkstra and Schuttelaars and Kranenburg 2022; Eidam and Sutherland and Ralston and Dye, et al. 2022; Rummel et al. 2025). Within these systems, typically, a transition point exists beyond which the landward salt flux is no longer (partially) dominated by estuarine circulation, but instead results primarily from tidal-dispersion mechanisms (Dijkstra and Schuttelaars and Kranenburg 2022). For such partially deepened systems, this transition point generally coincides with the depth transition (see Kranenburg et al. (2022) and Dijkstra and Schuttelaars and Kranenburg (2022) and Chapter 4). The fact that the contri-

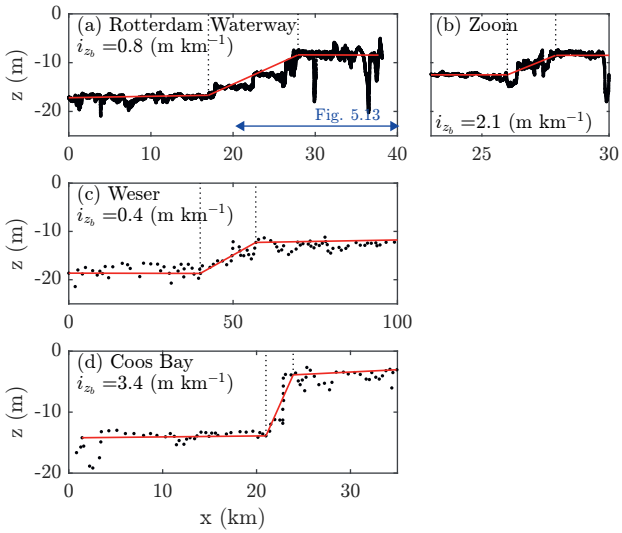


Figure 5.1: Examples of stepwise depth transitions in real estuaries. The bed-slope inclination i_{z_b} is estimated over the transition area between steps (see also Figure 5.2). (a) Rotterdam Waterway (The Netherlands), which exhibits several steps. Here, the slope is calculated over the whole transition area. The section highlighted by the double-headed arrow corresponds to the along channel transect shown in Figure 5.13, which presents observations of the salinity structure. (b) Zoom-in on the most up-estuary step in the Rotterdam Waterway. (c) Weser Estuary (Germany), bottom profile adopted from Rummel et al. (2025). (d) Coos Bay Estuary (USA), bottom profile adopted from Eidam and Sutherland and Ralston and Conroy, et al. (2021).

bution of estuarine circulation diminishes upstream of the step in channel depth is readily understood from the enhanced vertical mixing, which can overcome vertical stratification and thereby alter the dominant salt-transport mechanism (Hansen and Rattray Jr 1966a; Simpson and Brown, et al. 1990). For the Rotterdam Waterway, we noted in Chapter 4 that near the bed transition the contribution of estuarine circulation indeed decreases, while the salt transport associated with tidal-dispersion mechanisms shows a marked increase. Their analysis examined whether harbor exchange could explain the observed tidal dispersion and showed that this enhancement cannot be attributed to the presence of the harbors. Instead, they suggested that it results from the stepped channel depth. Here, we study the role of such stepped geometries in initiating tidal-dispersion mechanisms.

The role of the geometry of depth transitions in contributing to tidal dispersion has received limited attention. From the moving-plane analysis proposed by Dronkers and Van de Kreeke (1986), it is known that salt transport by tidal dispersion (i.e., tidal-oscillatory salt transport) equals the difference between the tide-averaged vertically and laterally sheared salt transport observed at a fixed Eulerian cross-section and that observed from a quasi-Lagrangian moving plane. Consequently, geometric features that induce strong spatial variations in sheared salt transport over distances smaller than the tidal excursion are typically associated with regions of locally enhanced tidal dispersion (Dronkers and Van de Kreeke 1986; Garcia and Geyer 2022). It is well known that abrupt geometric transitions are often associated with frontal formation as a result of hydraulic adjustment processes (Armi 1986; Largier 1992; Geyer and Ralston 2015; Corlett and Geyer 2020). At a depth transition, changes in cross-sectional area lead to spatial gradients in velocity, which modify vertical shear and the local horizontal Richardson number. If the flow

approaches a hydraulic control (i.e., the composite Froude number locally approaches 1), strong convergence and enhanced straining may develop, often resulting in frontogenesis. Analogously, near the mouth of an estuary, the increase in channel depth leads to a lift-off point near the end of the ebb (Horner-Devine et al. 2015; MacDonald and Geyer 2005), which has been shown to contribute to the salt transport associated with tidal dispersion (Garcia and Geyer 2022; Stommel and Farmer 1952) .

Despite these insights, it remains unclear how the steepness of bathymetric transitions between stepped depths influences the interplay between barotropic tides, estuarine salinity dynamics, and salt intrusion length. This is relevant in many modern estuaries, because such bathymetric features are very common. Therefore, this papers addresses the control of the steepness between stepped depths on the estuarine dynamics. The structure of this paper is as follows. Section 5.2 describes the setup of the numerical experiments and the applied model analysis. Section 5.3 presents the model results. First, we identify the response of the salt intrusion length (SIL) to mild and steep bed-slopes at depth transitions across different classes of estuaries (Section 5.3.1). Secondly, we explain the differing responses through analyses of the barotropic tide (Section 5.3.2), salt transport mechanisms (Section 5.3.3), and frontal dynamics (Section 5.3.4). In Section 5.4, we compare the model results with observational data from the Rotterdam Waterway and discuss the dependence of the along channel position of the depth transition area on the resulting tidal dynamics, the processes initiated by sharp channel depth variations, and the response under varying forcing conditions. Conclusions are drawn in Section 5.5.

5.2 Method and Analysis

5.2.1 Model set-up and experiments

To study the effects of the steepness of bathymetric transitions between stepped depths on the tides and salinity dynamics in the lower estuary, we set up a 2D vertical model using Delft-3D (Deltares 2021). The model solves the incompressible shallow water equations, with eddy viscosity and diffusivity represented using a k-ϵ turbulence closure.

The modelled geometries are inspired by the stepped bottom profiles shown in Figure 5.1. Figure 5.2 provides an overview of the modelled geometry and the notation applied. For the down-estuary section, a constant bed level $z_{b,1}$ of -12 m is assumed over a (fixed) distance $X_1 = 35$ km. This is a distance comparable to the location of the depth transition in the estuaries shown in Figure 5.1. Furthermore, a somewhat shallower depth than observed is used for the down-estuary section, because in the absence of additional geometric features this idealized setup tends to underestimate vertical mixing. Upstream of X_1, the bed elevation gradually increases to an elevation of $z_{b,2}$ -6 m over a distance X_2. In our analysis, we consider two cases: one with a gentle bed-slope and another with a relatively steep slope. In the first case, a bed slope of $i_{z_b} = 0.5\ \mathrm{m\,km^{-1}}$ is imposed, similar to the inclination observed in the Weser Estuary and to the overall slope across the transitional zone of the Rotterdam Waterway. In the second case, a slope of $i_{z_b} = \frac{z_{b,2} - z_{b,1}}{X_2} = 2\ \mathrm{m\,km^{-1}}$ is imposed, similar to the slope observed in Coos Bay and to that of the most landward step in the Rotterdam Waterway. Because the distance X_1 is kept constant, a steeper slope produces a greater overall shallowing of the estuary than a milder slope, which will allow us to demonstrate that greater mean depth may surprisingly reduce salt intrusion. Beyond this sloping section, the bed-level is kept constant over a distance X_3, after which the bed-level gradually increases again from -6 to 2 m above mean sea level over a distance of 70 km. This final section serves to dampen the tidal motion; a constant discharge is prescribed at the up-estuary boundary. In all cases, a constant channel width of $W = 500$ m is used.

The computational domain is discretized with a horizontal grid spacing of $\Delta x = 100$ m, and 20 equidistant σ-layers in the vertical. In the experiments, abrupt bed changes are avoided, as these can introduce numerical artifacts in circulation (Stelling and Van Kester

1994). Such artefacts arise when the relative depth change across a grid cell exceeds the vertical layer thickness, as expressed by the hydrostatic consistency criterion of Haney (1991): $\frac{i_{z_b}}{H}\Delta x < \Delta\sigma$, where $\Delta\sigma$ is sigma-layer height. For the presented grid, this condition is easily satisfied for the imposed steep bed slope of $i_{z_b} = 2\ \mathrm{m\,km^{-1}}$, indicating that the bathymetry is well within the numerically stable regime. A time step of $\Delta t = 1$ minute is used.

To verify that the imposed bed-slope inclination does not introduce significant non-hydrostatic effects, we assess the ratio of non-hydrostatic to hydrostatic barotropic pressure. Following the scaling of Baines (2022),

$$\frac{p'}{\rho g H} \sim Fr^2 \left(\frac{H}{L}\right)^2,$$

and using $H/L \approx i_{z_b}$ for a monotonic slope, this reduces to $\frac{p'}{\rho g H} \sim Fr^2\, i_{z_b}^2$. Using a representative depth of $H = 12$ m at the toe of the slope and a tidal current of $U = 0.5\ \mathrm{m\,s^{-1}}$, we obtain a non-dimensional pressure ratio of order 10^{-6}, and we therefore conclude that the contribution of non-hydrostatic barotropic pressure associated with the bed slope is negligible.

A summary of the model forcing for the experiments in the different sections is provided in Table 5.1. At the up-estuary boundary, the model is forced with a constant river discharge Q_{riv}, together with a constant river salinity s_{riv} which is 0 psu for all cases. At the down-estuary boundary, water level variations are represented by a single tidal constituent with a period of 12.00 h along with a constant salinity of $s_{sea} = 30$ psu. The water levels are represented by a single tidal constituent with a period of 12.00 h, corresponding to the S_2 tide. Friction is expressed using a constant Chézy value of 65 $\mathrm{m^{1/2}s^{-1}}$.

To support the interpretation of our results, we classify the modelled systems according to the estuary classes of Geyer and MacCready (2014), based on the freshwater Froude number and a tidal mixing parameter. The freshwater Froude number is defined as:

$$Fr_f = \frac{u_r}{\sqrt{\beta g s_{sea} H}}, \tag{5.1}$$

where u_r is the freshwater discharge related velocity, β the haline contraction coefficient, g the gravitational acceleration, s_{sea} the sea salinity, and H the water depth. The mixing parameter M quantifies the effectiveness of tidal mixing and is defined as:

$$M = \sqrt{\frac{c_d U_t^2}{\omega N_0 H^2}}, \tag{5.2}$$

where c_d is the drag coefficient, U_t the tidal velocity amplitude, ω the tidal angular frequency, and $N_0 = \sqrt{\frac{\beta g s_{sea}}{H}}$ the buoyancy frequency corresponding to the maximum top-to-bottom stratification.

Section	$z_{b,1}$ (m)	$z_{b,2}$ (m)	X_1 (km)	i_{z_b} (m km^{-1})	s_{sea} (psu)	η_0 (m)	Q_{riv} (m^3 s^{-1})
5.3.1	−12	−6	35	0.5; 2.0	30	0.75; 1.00; 1.25	100 . . . 2000
5.3.2–5.3.4	−12	−6	35	0.5; 2.0	30	1.00	250

Table 5.1: Overview of the model geometry and boundary forcings used in the different sections.

5.2.2 Analysis of Barotropic and Baroclinic Tides

To analyse the barotropic and baroclinic tides (see Section 5.3.2), a harmonic analysis was performed on the modelled water levels, cross-section integrated discharge, depth-averaged

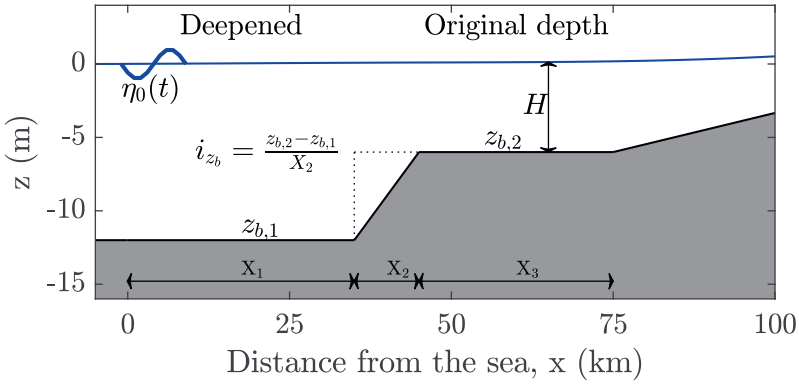


Figure 5.2: Illustration of the stepped depth profile used in the numerical model (also see Table 5.1) and the associated notations.

currents, and the depth-dependent component of the current to determine the semi-diurnal and quarter-diurnal amplitudes and phases, as well as the zero-frequency component.

To further enhance our understanding of the barotropic tide, we analyse the signal in terms of incident and reflected waves. In the modelled systems (Figure 5.2), we consider a domain without lateral convergence, and a channel bed that changes only locally over a the transition area. To assess whether this bed-level step behaves as a gradual geometric convergence or should instead be regarded as an abrupt depth discontinuity, we adopt the convergence parameter of Jay (1991), $\Delta = \frac{\sqrt{gH}}{2L_a\omega}$ which expresses the ratio of tidal wavelength to the channel's convergence length, where L_a is the convergence length scale of the cross-sectional area. We evaluate Δ over the region where the bed level increases gradually and compute its value at the toe of the bed slope. This yields $\Delta \approx 13$ and $\Delta \approx 3$ for the two configurations. Since Δ scales as the ratio of tidal wavelength to convergence length, $\Delta \sim \lambda/L_a$ (Jay 1991), these values imply $\lambda \gg L_a$, i.e. the topographic length scale is much smaller than the tidal wavelength. In this regime, the slowly varying approximation breaks down, and the tidal wave cannot adjust smoothly to the local depth change. The bed-level step should therefore be treated as a discontinuous geometric transition rather than as a gradual convergence.

To analyse the resulting along-channel variations in tidal amplitude and phase, we therefore apply the theory of Dronkers (1964) to locally evaluate the effect of wave reflection (see Appendix B). In the used formulations, channel convergence is not explicitly represented—as it is, for example, in Jay (1991), Winterwerp and Wang, et al. (2013) and Dykstra et al. (2024),—and reflection arises solely from an impedance mismatch between adjacent channel sections. This is fully consistent with the discontinuous nature of the bed-level steps implied by the large values of Δ. Dronkers (1964) showed that, by adopting simplified depth-averaged mass and momentum equations with a linearized friction term, a general solution for surface elevation and discharge can be obtained for a finite domain of constant width and depth. In this locally applied framework, the tidal response at any position is represented as the superposition of an incoming (incident) wave and a reflected wave, each described by its own complex amplitude:

$$\eta(t) = \mathrm{Re}\left(\hat{\eta}^- e^{i\omega t}\right) + \mathrm{Re}\left(\hat{\eta}^+ e^{i\omega t}\right), \tag{5.3}$$

where $\hat{\eta}^-$ and $\hat{\eta}^+$ denote the complex amplitudes of the incoming and reflected surface-elevation waves, respectively. The associated discharge is given by

$$Q(t) = \mathrm{Re}\left[-\left(\frac{Wc_0 i}{\sigma + i\chi}\right)\hat{\eta}^- e^{i\omega t}\right] + \mathrm{Re}\left[\left(\frac{Wc_0 i}{\sigma + i\chi}\right)\hat{\eta}^+ e^{i\omega t}\right], \tag{5.4}$$

where $c = \sqrt{gH}$ is the in inviscid wave celerity and W is the channel width. The parameters σ and χ depend on the non-dimensional friction coefficient r/ω and are defined as

$$\sigma = \sqrt{-\frac{1}{2} + \frac{1}{2}\sqrt{1 + \left(\frac{r}{\omega}\right)^2}}, \qquad \chi = \sqrt{\frac{1}{2} + \frac{1}{2}\sqrt{1 + \left(\frac{r}{\omega}\right)^2}}. \tag{5.5}$$

The linearized friction coefficient r is given by

$$r = \frac{8}{3\pi}\frac{g}{C^2}\frac{Q_t}{WH^2}, \tag{5.6}$$

where Q_t is the discharge amplitude and C is the Chézy friction coefficient.

In Eqs. 5.3 and 5.4, the complex amplitudes of the incoming and reflected waves are not known a priori and are typically obtained using a semi-analytical approach based on the governing equations (Talke et al. 2021; Dykstra et al. 2024). However, these amplitudes can also be expressed in terms of the resulting complex amplitudes of water level, $\hat{\eta}$, and discharge, $\hat{Q}$, as

$$\hat{\eta}^{\pm} = \frac{1}{2}\hat{\eta} \pm \frac{1}{2}\hat{Q}\frac{\chi - i\sigma}{Wc}. \tag{5.7}$$

We use the amplitudes and phases of the semi-diurnal tidal component obtained from the numerical model to estimate the complex amplitudes of the incoming and reflected waves by applying Eq. 5.3–5.7. The complex amplitudes are expressed as $\hat{\eta} = \eta\, e^{i\theta}$, where η is the real amplitude and θ the phase.

To analyse the resulting current amplitude and the phase difference between the discharge and the surface elevation of the observed tidal properties in a system with partial reflection, it is convenient to express these two quantities in terms of the reflection ratio $\gamma = |\hat{\eta}^-|/|\hat{\eta}^+|$ and the phase difference between the reflected and incident surface waves $\Theta = \arg(\hat{\eta}^-) - \arg(\hat{\eta}^+)$ (see Appendix B). This yields the following expression for the flow velocity amplitude:

$$|\hat{u}| = \frac{c_0}{H\,|\sigma + i\chi|}\left|1 - \gamma e^{i\Theta}\right|\left|\hat{\eta}^+\right|, \tag{5.8}$$

and for the phase difference between the horizontal and vertical tide:

$$\arg(\hat{\eta}) - \arg(\hat{Q}) = \arg\left(\frac{\chi - i\sigma}{\chi c_0}\right) + \arg\left(\frac{1 + \gamma e^{i\Theta}}{1 - \gamma e^{i\Theta}}\right). \tag{5.9}$$

Equation 5.8 shows that the flow velocity amplitude $|\hat{u}|$ attains a minimum when the reflected and incident waves are in phase ($\Theta = 0$) and have equal amplitudes ($\gamma = 1$). Furthermore, Eq. 5.9 separates the phase difference associated with frictional effects, which yields a maximum phase lag of 45°, from the phase shift introduced by (partial) wave reflection.

5.2.3 Analysis of salt dynamics

To gain insight into the salt transport mechanisms, we decompose the subtidal salt flux by expressing the flow velocity field as four distinct components (Fischer et al. 1979; Dronkers and Van de Kreeke 1986; Garcia and Geyer 2022). For the flow velocity, this yields:

$$\begin{aligned} u &= u_r + u_t + u_{s,s} + u_{s,v}, \\ u_r &= \langle \overline{u} \rangle, \\ u_t &= \overline{u} - u_r, \\ u_{s,s} &= \langle u \rangle - u_r, \\ u_{s,v} &= u - u_r - u_t - u_{s,s}, \end{aligned} \tag{5.10}$$

where u_r is the residual current, u_t the tidal variation of the cross-sectional mean velocity, and $u_{s,s}$ and $u_{s,v}$ denote the shear contributions, with the first subscript s indicating shear and the second distinguishing the steady (s) and time-varying (v) components.The operation $\langle\cdot\rangle$ indicates the tidal averaged and $\bar{\cdot}$ the cross-sectional average. The salinity field is decomposed in the same manner, which allows to express the subtidal salt flux F as:

$$\begin{aligned} F(x) &= F_r + F_t + F_{s,s} + F_{s,v} \\ &= u_r s_r A_0 + \langle u_t s_t A \rangle + \left\langle \int u_{s,s} s_{s,s}\, dA_0 \right\rangle + \left\langle \int u_{s,v} s_{s,v}\, dA' \right\rangle \end{aligned} \tag{5.11}$$

with F_r flushing by the residual current (including the river induced current and the Stokes drift). The second term, F_t, is the tidal oscillatory transport, which reflect the correlation between the tide-varying velocity and salinity components. The last two terms denote the contribution of shear $F_s = F_{s,s} + F_{s,v}$ observed at the cross-section, which we decompose into the steady shear contribution $F_{s,s}$ and a time-varying contribution $F_{s,v}$.

To gain insight into the origin of the tidal oscillatory contribution F_t observed at the Eulerian cross-section, we quantify the salt transport experienced by a moving Lagrangian plane using the method derived by Dronkers and Van de Kreeke (1986) and recently applied by Garcia and Geyer (2022). According to Dronkers and Van de Kreeke (1986), the salt transport through a plane that moves with the tide such that the upstream water volume remains constant can be expressed as:

$$\tilde{F}(x) = \tilde{F}_r + \tilde{F}_{s,s} + \tilde{F}_{s,v}, \tag{5.12}$$

where the tilde $\tilde{\cdot}$ indicates quantities defined with respect to the moving plane. Since the upstream volume is constant, the net volume transport $\tilde{Q}_t$ across the plane is zero. In an quasi-equilibrium situation, where the net tidally averaged salt transport is zero, the tidal contribution can be expressed as $F_t = \tilde{F}_s - F_s$, by combining Eq. 5.11 with Eq. 5.12. This decomposition shows that the tidal contribution corresponds to the difference between the shear exchange observed in the moving plane and that observed at a fixed Eulerian cross-section.

The position of the plane is determined by maintaining a constant upstream volume ($\int_{\tilde{x}}^{\infty} A dx$) from the moment of a chosen reference time t_0. The reference time is selected such that $s_r = \tilde{s}_r$, which in practice is close to peak flood or ebb (Dronkers and Van de Kreeke 1986). In this study, we calculate $\tilde{F}$ only when the plane remains within the main channel cross-section, as this condition is required for accurately tracking the plane's position. Consequently, the near-mouth region is excluded from this analysis, because jet–sink type exchange processes transport non-native water upstream, making the moving-plane method unsuitable there.

5.2.4 Analysis of Vertical Salinity Variation Generation

For a control volume, the total salinity field can be decomposed analogously to Eq. 5.10 as $s = \bar{\bar{s}} + s'_{\mathrm{tot}}$, where $\bar{\bar{s}}$ denotes the control-volume-averaged salinity and s'_{tot} the deviation from this mean. This deviation can be further partitioned into a vertical component, representing the local difference from the depth-averaged salinity, $s'_v = s - \bar{s}$, and a horizontal component $s'_h = s'_{\mathrm{tot}} - s'_v$. Here, $\bar{s}$ is the depth-averaged salinity and s'_v its associated vertical deviation. Using these expressions, the total salinity variance with a control volume can be expresses as (Burchard and Rennau 2008; Li and Geyer, et al. 2018):

$$\iiint (s'_{\mathrm{tot}})^2 dz dx dy = \iiint (s'_h)^2 dz dx dy + \iiint (s'_v)^2 dz dx dy, \tag{5.13}$$

To investigate the generation of vertical salinity variations, we consider the depth-integrated vertical salinity variance budget (Burchard and Rennau 2008; Li and Geyer, et al. 2018),

which in our 2DV setup simplifies to:

$$\frac{\partial}{\partial t}\int (s_v')^2 dz = -\frac{\partial}{\partial x}\int u(s_v')^2 dz - \int 2u_v' s_v' \left(\frac{\partial \overline{s}}{\partial x}\right) dz - \int 2A_v \left(\frac{\partial s}{\partial z}\right)^2 dz, \qquad (5.14)$$

with the A_v the vertical eddy-viscosity for salt. In Eq. 5.14, the term on the left-hand side represents the temporal tendency of vertical salinity variance, while the terms on the right-hand side represent, respectively, advection of variance, production (or destruction) through straining, and dissipation of variance by turbulent mixing. The evolution of horizontal variance is given by Li and Geyer, et al. (2018):

$$\frac{\partial}{\partial t}\iiint (s_h')^2 dz dx dy = \quad -\oint_B \int \bar{u}(s_h')dz \cdot dA + \oint_B \int 2u_v' s_v' dz \cdot s_h' dA + \iiint 2u_v' s_v' \left(\frac{\partial \overline{s}}{\partial x}\right) dz dx dy. \qquad (5.15)$$

From Eq. 5.15, it is seen that the generation of horizontal variance results from boundary advection, straining by the sheared flow at the boundaries, and the local conversion from vertical to horizontal variance.

5.3 Results

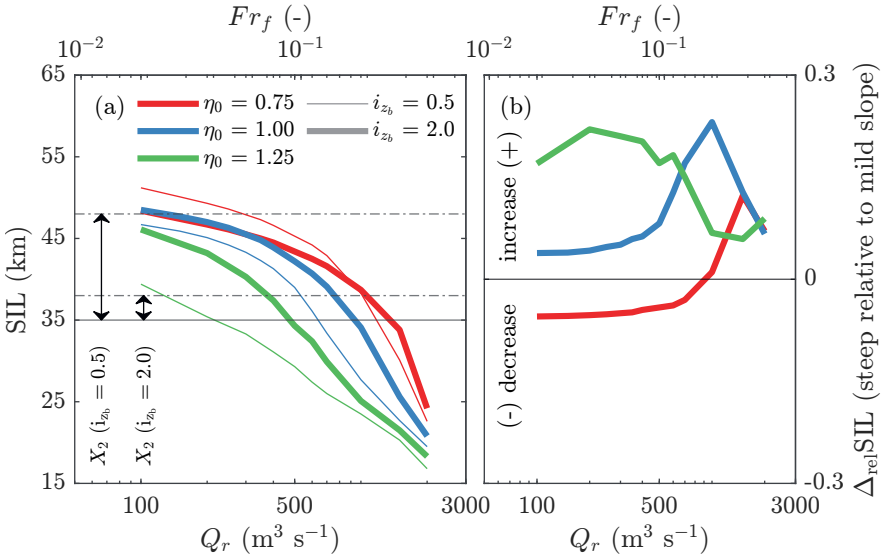


Figure 5.3: (a) Comparison of the salt intrusion length (SIL) for steep and mild bed-slope inclinations ($i_{z_b} = 2.0$ and $i_{z_b} = 0.50$) under different forcing conditions, including the tidal amplitude at the mouth (η_0) and river discharges (Q_{riv}). (b) Relative change in the SIL Δ_{rel}SIL calculated using Eq. 5.16.

5.3.1 Observed effects of depth transitions for different slopes

5.3.1.1 Salt intrusion lengths for different forcing conditions

In this section, we examine how bed-slope inclination affects the tide-averaged salt-intrusion length (SIL) under varying boundary conditions, comparing a mild ($i_{z_b} = 0.5$ m km^{-1})

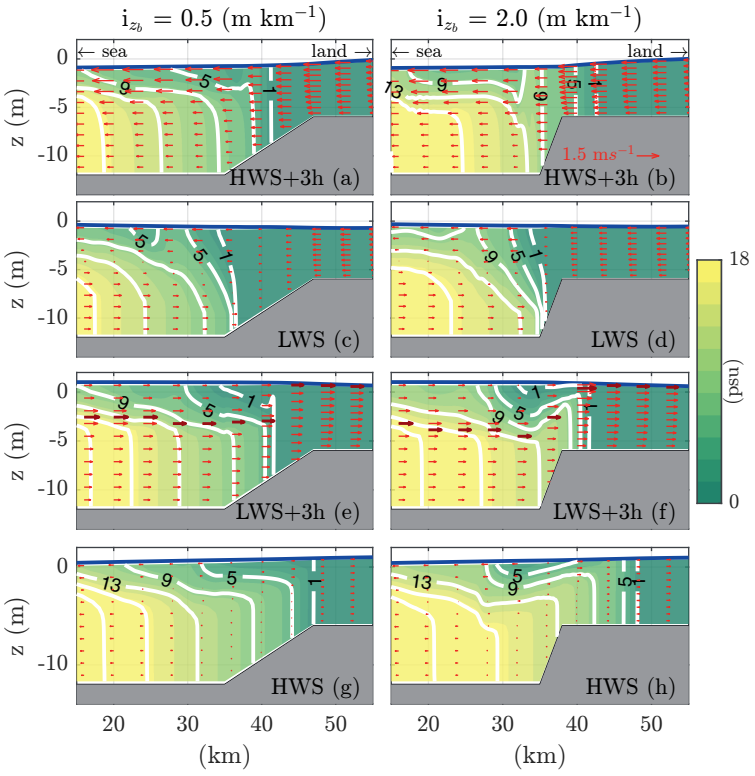


Figure 5.4: Comparison of simulated salinity fields near the depth transition for a relative mild ($i_{z_b} = 0.5$ m km^{-1}) and a relatively steep ($i_{z_b} = 2$ m km^{-1}) bed-slope inclination at various stages of the tidal cycle. The white lines indicate isohalines, the red arrows the along-estuary flow velocities. In panels (e) and (f), the maximum currents are highlighted by dark solid vectors, this to highlight the influence of the front on the mid-column jet.

and a sharp ($i_{z_b} = 2$ m km^{-1}) bed slope across different estuary classes.

Figure 5.3 shows the SIL under the different forcing conditions listed in Table 5.2. Panel (a) compares the SIL for the two bed-slope inclinations, while Panel (b) presents the relative change in SIL for the steeper slope with respect to the milder one, defined as:

$$\Delta_{\text{rel}}\text{SIL} = \frac{\text{SIL}_{i_{z_b}=2.0} - \text{SIL}_{i_{z_b}=0.5}}{\text{SIL}_{i_{z_b}=0.5}}. \tag{5.16}$$

Panels (a) and (b) show that if the salt intrusion limit is located within X_1, a steeper bed-slope consistently produces a greater SIL. When the salt intrusion limit extends beyond X_1, the steeper slope yields the greatest SIL for two of the three tidal forcing conditions ($\eta_0 = 1.00$ and 1.25 m). Only for the smallest tidal amplitude ($\eta_0 = 0.75$ m), the milder slope yields larger SIL than the steeper slope.

The freshwater Froude numbers Fr_f and mixing parameters M, calculated for the different tidal forcing conditions (Table 5.2), indicate that the estuaries range from highly stratified under the weakest tidal forcing to partially stratified conditions bordering the SIPS regime under the strongest forcing, based on the classification diagram of Geyer and

i_{z_b} (m km^{-1})	Q_{riv} (m^3 s^{-1})	η_0 (m)	Fr_f (-)	M (-)	Estuary class
0.5	100 . . . 2000	0.75	0.02 . . . 0.54	0.63 . . . 0.75	strongly stratified
2.0			0.02 . . . 0.54	0.58 . . . 0.68	
0.5	100 . . . 2000	1.00	0.02 . . . 0.54	0.79 . . . 0.92	partially/strongly stratified
2.0			0.02 . . . 0.54	0.73 . . . 0.82	
0.5	100 . . . 2000	1.25	0.02 . . . 0.54	0.95 . . . 1.07	partially stratified/SIPS
2.0			0.02 . . . 0.54	0.87 . . . 0.98	

Table 5.2: Resulting freshwater Froude numbers (Fr_f) and mixing parameters (M) for the different tested forcing conditions. The final column indicates where the results fall within the classification diagram of Geyer and MacCready (2014). Note that the tabulated classification correspond to the lowest values of Fr_f; for higher values the systems classify as salt-wedge to tide-dependent salt-wedge estuaries.

MacCready (2014). For the high-discharge conditions, the systems classify as salt-wedge to tide-dominated salt-wedge estuaries. However, under these conditions the SIL does not reach the sloping section.

Thus, first, when the SIL reaches the sloping region, the steeper slope produces a greater SIL, at least for the SIPS/partially stratified and partially/strongly stratified regimes. This is noteworthy because gravitational circulation—typically the dominant transport mechanism in these systems—is highly sensitive to depth (Hansen and Rattray 1965; Monismith et al. 2002). Yet, although the milder slope results in an overall deeper estuary, which would normally promote salt transport by gravitational circulation, it still produces a shorter SIL than the steeper slope. Second, when the SIL remains seaward of the slope, the steeper slope likewise yields a greater SIL for all tested conditions.

5.3.1.2 Effects on the salinity field around the depth transition

To further illustrate the influence of the steepness of the bed-slope inclination on the salinity dynamics, we study the velocity and salinity fields for the partially stratified system with $\eta_0 = 1$ m and Q_{riv} 250 (m^3 s^{-1}) (see Table 5.2).

Figure 5.4 shows results for the two bed-slopes at peak flood (LWS+3h), peak ebb (HWS+3h), and the corresponding slack waters (LWS and HWS). A key difference between the two bathymetries is the formation of a (surface) front in the simulation with the steeper bed slope (Figure 5.3d,f,h). This front develops near the low water slack, where isohalines are compressed at the toe of the depth transition. Here a stagnation point in the near-bed current is observed (Simpson and Linden 1989). At the toe of the bed-slope, flood begins first near the bottom transporting relatively saline water up-estuary over the sloping region (Figure 5.3e,f). As the channel shallows, the initially stratified water column undergoes rapid vertical mixing, a process that is less pronounced with a mild bed slope (Figure 5.3e,f). For the steeper bed slope, this process produces a local surface-salinity minimum just seaward of the depth transition. During early flood, a second stagnation point appears near the surface (Figure 5.3f), where the advancing flood tide plunges downward as a tidal intrusion front (Largier 1992). We will later show that the location and timing of this modelled surface front at the depth transition is consistent with actual observations in the Rotterdam Waterway (Figure 5.13).

5.3.2 Analysis of effects on water levels and current velocities

5.3.2.1 Impact on the Barotropic Tide

To understand through which mechanisms stepped bottom profiles affect the estuarine salt dynamics, we first analyse the barotropic tide (Figure 5.5).

For both bed configurations, the tidal-elevation amplitude of the dominant semi-diurnal tidal constituent $|\hat{\eta}|$ increases over the distance X_1, despite the fact that the channel

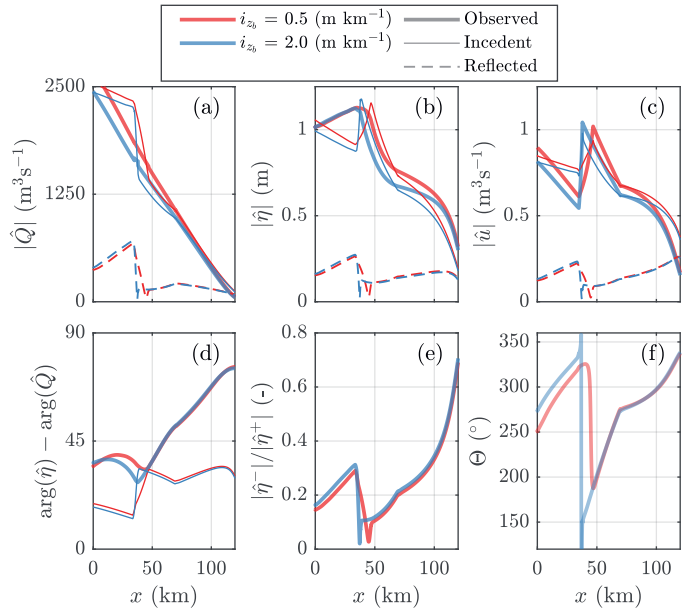


Figure 5.5: Overview of the barotropic tidal dynamics of the dominant semi-diurnal tidal constituent in the modelled domain for the two slopes of the depth transition i_{z_b}. (a)–(c) Semi-diurnal amplitude of the discharge ($|\hat{Q}|$), vertical tide ($|\hat{\eta}|$), and horizontal tide ($|\hat{u}|$), shown for the incoming/observed, incident, and reflected wave components. (d) Phase difference, expressed as the velocity phase lead of the discharge component relative to the surface elevation, shown for the incoming (observed) and the incident wave. (e) Ratio of the reflected to the incident surface-elevation amplitude, $|\hat{\eta}^-|/|\hat{\eta}^+|$. (f) Phase difference Θ between the reflected and incident wave components.

cross-sectional area remains constant over this section (Figure 5.5b). Upstream of X_1, the tides attenuate as the channel depth reduces over X_2, with a more pronounced attenuation for $i_{z_b} = 2$ m km^{-1}. The tidal current amplitudes $|\hat{u}|$ decrease over X_1 but exhibit a rapid amplification over X_2, followed by an attenuation further up-estuary (Figure 5.5c). The consistently smaller current velocity amplitudes along X_1 are a key effect of the shorter depth transition, which reduces the amount of tidal energy available for mixing of the salinity field.

The observed amplitude evolution cannot be explained by a balance between friction and convergence acting on the incident wave (Savenije 2006; Friedrichs 2010; Rijn 2011). The same applies to the phase difference between the vertical and horizontal tides, arg($\hat{\eta}$) − arg($\hat{Q}$) (Figure 5.5d). Along X_1, the phase difference is approximately 40°, close to the maximum velocity phase lag of 45° that can arise from frictional effects alone (Friedrichs 2010). This occurs despite the fact that frictional effects are weak, as indicated by the low non-dimensional friction coefficient ($r/\omega < 1$) (Friedrichs 2010). Furthermore, along X_2, the phase difference decreases and reaches a minimum at the end of the depth transition, even though depth convergence typically increases the phase lead (Friedrichs 2010).

To investigate whether the amplitude and phase evolutions can be explained by (partial) wave reflection due to the step in the channel depth, the observed amplitudes are decom-

posed into the contribution of the incident (dashed lines) and reflected wave (dotted lines), using Eqs. 5.3 to 5.7. Based on this, we identify two main regions where partial wave reflection occurs: (1) at the depth transition along X_2 and (2) toward the end of the model domain, where the bed-level exceeds mean sea level and tides rapidly attenuate (Kästner et al. 2019). These regions are clearly visible by an increase in the reflection ratio $\gamma = |\hat{\eta}^-|/|\hat{\eta}^+|$ (Figure 5.5e). The decay of the amplitudes in the direction of propagation for both incident and reflected waves are in line with expected influence of friction and depth convergence. The incident wave shows decaying amplitude over X_1 due to frictional effects, whereas the amplitude increases due to shoaling over X_2. The stronger reduction in the velocity amplitude observed for $i_{z_b} = 2$ m km^{-1} can be explained using Eq. 5.8. According to this equation, the resulting current amplitude $|\hat{u}|$ reaches its minimum when $\Theta = 0$ and $\gamma = 1$ (see Figure B.1). Both the difference in Θ and in γ contribute to a reduction of $|\hat{u}|$ along X_1 in the case of a bed slope $i_{z_b} = 2$ m km^{-1}, compared to the simulation with $i_{z_b} = 0.5$ m km^{-1} (Figure 5.2 panel c,e,f). Hence, the reduced along-channel current amplitude with steeper bed slope is attributed to stronger wave reflection. The observed minimum in $\arg(\hat{\eta}) - \arg(\hat{Q})$ can be explained using Eq. 5.9. Figure 5.5 panel d shows that the phase difference of the incoming wave is smallest over X_1, increasing in the shallower up-estuary regions due to enhanced frictional effects (i.e., the first term on the RHS of Eq. 5.9). The much larger phase difference along X_1 for the observed wave results from the combined effect of both incoming and reflected waves (contribution of the second term on the RHS of Eq. 5.9). Furthermore, the observed minimum at X_2 arises because along X_1, the reflected wave enhances the phase difference, whereas along X_2, with reduced reflection, the friction-driven phase difference becomes dominant.

It is worth noting that baroclinic effects have a substantial influence on barotropic tidal behaviour. Model simulations without salinity did not yield an amplification of tidal elevation along X_1. This difference compared to the simulations presented here can be attributed to the strong reduction in friction caused by vertical stratification, which suppresses turbulence. To further substantiate this, we calculated an effective Chézy coefficient, C_{eff}, from the momentum budgets following Bo and Ralston (2020). Our estimates yielded $C_{eff} \approx 75$ m$^{1/2}$ s^{-1} over X_1, where the water column is vertically stratified, whereas up-estuary, in the absence of salinity, the values were equal to the Chézy value of 65 m$^{1/2}$ s^{-1} used to describe friction. The estimates of C_{eff} were also used to determine the linearized friction coefficient r (Eq. 5.6) and were applied in the decomposition of the incoming and reflected wave components. We therefore attribute the tidal elevation amplification in the simulations with salt to the additional effect of the abrupt change in effective roughness at the depth transition, which induces additional wave reflection.

5.3.2.2 Impact on the Internal Currents

A harmonic analysis of the internal currents was performed to investigate the vertical current structure under influence of bed-slope inclination (Figure 5.6).

The results for the zero-frequency component (Panel a), clearly show that the steeper bed slope produces a stronger circulation just down-estuary of the depth transition, where the frontal zone develops. The presence of this front is also reflected in the phase and amplitude of the tidal constituents, with the u_2 constituent exhibiting locally reduced amplitudes near the surface (Panel c). In contrast, the u_4 component shows a local increase near the toe of the depth transition. We attribute this enhanced quarter-diurnal component primarily to frontal dynamics (Panel e).

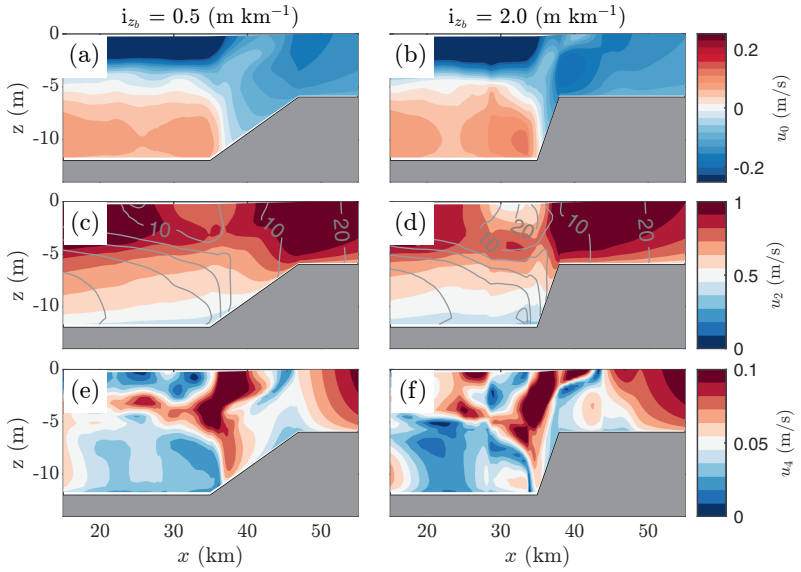


Figure 5.6: Tidal analysis of the internal currents. (a–b) Zero-frequency (residual) component, indicated by the subscript $_0$. (c–d) Amplitude of the semi-diurnal component, indicated by the subscript $_2$, with contour lines showing the phase. (e–f) Same as panels (c–d), but for the quarter-diurnal component, indicated by the subscript $_4$. Phase contour lines are omitted for readability.

5.3.3 Analysis of salt transport mechanisms

5.3.3.1 Along channel salinity gradient, stratification and tidal salinity range

Panels a and b in Figure 5.7 illustrate the general along-channel characteristics of the modelled salinity field for the two simulations. In both cases, the along-channel distribution of the tidally averaged salinity (s_0) shows a marked rapid decrease in the salinity upstream of X_1. This sharp decline implies a large along-channel salinity gradient and is accompanied by an increase in the tidal range of the depth-averaged salinity (s_R), as indicated by the grey shading. These effects are most pronounced in the simulation with the steeper bed slope ($i_{z_b} = 2$ m km^{-1}). Notably, a localized increase in stratification Δs is seen in this case where the front forms, whereas this is less clearly observed for the gentler bed slope ($i_{z_b} = 0.5$ m km^{-1}).

5.3.3.2 Subtidal salt transport contributions

The subtidal salt-transport contributions shown in Panels c and d of Figure 5.7 (computed using Eq. 5.11) clearly demonstrate that, in both simulations, up-estuary salt transport is dominated by the steady vertically sheared component ($F_{s,s}$) up to the depth transition. Its contribution decreases rapidly in the shallower regions. The contribution related to the correlation between tide-varying flow and salinity fields ($F_{s,v}$) is small and generally negative, except near the mouth, where this is likely an artifact of the seaward boundary condition. Between the upstream extent of X_1 and the salt intrusion limit, the tidal oscillatory salt transport (F_t) becomes the dominant salt transport, particularly in the simulation with the steeper bed slope ($i_{z_b} = 2.0$ m km^{-1}).

A key difference between the two simulations is the pronounced along-channel vari-

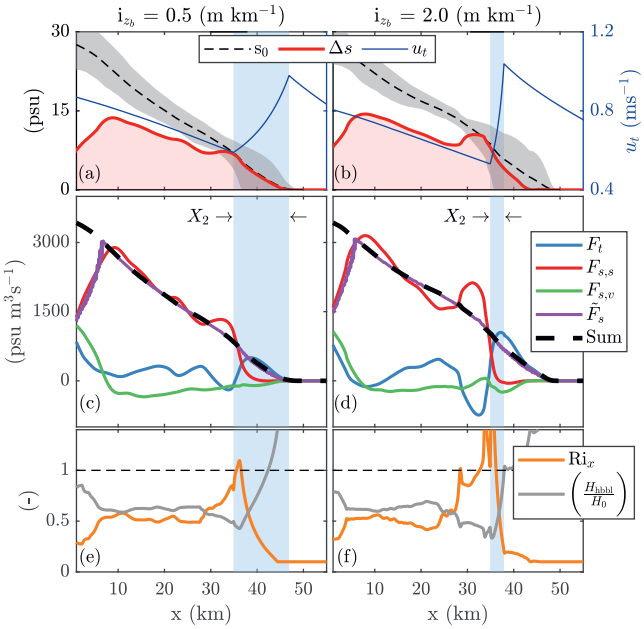


Figure 5.7: Comparison of the subtidal salt transport contributions for a gradual bed-slope inclination ($i_{z_b} = 0.5$ m km^{-1}) and a steep bed-slope inclination ($i_{z_b} = 2.0$ m km^{-1}). (a-b) Tidal-averaged salinity s_0 and the tidal salinity range (grey shading), the top-to-bottom salinity stratification Δs, and depth-averaged flow velocity amplitude u_t. (c–d) Decomposition of the subtidal salt transport showing the Eulerian tidal-oscillatory contribution (F_t), the steady-shear component ($F_{s,s}$), and the time-varying shear component ($F_{s,v}$), together with the quasi-Lagrangian total shear observed along a moving plane (see Section 5.2.3). (e-f) Horizontal Richardson number (Simpson number), calculated using a drag coefficient $c_d = g/C^2$, and the approximate normalized bottom-boundary layer height. The blue shading indicate the extent of the depth transition region X_2.

ability in both $F_{s,s}$ and the corresponding, mirrored variations in F_t for the case with $i_{z_b} = 2$ m km^{-1}. The most notable contrast occurs just down-estuary of the depth transition X_2, where the front forms. Here, a localized increase in $F_{s,s}$ is accompanied by a corresponding decrease in F_t. This local enhancement in $F_{s,s}$ coincides with the observed increase in Δs and a strengthening of the residual circulation (Figure 5.6). Further down-estuary, $F_{s,s}$ gradually decreases, which is mirrored by an increase in the magnitude of F_t. The relationship between $F_{s,s}$ and F_t is examined further in Section 5.3.3.3, where the increase in F_t is linked to the front-induced enhancement of $F_{s,s}$. Before addressing this interaction, we first assess the variability in $F_{s,s}$ in terms of the horizontal Richardson number.

The strength of estuarine circulation scales with the horizontal Richardson number (Burchard and Hetland 2010), defined as

$$Ri_x = \frac{\beta g \frac{\partial s_0}{\partial x} H^2}{c_d U_t^2}, \tag{5.17}$$

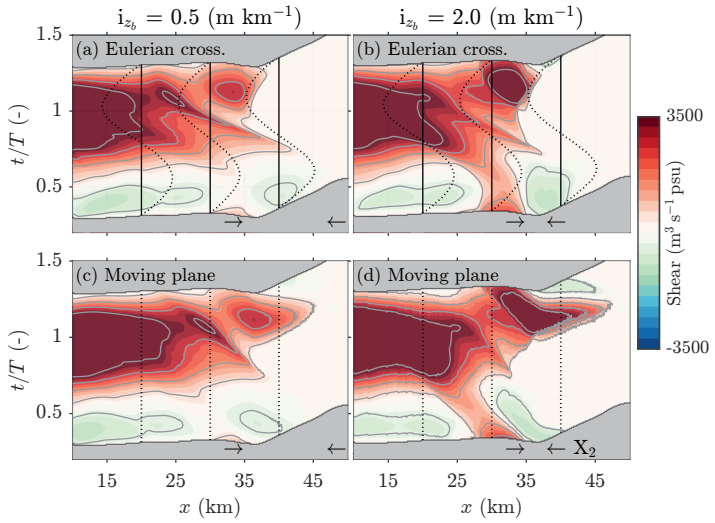


Figure 5.8: Overview of instantaneous shear salt transport observed at a fixed Eulerian cross-section and along a moving plane. (a–b) Shear at the Eulerian cross-section for simulations with sharp and mild bed inclinations. Dotted lines indicate the trajectory of the moving plane. (c–d) Shear transposed along the moving plane; the distance represents the reference coordinate.

which represents the ratio of the horizontal baroclinic pressure gradient driving the exchange flow to the turbulent mixing that opposes it (Simpson and Brown, et al. 1990; Stacey and Burau, et al. 2001). For small values of Ri_x, the kinetic energy associated with turbulence dominates over the stabilizing influence of vertical straining (Geyer and MacCready 2014). Permanent stratification typically occurs when $Ri_x \sim 0.2$ (Stacey and Ralston 2005). Stacey and Ralston (2005) showed that the normalised height of the bottom boundary layer (H_{bbl}) in a stratified water column is given by:

$$\frac{H_{\mathrm{bbl}}}{H} = \left(\frac{Ri_{cr}}{Ri_x}\right)^{\frac{1}{2}}, \tag{5.18}$$

where Ri_{cr} is the critical Richardson number taken here taken as 0.2 (Ralston and Stacey 2005).

Panels e and f indicate that the spatial variability in $F_{s,s}$ is closely reflected in the distribution of Ri_x. Since Ri_x is computed using a drag coefficient $c_d = g/C^2$ based on the prescribed Chézy value, its spatial variability primarily arises from changes in the tidal velocity amplitude U_t and the along-channel salinity gradient $\partial s_0/\partial x$. This suggests that variations in $F_{s,s}$ are predominantly linked to spatial variability in the along-channel salinity gradient, which drives the horizontal baroclinic pressure gradient, and to the monotonous decrease in U_t over X_1. In these experiments, the onset of frontal formation corresponds to locations where the horizontal Richardson number Ri_x locally exceeds unity. Note that an increase in Ri_x corresponds to a reduction in bottom boundary layer thickness immediately downstream of the depth transition. This is consistent with the observed local lowering of the mid-column jet (see Figure 5.4f), whose position is largely governed by the vertical extent of the bottom boundary layer (Nijs et al. 2011).

5.3.3.3 The tidal oscillatory salt transport

In section 5.3.3.2, an increase in F_t toward the intrusion limit was observed, which was more pronounced for $i_{z_b} = 2.0$ m km^{-1}, along with a clear negative spatial correlation with $F_{s,s}$

over X_1. The tidal-oscillatory transport at a fixed cross-section under quasi-steady-state conditions can be expressed as, $F_t = \tilde{F}_s - F_s$ and therefore depends on the spatio-temporal variability of the shear related transport contributions (Dronkers and Van de Kreeke 1986) (see also Section 5.3.3.2). The relationship between the instantaneous shear contribution in both reference frames is discussed below to examine these two aforementioned aspects in more detail.

Panels a and b of Figure 5.8 show that, for both bed configurations, the Eulerian instantaneous vertically sheared salt transport remains positive throughout the ebb and reaches a maximum near low-water slack. For the simulation with $i_{z_b} = 2$ m km^{-1}, the formation of a frontal zone toward low water slack is clearly visible by a local increase in the instantaneous salt transport near at the down-estuary side of the depth transition. During flood, the transport due to vertically shear is mostly negative due to the negative straining of the salinity field (Simpson and Brown, et al. 1990), as expected. However, in the simulation with $i_{z_b} = 2$ m km^{-1}, the flux remains positive throughout the flood period in the frontal region. This can be explained by the fact that front formation enhances the top-to-bottom salinity difference and lowers the vertical position of the pycnocline (Figure 5.7a,b). The vertical flow structure during flood is characterized by a mid column jet, whose height is largely controlled by the relative thickness of the bottom boundary layer that is locally lowered due to front formation. This effect is also reflected in the estimated tide-averaged relative boundary layer height, H_{bbl}/H (Figure 5.7f). The combination of peak currents occurring lower in the water column and enhanced top-bottom stratification enables a persistent positive shear flux, which, on a tide-averaged timescale, is reflected in an increase in $F_{s,s}$.

Panels c and d in Figure 5.8 show the instantaneous shear contribution observed along the moving planes, whose trajectories are indicated by the dotted lines in Panel a and b. For the cross-sections located upstream of the depth transition, it can be seen that the moving plane experiences substantial exchange through shear when it passes through the deeper part of the estuary on its way toward low-water slack. By contrast, the corresponding Eulerian cross-section, fixed in the shallower region, shows almost no shear related transport. For the simulation with $i_{z_b} = 2$ m km^{-1}, the difference between the shear contribution in the moving-plane framework and that in the Eulerian reference frame are most pronounced and arises from the frontal dynamics. This imbalance gives rise to the observed increase in the tidal oscillatory contribution upstream of the depth transition. Similarly, the spatial correlation between F_t and $F_{s,s}$ can be explained by local enhancement of shear due to intensified estuarine circulation. As a consequence of this exchange, the exchange flux is reduced either up- or down-estuary. Since these variations occur over distances comparable to the tidal excursion length, the moving planes either pass through these regions or largely avoid them.

5.3.4 Analysis of front formation due to depth transitions

5.3.4.1 Establishment of a lift of point

In Section 5.3.1, we showed that a steeper bed-slope between dredged and undredged sections can induce the formation of a front. Here we examine the presence of geometry-induced lift-off points by evaluating the composite Froude number (Armi 1986; Largier 1992; Geyer and Ralston 2015; Horner-Devine et al. 2015), defined as:

$$G = \left(\frac{u_1^2}{g' h_1} + \frac{u_2^2}{g' h_2} \right)^{1/2}, \tag{5.19}$$

where $g' = g\,\Delta\rho/\rho$ is the reduced gravity, u_1 and u_2 are the layer-averaged velocities, and h_1 and h_2 denote the depths of the upper and lower layers, respectively. A lift-off point is identified where the upper layer occupies the entire water column and the flow reaches critical conditions $\left(\frac{u_1^2}{g' h_1} \right)^{1/2} = 1$, with supercritical flow occurring both up- and

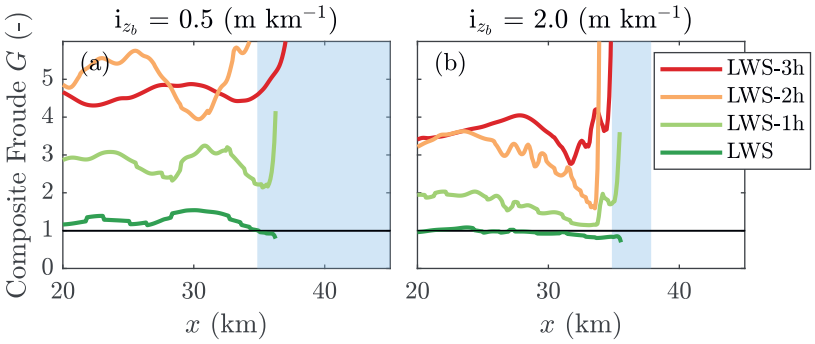


Figure 5.9: Comparison of the composite Froude number G from peak ebb (LWS–3 h) to low-water slack (LWS). (a) Mild bed slope at depth transition, $i_{z_b} = 0.5$ m km^{-1}. (b) Steep bed slope at depth transition, $i_{z_b} = 2.0$ m km^{-1}.

down-estuary from this location (Geyer and Ralston 2015; Horner-Devine et al. 2015).

Figure 5.9 shows the composite Froude number for the two cases between peak ebb and low-water slack. In the simulation with the steeper bed slope ($i_{z_b} = 2$ m km^{-1}), a distinct local minimum in G develops at the toe of the slope, approaching critical conditions ($G \approx 1$) approximately 1.5 h before slack water (Fig. 5.9b). This locally early and prolonged approach to criticality is consistent with observed near-bed flow convergence and indicates the development of a local hydraulic control. In contrast, for the weaker bed slope ($i_{z_b} = 0.5$ m km^{-1}), no comparable local minimum in G is observed; near-critical conditions are reached only at slack water, and no persistent hydraulic control develops (Fig. 5.9a). The formation of a front over the steeper slope is therefore consistent with the theory of topographically induced fronts described by Armi (1986) and Largier (1992). For the milder slope, stronger tidal velocities and a lower reduced gravity increase the theoretical critical depth for lift-off, $h_{1,c} = u_1^2/g'$, such that the flow does not attain hydraulic control at the slope, inhibiting front formation.

5.3.4.2 Intensification of the Along-channel Salinity Gradient

The previous section shows that a sufficiently steep bed slope produces dynamics consistent with a topographically induced lift-off point (Armi 1986), a mechanism that does not require the initial density non-uniformity assumed in the frontogenesis framework of Simpson and Linden (1989). Here, we examine the tidal variability of the depth-averaged along-channel salinity gradient. We begin with the one-dimensional salt storage equation:

$$\frac{\partial\left(\bar{s}A\right)}{\partial t} + \frac{\partial\left(\bar{s}\bar{u}A\right)}{\partial x} + \frac{\partial\left(\overline{u_v' s_v'} A\right)}{\partial x} = 0. \tag{5.20}$$

Equation 5.20 can be rewritten to derive an expression for the evolution of the depth-averaged along-channel salinity gradient by taking the along-channel derivative, yielding:

$$\frac{\partial}{\partial t}\frac{\partial \bar{s}}{\partial x} + \bar{u}\frac{\partial^2 \bar{s}}{\partial x^2} + \frac{\partial \bar{u}}{\partial x}\frac{\partial \bar{s}}{\partial x} + \frac{\partial}{\partial x}\left(\frac{1}{A}\frac{\partial}{\partial x}\left(\overline{u_v' s_v'} A\right)\right) = 0. \tag{5.21}$$

The four terms in Eq. 5.21 represent, respectively, the local tendency of the depth-averaged salinity gradient, advection of existing gradients, generation of gradients by convergence of the depth-averaged velocity, and sharpening of the gradient due to the divergence of vertically sheared salt flux.

Figures 5.10 and 5.11 illustrate the tidal variability of the along-channel salinity gradient, top and bottom salinities, and the associated gradient-generation terms for both

simulations. In both cases, the strongest gradients occur near the tidally varying salt intrusion limit, with several distinct intensification events. For the steep bed slope ($i_{z_b} = 2.0$ m km^{-1}), two periods of intensification occur. The first (indicated by 2) develops shortly after peak ebb, initiating a new local maximum in $\frac{\partial s}{\partial x}$ consistent with a lift-off–induced stagnation point (Section 5.3.4.1). The second (indicated by 3) occurs near low-water slack and amplifies a pre-existing maximum. Both intensifications are driven primarily by local maxima in the vertically sheared salt flux (panel c in Figure 5.10), with convergence of the depth-averaged flow playing a secondary role (panel d). The two intensifications merge during the onset of flood, contributing to the maximum near the salt intrusion limit. For the milder bed slope ($i_{z_b} = 0.5$ m km^{-1}), two gradient intensifications occur after high-water slack. The first (indicated by 1) develops during early ebb due to a local maximum in the vertically sheared salt flux (panel c in Figure 5.11), while the second (indicated by 3) represents amplification of a pre-existing gradient, similar to the sharp-slope case. No lift-off–induced intensification is observed, and convergence of the depth-averaged flow does not contribute to gradient maxima (panel d in Figure 5.11).

Thus, for the steeper bed slope, both lift-off–induced dynamics and the straining-driven amplification of existing salinity gradients contribute to frontogenesis and local maxima near the salt intrusion limit. For the milder bed slope, only amplification of pre-existing gradients is significant.

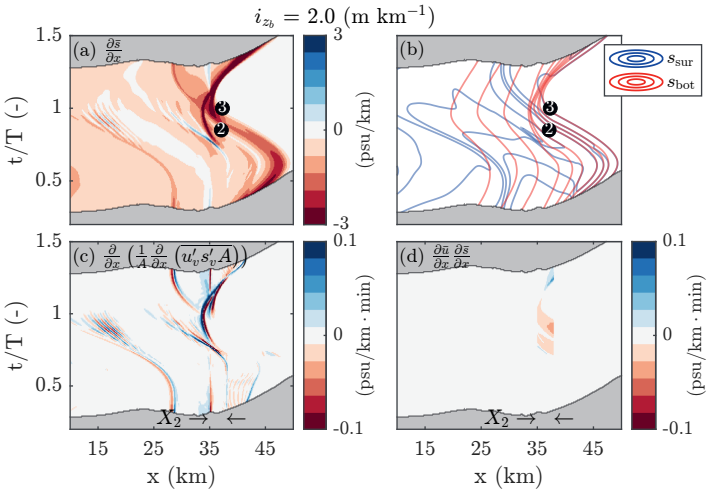


Figure 5.10: Sharpening and weakening of the along-channel salinity gradient in the simulation with $i_{z_b} = 2.0$ m km^{-1}. (a) Spatio-temporal evolution of the depth-averaged along-channel salinity gradient. The numbered markers indicate different moments in time when the gradient weakens or sharpens. (b) Contour plot of surface and bottom isohalines illustrating the changes in $\frac{\partial \bar{s}}{\partial x}$. (c) Sharpening and weakening of the along-channel gradient associated with convergence and divergence in the gradient of the vertically sheared salt flux (see Eq. 5.21). (d) Sharpening and weakening of the along-channel gradient associated with convergence or divergence in the depth-averaged along-channel current (see Eq. 5.21).

5.3.4.3 Analysis using the Salinity Variance balance

To gain insight into the conversion of the horizontal salinity gradient (Eq. 5.15) into vertical salinity variations (Eq. 5.14) in the frontal region, we analyse the salinity-variance balance

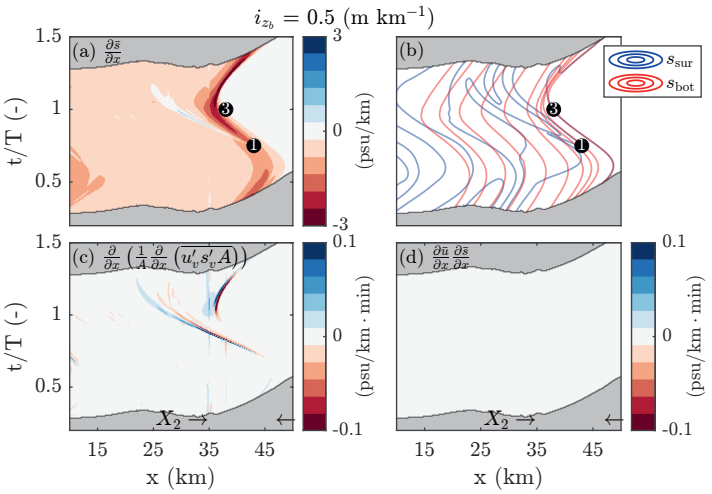


Figure 5.11: Same as Figure 5.10, but for $i_{z_b} = 0.5$ m km^{-1}.

for a control volume between 30 and 38 km near the toe of the bed slope (Figure 5.12). Panels a and b in Figure 5.12 compare the cross-sectionally averaged salinity gradient, $\frac{\partial \bar{s}}{\partial x}$, over one tidal cycle. High-water slack (HWS) is taken as the reference time. From the temporal along-channel gradient, it is seen that in the case with the mild bed slope a single maximum develops, which intensifies during the ebb, whereas in the case with the steep bed slope two marked peaks in develop as discussed in Section 5.3.4.2.

Panels c and d in Figure 5.12 show the change in the horizontal variance of the control volume in the frontal region. In both cases, changes in horizontal variance are minimal during first half of the ebb phase, but begin to increase in the second half, as the region with the existing salinity gradients reaches the control volume (also see panels a and b). The import of horizontal variance into the control volume (this occurs through advection over the boundaries of the control volume) is substantially larger for the simulation with $i_{z_b} = 2.0$ m km^{-1}. The conversion from horizontal to vertical variance occurs through straining of the velocity field (panels e and f in Figure 5.12). In both cases, this conversion occurs around the low-water slack (LWS). Thus, while both systems exhibit straining-driven variance conversion near LWS, the sharp bed slope produces a markedly stronger and more sustained response, consistent with its more intense frontal dynamics.

5.4 Discussion

5.4.1 Comparison with observations in the Rotterdam Waterway

The model results presented in Section 5.3 showed that a steeper bed-slope inclination can initiate the formation of freshwater plumes and strongly alter the estuarine dynamics. To assess whether these dynamics also occur in reality, we compare our model results with observations from the Rotterdam Waterway. In this system, the bed profile consists of several individual steps that together yield an overall slope of $i_{z_b} = 0.8$ m km^{-1}. The most upstream step has a local slope of $i_{z_b} = 2.1$ m km^{-1}, which is sufficiently sharp to generate a lift-off point that allows the development of a freshwater plume. Consistent with the model results, observational data collected by Wegman et al. (2025) during the 2022 drought reveal a freshwater plume located at this geometric step (near km 30), visible around high water (Figure 5.13).

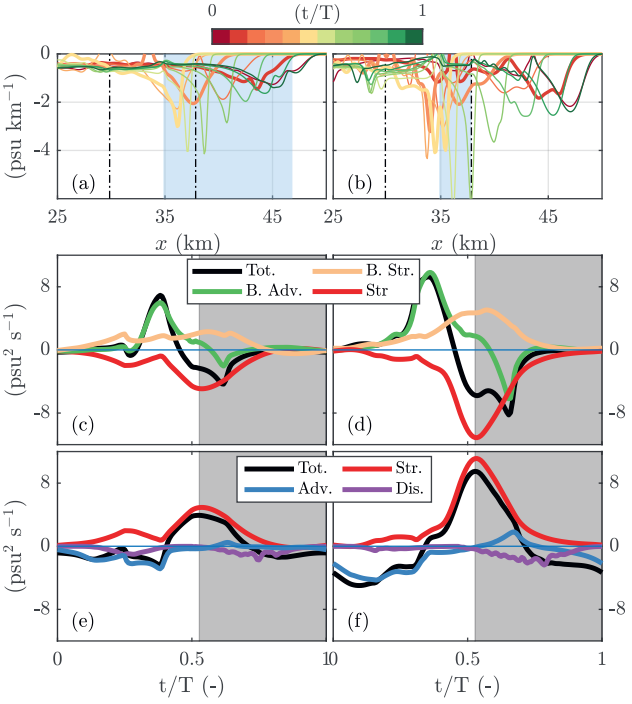


Figure 5.12: Comparison of horizontal variance and its conversion to vertical variance for sharp and mild bed-slope at the depth transition zone. (a–b) Evolution of the along-channel gradient of the cross-sectionally averaged salinity over one tidal cycle, with high water slack (HWS) taken as the reference time. (c–d) Horizontal salinity variance balance. (e–f) Vertical salinity variance balance.

The location where the plume is observed also contains several harbors, which were examined in Chapter 4. These harbors could, in principle, provide an alternative explanation for the observed plume through tidal trapping (Garcia and Geyer and Randall 2022; Corlett and Geyer 2020). However, Chapter 4 showed that these harbors predominantly exchange salt with the main channel through density currents, while the contribution of advective out-of-phase exchange is minimal. This vertically sheared exchange mechanism typically drives a net salt transport into the harbor during high-water slack (HWS), whereas near low-water slack (LWS) it drives a vertically sheared transport toward the main channel. Additional transects (not published, but collected in the context of research by Wegman et al. (2025), show that the lifft-of point like structure develops near LWS, consistent with the mechanism proposed here. At LWS, the typical exchange flow is a density current directed toward the main channel, with surface flow entering the harbor. Therefore, the observed front cannot be explained by harbor-trapped water being released later in the tidal cycle. Hence, these observations provide evidence that plume formation associated with steeper bed-slope steps indeed occurs in reality.

5.4.2 Position of the depth transition relative to the resonance length

The importance of the estuary length scale (i.e., the effective length of the full reflector) relative to the tidal resonance length has been highlighted by Wei and Williams, et al.

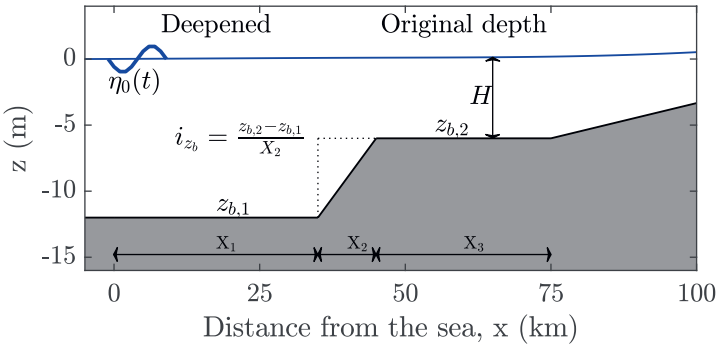


Figure 5.13: Observation of the salinity field in the Rotterdam Waterway near high water. (a) Map showing an overview of the Rotterdam Waterway and the location of the transect shown in panel b. (b) Observations by Wegman et al. (2025) of the salinity structure near depth transitions (see also panels a and b in Figure 5.1), revealing the formation of a low-salinity surface front in the New Meuse section of the Rotterdam Waterway.

(2022) and Figueroa et al. (2022). In the numerical experiments presented earlier, the position of the depth transition was fixed at 35 km from the mouth, a distance comparable to observations in several estuaries (Figure 5.1).

To explore the importance of the along channel position of the depth transition, we use a semi-numerical model following the theory of Dronkers (1964) to compute tidal elevation and velocity (Figure 5.14). Panel a shows the normalized along-channel tidal elevation amplitudes for the relatively steep bed-slope ($i_{z_b} = 2.0\ \mathrm{m\,km^{-1}}$) for different positions of the depth transition. When the depth transition is located near the resonant quarter-wavelength, the velocity amplitudes reach their maximum near the mouth (Panels b). Next, the difference compared to the case with a mild bed-slope ($i_{z_b} = 0.5\ \mathrm{m\,km^{-1}}$) was calculated. The largest discrepancies in the tidal elevation amplitudes $\Delta|\hat{\eta}|$ between the two channel-bed configurations also occur near the depth transition when its position is at the resonant quarter-wavelength (Panels c). The pattern in the relative velocity amplitude differences $\Delta|\hat{u}|$ is, however, more complex and shows relative lower currents for the steeper bed-slope inclination when the depth transition is at $X_1/\Lambda_0 \lesssim 1/4$, but yields larger velocity amplitudes when exceed this position (Panels d).

The behaviour of the relative velocity amplitudes can be understood from the phase difference Θ between the incoming and reflected tidal waves. For both bed-slope configurations, Θ follows nearly the same trajectory because it is primarily determined by (1) the phase shift accumulated during the round trip of the incident and reflected waves and (2) the reflection strength at the toe. As the distance between the toe and the estuary mouth approaches the resonant quarter-wavelength, constructive interference enhances the velocity amplitudes near the mouth. However, the sharp bed-slope introduces a small offset in Θ at the toe due to its stronger reflection. This offset shifts the locations of constructive and destructive interference slightly between the two bathymetries. Consequently, the steep bed-slope yields weaker velocity amplitudes when the depth transition is located at $X_1/\Lambda_0 \lesssim 1/4$, but produces slightly stronger near-mouth currents once the transition lies beyond the quarter-wavelength, approximately within $1/4 \lesssim X_1/\Lambda_0 \lesssim 1/2$, due to the small phase shift in the interference pattern. Also see Figure B.1 for the trajectories through the (Θ, γ)-plane for depth transitions located at $X_1/\Lambda_0 = \frac{1}{8}$ and $X_1/\Lambda_0 = \frac{3}{8}$. Thus, a steeper slope reduces the current amplitudes over the entire deepened section when $X_1/\Lambda_0 \lesssim 1/4$, but produces higher velocities over the region$x/\Lambda_0 \lesssim 1/4$ once the

distance to the toe exceeds the resonance length.

Overall, assuming that exchange over X_1 is dominated by steady, vertically sheared salt transport driven by gravitational circulation, these results imply a clear and general pattern. When the distance to the toe of the depth transition is shorter than the resonant quarter-wavelength ($X_1/\Lambda_0 \lesssim 1/4$), a steeper bed-slope consistently weakens the tidal velocities throughout the deepened section. Weaker tidal currents reduce vertical mixing and thereby strengthen gravitational circulation, leading to enhanced up-estuary salt transport. The numerical experiments presented in Section 5.3 fall within this regime. In contrast, once the distance to the toe exceeds the resonant quarter-wavelength ($X_1/\Lambda_0 \gtrsim 1/4$), the system approaches a resonant response. In this regime, the steep bed-slope can produce larger near-mouth velocities than the mild slope. The resulting increase in vertical mixing reduces the salt transport driven by gravitational circulation and can therefore potentially limit the SIL.

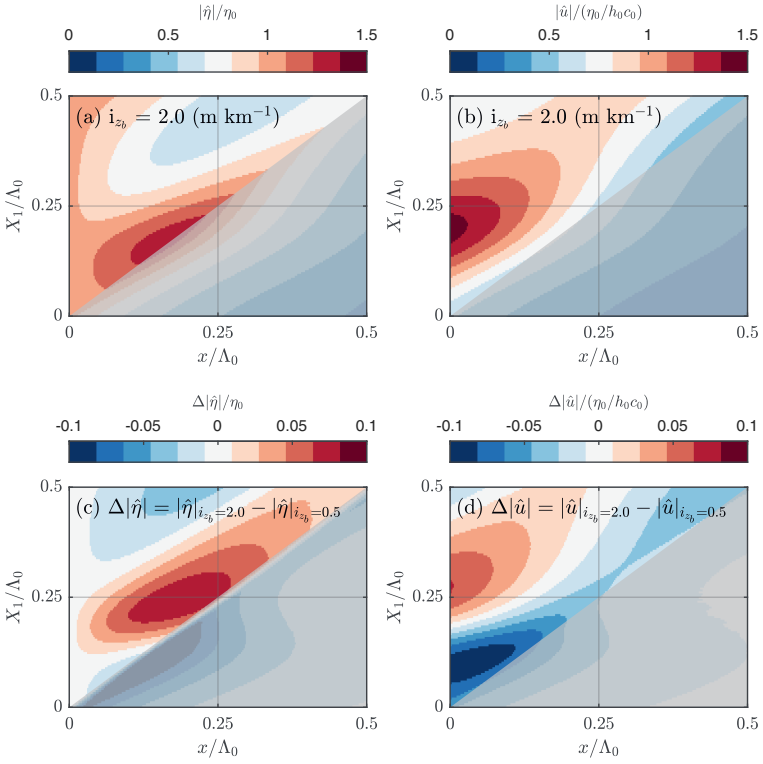


Figure 5.14: Influence of the position of the depth-transition area on the tidal dynamics for bathymetries with a steep bed-slope inclination ($i_{z_b} = 2.0$ m km^{-1}) and a relatively mild bed-slope inclination ($i_{z_b} = 0.5$ m km^{-1}), investigated by varying the length of X_1. (a) Modelled tidal elevation amplitudes for the steep bed-slope. (b) Corresponding tidal current amplitudes for the steep bed-slope. (c) Difference in tidal elevation amplitudes relative to the mild bed-slope case, $\Delta|\hat{\eta}|$. (d) Same as (c), but for the difference in tidal current amplitudes, $\Delta|\hat{u}|$. For all panels, the along-channel distances are normalized by the tidal wavelength at the mouth, Λ_0.

5.4.3 How depth transitions enhance tidal dispersion

The results show that a staircase-like bathymetry with a steeper bed slope can enhance salt intrusion in estuaries that fall within the SIPS or partially stratified classification regime of Geyer and MacCready (2014), even when the estuary as a whole becomes shallower (Figure 5.3).

Figure 5.15 presents a conceptual summary of the dynamics that lead to an increase in the SIL when the bed slope becomes steeper for the systems classified as SIPS and partially stratified estuaries (Geyer and MacCready 2014), see Table 5.2. Part of this increase results from weaker tidal currents caused by enhanced wave reflection when the depth transition is located below the quarter-wavelength resonance length (Figure 5.3 panel a,b; Sections 5.3.2 and 5.4.2), which strengthens estuarine circulation. This effect increases the SIL for all tested forcing conditions and estuary classes. At the same time, the abrupt depth transition prevents the salt intrusion from adjusting smoothly because the transport capacity drops sharply at the step. This reduction in transport capacity generates a pronounced along-channel salinity gradient. On an intertidal timescale, the barotropic forcing acts on this salinity field, setting the stage for the frontal dynamics described in Section 5.3.4. A steeper bed-slope inclination promotes the development of an intense along-channel salinity gradient at the toe of the depth transition toward the low-water slack (panel c,d in Figure 5.15). As discussed in Section 5.3.4, this maximum arises from two mechanisms: a stagnation point in the velocity field associated with a lift-off point (Armi 1986; MacDonald and Geyer 2005; Horner-Devine et al. 2015), and a persistent along-channel salinity gradient near the tidally varying salt-intrusion limit, which intensifies toward slack water due to enhanced vertical straining enabled by increased depth and reduced vertical mixing (Simpson and Linden 1989; Simpson and Brown, et al. 1990). During slack water, the detached dense layer spreads landward as a gravity current, and during the subsequent flood, saline water plunges beneath the overlying fresher water, forming a tidal intrusion front (Armi 1986; Largier 1992).

These frontal dynamics generate enhanced vertically sheared salt exchange at the toe of the bed slope. Because the salinity of the water expelled during ebb differs from the salinity of the water advected landward during the following flood (Figure 5.15e,f), a flood–ebb asymmetry develops. This asymmetry introduces a phase shift in the salinity signal and produces a substantial tidal-oscillatory salt flux. This tidal-dispersion mechanism resembles the flood–ebb asymmetries associated with jet–sink exchange near estuarine mouths (Stommel and Farmer 1952; Chen and Geyer, et al. 2012) and with frontal dynamics in mouth regions (MacDonald and Geyer 2005; Li and Geyer, et al. 2018; Garcia and Geyer and Randall 2022). A key distinction, however, is that for the mouth region the exchange ratio is primarily set by the contrast between the jet-like ebb outflow and the semi-circular inflow pattern (Chen and Geyer, et al. 2012). For the bathymetric steps within the estuary, by contrast, the exchange is governed by the intensity of the vertically sheared exchange flow that develops near the toe of the bed-slope.

The frontal dynamics described in the preceding section occur consistently across all tidal-forcing conditions, and thus across all estuary classes considered (see Table 5.2). However, in the strongly stratified cases the relative sharper bed-slope inclination does not lead to an increase in the SIL. We mainly attribute this to the fact that, in the strongly stratified cases, the tidal excursion length is substantially shorter. The reduced excursion limits the horizontal scale over which exchange can occur, thereby preventing the front-induced enhancement of estuarine circulation from increasing the intrusion length.

5.4.4 Spring–Neap Variability of the SIL

In partially stratified estuaries, the estuarine exchange flow, vertical stratification, and salt intrusion length (SIL) typically vary over the spring–neap cycle (Geyer and Trowbridge, et al. 2000; Lerczak and Geyer and Ralston 2009; Hetland and Geyer 2004). Such variability of the SIL has not been reported for the Rotterdam Waterway (Wegman et al. 2025), a system characterized by a stepped bathymetry (Figure 5.1). To examine whether

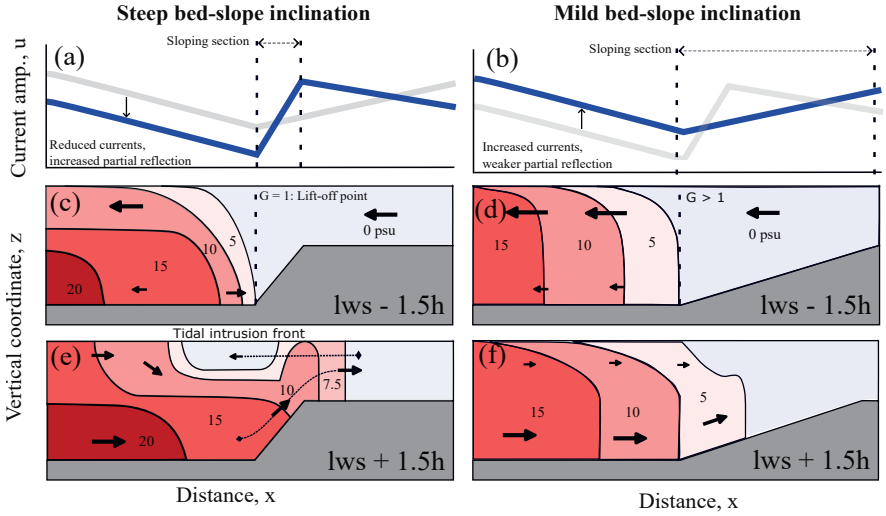


Figure 5.15: Conceptualization of the process responsible for the tidal salt flux observed upstream of the depth transition. For both cases, it is assumed that the deep and straight section is shorter than one-quarter of the tidal wavelength. (a–b) Schematic representation of the along-channel velocity amplitude. (c-d) Situation at LWS–1.5 h: frontal formation occurs near the depth transition, enhancing local exchange. (e-f) Situation at LWS+1.5 h: due to this exchange, relatively saline water is transported upslope, introducing an flood-ebb asymmetry in the salinity concentration.

the steepness of the bed-slope transitions modulates the spring-neap variability, both bed-slope configurations are forced with an M_2-S_2 tidal signal (elevation amplitudes of 1.00 m and 0.25 m at the mouth). The resulting model behaviour is summarized in Figure 5.16.

For the mild bed slope ($i_{z_b} = 0.5\ \mathrm{m\,km^{-1}}$), the salt intrusion length (L_s) exhibits a clear spring-neap modulation (Figure 5.16f). The system never fully adjusts to the tidal forcing, as evidenced by the minimum and maximum values of L_s lagging behind spring and neap tides, respectively. This spring-neap variability reflects the classical response described by (MacCready 1999). During the transition from spring to neap, the SIL is shortest, producing a strong along-channel salinity gradient. Combined with the reduced currents toward neap, this promotes enhanced stratification and increases the steady vertically sheared salt transport $F_{s,s}$ (Figure 5.16g). Consequently, the SIL lengthens, the along-channel salinity gradient relaxes, and straining weakens. However, as tidal forcing strengthens again after neap tide, stratification rapidly collapses and the SIL shortens toward spring tide.

For the sharp bed slope ($i_{z_b} = 2.0\ \mathrm{m\,km^{-1}}$), the SIL shows much weaker spring-neap variability (Figure 5.16c), even though the total salt storage still varies substantially (Figure 5.16b). The qualitative sequence is similar to the mild-slope case, with the strongest stratification and largest $F_{s,s}$ just after neap, followed by an increase in the SIL towards neap, but the steeper depth transition constrains the SIL's tendency to adjust. Consequently, stratification relaxes less effectively (Chant et al. 2018; Ralston and Geyer 2019), and a persistent, sharp along-channel salinity gradient develops near the depth transition. After neap, the tide-averaged straining near the toe of the slope intensifies, contributing to both $F_{s,s}$ and the tidal oscillatory transport F_t upstream of the slope (Figure 5.16d,e). This behaviour is explained by the increased barotropic forcing, which

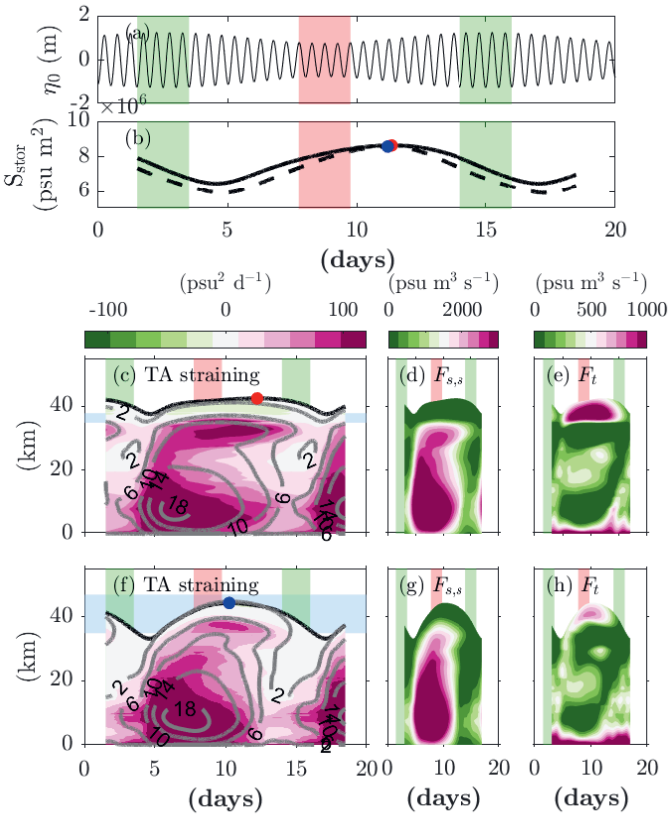


Figure 5.16: Comparison of the influence of spring–neap variability in the forcing for the two bed configurations. (a) Tidal amplitude at the mouth. (b) Total salt storage over the SIL, S_{stor}. The blue and red circles indicate the moments with the maximum salt intrusion length for i_{z_b} =0.5 and 2.0 m km^{-1}, respectively. (c) Modelled tide-averaged straining for $i_{z_b} = 2$ km^{-1}. Gray contour lines indicate the top–bottom tide-averaged stratification. (d) Salt transport associated with the steady vertically sheared flux ($F_{s,s}$). (e) Salt transport associated with the tidal-oscillatory flux contribution ($F_{s,s}$). The extend of the tide averaged salt intrusion length is shown by the thick black line. (f-h) Same as (c), but for $i_{z_b} = 0.5$ km^{-1}.

initially promotes straining and the frontal dynamics as the system remains sufficiently stratified to suppress bottom-boundary-induced mixing (Simpson and Brown, et al. 1990). Only during spring tide stratification fully breaks down, briefly reducing the SIL.

A steeper bed slope weakens the tidal forcing, which enhances the relative importance of the gravitationally driven salt transport compared to a milder bed slope. However, the steep slope also restricts the ability of the salt intrusion length (SIL) to adjust smoothly, producing a pronounced along-channel salinity gradient. As spring tide approaches, the increasing barotropic forcing acts on this pre-existing salinity structure at an intertidal timescale, promoting the formation of a local front. These fronts contribute to the steady

vertically sheared exchange flow and this process is maintained—or even intensified—as barotropic forcing strengthens. As a result, the salt intrusion length L_s remains relatively constant toward spring tide, in contrast to the mild-slope case, which exhibits a more pronounced spring–neap variability. We believe this dynamics also explains the near-absence of spring-neap variability in SIL in the Rotterdam Waterway.

5.5 Conclusions

This study demonstrates how the bed-slope inclination of the depth-transition zone in a staircase-like channel bed, when located within the quarter-wavelength resonance distance, influences estuarine dynamics and the resulting salt-intrusion length (SIL). Motivated from numerical experiments, we found that a milder bed-slope, which implies a greater dredging volume, can reduce the SIL depending on the estuary type. The numerical experiments were carried out using a 2DV model setup and an idealized stepped bathymetry, in which the bed-slope inclination between the deeper seaward section and a shallower landward section was analysed for a relatively mild and a steep slope. From the model analysis we identified two mechanisms that can lead to a relative increase in the SIL with a steeper bed slope inclination.

1. Analysis of the barotropic tide, obtained by decomposing the tidal signal into incoming and reflected waves, shows that reflection occurs at the depth transitions and that its magnitude increases with steeper bed slopes. Enhanced reflection reduces tidal currents down-estuary of the toe, which in turn decreases vertical mixing through bottom-friction-induced shear and thereby increases salt intrusion.
2. Steeper bed slopes promote the occurrence of lift-off points forming near low-water slack, creating low-salinity surface fronts during the subsequent flood. Initiated as a hydraulic response to channel deepening, these fronts locally enhance salt transport via steady shear and increase tidal oscillatory transport upstream of the bed slope. This upstream increase in tidal oscillatory transport occurs because low-salinity water is exported during late ebb to the deeper estuary, while relatively high-salinity near-bottom water is imported over the bed slope during early flood due to frontal formation. This generates an exchange mechanism similar to the jet-sink processes observed at estuary mouths.

Owing to the combined effects of reduced vertical mixing caused by enhanced partial tidal reflection and the increased salt transport associated with frontal formation, a steeper bed-slope inclination results in a greater SIL than a mild slope for systems classified as partially mixed and SIPS. Furthermore, our results suggest that the spring–neap variability of salt intrusion is substantially reduced in systems with sharp bed transitions relative to those with gentler bed slopes. These findings are consistent with observations from the Rotterdam Waterway, where the salt intrusion length has been reported to exhibit little to no spring–neap variability, and the observed low-salinity surface fronts are consistent with the modelled dynamics.

CHAPTER 6

A new harmonic regression approach to interpret and predict estuarine salinity variation

In this paper, we introduce a physics-inspired harmonic regression model to capture the non-stationary salinity dynamics at monitoring stations in well-mixed estuarine systems. Building on existing hybrid harmonic regression approaches, which modify the classical harmonic analysis to cope with non-stationary signals to predict tidal water levels, our model captures tidal and subtidal salinity variations using a simplified analytical salt intrusion model. The harmonic regression model was tested in the well-mixed Ems and Scheldt estuaries using datasets spanning 2 to 4 years, explaining 87.4% to 96.4% of the observed salinity variance at upstream stations. A key finding is that storm surge effects typically have longer wavelengths than the estuary's length scale, which justifies using a linear relation between vertical and horizontal excursions. In alluvial estuaries, where the system widens, unsteadiness of the river discharge shows to be increasingly important for more downstream stations. The model quantifies the characteristic response time of salinity to variation in discharge. Based on a critical evaluation of the model equations, we offer a physical interpretation of the optimized parameters. Specifically, we discuss the Van der Burgh constant, which is an empirical coefficient commonly used in salt intrusion models. Our findings reveal that the Van der Burgh coefficient scales with the spatial scales of dispersion and advection, relative to changes in channel geometry.

This chapter is based on: ***Keulen, D. V., W. M. Kranenburg, and A. J. F. Hoitink*** *(2025). A new harmonic regression approach to interpret and predict estuarine salinity variation. Journal of Geophysical Research: Oceans, 130, e2024JC022185. doi:10.1029/2024JC022185.*

6.1 Introduction

Estuaries are dynamic water bodies forming the transition zone between rivers and the coastal ocean, characterized by a region with brackish water resulting from mixing of freshwater and saline seawater. The longitudinal salinity distribution and the landward salt intrusion length change over time, resulting from the variable forcing at the boundaries. In this paper, we propose a new model to analyze estuarine salinity variations at monitoring stations.

Estuarine salinity levels are the result of a continuous competition between flushing by freshwater river discharge and inward transport by dispersive mechanisms. The dispersive salt flux comprises density-driven and tidal contributions (Hansen and Rattray Jr 1966b; Jay and Smith 1990; Geyer and Signell 1992; MacCready and Geyer 2010), which intrinsically involve two- and three-dimensional processes. The density-driven contribution results from a baroclinic pressure gradient along the river to sea continuum which drives a vertically sheared exchange flow (Pritchard 1952; Hansen and Rattray 1965; Chatwin 1976). This circulation can be strengthened by tidal straining, (Jay and Musiak 1994; Jay and Musiak 1996; Burchard and Hetland, et al. 2011), which can enhance stratification during ebb and suppress it during flood. This asymmetry in stratification leads to enhanced vertical mixing during flood and suppressed mixing during ebb, which induces momentum exchange enhancing the vertical circulation. Tidal dispersion encompasses multiple mechanisms including tidal trapping, horizontal residual circulation and tidal pumping (Fischer et al. 1979). Although the underlying processes are different, each of these mechanisms is the result of vertical and/or lateral velocity and salinity variations. The tide-driven dispersive mechanisms strongly depend on the local geometry, flow and density, making it difficult to parameterize the resulting dispersion process (Geyer and Signell 1992). Which mechanism is dominant strongly depends on the setting of the estuary, and often changes along the estuary.

Although the estuarine salinity variations involve processes that are intrinsically three-dimensional and that depend on the local geometry, various analytical formulations have been derived to describe and predict the cross-sectional averaged steady-state salinity distribution (Ippen and Harleman 1961; Chatwin 1976; Prandle 1981; Savenije 1986; MacCready 1999; Brockway et al. 2006; Gay and O'Donnell 2007; Kuijper and Van Rijn 2011; Xu et al. 2019). All these analytical expressions greatly simplify the estuarine dynamics by reducing the dispersive mechanisms involved, assuming a simplified channel geometry and using calibration parameters related to the dispersion coefficients. Arguably, the best substantiated models are derived for estuaries with a constant cross-sectional area where density-driven circulation is the dominant exchange mechanism. For converging systems, Prandle (1981) was among the first to derive a predictive model without a predictive expression for the bulk dispersion coefficient at the mouth. A full set of predictive equations for the salinity balance in converging estuaries was proposed by Savenije (1989), and applied for a variety of systems (Savenije 1986; Savenije 1989; Savenije 1993; Nguyen and Savenije 2006; Zhang and Savenije, et al. 2011; Cai et al. 2015; Gisen and Savenije 2015). The model uses the empirical Van der Burgh relation (Vd Burgh 1972) to obtain an expression for the longitudinal dispersion coefficients and resulting salinity. Although the model proposed by Savenije (1989) has been successfully applied for a variety of systems, its physical validity has limitations. Similar empirical expressions that avoid the use of the Van der Burgh formulations have been derived by Kuijper and Van Rijn (2011) and Zhang and Savenije (2019), which resulted in nearly identical relationships. Alternatively, Gay and O'Donnell (2007) derived a theoretically well-substantiated expression for the salinity distribution for linearly tapered systems, adopting a constant dispersion coefficient in segments of the estuary. Their model provides insight into the along-channel salinity distribution based on the physical parameters.

On an intertidal time-scale, the tidal averaged salinity distribution is altered by the tides. Ippen and Harleman (1961) showed that for stratified systems experiencing a weak tidal forcing, the longitudinal salinity distribution migrates between the two periods of

slack water over a distance approximately equal to the tidal excursion length, without significantly changing its shape. For vertically well-mixed systems, Savenije (1989) used his steady-state model to derive an expression for the high- and low water salinity distribution, adopting a Lagrangian approach to describe the salinity variations over the excursion length. For these well-mixed systems, a longitudinal salinity distribution function that does not change its shape between the slacks can be devised. However, for many systems the longitudinal distribution may change over the tide, e.g., due to tidal asymmetries like tidal straining (Simpson and Brown, et al. 1990). Analytical models for the unsteady salt distribution have been derived by Ippen and Harleman (1961) for stratified prismatic channels and Xu et al. (2019) for well-mixed converging systems. These analytical models do not account for tidal asymmetries. However, they clearly indicate how the intertidal salinity variations depend on the boundary conditions, tidal excursion length and longitudinal coordinate.

Next to the tidal motion, storm surges also influence salt intrusion lengths. In literature, the important influence of storm surges on the along estuary salinity distribution has received little attention, especially compared to their associated wind effects (Scully et al. 2005; Chen and Sanford 2009; Jongbloed and Schuttelaars, et al. 2022). Gong et al. (2018) studied storm wave-current interaction and effects on salt intrusion in the stratified Modaomen Estuary during typhoons. They show that advective transport resulting from a barotropic pressure gradient prevailed along the different inlets during the surge events. These results agree with Kranenburg et al. (2022), who showed that during surge events in the partially mixed Rhine-Meuse estuary the advective salt flux reversed. The wave dynamics of storm surge waves in estuaries was explored by Familkhalili and Talke and Jay (2020), who found that the dynamics are similar to those of tidal waves. Hence, tidal dynamics may be used to describe the salt dynamics resulting from storm surge waves. Most of the aforementioned studies focused on stratified systems where destratification is short-lived and predominately attributed to wind effects (Li and Zhong, et al. 2006; Li and Zhong, et al. 2007; Cho et al. 2012), with restratification occurring within days.

The main aim of this paper is to develop a harmonic regression model that captures non-stationary salinity level time series influenced by weekly or seasonal discharge variations, as well as aperiodic variations caused by storm surges at a monitoring station. This objective is achieved through the following steps: (1) We extend the concept that estuarine salinity levels depend on the intertidal dynamics as addressed by Xu et al. (2019). To achieve this, we reformulate the approach used by Matte and Jay, et al. (2013) and Matte and Secretan, et al. (2014) to adjust the classical harmonic analysis to allow for predictions of non-stationary water levels (referred to as hybrid harmonic models (Hoitink et al. 2017)), and apply the result to estuarine salinity records. This involves extending the analytical salt intrusion model by Savenije (1986), which describes non-tidal salinity variations with a hybrid harmonic model that captures the intertidal variability. (2) We explore the predictability of salt intrusion resulting from storm surges and vertical excursions of the estuarine water mass in well-mixed systems, and show how these dynamics can be integrated into this framework. (3) We modify the harmonic analysis approach to handle a clipped harmonic signal (periodically truncated tidal record) and focus on optimal constituent selection. (4) The model is then extended to account for the unsteadiness term in the salt balance equation.

The resulting model is applicable to analyze time-series of yearly salinity variations that are long enough to distinguish between the dominant tidal constituents (i.e., the time-series should typically cover at least one year). For these periods, the model helps to unravel the contribution of various physical forcings to site-specific salinity variations, and provides insight into how salt intrusion behaves. The mechanistic salt transport processes are modeled using a parameterized approach, where model coefficients offer a synoptic understanding of the system's functioning. The salinity time series may include prolonged periods of low salt levels, representing river salinity, as well as occasional periods when the salt front reaches the station, although this limits the identification of tidal constituents. Finally, the model allows for short- to medium-term predictions (days to

weeks in advance), which is the typical period for which predictions of discharge and water levels at the seaward boundary are available.

The structure of the remainder of this paper is as follows. Section 6.2 outlines the theoretical background of the harmonic regression model, including the steady-state salinity distribution as described by Savenije (1986), and discusses storm surge effects. Section 6.3 focuses on the harmonic regression model itself. In Section 6.3.1, the regression equations are derived, accounting for subtidal, intertidal, storm surge, and unsteadiness effects. Section 6.3.2 provides a summary of the regression and optimization procedures. In Section 6.4, a concise description of the Ems and Scheldt estuary systems is provided, along with a discussion of the observations used. Subsequently, the steady-state harmonic regression model is applied, followed by a sensitivity analysis of the results to the model parameters. Section 6.5 assesses the influence of the down-estuary boundary condition and unsteadiness effects, and tests the model formulation that account for unsteadiness. A critical evaluation of the adopted model is presented in Section 6.6, where the formulation of Savenije (1986) is compared with that of Gay and O'Donnell (2007) to discover the physical meaning of the optimized model powers. Section 6.7 discusses the broader implications of the model results, and conclusions drawn in Section 6.8.

6.2 Theoretical background

6.2.1 The one-dimensional salt-balance

Temporal variations of estuarine salinity are generally the result of flushing by the river discharge, longitudinal exchange mechanisms and dispersion of salt through tidal dynamics. In a one-dimensional perspective, temporal salinity variations are the result of advection of the salinity gradient and dispersion through a Fickian dispersion coefficient. The latter describes the down-gradient salt flux resulting from exchange flows and/or tidal dispersion. The one-dimensional cross-sectionally and tidally averaged salt balance reads:

$$A_x \frac{\partial S_x}{\partial t} + \frac{\partial \left(Q S_x\right)}{\partial x} - \frac{\partial}{\partial x}\left[A_x D_x \frac{\partial S_x}{\partial x}\right] = 0, \tag{6.1}$$

with S_x being the cross-sectional averaged salinity, A_x the average cross-sectional area, x the longitudinal coordinate, Q the discharge and D_x is the longitudinal dispersion coefficient. If the subtidal salinity distribution is in a quasi-steady-state it may be described by the balance between advection and dispersion:

$$Q_r S_x - A_x D_x \frac{\partial S_x}{\partial x} = 0. \tag{6.2}$$

Eq. 6.2 describes the subtidal salt balance best when the discharge has remained constant long enough for the salt front to adjust (Monismith et al. 2002; Kuijper and Van Rijn 2011) and requires that there is a zero net salt-flux trough the estuary.

6.2.2 Salt intrusion model

The harmonic regression model requires a shape function for the longitudinal salinity distribution, for which the empirical steady-state formulation of Savenije (1986) is adopted. To obtain an expression for the longitudinal profiles of salinity, Savenije (1986) employs an empirical relation for the longitudinal gradient of the dispersion coefficient (Vd Burgh 1972), which reads:

$$\frac{dD_x}{dx} = -K \frac{|Q_r|}{A_x}, \tag{6.3}$$

where K is a dimensionless coefficient. Substituting Eq. 6.2 into Eq. 6.3 and integrating over x yields a relationship between the salinity and dispersion coefficients, as in:

$$\frac{S_x - S_r}{S_0 - S_r} = \left(\frac{D_x}{D_0}\right)^{\frac{1}{K}}, \tag{6.4}$$

where D_0 is the dispersion at the mouth, S_x is the local salinity, S_0 is the salinity at the downstream boundary and S_r is the river salinity. An equation for the longitudinal dispersion coefficient is obtained by integrating Eq. 6.3. Depending on whether the cross-sectional area is assumed to be constant or converging in the landward direction, an equation for the longitudinal dispersion coefficient is obtained for a prismatic or a converging channel. Substituting the relation for an exponentially decaying cross-section into Eq. 6.4 yields:

$$\frac{S_x - S_r}{S_0 - S_r} = \left(1 - \frac{KL_a|Q_r|}{A_0 D_0}\left(e^{\frac{x}{La}} - 1\right)\right)^{\frac{1}{K}}, \tag{6.5}$$

where A_0 is the cross-sectional area at the mouth and L_a is the convergence length of the cross-sectional area. In Eq. 6.5, the parameters D_0 and K are used to tune the salinity curve.

Focusing on the dispersion coefficient at the mouth, various predictors have been proposed (Savenije 1993; Kuijper and Van Rijn 2011; Gisen and Savenije 2015). Gisen and Savenije (2015) derived a predictive equation from bulk estuarine parameters, based on re-analysis of the dimensionless parameters used by Savenije (1993). Using data from 30 different estuaries, the following expression for the non-dimensional dispersion coefficient was found:

$$\frac{D_0}{v_0 E_0} = 0.40 N_{r,0}^{0.57}\left(\frac{g}{C^2}\right)^{0.21}, \tag{6.6}$$

with v_0 the tidal velocity amplitude, E_0 the tidal excursion length, $N_{r,0}$ the horizontal Estuarine Richardson Number, g the gravitational acceleration and C the Chézy coefficient. The subscript $_0$ indicates that the parameters have been evaluated at the downstream boundary. The horizontal Estuarine Richardson Number, introduced by Fischer (1972), expresses the balance between the potential energy required for full mixing against buoyancy and the available kinetic energy from the tidal currents, to accomplish mixing, and reads:

$$N_{r,0} = \pi \frac{\Delta\rho_0}{\rho} \frac{g h_0}{v_0^3} \frac{Q_r}{A_0}, \tag{6.7}$$

with h_0 the average depth, $\Delta\rho_0$ the horizontal density difference over the intrusion length and ρ the density of fresh water. The estuarine Richardson number can be used to quantify the degree of stratification for an estuary (Fischer 1976).

6.2.3 Storm surges and their effects

Advective transport (i.e., excursion of the salinity curve) is assumed to be the dominant mechanism of storm surges for well-mixed systems. Tidal theory can be adopted to estimate the relation between surge water levels and the resulting excursion length, since storm surges have typical periods close to those of tides and both are long waves (Familkhalili and Talke and Jay 2020).

A relation between the water level variations, estuarine shape and the resulting vertical excursion length for funnel-shaped and long estuaries is given by the geometry-tide relationship (Savenije 2006; Toffolon et al. 2006):

$$E = H\left(\frac{r_s L_a}{h}\right)\left(\frac{\cos\varepsilon}{1 - \delta_u L_a}\right), \tag{6.8}$$

with E the tidal excursion length, H the tidal range, L_a the convergence length of the cross-sectional area, δ_u the damping number of the horizontal tide, ε the phase lag between high water and high-water slack (describing the wave character) and r_s is the dimensionless ratio of the storage width to stream width. The wave has a standing character when ε equals 0, a mixed character when $0 < \varepsilon < \frac{\pi}{2}$ and is progressive when ε is $\frac{\pi}{2}$. Toffolon et al. (2006) derived explicit formulations for ε and δ_u for mixed and standing waves, expressed in terms of the estuary number $\gamma = \left(\frac{c_0}{\omega L_a}\right)$ and the friction number $X = \left(\frac{g}{C^2}\frac{c_0}{h\omega}\frac{\eta}{h}\right)$,

where c_0 is the classical wave celerity, ω the angular frequency ($\omega = \frac{2\pi}{T}$), η is the tidal amplitude and T the tidal period. Based on these equations, the wave character of storm surges and the resulting excursion length may be estimated when the amplitude and duration are known. As γ increases, the phase lag ε becomes independent of the estuary and the friction number. Similarly, δ becomes independent of the friction number, and the damping is solely determined by the shape of the estuary and the surge wave length. When the typical wavelengths of storm surge events are larger than the length scale of the estuary, the relation between the vertical and horizontal excursion may be approximated by the classical relation $E \approx H\left(\frac{r_s L_a}{h}\right)$. Avoiding a dependence on ε and δ_u has the advantage that a (near) unique relation exists between storm surge water levels and the resulting horizontal excursion over a range of frequencies.

6.3 Regression model for salinity time-series

This section proposes a harmonic regression model for estuarine salinity. First, Section 6.3.1 describes the modified version of Savenije (1986) and the extensions to capture tidal and surge variations. Secondly, Section 6.3.2 describes the implementation and optimization procedure.

6.3.1 The regression equations

6.3.1.1 Tidal averaged salinity variations

For width-converging systems, the tide averaged salinity distribution can be described by Eq. 6.5. To describe the salinity variations at a monitoring station, indicated by the subscript s, Eq. 6.5 is simplified by lumping all time-independent variables in a single term:

$$\left(\frac{S_s - S_r}{S_0 - S_r}\right)^K = \frac{D_s}{D_0} = 1 - a_0 \frac{K|Q_r|}{D_0}. \tag{6.9}$$

The coefficient a_0 describes the degree in which the relative dispersion coefficient is reduced at x_s. Note that K is maintained in Eq. 6.9 since it appears in the power of the RHS of Eq. 6.9. The tide-averaged salinity variations at the location of the monitoring station are described by Q_r and D_0.

6.3.1.2 Intertidal salinity variations

Savenije (1989) approximated the tide averaged (TA) and low-water slack (LWS) salinity distribution by assuming that the high-water slack distribution migrate over the horizontal excursion length (E). Following this reasoning, the salinity variations observed over a tidal cycle, relative to the tide-averaged salinity, approximate the salinity observed at any $x_t = x_s + \frac{E}{2}\cos(\omega t + \phi)$, where t is time, and ω and ϕ are the angular frequency and phase of the dominant tidal constituent, respectively. To obtain an expression for the intertidal salinity variations and parameters that can be determined through regression, x in Eq. 6.5 is substituted by x_t. We simplify the equation to separate the tide-average from the intratidal variations, which yields:

$$\left(\frac{S_s - S_r}{S_0 - S_r}\right)^K = \frac{D_s}{D_0} \approx 1 - K\frac{|Q_r|}{D_0}\frac{L_a}{A_0}\left(e^{\frac{x_s}{L_a}} - 1\right) + \left(\frac{1}{2}K\frac{|Q_r|}{D_0 A_0}e^{\frac{x_s}{L_a}}\right) E\cos(\omega t + \phi). \tag{6.10}$$

The third therm on the RHS of Eq. 6.10 is obtained by subtracting the TA expression from the modified version, including the tidal excursion. Subsequently, a first order Taylor approximation for E ($e^{(\delta)} \approx 1 + \delta$) around 0 is used in the natural exponent, to separate the tide-average from the tidal variation. By lumping all time-independent variables in Eq.

6.10, rewriting the harmonic part in terms of tidal constituents yields:

$$\left(\frac{S_s - S_r}{S_0 - S_r}\right)^K = 1 - a_0 K \frac{|Q_r|}{D_0} + \sum_{k=1}^{n} \left[a^c_{1,k} K \frac{|Q_r|}{D_0} \cos(\omega_k t) + a^s_{1,k} K \frac{|Q_r|}{D_0} \sin(\omega_k t) \right]. \quad (6.11)$$

In Eq. 6.11, the amplitudes $a^c_{1,k}$ and $a^s_{1,k}$ determine the phase and amplitude of each tidal constituent k. Note that based on the Taylor approximation, an error is made which is small when $\frac{E}{La} < 1$. Eq. 6.11 is more accurate when the channel geometry is closer to being prismatic. For prismatic channels, the equation is exact.

6.3.1.3 Storm surge variations

Sections 6.2.3 discussed how storm surge waves, under the assumption that tidal theory applies to storm surges, depend on the dimensionless friction number and the estuary shape number. Since storm surge waves do not act on a predefined frequency and amplitude, some simplifications are required. Here, we assume that storm surges act as standing waves, which applies when the typical wave lengths are larger than the length scale of the estuary. For a standing wave, high and low water is reached everywhere at the same time (i.e., no phase lag and $\varepsilon = 0$). Damping becomes independent of friction, causing that damping coefficients vary little between different periods. Under these conditions, the surge related excursion lengths may be approximated by $E = H \frac{L_a r_s}{\overline{h}}$. The salinity variation introduced by storm surges, under the assumption of a linear relation between water-levels and currents, are implemented similarly as the intertidal variations:

$$\left(\frac{S_s - S_r}{S_0 - S_r}\right)^K = \underbrace{1 - a_0 K \frac{|Q_r|}{D_0}}_{\text{TA}} + \underbrace{a_1 K \frac{|Q_r|\delta_w}{D_0}}_{\text{SURGE}} + \underbrace{\sum_{k=1}^{n} \left[\left(a_{2,k}^c K \frac{|Q_r|}{D_0} + a_{3,k}^c K \frac{|Q_r|\delta_w}{D_0} \right) \cos(\omega_k t) + \left(a_{2,k}^s K \frac{|Q_r|}{D_0} + a_{3,k}^s K \frac{|Q_r|\delta_w}{D_0} \right) \sin(\omega_k t) \right]}_{\text{TIDAL}} . \quad (6.12)$$

In Eq. 6.12, δ_w denotes the surge water level. In addition, the surge related water level fluctuation amplifies or attenuates the amplitudes of the intertidal salinity variation. Hence, the surge-induced salinity variation also appears in the harmonic model.

6.3.1.4 Accounting for unsteadiness

Equations 6.11 and 6.12 rely on that the system can be adequately described by a steady-state model. However, in many systems, variations in river discharge can occur over periods shorter than the time required for the salinity field to fully adjust. To account for this, empirical models for the salt intrusion length often incorporate these effects trough an auto-correlation process (Monismith et al. 2002; Reyes-Merlo et al. 2013). This approach is also adopted here. Specifically, Eq. 6.11 and 6.12 can be extended with an auto-regressive AR(1) term, which for Eq. 6.12 yields:

$$\left(\frac{S_s - S_r}{S_0 - S_r}\right)^K = \underbrace{1 - a_0 K \frac{|Q_r|}{D_0}}_{\text{TA}} + \underbrace{a_1 K \frac{|Q_r|\delta_w}{D_0}}_{\text{SURGE}} + \underbrace{a_2 \tilde{D}_t}_{\text{LAG}} + \underbrace{\sum_{k=1}^{n} \left[\left(a_{3,k}^c K \frac{|Q_r|}{D_0} + a_{4,k}^s K \frac{|Q_r|\delta_w}{D_0} + a_{5,k}^c \tilde{D}_t \right) \cos(\omega_k t) + \left(a_{3,k}^s K \frac{|Q_r|}{D_0} + a_{4,k}^s K \frac{|Q_r|\delta_w}{D_0} + a_{5,k}^s \tilde{D}_t \right) \sin(\omega_k t) \right]}_{\text{TIDAL}}, \tag{6.13}$$

where $\tilde{D}_t = \left(\frac{S_s - S_r}{S_0 - S_r}\right)^K - 1\Big|_{t-\Delta t}$, where Δt is set to 1 day. Furthermore, Eq. 6.13 implicitly assumes a time step Δt, which in lumped into the regression parameters coefficients. An empirical response time, T_R, can be defined as $T_R = 1/(1 - a_2)$. Typically, this response time varies between high and low discharge conditions. However, in this study, a single response time is used. Although Eq. 6.13 allows for more accurate predictions when unsteadiness is significant, this approach does not handle truncated salinity signals effectively.

6.3.1.5 Modelling the dispersion coefficient at the mouth

The dispersion coefficient at the downstream boundary D_0 is not yet specified in Equations 6.9 through 6.13. A modified version of Eq. 6.6 is here proposed. First, based on Eq. 6.6 it

can be seen that D_0 is proportional to $N_{r,0}$, as in the power law $\frac{D_0}{v_0 E_0} = \alpha N_{r,0}^P$, where α is a constant. In the regression model we devise, the power P is allowed to deviate from the empirically derived value of 0.57 to optimize the model. Secondly, assessing $N_{r,0}$ requires velocity time-series. Generally, only records of tidal elevation are available. Therefore, the horizontal tidal amplitude at the downstream boundary (v_0) is replaced by an appropriate velocity scale $v = \eta\omega\frac{L_a}{h}$ and the tidal excursion length is written as $E = \frac{vT}{\pi}$. For ω, the typical tidal frequency of the system is used. Substituting these relations into Eq. 6.6 and rearranging the variables related to $N_{r,0}$ into a new dimensionless group yields:

$$D_0 \propto \left(\underbrace{\frac{h_0^3 \pi}{L_a^3 B_0} \left(\frac{g}{\omega^2}\right)}_{\text{constant}} \right)^P \left(\underbrace{\frac{\Delta\rho_0}{\rho} \frac{Q_r}{\eta_0^3 \omega}}_{\text{varying}} \right)^P \underbrace{\left(\frac{L_a}{h_0}\right)^2}_{\text{constant}} \underbrace{(\eta_0^2 \omega)}_{\text{varying}} . \tag{6.14}$$

In Eq. 6.14, two constant and two variable terms are indicated. The constant terms in Eq. 6.14 can be absorbed in the coefficients α_i of Eq. 6.9 − 6.13, and are resolved based on regression.

6.3.1.6 Salinity at the boundaries

The relative salinity in Eq. 6.9 − 6.13 depends on the salinity input from the river, which generally varies with the discharge. These variations are relatively small (i.e., within 0−1 PSU), but are important to distinguish when the salinity is influenced by the oceanic boundary or is solely determined by the river (also see Section A.1.1). In order to estimate the river salinity for the discharge the following model is adopted:

$$S_r = \frac{C_b}{Q_r} + S_c, \tag{6.15}$$

were S_c is the salinity concentration of the discharge and C_b a background load that is diluted by the discharge. The values for S_c and C_b are determined by regression according to Eq. 6.15, using observed river salinity.

Similarly, the salinity at the used down-estuary boundary S_0 can either be considered constant. Alternatively, measured values of S_0 can be used, or a parameterization which proceeds from a simplified version of Eq. 6.13:

$$\left(\frac{S_0 - S_r}{S_{oc} - S_r}\right)^K = 1 - a_0 K \frac{|Q_r|}{D_0} + a_1 \tilde{D}_t, \tag{6.16}$$

where S_{oc} is the salinity at sea. The advantage of Eq. 6.16 is that it allows to partially account for unsteadiness effect trough the parameterized boundary condition such as used in Eq. 6.9 − 6.12, which can deal with truncated salinity signals.

6.3.2 The regression and optimization procedure

Estuarine salinity records often contain tidally periodic or prolonged periods of low salinity, where the salinity matches that of the river water (this introduces clipped harmonic records). To facilitate the optimization procedure, a priori assessment is conducted to isolate data windows where the salinity does not significantly exceed river salinity, excluding those windows from the optimization. The optimization procedure optimizes the regression coefficients and powers in Eq. 6.9−6.12 through an iterative process that extends NS-TIDE (Matte and Jay, et al. 2013; Matte and Secretan, et al. 2014). Furthermore, an adjusted version of the two-fold strategy used by Matte and Jay, et al. (2013) is applied for constituent selection and error estimates. However, for irregularly sampled data—introduced by excluding data points where salinity does not exceed river salinity—the degree to which tidal constituents can be properly resolved is influenced. Following Foreman et al. (2009), the correlation coefficients of the significance-tested constituents are monitored, discussed in Section 6.4.4.2. Details regarding constituent selection, optimization, and significance testing can be found in Appendix C.1.

6.4 Application to two estuaries

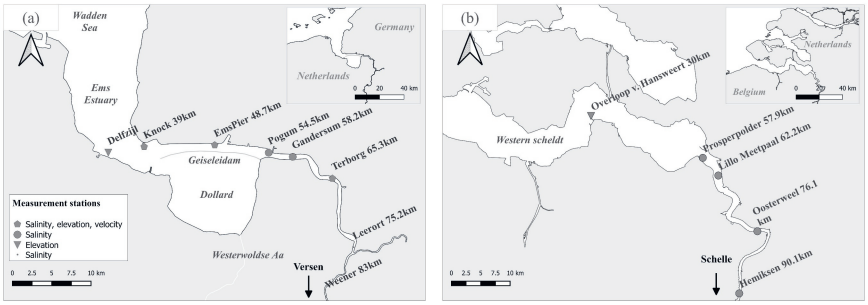


Figure 6.1: (a) Map of the Ems Estuary and locations of the measurement stations. The river kilometers are referenced against the barrier island Borgum, located between the Wadden Sea and the North Sea. (b) Same as *a* but for the Scheldt Estuary. The river kilometers are referenced against the city of Vlissingen.

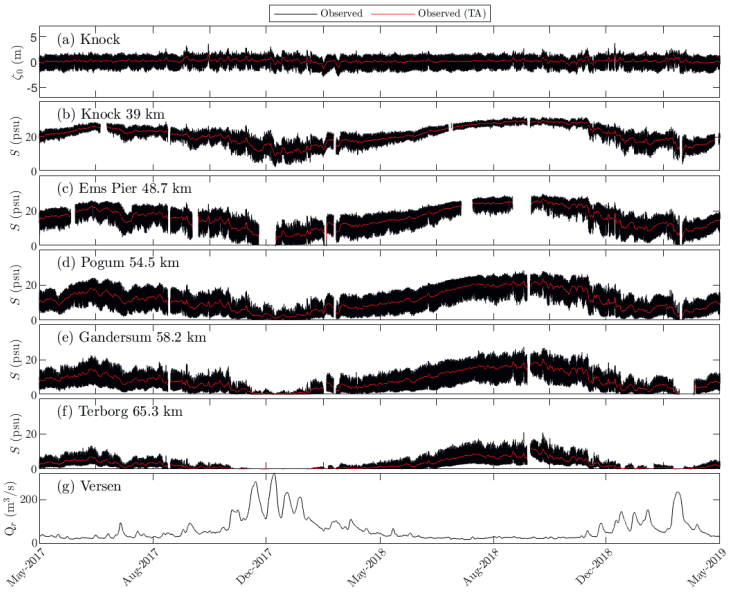


Figure 6.2: Overview of the observed salinity time-series in the Ems Estuary and the forcing at the up- and downstream boundaries. (a) Observed and Godin-filtered water levels at Knock. (b-f) Observed and tide-averaged (TA) salinity at the individual stations. Distance is relative to the barrier island of Borkum. (g) River discharge measured at Versen.

6.4.1 The Ems Estuary and Scheldt Estuary

The Ems Estuary is located at the border between The Netherlands and Germany (see Figure 6.1a). It contains a large basin that consists of ∼80% tidal flats referred to as the Dollard. Exchange between the Dollard and the main channel of the Ems is limited by a permeable, longitudinal training dam (the Geiseleidam). Tides in the Ems Estuary have a semi-diurnal character with a tidal range of about 2.5 m near the entrance, but significantly amplify upstream of the Dollard (Winterwerp and Vroom, et al. 2017). The tidal wave upstream of the Dollard has a standing wave character. A storm surge barrier is located upstream of the city of Pogum and is occasionally closed. Fresh water input predominantly originates from the Ems River, which has an average discharge of ∼125 m^3/s. The Westerwoldse Aa constitutes another source of fresh water input, which drains ∼12.5 m^3/s into the Dollard basin.

The Scheldt Estuary runs from Belgium to the south of the Netherlands (Figure 6.1b). The Dutch part of the Scheldt (the Western-Scheldt) is relatively wide and consists of multiple flood-ebb channel loops (Nguyen and Savenije, et al. 2008). In the Belgium part, the channels converge into a single channel that is kept at depth for the port of Antwerp. The mean tidal range is about 3.8 m near the entrance of the system and amplifies in the upstream direction. The wave propagation reflects that of an apparent standing wave (Savenije et al. 2008). The major contributors to the Scheldt are the Dender and the Rupel (Struyf et al. 2004); the average discharge of the Scheldt is estimated to be ∼85 m^3/s.

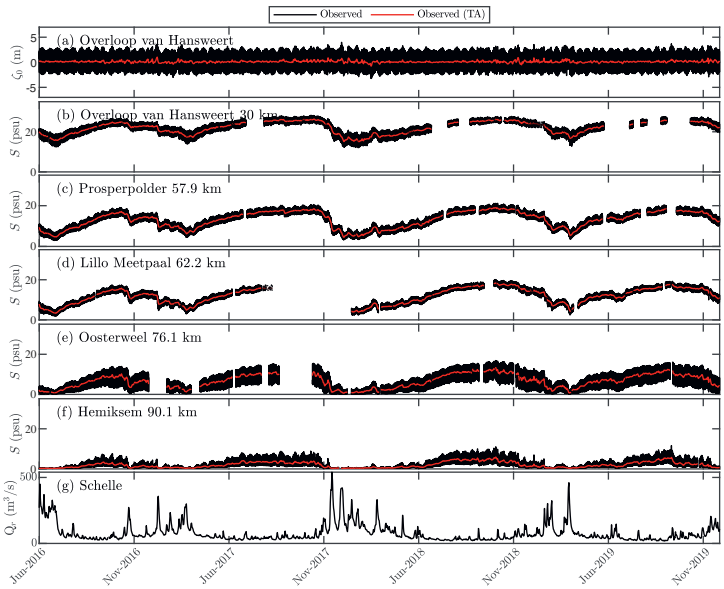


Figure 6.3: Overview of the observed salinity time-series in the Scheldt Estuary and the forcing at the up- and downstream boundaries. (a) Observed and Godin-filtered water levels at Overloop van Hansweert station. (b-f) Observed and tide-averaged (TA) salinity at the individual stations. Distance is relative to the city of Vlissingen. (g) River discharge calculated at Schelle station.

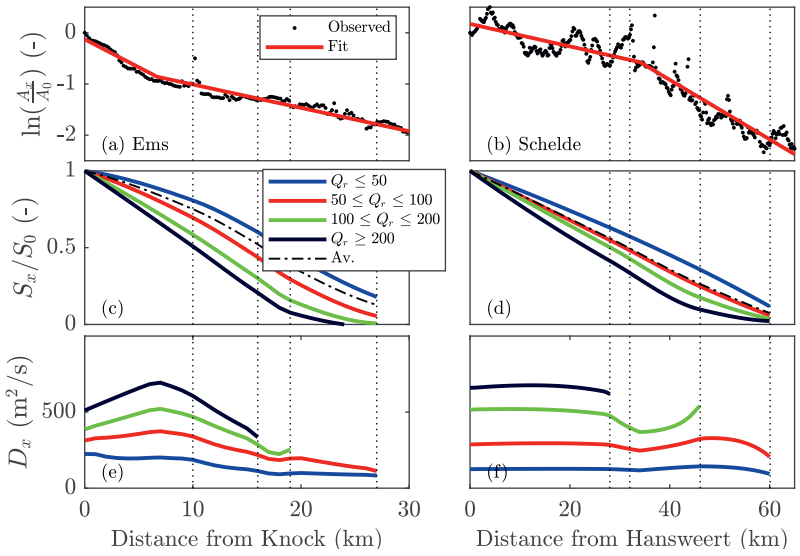


Figure 6.4: Overview of the geometry, typical along-channel salinity distributions, and estimated dispersion coefficients for the Ems and Scheldt Estuary. (a-b) Cross-sectional area and fitted exponential decay model ($A_x = A_0 e^{\frac{-x}{L_a}}$). (c-d) Typical along-channel salinity distributions under different discharge conditions. (e-f) Steady-state dispersion coefficients corresponding to the shown along-channel salinity distributions. Dashes vertical lines indicate the location of the salinity stations.

6.4.2 Data and observations

To evaluate the proposed regression model, time-series datasets from the Ems Estuary (two years) and the Scheldt Estuary (four years) are used. These datasets include information on salinity, water levels, velocity and discharge (locations are shown in Figure 6.1). Here, the data is used to estimate the importance of the unsteadiness term at different stations and to assess the extent to which a steady-state approach is justified. Furthermore, the along channel variations in geometry, salinity and of the dispersion coefficients are discussed and salinity variations due to surges are examined.

Figures 6.2 and 6.3 show the measured salinity levels and forcing variables. Both estuaries exhibit strong seasonality, with the lowest salinity during winter. In the Ems Estuary, downstream of Pogum, salinity is affected by partial closures of the storm surge barrier, such as the closure on October 7–9, which elevated salinity for about 2-3 weeks (Figure 6.2). Figure 6.4 shows the geometry, the typical salinity distributions and associated dispersion coefficients for different discharge conditions from the measurements in Figure 6.2 and 6.3. The geometry, in both systems can be described by an exponential decay (Figure 6.4a,b), with a break in the channel convergence observed in both systems (most pronounced in the Scheldt). Figure 6.4c,d shows the average salinity distributions for different discharge conditions, which are bin-averages of spline interpolated salinity values at monitoring stations. The longitudinal salinity distribution in the Ems is characterized by a hyperbolic shape, whereas that of the Scheldt Estuary changes from concave to a convex shape with increasing discharge. Figure 6.4e,f shows the corresponding steady-state dispersion coefficients, estimated using Eq. 6.2. The variations associated with these values are quit large and therefore are only used qualitatively. For the Ems Estuary, the resulting dispersion coefficients show a (local) amplification with increasing discharge,

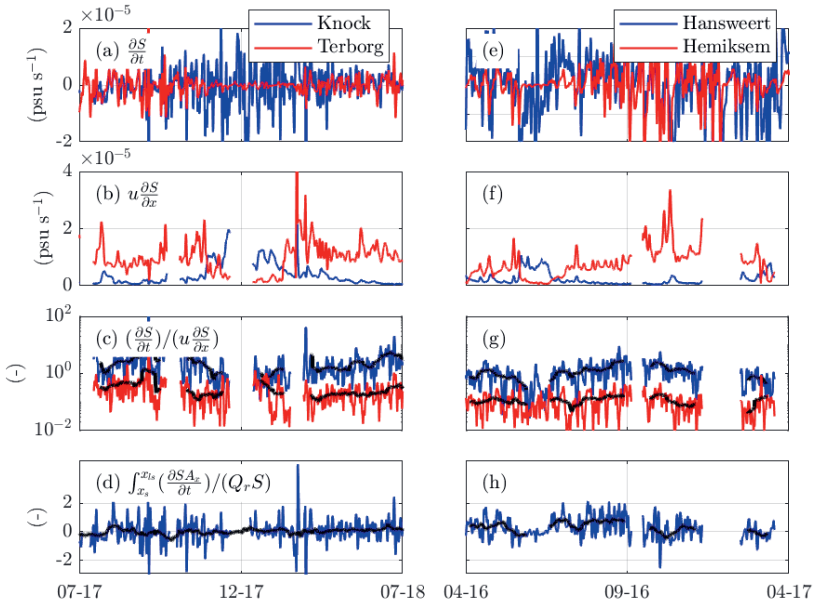


Figure 6.5: Evaluation of the importance of the (neglected) unsteadiness Term. (a) Comparison of the unsteadiness term estimated from the tidally averaged salinity signal at the most down- and upstream stations in the Ems Estuary. (b) Same estimation for the advection of salt. (c) Ratio of the unsteadiness term to the advection term, used to measure the importance of the unsteadiness term in the salt-balance equation (Eq. 6.1). The solid black lines indicates the monthly average. (d) Estimation of the error introduced by neglecting the unsteadiness term in the dispersion coefficient. Note: When using Eq. 6.2, the dispersion coefficient is calculated as $D_x = \frac{Q}{A_x}\frac{S}{\partial S/\partial x}$. When using Eq. 1, it is given by $D_x = \left(\int_{x_s}^{x_l} \frac{\partial S}{\partial t} A_x dx + Q_r S\right) \frac{1}{A_x \partial S/\partial x}$, where x_s the location of the station and x_{ls} is the location where the salinity approaches zero; the most upstream station is used here. (e-h) Same as (a-d), but for the Scheldt Estuary.

which corresponds to estimates from Helder and Ruardij (1982) and De Swart et al. (1997). In the Scheldt Estuary, the dispersion coefficient remain nearly constant in the downstream reach, but amplify slightly in the upstream region.

To assess the importance of the unsteadiness term $\left(\frac{\partial S}{\partial t}\right)$ relative to the advective term $\left(u\frac{\partial S}{\partial x}\right)$ in the salt balance at various monitoring sites, the ratio of the unsteadiness term to the advective term is evaluated (Figure 6.5a–h). In both estuaries, unsteadiness is most pronounced at the down-estuary stations. Figure 6.5g,h evaluate the (potential) errors in dispersion coefficients when the unsteadiness term is neglected, highlighting persistent errors in the Scheldt due to the influence of unsteadiness. Thus, while the unsteadiness term is larger in the Ems, its sign is more persistent in the Scheldt, indicating a longer adjustment response time. Given these findings, a steady-state approach is likely more suitable for upstream stations and may introduces systematic errors for the down-estuary station. Furthermore, the admittance of the semi-diurnal vertical tide (i.e,

water level elevations), determined through a Continuous Wavelet Transform, was tested for the Ems and Scheldt estuaries, but was found to show little temporal variations and is assumed stationary.

An analysis of water level, salinity and discharge variations occurring in the 1.2−6 day

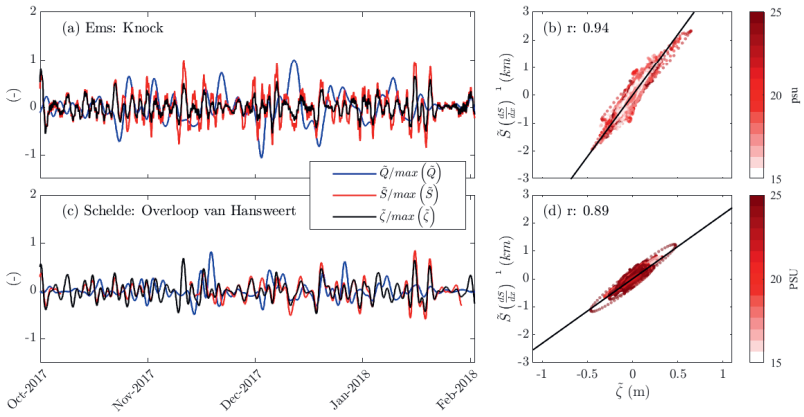


Figure 6.6: Relationship between storm surge water levels and horizontal excursion for the Ems and Scheldt estuaries. (a,c) Observed band-pass filtered variation of salinity $\tilde{S}$, water elevation $\tilde{\zeta}$, and discharge $\tilde{Q}_r$, normalized by the maximal observed value. The band-pass filter retains variation in between 1.2 and 6 days. (b,d) Linear relationship between water elevations $\tilde{\zeta}$ and estimated horizontal excursions. The latter is approximated by dividing $\tilde{S}$ by the local salinity gradient $\frac{dS}{dx}$.

range is performed to investigate salinity response during surge events. The lower limit of 1.2 days is used to distinguish the tidal signal from the surge variations. However, storm surges can act in the same frequency range as tides. The upper limit was set at 6 days, as choosing higher values caused that the filtered signal started to show variations that did not resembled the water level variations. The filtered salinity variations co-vary with the filtered water levels (Figure 6.6a, c). The water level variations are, however, not directly proportional to the observed salinity variations. This is because the resulting salinity variations depend both on the local, instantaneous salinity gradient and the salt water excursion resulting from storm surges. Dividing subtidal salinity variations by the local salinity gradient yields a length scale for the surge-induced excursion (Figure 6.6b, d). The relation between surge water levels and the surge-induced excursions shows a near-linear relation for both systems. This implies that the surge water level variations that occur over the 1.2−6 day range are directly proportional to the horizontal excursion of the estuarine water mass (Section 6.2.3).

6.4.3 Performance of the regression model

This section tests the predictive skill of the steady-state formulations (Eq. 6.11 and 6.12) in predicting salinity variations at the stations where salinity often matches river levels and unsteadiness effects between the station and the downstream boundary are assumed minimal.

Table 6.1: Overview of the model experiments performed for the Ems Estuary and results discussed in Sections 6.4.3. The missing percentage refers to the total percentage of missing and rejected data points, while Un. Var. refers to the unexplained variance in the model results.
[1]: Fortnightly averaged salinity at Knock station for the seaward boundary condition.
[2]: Constant value of 35 psu for the seaward boundary condition.
[3]: Parameterized seaward boundary condition.
[4]: Total of the fitted proportionality coefficients.

Regression model:	Boundary:	Calibration:	Prediction:	Station:	Missing	Pars[4]	P/K	Cal.		Pred.	
								rmse	Un. Var.	rmse	Un. var.
				(-)	(%)	(-)	(-)	(psu)	(%)	(psu)	(%)
Tides (Eq. 6.11)	Obs[1]	17 months	7 months	Emspier	13	31	0.57/0.77	1.8	6.8	1.8	6.6
				Pogum	4	29	0.58/0.50	1.9	7.2	1.9	7.9
				Gandersum	8	31	0.61/0.46	1.8	8.4	1.9	10.6
				Terborg	37	25	0.66/0.29	1.3	12.2	1.0	12.6
Tides + surges (Eq. 6.12)	Obs[1]	17 months	7 months	Emspier	13	40	0.60/0.82	1.7	6.0	1.6	4.9
				Pogum	4	30	0.62/0.53	1.8	6.5	1.6	5.9
				Gandersum	8	34	0.64/0.48	1.7	7.6	1.6	8.0
				Terborg	37	32	0.67/0.44	1.2	9.8	0.9	11.1
Tides + surges (Eq. 6.12)	Con [2]	17 months	7 months	Emspier	13	22	0.57/0.71	2.9	18.8	3.3	23.6
				Pogum	4	24	0.50/0.48	2.9	17.4	2.8	17.7
				Gandersum	8	20	0.51/0.47	2.6	17.5	3.6	19.3
				Terborg	37	18	0.59/0.45	1.7	23.0	2.4	14.7
Tides + surges (Eq. 6.12)	Pred [3]	17 months	7 months	Emspier	13	38	0.57/0.77	1.6	5.6	1.5	4.3
				Pogum	4	44	0.58/0.50	1.8	6.0	1.5	5.3
				Gandersum	8	36	0.61/0.46	1.7	7.0	1.6	7.2
				Terborg	37	28	0.66/0.30	1.2	10.2	0.8	8.4
Tides + surges (Eq. 6.13)	Con [2]	17 months	7 months	Knock	10	15	0.29/0.83	1.1	4.5	1.9	8.9

Table 6.2: Overview of the model experiments performed for the Scheldt Estuary and results discussed in Section 6.4.3. The missing percentage refers to the total percentage of missing and rejected data points, while Un. Var. refers to the unexplained variance in the model results.
[1]: Fortnightly averaged salinity at Prosperpolder for the seaward boundary condition.
[2]: Constant value of 35 psu for the seaward boundary condition.
[3]: Parameterized seaward boundary condition.
[4]: Total of the fitted proportionality coefficients

Regression model:	Boundary:	Calibration:	Prediction:	Station:	Missing	Pars[5]	P/K	Cal.		Pred.	
								rmse	Un. var.	rmse	Un. var.
				(-)	(%)	(-)	(-)	(psu)	(%)	(psu)	(%)
Tides (Eq. 6.11)	Obs[1]	2.5 years	1 year	Lillo Meetpaal	13	31	0.72/0.97	0.5	1.5	0.6	3.8
				Oosterweel	25	39	0.60/0.29	1.0	5.2	1.1	7.7
				Hemiksem	19	25	0.60/0.20	0.6	9.7	0.6	12.8
Tides + surges (Eq. 6.12)	Obs[1]	2.5 years	1 year	Lillo Meetpaal	32	34	0.71/0.94	0.5	1.4	0.6	3.6
				Oosterweel	26	58	0.60/0.30	0.9	4.7	1.1	6.9
				Hemiksem	27	24	0.60/0.20	0.5	8.8	0.6	12.0
Tides + surges (Eq. 6.12)	Con [2]	2.5 years	1 year	Lillo Meetpaal	26	8	0.65/0.29	2.8	43.0	3.2	69.2
				Oosterweel	26	28	0.66/0.45	2.2	26.3	2.2	27.9
				Hemiksem	27	18	0.63/0.30	1.0	27.6	1.0	34.4
Tides + surges (Eq. 6.12)	Pred [4]	2.5 years	1 year	Lillo Meetpaal	26	28	0.73/0.94	0.5	1.4	0.6	3.6
				Oosterweel	26	48	0.60/0.29	0.9	4.6	1.0	6.9
				Hemiksem	27	30	0.60/0.14	0.5	8.9	0.6	12.2
Tides + surges (Eq. 6.13)	Con[2]	2.5 years	1 year	Hansweert	19	31	0.46/0.98	0.5	2.3	0.9	11.6
				Prosperpolder	7	29	0.47/0.47	0.5	1.1	1.4	8.9
				Lilo Meetpaal	13	17	0.47/0.48	0.4	1.1	1.1	10.5

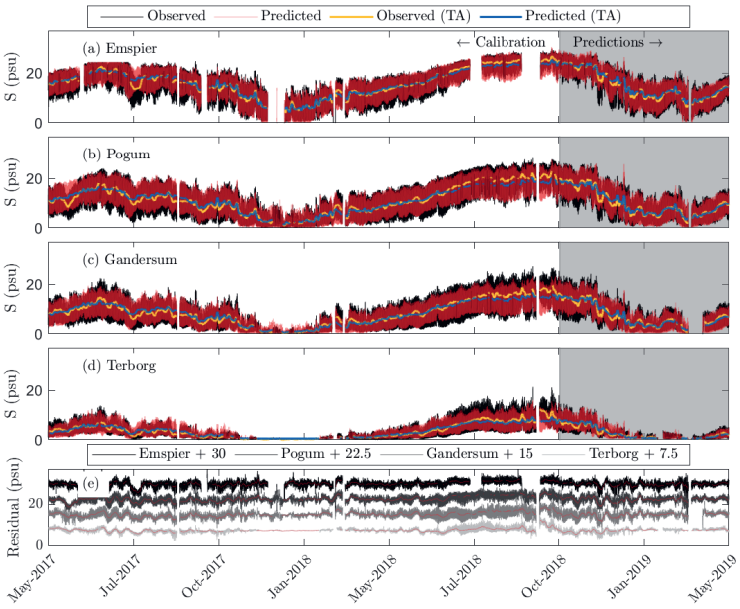


Figure 6.7: Data-model comparison for salinity in the Ems Estuary, with salinity predicted using Eq. 6.12 and the fortnightly averaged salinity at Knock as seaward boundary condition. (a-d) Observed and predicted salinity variations and TA (determined by a moving average, 1 day window). The period for which the salinity is predicted is highlighted by a gray background. (e) Residuals (predictions minus observations) of panel a-d. The residuals include an offset for clarity of the figure.

The model inputs consist of river discharge, river salinity, and tidal elevation. Furthermore, observed salinity at a down-estuary station, where unsteadiness effects become important, are provided for the downstream boundary condition. The datasets are divided into a calibration period and a prediction period. For the Ems, the first 15 months are used to optimize model coefficients, with the remaining 7 months testing predictive skill. Similarly, for the Scheldt, the last year of data is used for prediction testing. The low-pass filtered salinity signals at Knock and Prosperpolder provide the boundary conditions, S_0, for the Ems and Scheldt Estuaries, respectively.

In the Ems Estuary, the best results were achieved using Eq. 6.12 (Figure 6.7). This model, fitted with 40 to 32 regression coefficients for the various stations (used tidal constituants are listed in Table S1), had an unexplained variance of 4.9−11.1% and an RMSE of 1.2–1.8 psu during calibration (Table 6.1). The unexplained variance increased slightly to 4.8−11.4% with an RMSE of 0.9−1.6 psu during the predictions, with the greatest decrease in predictive skill observed at the most upstream station. Figure 6.9 provides additional details for the Gandersum station. Figure 6.9a shows that the model effectively captures the harmonic variations in intertidal salinity, supported by the power spectra comparison (Figure 6.9d). It also accurately represents period where the salinity signal was clipped (Figure 6.9c) and two significant surge events with sea level increases of 0.96 m and 1.45 m (Figure 6.9b). When surge variations are not included (Eq. 6.11), the unexplained variance increased by approximately 1–2% during the prediction period.

Similar results were obtained for the Scheldt Estuary (Figure 6.8 and S4). Using 24−58 regression coefficients, depending on the station, the model using Eq. 6.12 achieved

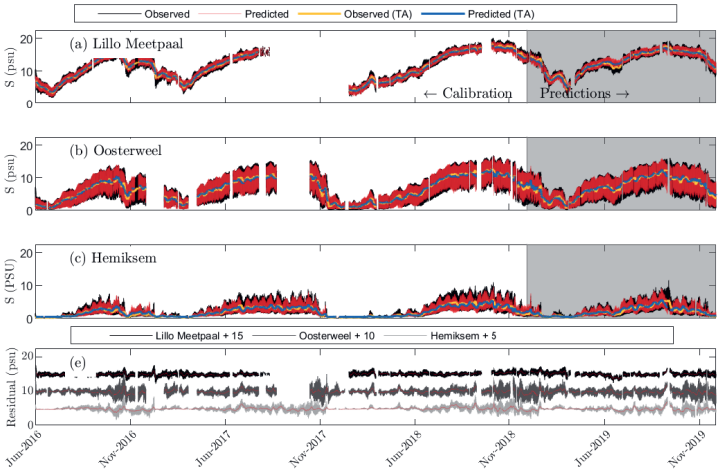


Figure 6.8: Data-model comparison for salinity in the Scheldt Estuary, with salinity predicted using Eq. 6.12 and the fortnightly averaged salinity at Overloop van Hansweert station as seaward boundary condition. (a-d) Observed and predicted salinity variations and TA (determined by a moving average, 1 day window). The period for which the salinity is predicted is highlighted by a gray background. (e) Residuals (predictions minus observations) of panels a-d. The residuals include an offset for clarity of the figure.

an unexplained variance of 1.4−8.8% and an RMSE of 0.5−0.9 psu during calibration (Table 6.2). Prediction variance increased to 3.6−12.0% with an RMSE of 0.6−1.1 psu. Compared to the Ems case, excluding storm surge effects had a smaller impact on the regression model's performance in the Scheldt Estuary, likely due to its longer salt intrusion length and weaker sensitivity to storm surge water levels (see Figure 6.6).

Figures 6.7 and 6.8 show that the low-pass filtered variations closely align with observed averages, indicating that the mean signal is well-captured and suggesting minimal unsteadiness effects upstream of the imposed boundary. However, residuals still exhibit autocorrelation. To assess the importance of the neglected unsteadiness term, it was assumed that the low-pass filtered residuals reflect the mismatch due to unsteadiness. This accounted for 3.2–3.8% of the variance in the Ems, with little variation between stations, while in the Scheldt, this percentage increased upstream, ranging from 0.4% to 4.8%.

6.4.4 Model- and parameter sensitivity

6.4.4.1 Optimized powers and fitted coefficients

Section 6.4.3 demonstrated that accurate predictions can be achieved using Eqs. 6.11 and 6.12. In this section, we assess the robustness and consistency of the model, focusing on the optimized power coefficients and fitted regression parameters.

First, three experiments were conducted for both systems using Eq. 6.12: one where both power coefficients were optimized, and two where either P or K was held constant. These experiments aim to determine whether optimizing both powers is necessary. Second, for the model with both power coefficients optimized, four additional experiments were performed to evaluate the consistency of the best-fit values of the power and regression coefficients when using different periods for model optimization and different discharge

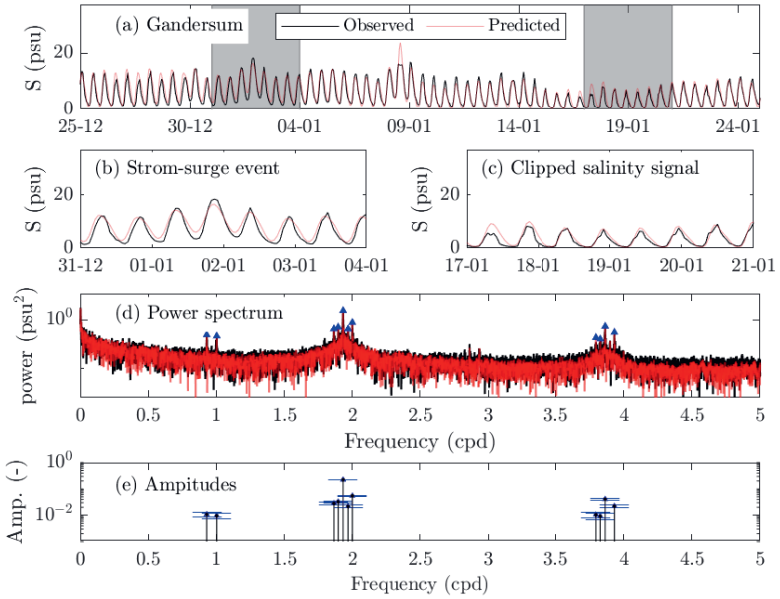


Figure 6.9: Data-model comparison for salinity at Gandersum station (data same as in Figure 6.7). (a−c) Zoom of the observed and predicted salinity. The gray boxes in panel a indicate the periods shown in panels b−c. (d) Power spectrum of the predicted observed salinity and predicted salinity signal. The blue triangles indicate the included tidal coefficients. (e) Amplitude of the tidal constituents included (derived using Eq. C.8) and the blue error bars indicate the associated confidence bounds.

conditions. The best-fit model coefficients are shown in Figures 6.10 and 6.11 for the Ems Estuary and the Scheldt Estuary, respectively.

In the first experiment, both P and K were optimized (Figures 6.10a−c and 6.11a−c). For the Ems Estuary, the best-fit values for P increased from 0.56±0.01 to 0.67±0.02. The obtained values for $1/K$ varied significantly between stations, increasing from 1.26±0.07 to 4.30±0.06 at the upper station. In the Scheldt Estuary, P decreased from 0.76±0.01 to 0.62±0.01, while $1/K$ increased upstream from 1.20±0.04 to 5.00±0.04 at the most upstream station. In the second experiment, P was optimized while $1/K$ was set to 2, consistent with the values found by Kuijper and Van Rijn (2011) and Zhang and Savenije (2019). With $1/K$ fixed, the model performance was slightly adjusted, as along-channel variations in $1/K$ were compensated by changes in the best-fit value of P. Similarly, in the third experiment, K was optimized while adopting the power found by Gisen and Savenije (2015) for P. These experiments highlight the equifinality in the model, where alternative sets of K and P can yield similar outcomes. Fixing K influences the optimized value of P, and vice versa . However, optimizing both powers yields the most robust parameter set, and consistent regression coefficients.

In the second set of experiments (where both P and K were optimized), the model was optimized using either the entire dataset or a portion of it (as done in Section 6.4.3). Additionally, experiments were conducted where only data points with below-average discharge were used for optimization (Figures 6.10d−i and 6.11d−i). These experiments show

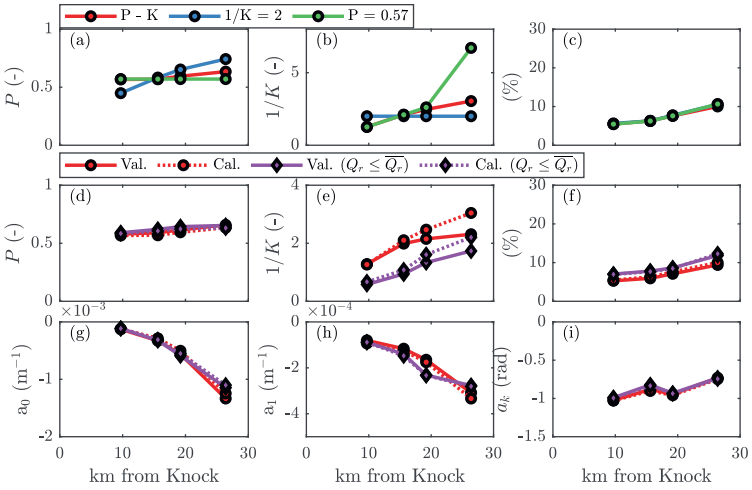


Figure 6.10: Overview of model coefficients for the Ems Estuary and the resulting unexplained variance, using alternative settings to optimize the power coefficients. Results are derived from Eq. 6.12. (a-b) Longitudinal profiles of the power coefficients P and K under different optimization conditions: when both powers are optimized (P - K), when $1/K = 2$, or when $P = 0.57$. (c) Resulting unexplained variance. Same as Panels a-c, showing the difference in optimized powers P and K when part of the dataset is used for optimization (Val.), compared to when the entire dataset is used (Cal.). Additionally, the influence of discharge on the obtained power is analyzed by using only below-average discharge conditions (Val. ($Q_r \leq \overline{Q_r}$) and Cal. ($Q_r \leq \overline{Q_r}$)), emphasizing the dependence of K on the discharge conditions. (d-e) Longitudinal development of the fitted model coefficients of the river and surge terms. (f) Amplitudes coefficients for the M_2 constituent.

that the selected period for model optimization has little influence on the best-fit values of P. However, the best-fit values of K showed more variability between periods, particularly at the most upstream stations. Notably, when only below-average discharge conditions were used, the values of $1/K$ displayed a clear offset in both estuaries, but maintained a similar along-channel trend. These results suggest that K is spatially variable and depends on discharge conditions. The interpretation of K is further explored in Section 6.6.

Figures 6.10g–h and 6.11g–h compare the best-fit regression coefficients a_0 and a_1. The values of these coefficients varied between experiments and were dependent on the values of P and K. Although K differed significantly, the longitudinal variations in a_0 primarily reflect the reduction in relative dispersion as a function of longitudinal coordinate and channel convergence, following a similar trend across all experiments. A *t-test* (p-value <0.05) confirmed that the values of a_0 and a_1 were significantly different from zero for all experiments. Figures 6.10f and 6.11f show the constant phase α_k of the M_2 constituent (see Eq. C.9), which increases upstream and shows little variation between experiments.

6.4.4.2 Constituent selection and the influence of missing data points

In the regression model, the constituents are selected using the adjusted Rayleigh criterion based on the length of record and post-fit significance testing. In addition, for each tidal constituent, it is tested if the contribution of the amplitudes related to the storm surge variations are significant (also see Appendix C.1.5). Furthermore, the selection procedure summarized above does not account for the possible influence of clipping on constituent

selection. These two aspects are further addressed in this section.

Significant surge events occur only several times in a year. Therefore, the statistical uncertainty is higher for the coefficients associated to storm surge terms in Eq. 6.12. In the performed experiments, the total number of included tidal constituents roughly varied between 10 through 18. However, only for a few constituents, the amplitude of storm surge terms were found to contribute significantly (Table S1 and S2). By testing the individual amplitudes, instead of the overall resulting amplitudes, overfitting is prevented and the total number of model coefficients is reduced.

To illustrate the influence of missing data, the correlation matrix of the model coefficients of the constant tidal variations are visualized for the most down- and upstream stations of the Ems Estuary in Figure 6.12. For both stations shown in Figure 6.12, a 518-day period was available to optimize the regression model for the Ems, and based on the adjusted Rayleigh criterion, a frequency separation of 1.1 10^{-2} d^{-1} is required. Missing and rejected data points significantly differed between the two stations. At Emspier, in total, 12% data points were missing due to gaps in the dataset, which increased by 1% after removing the data points where salinity is insignificantly different from the river salinity. At Terborg, 4% of the data points were missing, and an additional 33% of the data is rejected from the optimization of the harmonic model. This allows for the use and optimization of the harmonic model, but it influences the ability to distinguish between several tidal constituents. Constituents can become poorly identifiable because the low stages of the tidal cycles are less frequently sampled (i.e., these data points are rejected from the analysis).

Fore example, at Emspier, the correlation coefficients are found to be low (Figure 6.12a). As expected, the highest correlation coefficients occur between neighboring tidal constituents, peaking at 0.1 for O_1 and K_1. At Terborg, the correlation between neighboring tidal constituents increased, amounting to 0.18 for O_1 and K_1. However, a more distinct correlation exists between astronomical and shallow water constituents that differ in frequency by a factor two. For example, at Emspier, the correlation between M_2 and M_4 is only 5.7 10^{-3}, but increases for Terborg station to 0.22. Similar results are found for example for S_2 and MS_4, and for N_2 and MN_4 (Figure 6.12b).

The correlation between these constituents is not caused by an insufficiently long

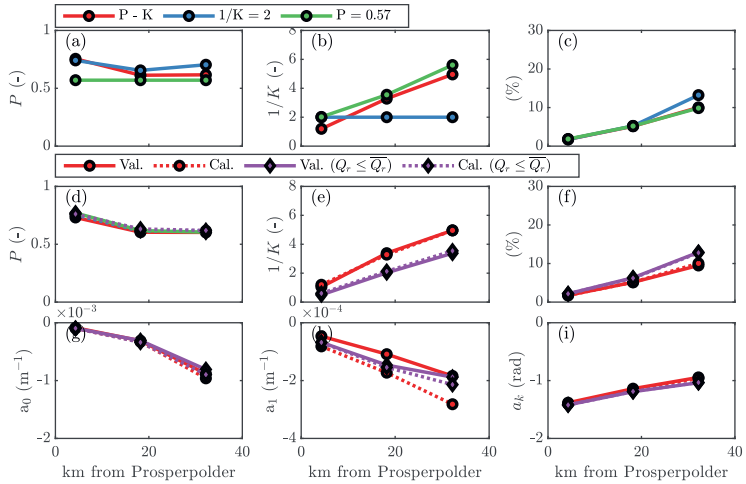


Figure 6.11: Same as Figure 6.10, but for the Scheldt Estuary.

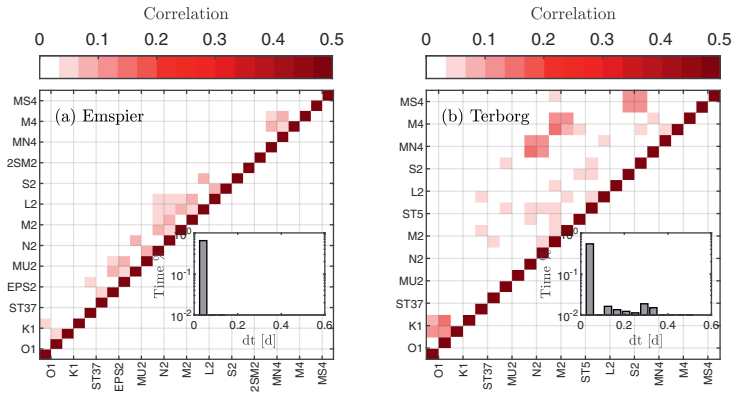


Figure 6.12: Correlation matrix of the model coefficients fitted for the harmonic model (storm surge terms are not included) at two station in the Ems Estuary, sub panels indicate the time-step distribution after the data point selection. (a) Correlation matrix for the downstream station Emspier. Model coefficients very weakly correlate for neighboring tidal constituents. (b) Correlation matrix for the most upstream station Terborg. Weak to modest correlation is observed between neighboring constituents K_1/O_1 and between the astronomical and shallow water constituents with (approximately) twice the frequency of the astronomical constituent.

data set, it only requires about 2 days to distinguish M_2 from M_4. The correlation arises from the fact that the salinity signal is less frequently sampled near low water slack, which hampers the isolation of shallow water tides from astronomical tides. In our analysis, the correlations as obtained are relative weak. However, additional synthetic experiments indicate that serious errors in the amplitudes and phases occur when ∼50% of the data signal is clipped, which agrees with the results of Evans and Pugh (1982). When the signal contains substantial clipping, results can be improved by rejecting the shallow water constituents from the analysis.

6.5 Influence of the down-stream boundary and unsteadiness

Section 6.4.3 has demonstrated the ability of steady-state regression models to effectively predict truncated salinity signals with an appropriate boundary condition. In the evaluation so far, the model's predictive performance depends on the assumption of a steady state, and on salinity measurements from a down-estuary station a boundary condition. This section evaluates the impact of unsteadiness and of the down-estuary boundary condition. We explore the parameterizations that eliminate the need for measured salinity at the seaward boundary.

The influence of unsteadiness in the salt balance increases for stations located closer to the coast (see Section 6.4.2). In Section 6.4.3 good results where obtained by using the low-passed filtered measured salinity signal from a down-estuary station as a boundary condition. This approach captures the salinity variations caused by unsteadiness in the lower estuary, allowing for the use of a steady-state formulation. Relying on a constant salinity value ($S_0 = 35$ psu) instead of a time-varying boundary (significantly) reduces the model's predictive skill. In the Ems, this leads to a reduction of about 15% in the

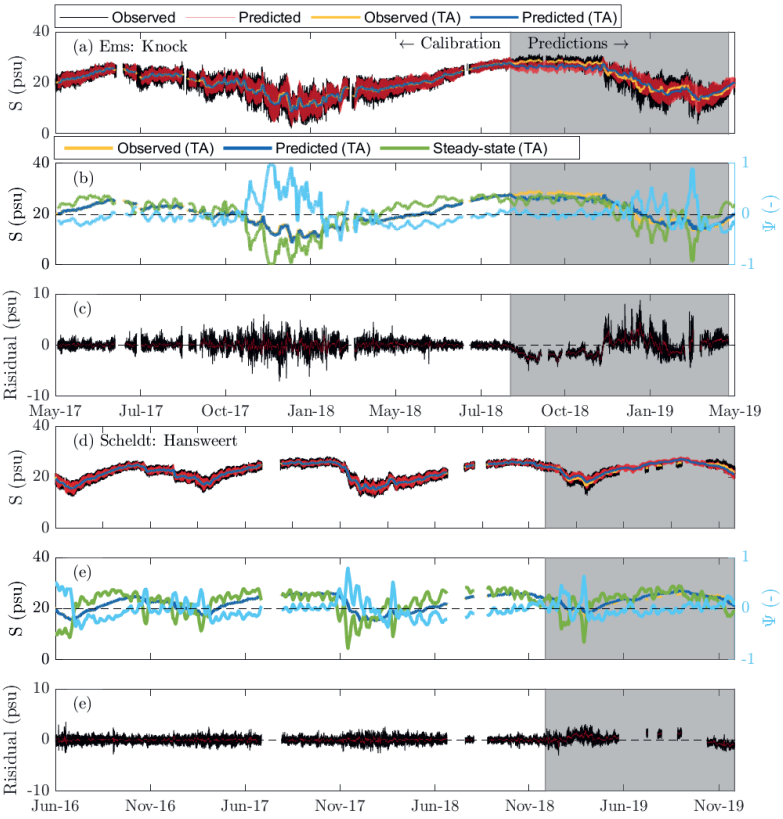


Figure 6.13: Data-model comparison using Eq. 6.13 and a constant salinity (35 psu) for the seaward boundary condition. (a) Observed and predicted salinity variations and TA (determined by a moving average, 1 day window) for the station Knock in the Ems estuary. The period for which the salinity is predicted is highlighted by a gray background. (b) Comparison between TA observed, TA predicted salinity variations, its equivalent steady-state salinity, and the TA predicted salinity when a steady-state approach is adopted 6.12a. (c) Residuals. (d-e) Same but for the station Overloop v. Hansweert in the Scheldt estuary.

explained variance. For the Scheldt, this reduction reached up to 50% at downstream stations and 15–25% at upstream stations when using Eq. 6.12 (see Tables 6.1, 6.2).

Eq. 6.16 parameterizes the salinity at the downstream station, where unsteadiness becomes significant. This approach enables accurate predictions of salinity at the upstream stations (with truncated signals) without the need to know the salinity values at the downstream boundary during the prediction phase. This approach led to a less then 5% reduction in explained variance for the Ems estuary. In the Scheldt estuary, it improved the models accuracy especially for the downstream stations, reducing the explained variance by 2–5% compared to the results in Section 6.4.3.

For non-truncated signals where unsteadiness effects are important, Eq. 6.13, which directly incorporates the AR(1) lag into the model formulation, can be applied. This model is demonstrated for the two most downstream stations—Knock and Hansweert (see Figure 6.13)—where unsteadiness is most pronounced. For these stations, the unexplained variance was 8.9% and 11.5%, with RMSE values of 1.9 and 0.9 psu, respectively. In contrast, the steady-state approach explained only 34% and 77% of the variance. The empirical response times (T_r) for adjustment, derived from the model, were 24 and 35 days, which is notably longer than the typical period over which discharge variations occur. While Eq. 6.13 better captures the salinity variations at these stations and significantly reduces the auto-correlation in the residuals, it still does not fully capture the dynamics, but presents an improvement over the steady-state approach.

In the steady-state approach, salt concentrations directly reflect the current forcing conditions. In contrast, the unsteady approach depends on both the previous state and the changes introduced by variations in the forcing conditions. The model embedding Eq. 6.13 can be used to express the salinity that would be reached under unchanged forcing conditions (i.e, steady-state), and infers whether the system is gaining or losing salt:

$$\tilde{S}_s = \left(1 - a_0 K \frac{|Q_r|}{D_0} + a_1 \tilde{D}t\right)^{1/K}, \tag{6.17a}$$

$$\tilde{S}_{st} = \left(1 - \frac{a_0}{1 - a_1} K \frac{|Q_r|}{D_0}\right)^{1/K}, \tag{6.17b}$$

$$\Psi = \frac{\tilde{S}_s - \tilde{S}_{st}}{\tilde{S}}, \tag{6.17c}$$

where $\tilde{S}_s$ represents the predicted scaled subtidal salinity, $\tilde{S}_{st}$ is the equivalent steady-state salinity, and Ψ is the scaled difference. Specifically, $\Psi < 0$ indicates gaining salt, $\Psi > 0$ indicates a loss of salt, and $\Psi = 0$ indicates a steady state. Figure 6.13b,e illustrates the resulting values for Ψ, showing a clear seasonal cycle in both systems. Typically, during spring and summer, the estuary gains salt, while in autumn and winter, salt loss dominates. Similarly, the amplitudes of the harmonic component can be calculated, showing that the amplitudes are relatively larger during periods of increased discharge ($\Psi > 0$), leading to stronger along-estuary gradients compared to periods of decreased discharge ($\Psi < 0$).

6.6 Critical evaluation of adopted model formulation

The previous sections show that the proposed model, which embeds the Savenije (1986) is formulation, is well-capable of prediction the salinity variations. This formulation is empirical rather than based on first principles. Therefore, in this section, we compare the Savenije (1986) model with the more theoretically substantiated Gay and O'Donnell (2007) formulation, and use the Gay and O'Donnell (2007) formulation to evaluate the obtained best-fit powers and interpret the meaning of the Van der Burgh constant.

6.6.1 Comparison with Gay and O'Donnell model

Savenije (1986) assumes that the Van der Burgh coefficient (K) is constant. This assumption conflicts with our best-fit values of K, which exhibit significant site-to-site variations, specifically in the Scheldt Estuary. Also, the physical interpretation of K provided by Savenije (2015) does not match with the best-fit values, and with the general knowledge of both systems.

Alternative models that avoid the use of Eq. 6.3 have been proposed by Kuijper and Van Rijn (2011) and Zhang and Savenije (2019), resulting in similar model structures, where K is set to 0.5. Alternatively, in the Gay and O'Donnell (2007) formulation, who derived a descriptive equation for along-channel salinity variations directly from Eq. 6.1, the power in their formulation is described by physical properties. Assuming a linearly

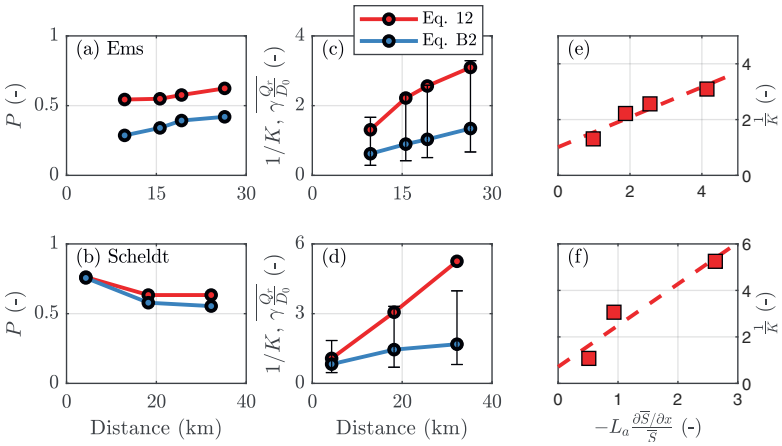


Figure 6.14: (a) Comparison of the power P obtained using Eq. 6.12 and Eq. C.15 in the Ems estuary. (b) Same as (a), but for the Scheldt estuary. (c) Comparison of the power $1/K$ from Eq. 6.12 with the time-series averaged power $\gamma\overline{\frac{Q_r}{D_0}}$ obtained with C.15, along with its variability, in the Ems estuary. (d) Same as (c), but for the Scheldt estuary. (e) Relationship between $-L_a\frac{\partial\overline{S}/\partial x}{\overline{S}}$ and the best-fit values of K, expressed as $\frac{1}{K}$. The dashed lines represent the fitted regression line. (f) Same as (e), but for the Scheldt estuary.

tapered estuary and a constant along-channel dispersion coefficient, at equilibrium, their model reduces to:

$$\frac{S_x - S_r}{S_0 - S_r} = \left(1 - \frac{a}{A_0}x\right)^{\frac{Q_r}{aD_x}}, \tag{6.18}$$

where a represents the estuary tapering factor, and the dispersion coefficient is constant in this model ($D_0 = D_x$). A key difference with Eq. 6.5 is that the exponent $\frac{Q_r}{aD_x}$ consists of physically interpretable variables. Here, Eq. 6.18 is used to obtain analogous equations to Eq. 6.11 and 6.12 for the harmonic regression model, resulting in Eq. C.14 and C.15 in Appendix C.2. With Eq. 6.18 as a base-function, two power coefficients are optimized: again the power P for the dispersion coefficient, and γ, which determines the magnitude of the power $\gamma\frac{Q_r}{D_0}$. Extending this model with an AR(1) component is less straightforward due to the time-varying component appearing in the power. For this reason, we used the Savenije (1986) formulation in our approach, rather than the Gay and O'Donnell (2007) formulation.

The predictive skill of Eqs. C.14 and C.15 is comparable to the results discussed in Section 6.4.3, although the explained variance is approximately 2% lower for both estuaries (Table C.1 and C.2). With both models resulting in similar predictive skill, it is interesting to compare the best-fit value of the optimized powers (Figure 6.14 a-d). Panels a and b in Figure 6.14 compare the best-fit values for P. The values show similar along-channel variations; however, the value obtained using Eqs. C.14 and C.15 are substantially lower in the Ems, whereas more comparable values are obtained for the Scheldt. Panels c and d in Figure 6.14 compare the best-fit values of $1/K$ with the time-series averaged power $\left(\gamma\overline{\frac{Q_r}{D_0}}\right)$ and its variability, where the overbar denotes the

long-term average. Again, both powers show a similar trend in the up-estuary direction, but their magnitude differs. This suggests that the locally optimized Van der Burgh constant may have a similar physical meaning as the power in the model by Gay and O'Donnell (2007). This is further explored in the next section.

6.6.2 Interpretation of the Van der Burgh constant

In the model of Gay and O'Donnell (2007), the power governs the time varying spatial scale of dispersion and advection relative to the imposed scale over which channel geometry changes. To evaluate whether the locally optimized Van der Burg constant could have a similar meaning as the power in the model of Gay and O'Donnell (2007), the values of $1/K$ are plotted against $-L_a \dfrac{\partial \overline{S}/\partial x}{\overline{S}}$. The latter can be expressed using Eq. 6.2 as $-(\overline{Q_r} L_a)(\overline{D_x} A_x)^{-1}$, and the same group of parameters is recognized as in Eq. 6.5, which determines the relative dispersion coefficient. Recognizing that $-L_a = \dfrac{A_x}{\partial A_x/\partial x}$ allows to write $1/K \propto \left(\dfrac{\overline{Q}_r}{\overline{D}_x \partial A_x/\partial x}\right)$ or $1/K \propto \left(\dfrac{\overline{u}_r}{\overline{D}_x} \dfrac{A_x}{\partial A_x/\partial x}\right)$, which results in the same parameter group as the power term in Eq. 6.18. We calculate the long-term average salinity and its along channel derivative from the average salinity distribution shown in Figure 6.4. For the cross-sectional convergence lengths (L_a), values of 2.2×10^3 m for the Ems and 1.8×10^3 m for the Scheldt estuaries were used.

Based on the above, panels e and f in Figure 6.14 show the ratio $-L_a \dfrac{\partial \overline{S}/\partial x}{\overline{S}}$ obtained from the data against the best-fit values for $1/K$ for both estuaries, which results in near-linear relation for the values within one systems. The relationships differ between the Ems and the Scheldt estuaries, which is confirmed by a statistically significant difference in the slopes of the fitted regression lines. Whether this difference in slope is due to inherent physical properties of the estuaries or represents an artifact of the model, remains unclear. However, if the relationship seen in panels e and f in Figure 6.14 holds within one system, it suggests that the power $1/K \propto \left(\dfrac{\overline{u}_r}{\overline{D}_x} \dfrac{A_x}{\partial A_x/\partial x}\right)$ and the locally optimized Van der Burgh constant indeed has a similar physical meaning as the power in the model of Gay and O'Donnell (2007). The inverse of our locally fitted Van der Burgh constant may then be interpret as an empirical coefficient that scales with the average spatial scale of the dispersion and advection magnitude, relative to imposed scale of channel geometry change. Finally, this also explains the substantially lower values for $1/K$ when only using low discharge condition to optimize the model (see Section 6.4.3).

6.6.3 Sensitivity to the river discharge

In Section 6.6.1, we observes that the best-fit values for the power P, derived from using either Eq. 6.5 or Eq. 6.18 as the base function, show comparable trends along the channel. However, in the Ems, values obtained with Eq. 6.18 are noticeably lower, while in the Scheldt, both equations yield similar values. Here we further evaluate the observed difference in the best-fit values of P, which has a relation to the difference in importance of the river discharge.

To find out if the power P differs between the Ems and Scheldt Estuaries, the relationship between Q_r and D_0 was examined by calculating the dispersion coefficient according to Eq. 6.2, using salinity time-series and the observed gradients between different stations. The obtained dispersion coefficients are subsequently used to obtain an estimate of P in $Q_r^P \propto D_x$, where the power is estimated by means of a regression. For the Ems Estuary, lower values of P (0.4–0.55) are obtained from the data compared to the Scheldt Estuary (0.66–0.79), which is in agreement with a substantial difference in the value of P for the two estuaries that can be expected based on Eq. 6.18. A likely reason for the

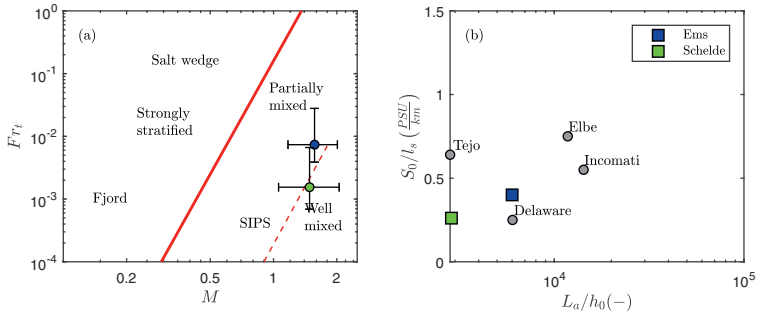


Figure 6.15: (a) Classification of the Ems and Scheldt Estuary in the Geyer and MacCready (2014) diagram, including variability around the average location in the diagram that results from spring-neap tide and discharge variations. (b) Matrix to assess the sensitivity of advective displacements by storm surges, based the dimensionless shape factor $\frac{L_a}{h_0}$ for converging estuaries and a typical salinity gradient $\frac{S_0}{l_s}$. Location of different estuaries are based on literature (Gisen and Savenije 2015).

fact that this effect is not fully captured by Eq. 6.5 lies in the model structure. The sensitivity to discharge variations can be accommodated by modifying K in Eq. 6.5. Hence, differences in the actual values of P are compensated for by an altered value of K. This model characteristic may partially account for the variations observed between the two systems in the previous section. However, in both systems, estimates of P derived from the data show an increase in the up-estuary direction. This aligns with the along-channel trend of best-fit values for P in the Ems. In the Scheldt, however, the best-fit values indicate a decrease. The elevated value at the first station in the Scheldt is likely due to its close proximity to the downstream boundary station, which limits the sensitivity to discharge fluctuations.

6.7 Discussion

6.7.1 Possibilities and limitations of the model

The proposed harmonic regression model to predict estuarine salinity variations at monitoring sites yields favorable results for two applications. To demonstrate in which type of systems the model works best, the Ems and Scheldt Estuary can be projected onto the classification diagram by Geyer and MacCready (2014). This diagram maps the estuarine parameter space based on a mixing parameter M and the freshwater Froude number Fr_f. M quantifies the effectiveness of tidal mixing for stratified estuaries and Fr_f is a measure for stratification driven by gravitational circulation, which scales as $Fr_f^{\frac{2}{3}}$ (MacCready 1999). To classify the Ems and Scheldt Estuary in the $M - Fr_f$ plane, we used the observed forcings at the boundary and geometry estimates from Gisen and Savenije (2015), shown in Figure 6.15a. Both estuaries fall in the lower right quadrant of the diagram. The Scheldt Estuary is classified as a well-mixed system, bordering the weakly stratified SIPS (strain-induced periodic stratification) regime. The Ems Estuary falls in the SIPS regime and approximates the partially mixed regime for higher discharges. The fact that the Ems Estuary is located in the SIPS regime may explain why the portion of unexplained variance was higher compared to the Scheldt.

The proposed regression model is based on a steady-state salinity distribution, best applicable when the adjustment time-scales of the salinity front are shorter than the time-scales at which the discharge varies (Kranenburg 1986; Monismith et al. 2002). An expression for the adjustment time is $T_A = l_s \frac{1}{2} \frac{A}{Q_r}$ for systems dominated by tidal stirring and $T_A = l_s \frac{1}{6} \frac{A}{Q_r}$ for exchange dominated systems (MacCready and Geyer 2010). These expressions indicate that the adjustment time increases with the length of the system and is inversely related to the strength of the residual current. This suggests that the proposed steady-state model is best applicable to systems with relatively shorter salt intrusion lengths and stronger residual currents, which allow for quicker adjustment to variations in discharge. For the systems evaluated in this study, spectral analysis of the discharge time series reveals that the majority of discharge variations (over 75%) occurs at periods below 14 days, for both systems. The adjustment times calculated for exchange-dominated systems, based on average intrusion lengths (98 km for the Ems, 66 km for the Scheldt), discharges (79 m^3/s for the Ems, 66 m^3/s for the Scheldt), and cross-sectional areas ($1.4{\cdot}10^4$ m^2 at Knock, $1.1{\cdot}10^4$ m^2 at Hansweert), are 22 days for the Ems and 33 days for the Scheldt. These values agree reasonable well with the empirical derived response times. In both cases, the adjustment time exceeds the typical time scale of discharge variations.

The effects of unsteadiness were found to increase in the down-estuary direction, while remaining relatively small at the more up-estuary station (Figure 6.5). Hence, although in both systems the adjustment time scale exceeds the typical timescale of discharge variations, a steady-state model can still be applied successfully in the more up-estuary sections. This is possible by using a time-varying boundary condition at a down-estuary station, where unsteadiness becomes more significant (see Section 6.4.3), or by employing a parameterized boundary condition (see Section 6.5). For stations where unsteadiness is significant and the salinity signal is not truncated, the formulation with the AR(1) extension can be effectively applied. Ideally, this approach would also be useful for stations with truncated signals. However, for these cases, we were unable to obtain reliable estimates of the AR(1) coefficient. Additionally, a constant empirical response time is currently used, but theoretically, an adjustment time that varies with discharge would be more appropriate.

The importance of storm surges varied between the two systems. Including the effect of storm surges improved the explained variance by $1-2\%$ and $0.2-0.5\%$, respectively for the Ems and Scheldt Estuary (see Section 6.4.3). The latter suggests that the Scheldt Estuary is less sensitive to storm surges compared to the Ems Estuary. This can be explained by differences in the geometry and the intrusion lengths. A shorter intrusion length results in larger longitudinal salinity gradients, i.e. a higher sensitivity to salinity variations caused by advective displacements. Similarly, the influence of tides and storm surges on local salinity often increases for higher discharges (Figure 6.16). The shape of the estuary largely determines the relation between the vertical and horizontal excursions (Eq. 6.8), and scales with the channel convergence to depth ratio ($\frac{L_a}{h}$). This ratio is higher for the Ems compared to the Scheldt Estuary, and hence a larger vertical excursion length is found for the Ems Estuary (Figure 6.6b, d). Figure 6.15b shows a simple matrix, based on the intrusion length and estuary shape, to demonstrate the sensitivity of a (converging) estuary to storm surges. Estuaries where the salt intrusion length is closer to the tidal excursion are likely more sensitive to storm surges.

The horizontal excursion resulting from storm surges is remarkably well-captured by a simple linear relation. The appropriateness of this relation depends on the wave character of the occurring storm surge. When a storm surge wave has a standing wave character, the resulting horizontal tidal excursion varies near-linearly with the surge water levels (Figure 6.6). For the Ems and Scheldt estuaries, adding the extra horizontal excursion resulting from storm surge water levels allowed us to reconstruct the observed salinity variations. However, it is likely that in other systems such a simple relation cannot describe the dynamics. For example, Li and Weeks, et al. (2010), Gong et al. (2018) and Kranenburg et al. (2022) found that in partially- and stratified systems, storm surge events can significantly increase mixing and reduce stratification, arresting the estuarine

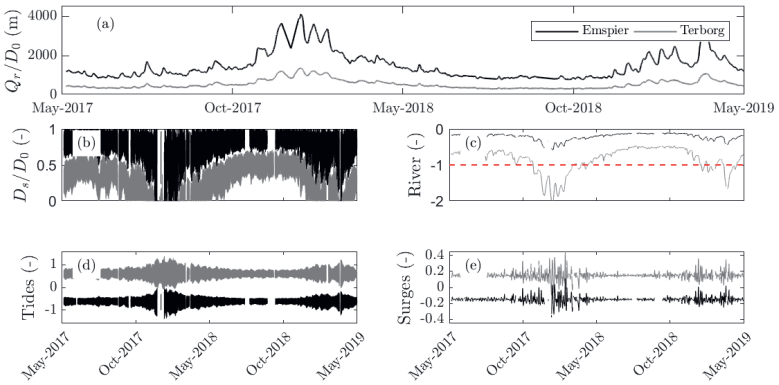


Figure 6.16: Components of the harmonic regression model, based on Eq. 6.12, illustrated for the stations Emspier and Terborg. (a) Temporal variation in $\frac{Q_r}{D_0}$, which scales each term in the regression model. (b) Full signal (i.e., relative dispersion) of panels c−e. (c) Contribution of the tide-average term, resulting from a balance between dispersion and flushing. The red dashed line indicates the threshold value at which the signal is truncated. (d-e) Contribution of the tidal and storm surge terms, resulting from a horizontal excursion of the salinity distribution. For clarity of the figure, an offset of ±0.6 in d and ±0.15 in e is used.

circulation. In our regression model, surge water levels increase the tidal range and mixing through Eq. 6.14. Whether or not the regression model is capable of capturing storm surge dynamics in more stratified systems requires further testing. In long estuaries, where the typical wavelength of a surge wave does not exceed the length scale of the estuary, storm surge waves may have a progressive character. These systems may require a frequency specific approach to capture the storm surge variations.

6.7.2 Interpretation on causes of salinity variations

The regression model facilitates the examination of various factors influencing along-channel salt distribution and variability in salt concentration at individual sites. As discussed in Section 6.6, the along-channel variations in the best-fit values of K seem to reflect changes in dispersive and advective magnitudes relative to the imposed scale of channel geometry change $\left(1/K \propto \frac{\overline{u}_r}{\overline{D}_x}\frac{A_x}{\partial A_x/\partial x}\right)$. Further research is needed to confirm this relationship across different systems and explore the sensitivity to the value of P. The harmonic regression model can elucidate the causes of salinity variations at specific sites. For example, predictions for the Ems Estuary (see Section 6.4.3) are divided into contributions from tide-averaged oscillations, tidal dynamics, and surge-induced variations, as shown for the most down- and upstream stations in Figure 6.16. For these stations, approximately 75% of the variance is attributed to tidal dynamics, whereas for Pogum and Gandersum, tide-averaged oscillations contribute around 35% to 40% of the variance. The overall contribution of storm surge variations is limited to about 2%. In the steady-state models, each term is scaled by $\frac{Q_r}{D_0} \propto Q^{P-1}$, which predominantly reflects the discharge variations. Hence, each term amplifies with increasing discharge. With the model to include unsteadiness effects (trough auto-regressive term) as proposed, the interpolation of the terms changes, but allow for a similar decomposition of the salinity signal.

6.7.3 Comparison with other predictive methods

The goal of this paper is to develop a tool capable of providing accurate short-to-medium term predictions, while also providing insights in the contributing mechanisms. An alternative approach for obtaining short-to-medium term predictions is the use of artificial neural networks (ANNs). Several studies showed that ANNs are well capable of providing accurate estimates of estuarine salinity (Rath et al. 2017; Zhou and Yang, et al. 2017; Zhou and Liu, et al. 2020). A well-trained ANN may outperform the regression model proposed herein in terms of predictive skill, especially when the salinity signal contains non-tidal variations and the unsteadiness of the estuary is high. Compared to an ANN, the advantage of the proposed harmonic regression methodology is the transparency in the model structure, offering insight into the contribution of various physical mechanisms. This is in contrast to an ANN approach, in which the relation between the input and the explained variables is unclear. Our approach may better predict events of salinity intrusion, in which conditions are more extreme than what is captured by the training data.

6.8 Conclusion

A harmonic regression model has been developed and evaluated to analyse and predict salinity variation at monitoring stations. The model is based on the steady-state salt intrusion model of Savenije (1986) and is extended to capture variations caused by tides and storm surges. Tidal variations are represented using harmonic functions, while storm surge-induced changes are modeled through a linear relationship, which is theoretically justified when the typical wavelengths of storm surges have longer wavelengths than the estuary's length scale. An autoregressive term is introduced to capture unsteadiness effects. To accurately reproduce local salinity, the model optimizes two power coefficients and proportionality constants. Salinity predictions are truncated to account for periods when the intrusion length occasionally reaches the monitoring station, though this truncation affects the identifiability of higher harmonics. The model's predictive performance was demonstrated at seven stations in the upper sections of the Ems and Scheldt Estuaries, explaining between 87.4% to 96.4% of the observed variance. The dominant salinity response to storm surge variations was well captured, with horizontal displacement of the longitudinal salinity profile being the primary response. This reveals the sensitivity of salinity in well-mixed systems to storm surges, based on a simple matrix relating geometry and intrusion length. Close to the coast, where the estuary has widened, effects of river discharge unsteadiness increases. For stations with untruncated signals, the extended autoregressive model enabled accurate predictions at these sites, and assessed the lagged response. The best-fit power coefficients were critically evaluated, providing insights into the physical interpretation of the Van der Burgh constant, showing that it scales with the spatial scales of dispersion and advection, relative to changes in channel geometry. The proposed harmonic regression model is expected to accurately predict estuarine salinity in well-mixed systems. For those systems, the model can act as an analytical tool to interpret and predict non-stationary salinity signals at monitoring stations, requiring minimal input.

CHAPTER 7

Synthesis

7.1 Main findings in a broader perspective

Many important insights into how channel complexities contribute to up-estuary salt transport through mechanisms associated with tidal dispersion originate from analytical work conducted between the 1950s and 1980s (Stommel and Farmer 1952; Taylor 1953; Schijf and Schönfled 1953; Okubo 1973; Fischer et al. 1979; Dronkers 1978; Dronkers and Van de Kreeke 1986). In the 1990s and 2000s, estuarine research focused particularly on understanding the estuarine circulation resulting from both classical gravitational circulation and strain-induced circulation, the role of spring–neap variability, and the lateral exchange processes influencing the estuarine circulation, as summarised in MacCready and Geyer (2010) and Geyer and MacCready (2014). Over the past decade, more attention is given again to the influence of geometric complexity and tidal-dispersion mechanisms on salt transport, including the development of new analytical frameworks and insights for tidal-dispersion processes (Nguyen and Savenije, et al. 2008; MacVean and Stacey 2011; Chen and Geyer, et al. 2012; Dijkstra and Schuttelaars and Kranenburg 2022), and efforts to identify the origins of observed dispersive signatures associated with geometric features (Garcia and Geyer 2022; Garcia and Bo, et al. 2025). In the context of this renewed interest in tidal-dispersion processes, this thesis advances the mechanistic understanding of salt dispersion in estuaries with complex geometries by revisiting classical tidal-trapping theory, isolating key exchange processes through idealised numerical modelling, and analysing their behaviour in the geometrically complex Rhine–Meuse estuary, with a particular focus on tidal-dispersion mechanisms of baroclinic origin.

Classical analytical descriptions of tidal trapping assume simplified geometries and a single, well-defined exchange mechanism, allowing the resulting dispersive effect to be expressed in one-dimensional dispersion coefficients for the additional transport. However, as shown in Chapter 2, these formulations contain ambiguities regarding how the dispersive effect depends on the phasing between main-channel and side-channel currents. Using an idealised numerical model, this thesis demonstrates that the dispersive effect scales with the velocity phase difference in a manner consistent with early theoretical work (Schijf and Schönfled 1953; Dronkers 1978), and clarifies why the framework of MacVean and Stacey (2011) yields contrasting results (Chapter 3): its one-dimensional salinity balance neglects changes in the phasing of the main-channel current and therefore misrepresents the underlying mechanism. By extending the idealised model to include both barotropic filling and emptying and exchange of a diffusive nature, the thesis shows that their combined effect can be quantified using a Péclet number specific to tidal trapping. Importantly, this combined effect is not a simple superposition of barotropic and diffusive contributions.

Beyond these mechanistic insights, the analysis also provides a methodological framework, extending the theoretical approach of Dronkers (1978), for evaluating the potential additional transport arising from different channel-trap exchange mechanisms and for identifying where this transport is to manifest spatially. A limitation of the presented analysis is that the diffusive exchange was represented by a constant diffusion coefficient. Baroclinic processes often dominate both the channel–trap exchange and the internal

redistribution of the trapped salinity field. The strength of these baroclinic processes is often largely controlled by the along-channel density gradient in the main channel and result in a response that cannot be represented by a constant diffusion coefficient. Improving our understanding of how the transport mechanisms associated with tidal dispersion (including the effects of baroclinicity) vary across different regimes is therefore an important direction for future research to advance our understanding of tidal trapping (see recommendations Section 7.3). We hypothesise that the role of baroclinic processes in tidal trapping may not differ substantially between traps under low-energy conditions, where density-driven (diffusive) exchange primarily occurs at the mouth of the junction. In contrast, under highly energetic conditions, this exchange is displaced into the weakly energetic parts of the system, yielding a broadly comparable overall exchange efficiency, albeit with a shift in the relative contributions of lateral and vertical shear.

Chapters 4 and 5 extend the analysis to the Rhine–Meuse estuary, where channel complexities such as harbors and bathymetric steps occur within a single tidal-excursion length and interact with the larger estuarine channel network. Observations and 3D modelling show that channel–harbour exchange in the Rotterdam Waterway is dominated by baroclinic processes and varies strongly between harbours due to spatial variability in the salinity field. An analytical expression is proposed for the (along-estuary) dispersive effect of density driven channel–harbour exchange. This expression demonstrates that (unlike classical formulations for dispersion coefficients derived for barotropic filling and emptying of traps or for purely diffusive exchange) the effective dispersion coefficient depends directly on the along-channel salinity gradient, reflecting its dependence on the underlying baroclinic driving processes. This dependence of the dispersive effect on the along-channel salinity variation explains the pronounced site-to-site variability in the contribution of individual harbours within the Rotterdam Waterway, reflecting the spatial heterogeneity of the baroclinic exchange processes rather than the more uniform behaviour expected from classical tidal trapping driven by barotropic filling and emptying, which typically scales with the discharge-amplitude ratio (Dronkers 1978; MacVean and Stacey 2011).

We identified through which mechanism channel-harbour exchange contributes to the up-estuary salt transport. However, the overall effect of channel-harbour exchange was found to be limited. Bathymetric steps along the Rotterdam Waterway were identified as another geometric feature capable of initiating exchange mechanisms associated with tidal-dispersion, providing an explanation for the observed increase in tidal dispersion upstream of the depth transition that could not be accounted for by channel–harbour exchange alone (Chapter 5). Numerical modelling shows that, in a set-up similar to the Rotterdam Waterway, these steps influence salt intrusion in two distinct ways: (1) by modifying tidal-wave reflection and reducing tidal currents downstream of the transition, which strengthens the estuarine circulation; and (2) by creating a defined location where salinity fronts develop, locally enhancing transport by the estuarine circulation and, due to their highly localised nature, amplifying the tidal-dispersion-driven salt transport upstream of the depth transition. As with the harbour-driven baroclinic tidal-trapping mechanism, the resulting increase in tidal dispersion upstream of the depth transition is baroclinic in origin. Although this mechanism was not explicitly expressed in terms of an effective dispersion coefficient, it is likewise expected to depend on the along-channel salinity gradient, in addition to the geometric properties of the steps themselves. These bathymetric steps were found to exert a profound influence on the heterogeneity of the salinity field, which in the Rotterdam Waterway is observed to have a strong effect on the channel–harbour exchange. Because features such as harbours, bathymetric steps, and the larger-scale channel-network interactions are all present within a single tidal-excursion length, a more complete understanding of tidal dispersion in the Rhine–Meuse estuary requires applying a quasi-Lagrangian salt-flux decomposition method, such as that of Dronkers (1978), to the full channel network (see recommendation Section 7.3.1). Furthermore, their combined response may not withhold us from parametrising the processes individually in a physically grounded dispersion formulation, but the overall system response cannot adequately be described as the sum of the individual contributions. Their added value is therefore predominantly to summarise the processes in a synoptic manner that can be used to

interpret how the system functions.

In Chapter 6, the thesis shifts from mechanistic understanding to prediction by proposing a hybrid-harmonic regression model for short-to-medium-term salinity forecasts at monitoring stations. The proposed model provides an easily applicable and efficient way to predict salinity variations at monitoring stations with minimal data requirements. The method performs well in the relatively well-mixed Ems and Scheldt estuaries, providing fast and accurate predictions with minimal data requirements. Beyond its predictive capability, the fitted harmonic coefficients offer a compact diagnostic summary of system behaviour, reflecting the relative importance of advective and dispersive processes imposed by local geometry. Several limitations remain: the model requires sufficient training data, loses interpretability in stratified systems, and assumes a single dominant longitudinal axis, making it less suitable near geometric complexities such as junctions or multi-branch networks. Yet, the performed analysis showed that this type of model provides an additional tool for analysing salinity records at stations located within a single branch, where the underlying dynamics remain sufficiently coherent for harmonic-based diagnostics.

Overall, a central insight of this thesis is that the tidal-dispersion mechanisms due to geometric complexities in the Rhine–Meuse estuary are predominantly baroclinic in origin. Because the driving mechanisms differ fundamentally from the barotropically driven tidal-dispersion mechanisms described in classical theory (Stommel and Farmer 1952; Okubo 1973; Fischer et al. 1979; Dronkers 1978; Geyer and Signell 1992; MacVean and Stacey 2011), they obey different dispersion relationships which are expected to depend on the along channel salinity gradient. These differing dynamics imply that the relative importance of barotropic and baroclinic tidal-dispersion mechanisms will vary between estuaries depending on their characteristic length, and may also vary among different sections within a single estuary. Furthermore, this thesis highlights that the dispersive effects of complex geometries—such as side channels, harbours, and bathymetric steps—can be understood in isolation under idealised conditions. However, in real estuaries these features often lie within each other's dynamical reach and interact within a single tidal-excursion length. Their combined influence is therefore different from the sum of their isolated contributions.

A more complete understanding of these interactions requires clarifying how individual features modify the main channel flow and salinity field, which in turn calls for extending quasi-Lagrangian analyses to study channel networks containing multiple, closely spaced geometric features. Moreover, because these features do not contribute to dispersion locally, representing their influence through typical physics-grounded one-dimensional dispersion parameterisations presents a serious challenge. For the specific purpose of describing the overall combined dispersive effect, data-driven and machine-learning methods are likely to offer a more efficient and flexible framework for parameterising these processes.

7.2 Implications of Our Findings for Possible Salt Intrusion Mitigation Measures

Salt intrusion in the Rhine–Meuse estuary is an increasing problem. Based on the insights gained from this thesis, several recommendations are presented below.

1. Is the infilling of harbours or the transformation of harbours into tidal parks beneficial to mitigating salt intrusion?

The analysis and insights presented in Chapter 4.4 provide input for the following consideration: In a partially stratified system, the role of harbours can, from a simplified perspective, be understood as the result of two opposing effects: (1) they contribute to up-estuary salt transport by enhancing tidal dispersion mechanisms (Chapter 4), and (2) they enlarge the tidal prism, thereby increasing tidal currents which promote vertical mixing in the main channel and reduce the strength of the gravitational circulation

(Abraham et al. 1986). Chapter 4 shows that the contribution of individual harbours to up-estuary salt transport is largely governed by the tidal salinity range in the main channel, which explains the substantial differences in the resulting additional salt transport between neighbouring harbours. The increase in tidal prism depends primarily on the additional intertidal storage area introduced by the harbours. Consequently, the net balance between the additional tidal dispersion and enhanced mixing varies between individual basins, implying that the potential benefits of harbour closure differ from one basin to another. In the New Meuse, the tidal salinity range is lowest near the two largest harbours (Eem/HB-4 and Waal/HB-5) during lower discharges, resulting in a limited contribution to up-estuary salt transport (see Chapter 4). However, owing to their large size, these harbours substantially increase the tidal prism. Exploratory model results indeed indicated that closing these harbours increased salt intrusion, supporting the hypothesis that the reduction in tidal currents, and the associated strengthening of estuarine circulation, outweighs the loss of the additional salt transport introduced by the channel–harbour exchange. The smaller, upstream estuary located harbours (Rijn/HB-6 and Maas/HB-7) contribute relatively strongly to up-estuary salt transport, while their small size limits their effect on the tidal prism. Model results indicate that closing these harbours would decrease salt intrusion. Hence, whether complete harbour closure is beneficial for reducing salt intrusion is site-dependent and governed by the interplay between intertidal storage area, main channel tidal salinity range, and harbour depth.

In the previous paragraph, complete harbour closure was considered. An alternative is to reduce harbour depth while preserving the intertidal area, effectively transforming them into tidal parks (Gemeente Rotterdam 2024). Such a measure would likely reduce the salt intrusion length for most harbours, provided that the intertidal storage area is maintained. This is because the tidal prism in the main channel would remain largely unchanged, while the additional salt transport dominated by density-driven exchange between the harbour and the main channel would be substantially reduced (Chapter 4). Reducing the depth weakens the density driven exchange and thereby limits the harbour-induced contribution to up-estuary salt transport. As a consequence of the depth reduction, the dominant tidal trapping mechanism is expected to shift from exchange that is diffusive in nature to advective out-of-phase exchange (Chapter 2). However, the contribution of advective out-of-phase exchange to the up-estuary salt transport remains small, as the ratio of harbour-to–main-channel discharge amplitude is limited (see Chapter 2 and Dronkers (1978)).

2. Could (partial) shallowing of the New Meuse help reduce salt intrusion?

Partial channel depth reduction is often proposed (or discussed) as a measure to limit salt intrusion, as gravitational circulation is highly sensitive to channel depth (Hansen and Rattray 1965; Chatwin 1976). As highlighted in Chapter 5, the way in which the transition from a deep, navigation-maintained dredged section to shallower parts of the estuary is implemented is crucial. The optimal bathymetric configuration depends on local estuarine conditions, implying that depth-reduction strategies must be carefully tailored to the specific system. The results presented in Chapter 5 suggest that a transition with a mild longitudinal slope, with the depth change located further downstream, is more effective than an abrupt shallowing. Sharp transitions tend to promote partial reflection of the barotropic tide, resulting in a reduction of the cross-sectionally averaged currents. This, in turn, weakens bottom-boundary-induced mixing and favours the formation of salinity fronts, which can reduce mixing efficiency and counteract the intended mitigation of salt intrusion. From this perspective, positioning a mild bed-slope transition further down-estuary is likely to be more beneficial than extending the non-dredged river section and creating an abrupt depth transition.

The main channel depth and the present location of the depth transition in the New Meuse play a controlling role in how harbours salt is exchanged with main channel. First, in the current situation, the largest harbours, Eem (HB-4) and Waal (HB-5), are situated within the region characterized by reduced salinity dynamics, which limits their dispersive

contribution through the tidal trapping mechanism. If the position of the depth transition were to shift slightly seaward of the harbours, they would then be located in a region with the strongest tidal salinity range. This may substantially increase their contribution to the overall salt intrusion. How this truly plays out depends on how the effect of an increase in the tidal salinity range compares to the reduction of the gravity dynamics driven salt exchange. Secondly, when the depth of the main channel (and adjacent harbours) is substantially reduced, the relative importance of tidal trapping through advective, out-of-phase exchange for the main-channel salt balance is expected to increase. This occurs because the discharge through the main channel decreases, whereas the discharge associated with harbour filling and emptying remains of comparable magnitude. This effect should be considerer and further evaluated when the depth in the New Meuse would be substantially reduced.

7.3 Recommendations for Follow-Up Research

7.3.1 Regime Transitions in Channel–Trap Exchange Across Estuarine Configurations

In Chapter 2, the transition from a regime where tidal trapping is dominated by advective out-of-phase exchange to a regime where exchange is diffusive in nature was explored using a highly simplified setup. Within this framework, the strength of the diffusive exchange was prescribed through a constant dispersion coefficient, allowing the overall behaviour to be assessed as a function of the relative importance of these two exchange mechanisms. In more realistic set-ups, this dispersion coefficient would emerge from the local estuarine conditions and reflect the underlying exchange processes. A more process-based representation would make it possible to identify, for example, the geometric configurations in which the trapped salinity field becomes stratified due density currents that develop within the trap, while the main channel remains well mixed, as observed by Garcia and Geyer and Randall (2022). Or to determine under which conditions the system transitions to a regime where channel–trap exchange becomes dominated by reversing, density-driven currents, as described in Chapter 4. These transitions between exchange regimes cannot be adequately represented using a constant dispersion coefficient.

To further improve our understanding of tidal trapping through the temporal storage of saline water in dead-end side channels, it would be valuable to investigate how these dynamics vary and transition across different geometric configurations, using models that can explicitly resolve the underlying exchange mechanisms. Such work should aim to clarify how exchange between the main channel and the trap, as well as the exchange processes occurring within the trap, vary for different geometric properties and dominant dynamical balances. Relevant geometric parameters include the length scale of the dead-end side channel and the depths of both the main channel and the side channel. In addition, the influence of main-channel conditions, such as the along-channel salinity gradient and the tidal excursion length, should be assessed. Together, these factors could be synthesized into regime plots based on relevant estuarine similarity parameters, analogous to those derived for the main-channel structure by Dijkstra and Schuttelaars (2021) and Dijkstra and Schuttelaars and Kranenburg (2022). Furthermore, as discussed in Chapter 4, a more detailed description and understanding of gravity currents in harbour basins would be valuable to reveal how dead-end side channels, such as harbours, contribute to the salt dispersion in the main channel.

7.3.2 Understanding and Quantifying Tidal-Dispersion Processes in Channel Networks

In this thesis, two different methods were used to quantify salt transport associated with tidal dispersion mechanisms. In Chapters 2 and 4, the approach first proposed by Dronkers (1978) was applied to quantify the additional up-estuary salt flux. This method focuses on the redistribution of salt over a distance comparable to the tidal excursion length to

quantify the additional salt transport. The underlying salt balance essentially quantifies asymmetries in the transport of salt into and out of the trap relative to the tidal motion in the main channel. This approach neglects how water released from the trap subsequently interacts with the ambient flow salinity structure in the main channel. Such interactions may initiate lateral and vertical straining of the salinity field (Giddings et al. 2012; Corlett and Geyer 2020), thereby influencing the overall estuarine circulation (Lerczak and Rockwell Geyer 2004). As a result, some of the indirect and dynamically coupled effects of tidal trapping on estuarine salt transport are not fully captured by this framework.

In Chapter 5, a second approach was applied, namely the Lagrangian moving-plane analysis of Dronkers and Van de Kreeke (1986), to examine the origin of the tidal oscillatory salt flux in a single-channel system with staircase bathymetry. In this work, the interactions and processes discussed above, occurring both in the main channel and within the trap, are implicitly captured in the resulting salt fluxes. However, although this approach is particularly useful in identifying the origin of oscillatory salt transport by diagnosing the balance between local and non-local shear induced salt transport, it provides less direct insight into the redistribution effects associated with trap-like features such as dead-end side channels. Furthermore, with respect to the application of this method to the Rhine–Meuse estuary, a limitation of the moving-plane analysis is that it has not yet been applied within a true channel network. Notably, in Garcia and Bo, et al. (2025), creeks and inter-tidal areas are treated as part of an along-channel cross-section, rather than being represented explicitly as separate channels within a network. Extending the moving-plane approach to multi-channel systems would therefore be a valuable first step, as it would provide deeper insight into the origin of tidal oscillatory salt transport in the various branches of the Rhine–Meuse estuary. A second valuable step would be to combine, or at least systematically compare, the quantification approach proposed by Dronkers (1978) with the moving-plane analysis of Dronkers and Van de Kreeke (1986). Such an integrated perspective would help to develop a more complete understanding of both the direct redistribution of saline water associated with tidal trapping and the secondary effects arising from newly generated salinity gradients in the main channel.

7.3.3 Improved Understanding of the Resulting Tidal Currents in Complex Channel Networks such as the Rhine–Meuse Estuary

The up-estuary salt transport in a partially stratified system such as the Rhine–Meuse estuary is largely governed by the salt transport associated with gravitational circulation, particularly in the New Waterway (Kranenburg et al. 2022; Dijkstra and Schuttelaars and Kranenburg 2022; Biemond et al. 2025). The strength of this exchange flow typically diminishes with increasing vertical mixing induced by bottom-boundary shear generated by tidal currents (Hansen and Rattray 1965). Consequently, measures that strengthen tidal currents in the main channel tend to reduce the salt-intrusion length. Large harbour basins can enhance tidal currents and thereby decrease salt intrusion, as suggested in Chapter 4 and consistent with the observations of Abraham et al. (1986)). Increased intertidal area has a similar effect by enlarging the tidal prism (Hendrickx and Pearson 2024), and man-made rapid bathymetric transitions induce partial tidal reflection that modulates tidal currents and influences salt intrusion (Chapter 5). Chapter 5 highlighted the importance of partial reflection of the barotropic tide initiated by stair-case-like bathymetries on the resulting tidal currents and its influence on the salt-intrusion length.

Field observations suggest that the stair-case-like bathymetric steps are not the only source of reflection in the Rhine–Meuse estuary. For example, in the Old Meuse, the phase difference between water level and velocity reaches values around –20° (not reported within this thesis), well outside the 0–45° range expected for a purely incoming wave in a straight channel (Dronkers 1964; Friedrichs 2010). This strongly suggests that the local tidal signal results from the superposition of incoming and reflected components. Yet, in this complex network—with multiple interconnected branches and a hydraulic link to the closed-off former estuary, the Haringvliet—the origin of the reflected wave is difficult to

identify but likely crucial to understand salinity dynamics in these branches. The influence of partial reflection on tidal behaviour is reasonably well understood for single-channel systems (Dronkers 1964; Talke et al. 2021; Dykstra et al. 2024), and the effects of full reflection on salinity dynamics have been demonstrated by Figueroa et al. (2022) and Wei and Williams, et al. (2022). Yet, a more complete understanding of how tides propagate through a complex, branching channel network such as the Rhine–Meuse estuary—see Hill and Souza (2006), Alebregtse and Swart (2016), and Wang et al. (2021) for examples in other systems—and how the resulting tidal signal emerges from the interaction of incoming and reflected waves, may substantially improve our ability to design effective management strategies for the Rhine-Meuse estuary. Such insights could support channel-redesign efforts aimed at reducing salt intrusion in ways that are more efficient and sophisticated than regulating river discharge or introducing engineered salt-intrusion barriers, which often come with high costs and impose constraints on navigation.

7.3.4 Dispersion Formulations for 1D Numerical Models

Although not an explicit objective, a recurring underlying motivation throughout this thesis was that the findings would ultimately support improved one-dimensional formulations of tidal-dispersion processes in estuarine salinity models. The results clarify ambiguities in the parameterisation of tidal trapping, elucidate the dynamics of gravity-driven trapping (Chapters 2 to Chapters 4), and assess how stair-case-like bathymetries influence tidal-dispersion processes (Chapter 5). These insights strengthen our conceptual understanding of tidal dispersion and may support improved parameterisations of processes that are often oversimplified in one-dimensional model schematisation's used in numerical suites such as SOBEK and SOBEK-RE (Deltares 2025; Deltares 2023). The following recommendations may improve these one-dimensional models:

- Use physically grounded, time-scale-consistent dispersion formulations. Existing SOBEK formulations rely on tidally averaged, largely empirical dispersion relations (Savenije 1989; Kuijper and Van Rijn 2011). Because these parameterisations are empirically derived and not linked to specific transport mechanisms, they produce inconsistent sensitivities to the dominant processes and make it difficult to extend the model with missing mechanisms. Furthermore, by representing only the tidally averaged salt flux, they misrepresent intertidal salinity dynamics, as most salt transport may occur during short, concentrated periods of the tidal cycle (Stacey and Burau, et al. 2001). Improved accuracy therefore requires parameterisations that represent instantaneous vertically and laterally sheared salt fluxes, consistent with the temporal resolution at which flow and salinity are solved.
- Using more physically based relations may improve model performance and enhance understanding of the underlying processes. However, in highly (geometrically) complex systems these formulations may still fail to capture all relevant interactions, which limits their ability to accurately predict the salt-intrusion length. Blended machine-learning approaches can possibly capture unresolved dispersive processes. Combining a simplified 1D advection–dispersion model with a machine-learning component—such as a Recurrent Neural Network (RNN) trained on instantaneous salt-flux fields from high-resolution 3D models—offers a promising way to represent missing along-channel dispersion. Such blended models can improve predictive skill and yield dispersion coefficients that better reflect the instantaneous salt-transport processes.

7.4 Broader Scientific Questions

Beyond the immediate follow-up steps identified in Section 7.3, this research trajectory has highlighted several broader scientific questions that extend the scope of the present work:

1. The first question concerns the limitations inherent in how turbulent exchange is represented in hydrostatic models. These models typically rely on parameterisations of turbulence, such as the k–ϵ closure models (Rodi 2017; Uittenbogaard et al.

1992). In the authors' experience, the latest model schematisations of the Rhine–Meuse estuary that employ z–σ layering (chosen to reduce numerical diffusion compared to pure σ-layering) struggle to accurately reproduce the strength of the vertical stratification and tend to produce unrealistically strong stratification. This excessive stratification is hypothesised to arise from the fact that the generation and breaking of internal waves are not explicitly resolved in these hydrostatic models and are not parameterised in the aforementioned closure models. Whereas the recommendations for immediate follow-up research in Section 7.3 focus on improving system understanding, this issue concerns the fundamental limits of how well we can model salinity dynamics in systems such as the Rhine–Meuse estuary. As a non-expert in turbulence modelling but an active user of these models, the author sees a clear need for robust quantification of the spatial and temporal contribution of internal-wave generation and breaking to the observed turbulent eddy-viscosity and diffusivity profiles. Such quantification is essential for developing improved parameterisations of these non-resolved processes and for implementing them in next-generation model schematisations.

2. In recent years, the application of machine-learning techniques to predict system responses or to extract patterns from complex datasets has gained substantial attention and funding. These techniques can be particularly valuable when parameterising complex relationships that are difficult, if not impossible, to express in a clean analytical form. For example, attempting to unravel all individual salt-transport mechanisms and condense them into a single dispersion coefficient for use in 1D models may be highly inefficient. Machine-learning approaches could, in principle, be used to parameterise the resulting effective dispersion coefficient directly from high-resolution model output or observational data (also see Section 7.3.4). However, the extent to which such approaches will advance our fundamental understanding of the underlying processes remains unclear. Analytical derivations based on first principles, although often incomplete in capturing the full system complexity, provide essential conceptual clarity about how processes operate and interact. Machine-learning models, by contrast, may offer predictive skill without necessarily improving mechanistic insight. The challenge, therefore, lies in leveraging data-driven techniques for improved predictive performance and maintaining the physical interpretability.

Appendices

APPENDIX A

Harbor-induced tidal salinity dispersion in partially stratified estuaries

A.1 The salt balance

A.1.1 Decomposition of the Subtidal Salt Transport

The observed and modeled tidally averaged salt transport is decomposed to identify and quantify the underlying salt transport mechanisms. The following quantities are defined:

$$\begin{aligned} s(t,y,z) &= s^0 + s^1(t) + s^2(y,z) + s^3(t,y,z), \\ u(t,y,z) &= u^0 + u^1(t,z) + u^2(y,z) + u^3(t,y,z), \end{aligned} \tag{A.1}$$

here the superscript ^{0} represents the cross-sectionally averaged and tidally averaged property, ^{1} is the cross-sectionally averaged but time-varying property, ^{2} is the cross-sectional variations of the time-averaged property (the steady shear component) and ^{3} is the time-varying cross-sectional variation (time-varying shear component). The subtidal salt transport is given by (Dronkers and Van de Kreeke 1986; Garcia and Geyer and Randall 2022):

$$\begin{aligned} F &= F^{\text{res}} + F^{\text{tide}} + F^{\text{st,shear}} + F^{\text{var,shear}} \\ &= u^0 s^0 A^0 + \langle u^1 s^1 A \rangle + \int u^2 s^2 \, dA^0 + \langle \int u^3 s^3(t,y,z) \, dA \rangle, \end{aligned} \tag{A.2}$$

where A^0 is the tidally-averaged cross-sectional area, and the operator $\langle \cdot \rangle$ denotes a tidal average. The first term in Eq. A.2 is associated with flushing by the residual flow (F^{res}), which is primarily driven by the river discharge. The second term, F^{tide} is the tidal oscillatory contribution, often referred to as the non-local salt flux contribution (Dronkers and Van de Kreeke 1986). The third term, $F^{\text{st,shear}}$, captures the contribution of steady shear associated with the estuarine circulation (Lerczak and Geyer and Chant 2006; Geyer and MacCready 2014), while the fourth term, $F^{\text{var,shear}}$, accounts for non-steady shear or local tidal salt transport (Garcia and Geyer and Randall 2022).

A.1.2 Decomposition of the Measured Subtidal Salt Transport

Figure A.1 presents the salt transport contributions computed from the 13-hour surveys and decomposed using Eq. A.2. During all four surveys, there was a substantial net seaward salt transport and the balance can be considered as unsteady (i.e., the tendency term in the salt balance is non-zero). The net seaward salt transport driven by F^{res} is consistently greater down-estuary of the harbor, with the difference balanced by a net salt transport from the harbor. Up-estuary salt transport occurred mostly through steady shear ($F^{\text{st,shear}}$), with a greater contribution observed at the cross-section upstream of the harbor. The tidal oscillatory contribution (F^{tide}) introduced a net seaward salt transport,

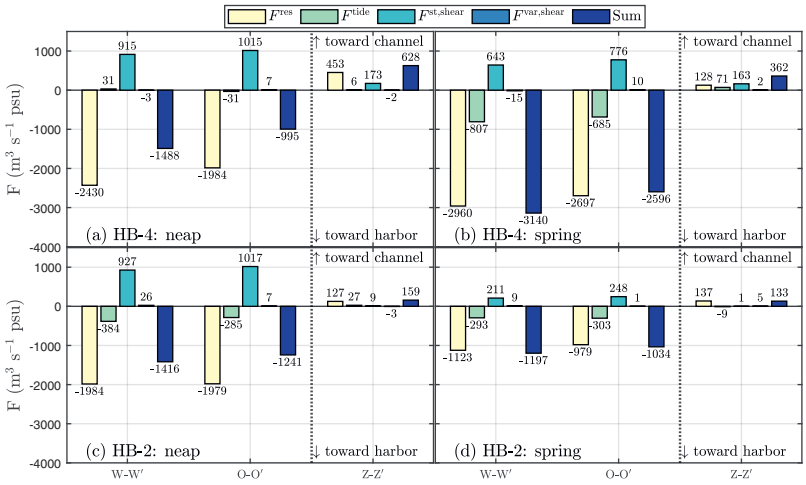


Figure A.1: Salt transport decomposition of the tidally averaged salt transport (Eq. A.2)through the cross-sections surveyed during the 3-hour boat surveys. Results are shown for the two main channel cross-sections—down-estuary (W–W') and up-estuary (O–O') of the harbor—and for the cross-section at the harbor entrance (Z–Z') (see Figure 4.1d,e). Numbers on the bars indicate the exact salt transport values. Positive values in the main channel correspond to up-estuary transport, whereas at the harbor entrance they indicate transport toward the channel. The subscripts $_c$ and $_h$, indicating whether a variable applies to the main channel or the harbor, have been omitted from the legend for clarity.

except during the neap-tide survey at HB-4. Finally, the contribution of the non-steady shear ($F^{\mathrm{var,shear}}$) is small.

A.2 Expression for Tidal Trapping Driven by Gravitational Dynamics

To obtain an expression for tidal trapping in which the channel–trap exchange results from density dynamics, and where the salt transport associated with vertical shear reverses direction throughout the tidal cycle, we start from a simplified version of Eq. 4.5. Assuming purely diffusive channel–trap exchange and a sinusoidal tidal current in the main channel, and setting $t = 0$ at LWS in the main channel, Eq. 4.5 simplifies to:

$$\Delta F_c^{\mathrm{trp}}(x^{\mathrm{ini}}) = \int_{T/2-\Delta t_c}^{T/2+\Delta t_c} F_h^V \, dt, \tag{A.3}$$

where the integral bounds are relative to HWS, and Δt_c is the time window bounded by the moments for which the plane passes the along-channel position of the trap for the first and second time. Based on Eq. 4.13, we assume that the amplitude of the diffusive transport is proportional to the salt transport expected from density dynamics (Benjamin 1968), with the density difference is approximated as $\Delta\rho = \rho_0 \beta s_c^R$, i.e., equal to the salinity range (Maren et al. 2009):

$$\hat{F}_h^V \approx \frac{1}{4}(\beta g)^{1/2}(s_c^R H_h)^{3/2} B_h. \tag{A.4}$$

Alternatively, it may be assumed that the maximum salinity difference between the back of the harbor and the channel is given by $\Delta\rho = \frac{1}{2}\rho_0\beta s_c^R$. This corresponds to the situation where the salinity at the back of the basin remains equal to the tidally averaged salinity in the main channel. Then, we obtain:

$$\hat{F}_h^V \approx \frac{1}{8}\sqrt{\frac{1}{2}}(\beta g)^{1/2}(s_c^R H_h)^{3/2} B_h. \tag{A.5}$$

When s_c^R is the result of advection of an arrested salinity field, we can define $s_c^R = L_c \dfrac{\partial s_c^0}{\partial x}$ where L_c is the tidal excursion length in the main channel. Eqs. A.4 and A.5 provide an estimate of the magnitude of the exchange between channel and trap. Assuming that F_h^V varies sinusoidally and peaks at slack water —i.e., it is in quadrature with the cross-sectionally averaged current— we define:

$$F_h^V \approx \hat{F}_h^V \cos(\omega t). \tag{A.6}$$

It should be noted that Eq. A.6 gives an overly simplified representation and ideally would be replaced by a more theoretically substantiated formulation. Substituting Eq. A.6 into Eq. A.3, evaluation of the integral results in:

$$\Delta F_c^{\mathrm{trp}}(x^{\mathrm{ini}}) = \frac{2}{w}\hat{F}_h^V \sin(w\Delta t_c). \tag{A.7}$$

To simplify Eq. A.7, the time window Δt_c can be expressed in terms of the initial position x^{ini} of the plane that moves with the tidally varying discharge component at $t = 0$, using that the distance traveled by this plane is expressed as $\Delta x = \frac{1}{2}L_c(1 - \cos(\omega t))$:

$$\Delta t_c = \frac{T}{2} - \frac{1}{\omega}\cos^{-1}\left(\frac{2x^{\mathrm{ini}}}{L_c} - 1\right). \tag{A.8}$$

Substituting this into Eq. A.7 results in the following expression:

$$\Delta F_c^{\mathrm{trp}}(x^{\mathrm{ini}}) = \frac{2}{w}\hat{F}_c^V \cdot \left[1 - \left(\frac{2x^{\mathrm{ini}}}{L_c} - 1\right)^2\right]^{1/2}. \tag{A.9}$$

Eq. A.3 represents the total transport over a tidal cycle. Expressing F_c^{trp} as the tidally averaged additional salt transport and substitution of Eq. A.4 results in:

$$F_c^{\mathrm{trp}}(x^{\mathrm{ini}}) = \frac{1}{4\pi}B_h\Big(\beta g\Big)^{1/2}\Big(s_c^R H_h\Big)^{3/2}\cdot\Big[1 - (\frac{2x^{\mathrm{ini}}}{L_c} - 1)^2\Big]^{1/2}. \tag{A.10}$$

Alternatively, Eq. A.5 can be substituted, which yields:

$$F_c^{\mathrm{trp}}(x^{\mathrm{ini}}) = \frac{1}{8\pi}\sqrt{\frac{1}{2}}B_h\Big(\beta g\Big)^{1/2}\Big(s_c^R H_h\Big)^{3/2}\cdot\Big[1 - (\frac{2x^{\mathrm{ini}}}{L_c} - 1)^2\Big]^{1/2}. \tag{A.11}$$

Given that the system is in steady-state and there is no net salt transport through the cross-sections, $K_c^{\mathrm{trp}} = F_c^{\mathrm{trp}}/\Big(A_c^0\dfrac{\partial s_c^0}{\partial x}\Big)$, which results in the following expression when we use $s_c^R = L_c\dfrac{\partial s_c^0}{\partial x}$ in Eq. A.10:

$$K_c^{\mathrm{trp}}(x^{\mathrm{ini}}) = \frac{1}{4\pi}\left(\frac{H_h B_h}{A_c}\right)\left(\beta L_c\frac{\partial s_c^0}{\partial x}\right)^{1/2}\Big(gH_h\Big)^{1/2}L_c\cdot\Big[1 - (\frac{2x^{\mathrm{ini}}}{L_c} - 1)^2\Big]^{1/2}, \tag{A.12}$$

or, when we use $s_c^R = L_c\frac{\partial s_c^0}{\partial x}$ in Eq. A.11:

$$K_c^{\mathrm{trp}}(x^{\mathrm{ini}}) = \frac{1}{8\pi}\sqrt{\frac{1}{2}}\left(\frac{H_h B_h}{A_c}\right)\left(\beta L\frac{\partial s_c^0}{\partial x}\right)^{1/2}\Big(gH_h\Big)^{1/2}L_c\cdot\Big[1 - (\frac{2x^{\mathrm{ini}}}{L_c} - 1)^2\Big]^{1/2}. \tag{A.13}$$

APPENDIX B

Salinity Dynamics in Partially Deepened Estuaries With stepwise Bathymetry

B.1 Reformulation of Dronkers (1964) Equations

In order to identify and analyse the role of wave reflection in our numerical model results, we used the theory of Dronkers (1964). By adopting a simplified depth-averaged mass and momentum equations with a linearized friction term, the following solution for the along channel water level amplitudes and discharge amplitudes are obtained:

$$\begin{aligned}\eta(x,t) &= \mathrm{Re}\Big(\hat{\eta}^{-}\exp\Big[\omega\sigma\frac{x}{c_0}+i\omega t+i\omega\chi\frac{x}{c_0}\Big]\Big)\\ &\quad \mathrm{Re}\Big(\hat{\eta}^{+}\exp\Big[-\omega\sigma\frac{x}{c_0}+i\omega t-i\omega\chi\frac{x}{c_0}\Big]\Big),\\ Q(x,t) &= \mathrm{Re}\Big(-\frac{Wc\,i}{\sigma+i\chi}\,\hat{\eta}^{-}\exp\Big[\omega\sigma\frac{x}{c_0}+i\omega t+i\omega\chi\frac{x}{c_0}\Big]\Big)+\\ &\quad \mathrm{Re}\Big(\frac{Wc\,i}{\sigma+i\chi}\,\hat{\eta}^{+}\exp\Big[-\omega\sigma\frac{x}{c_0}+i\omega t-i\omega\chi\frac{x}{c_0}\Big]\Big).\end{aligned} \tag{B.1}$$

In Eq. B.1 $\hat{\eta}^{\pm}$ are the complex amplitudes at $x=0$ of the incident and reflected wave, $c=\sqrt{gH}$ is the in inviscid wave celerity and W is the channel width and the parameters σ and χ depend on the non-dimensional friction coefficient r/ω and are defined as

$$\sigma=\sqrt{-\frac{1}{2}+\frac{1}{2}\sqrt{1+\Big(\frac{r}{\omega}\Big)^2}},\qquad \chi=\sqrt{\frac{1}{2}+\frac{1}{2}\sqrt{1+\Big(\frac{r}{\omega}\Big)^2}}. \tag{B.2}$$

In the performed analysis we evaluate Eq. B.1 locally by setting the coordinate origin at $x=0$:

$$\begin{aligned}\eta(t) &= \mathrm{Re}\big(\hat{\eta}^{-}e^{i\omega t}\big)+\mathrm{Re}\big(\hat{\eta}^{+}e^{i\omega t}\big),\\ Q(t) &= \mathrm{Re}\big(-T\,\hat{\eta}^{-}e^{i\omega t}\big)+\mathrm{Re}\big(T\,\hat{\eta}^{+}e^{i\omega t}\big),\end{aligned} \tag{B.3}$$

where

$$T=\frac{Wc\,i}{\sigma+i\chi},$$

The incident and reflected complex amplitudes follow from the algebraic decomposition (Dronkers 1964)

$$\hat{\eta}^{\pm}=\tfrac{1}{2}\hat{\eta}\pm\tfrac{1}{2}\hat{Q}\,\frac{\chi-i\sigma}{Wc}. \tag{B.4}$$

Using Eq. B.3 together with Eq. B.4, we estimate the incident and reflected wave contributions from the complex amplitudes $\hat{\eta}$ and $\hat{Q}$ obtained directly from the modelled tidal

amplitudes and phases through harmonic analysis.

To combine the incident and reflected contributions into a single expression, we introduce the complex reflection coefficient

$$\frac{\hat{\eta}^-}{\hat{\eta}^+} = \frac{|\hat{\eta}^-|e^{i\theta^-}}{|\hat{\eta}^+|e^{i\theta^+}} = \gamma e^{i\Theta}, \tag{B.5}$$

where $\gamma = |\hat{\eta}^-|/|\hat{\eta}^+|$ is the reflection magnitude and $\Theta = \arg(\hat{\eta}^-) - \arg(\hat{\eta}^+)$ is the associated phase difference. Using this definition, the complex amplitudes of surface elevation and discharge can be written as

$$\begin{aligned} \hat{\eta} &= \hat{\eta}^+ + \hat{\eta}^- = \hat{\eta}^+ \left(1 + \gamma e^{i\Theta}\right), \\ \hat{Q} &= \hat{Q}^+ + \hat{Q}^- = T\,\hat{\eta}^+ \left(1 - \gamma e^{i\Theta}\right). \end{aligned} \tag{B.6}$$

The depth-averaged velocity amplitude is obtained from $\hat{u} = Q/(WH)$. Substituting the expression for T and taking the absolute value yields

$$|\hat{u}| = \frac{c}{H\,|\sigma + i\chi|} \left|1 - \gamma e^{i\Theta}\right| \left|\hat{\eta}^+\right|, \tag{B.7}$$

This expression provides a compact relationship showing how the velocity amplitude depends on the degree of reflection and on the local phase difference between the incident and reflected waves. The structure is directly analogous to the classical standing–wave pattern of nodes and antinodes that arises under full reflection. To illustrate this behaviour, the resulting amplitude planes for $|\hat{\eta}|$ and $|\hat{u}|$ are shown in panels a and b of Figure B.1. For the water levels, the maximum amplitudes occur under complete reflection ($\gamma = 1$), when the incident and reflected waves are in phase ($\Theta = 0$). This corresponds to the elevation antinode of a standing wave. At this location, the current amplitude is minimal because the discharge contributions from the incident and reflected waves cancel. Conversely, the maximum velocity amplitude occurs where the water-level amplitudes interfere destructively but the discharge components interfere constructively. This happens at $\Theta = \pi$, corresponding to the velocity node of the standing-wave pattern.

The phase difference between discharge and water level then follows as

$$\arg(\hat{\eta}) - \arg(\hat{Q}) = \arg\left(\frac{\hat{\eta}}{\hat{Q}}\right) = \arg\left(\frac{1}{T}\,\frac{1 + \gamma e^{i\Theta}}{1 - \gamma e^{i\Theta}}\right). \tag{B.8}$$

Using the identity $\arg(z_1 z_2) = \arg(z_1) + \arg(z_2)$ allows to decomposed as

$$\arg(\hat{\eta}) - \arg(\hat{Q}) = \arg\left(\frac{1}{T}\right) + \arg\left(\frac{1 + \gamma e^{i\Theta}}{1 - \gamma e^{i\Theta}}\right). \tag{B.9}$$

The two terms in Eq. B.9 have clear physical interpretations. The first term represents the intrinsic long wave phase difference between water level and discharge, governed by channel properties such as wave celerity c_0 and the dimensionless friction parameters through σ and β. The maximum phase difference induced by this term is 45 °, equal to the maximum phase difference due to a frictional effect alone, found by Friedrichs (2010). The second term represents the phase shift induced by partial reflection, determined by both the reflection magnitude γ and the local phase difference Θ between the incident and reflected waves. The resulting phase behaviour across the (Θ, γ)-plane is shown in panel c of Figure B.1.

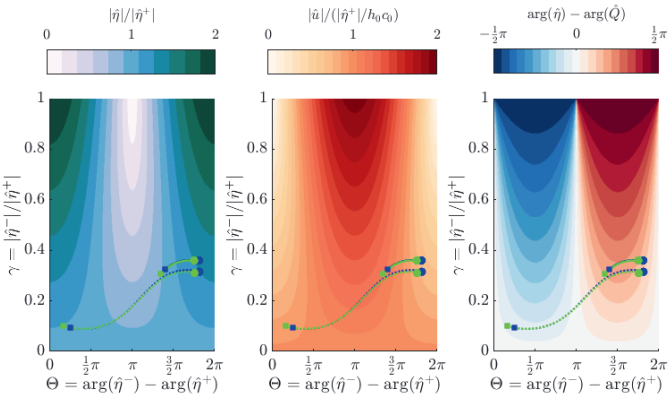


Figure B.1: Visualizations of the tidal quantities derived from the reformulated expressions based on the theory of Dronkers (1964), shown across the (Θ, γ)-plane. Here, Θ denotes the phase difference between the reflected and incident wave, and γ is the reflection magnitude. (a) Normalized tidal water-level amplitudes computed from Eq. B.6. (b) Normalized depth-averaged velocity amplitudes based on Eq. B.7. (c) Phase difference between water level and discharge derived from Eq. B.9. The lines indicate the trajectories through the (Θ, γ)-plane for the four individual runs shown in Fig. 5.14, for configurations with $\frac{X_1}{\Lambda_0} = \frac{1}{8}$ (solid lines) and $\frac{X_1}{\Lambda_0} = \frac{3}{8}$ (dashed lines). Blue lines correspond to the bathymetry with the steep bed-slope inclination, and green lines to the mild bed-slope configuration.

APPENDIX C

A new harmonic regression approach to interpret and predict estuarine salinity variation

C.1 Details regarding the solution procedure

C.1.1 Data preprocessing

The harmonic regression models are optimized using data points that exceed a minimum salinity threshold, S_{min}. Salinity sensors often exhibit deviations in their minimal detection range and accuracy, which may make the salinity values from an upstream station unsuitable for S_{min}. Instead, S_{min} can be based on the 95% confidence upper bounds derived from the regression model for river salinity (Eq. 6.15). Alternatively, a constant threshold value may be used, although this could lead to the unnecessary rejection of data points from the analysis.

The use of Eq. 6.12 requires storm surge induced water level variations (δ_w). In de code, δ_w is inferred from provided water levels record at the downstream boundary. The astronomical water level variations are estimated using T-TIDE (Pawlowicz et al. 2002), the non-explained variations (residuals) are assumed to be atmospherically forced, and subsequently band pass filtered to isolate the range of oscillations at periods between 1.2−14 days. Surge variations at time-scales smaller than 1.2 days and exceeding 14 days cannot properly be distinguished from the tidal motion, including fortnightly variations. For the experiment discussed in Section 6.4, the upper limit is set to 6 days. Futhermore, salinity variation are translated to density series based on the Unesco (1981) formulation, which is required for Eq. 6.14.

C.1.2 The regression matrix

For the optimization to obtain the best-fit regression coefficients and model powers, Eq. 6.9−6.12 are rewritten in matrix notation:

$$\mathbf{S} = \mathbf{D} \cdot \mathbf{x}, \tag{C.1}$$

where $\mathbf{S}$ is a vector of the resulting relative dispersion over time minus one (i.e., the LHS minus the first term on the RHS):

$$\mathbf{S} = \left(\frac{S_{s,i} - S_{r,i}}{S_{0,i} - S_{r,i}} \right)^K - 1, \tag{C.2}$$

with the index i ($i = 1 : m$) for the moment in time, used in the regression analysis (see Appendix C.1.1). The design matrix $\mathbf{D}$ for Eq. 6.12 reads:

$$= K \frac{Q_r}{\left(\frac{\Delta\rho}{\rho}\frac{Q_r}{\eta^3\omega}\right)^P (\eta^2\omega)} \Big[1 \;\; \delta_{w,t_i} \;\; \cos(\omega_1 t_i) \;\; \ldots \;\; \cos(\omega_n t_i) \;\; \sin(\omega_1 t_i) \;\; \ldots \;\; \sin(\omega_k t_i) \\ \delta_{w,t_i}\cos(\omega_1 t_i) \;\; \ldots \;\; \delta_{w,t_i}\cos(\omega_n t_i) \;\; \delta_{w,t_i}\sin(\omega_n t_i) \;\; \ldots \;\; \delta_{w,t_i}\sin(\omega_n t_i)\Big], \tag{C.3}$$

with the index k ($k = 1 : n$) for a tidal constituent added in the model. The unknown coefficients $\mathbf{X}$ are given by:

$$\mathbf{X} = \Big[a_0 \;\; a_1 \;\; a^c_{2,1} \;\; \ldots \;\; a^c_{2,n} \;\; a^s_{2,1} \;\; \ldots \;\; a^s_{2,n} \\ a^c_{3,1} \;\; \ldots \;\; a^c_{3,n} \;\; a^s_{3,1} \;\; \ldots \;\; a^s_{3,n}\Big], \tag{C.4}$$

which contains the proportionality coefficients of the subtidal (a_0) and storm surge variations (a_1), and the amplitudes for the intertidal variations ($a^c_{2,n}, a^s_{2,n}, a^c_{3,n}, a^s_{3,n}$).

C.1.3 The optimization procedure

The proportionality coefficients $\mathbf{X}$ and the powers P and K of the model are iteratively optimized. First, an initial estimate for the proportionality coefficients is determined by minimizing the merit function through an ordinary least squares regression (OLSR):

$$\mathbf{R}^2 = \mid \mathbf{D} \cdot \mathbf{x} - \mathbf{S} \mid^2, \tag{C.5}$$

with $\mathbf{R}$ being the residuals. Hereafter, the best-fit values for the powers are found using MATLAB's *lsqcurvefit* function, which minimizes the least squared error between the predicted and the observed salinity. For the OLSR, only data points where the observed salinity exceeds S_{min} are used. For the predicted salinity, all valid data points are considered. However, the predicted relative dispersion (RHS Eq. 6.9−6.12) may fall outside the range yielding physical solutions. To prevent this, a truncation is applied:

$$\frac{D_{s,i}}{D_{0,i}} = \begin{cases} \dfrac{D_{s,i}}{D_{0,i}}, & \text{if } \dfrac{D_{s,i}}{D_{0,i}} \geq 0 \\ 0, & \text{otherwise,} \end{cases} \tag{C.6}$$

which avoids below zero values. For each new estimate for P and K, a new estimate for the proportionality coefficients is made through Eq. C.5, until a (local) minimum is found in the sum of squares. For the initial estimate, $P = 0.57$ (from Gisen and Savenije (2015)) is used and varies between 0 and 1 in the optimization, while K has a default for $K = 0.5$ and is optimized within $0.05 < K < 2$. The included tidal constituents are determined based on the adjusted Rayleigh criterion and depend on the power P (see Appendix C.1.5).

C.1.4 Amplitudes and phases of the tidal constituents

The coefficients $a^c_{2,n}, a^s_{2,n}, a^c_{3,n} a^s_{3,n}$ in Eq. C.4 are associated to the intertidal dynamics. The coefficients related to the intertidal variations can be expressed in terms of (time varying) amplitudes and phases for each individual tidal constituent added in the model (Matte and Jay, et al. 2013). For this purpose, the amplitudes (A_k and B_k) and corresponding phases (α_k and β_k) are defined as:

$$A_k = \sqrt{\left(a^{c\#}_{2,k}\right)^2 + \left(a^{s\#}_{2,k}\right)^2}, \tag{C.7}$$

$$B_k = \delta_{w,T}\sqrt{\left(a^{c\#}_{3,k}\right)^2 + \left(a^{s\#}_{3,k}\right)^2}, \tag{C.8}$$

$$\alpha_k = \arctan\frac{a^s_{2,k}}{a^c_{2,k}}, \tag{C.9}$$

$$\beta_k = \arctan \frac{a^s_{3,k}}{a^c_{3,k}} \tag{C.10}$$

where the constant amplitude A_k represents the contribution to the constant intertidal variations and B_k is the time varying amplitude resulting from by storm surges introduced intertidal variations. The constant phases are given by α_k and β_k, respectively. As shown by Matte and Jay, et al. (2013), for each tidal constituent, the resulting time varying amplitude and phases can be derived from C.4 - C.7, and they are given by:

$$|D_k(t)| = |d_k(t)| + |d_{-k}(t)| \tag{C.11}$$

$$\psi(t) = \arctan \frac{\mathrm{Im}(d_{-k})}{\mathrm{Re}(d_{-k})} \tag{C.12}$$

with d_{-k} and its complex conjugate d^*_{-k} obtained from:

$$d_{-k} = d^*_{-k} = \frac{1}{2}(A_k \cos(\alpha_k) + B_k \cos(\beta_k)) + i\frac{1}{2}(A_k \sin(\alpha_k) + B_k \sin(\beta_k)). \tag{C.13}$$

The resulting amplitudes and phases in Eq. 6.11 are equivalent to the amplitudes A_k and phases α_k.

C.1.5 Constituents selection and error estimates

An adjusted version of the two-folded strategy (Matte and Jay, et al. 2013) is used for the constituent selection and error estimates. The importance of the constituents is obtained from an initial harmonic analysis performed on salinity time series at the target station. The lower bound frequency that can be resolved under the assumption of a regularly sampled signal is set by the Rayleigh criterion, which states two frequencies can be distinguished when $\frac{|\,\omega_1 - \omega_2\,|}{LOR} < R$, with R set to one and LOR is the length of record. In addition, the degree in which constituents can properly be distinguished is also affected by non-stationary influences (Matte and Jay, et al. 2013). In the case of salinity time series broadening of spectral lines can either be introduced by non-stationarity of the salinity distribution itself or indirectly via a non-stationary tidal signal. For the frequency selection, only the influence of non-stationarity in the salinity distribution is considered (additional to the traditional Rayleigh criterion). The minimal allowable frequency separation is evaluated using an adjusted Rayleigh criterion (Matte and Jay, et al. 2013), for which the normalized spectrum of Q^{1-P} is evaluated. If the time series contain gaps, the two frequencies cannot properly be identified and R should be adjusted accordingly. There is, however, no accepted practice to adjust the Rayleigh criterion for irregularly sampled data (Codiga 2011). For irregularly sampled data, the degree in which tidal constituents can properly be resolved is monitored through the correlation between the model coefficients, following Foreman et al. (2009).

The significance of added constituents and error estimates of the amplitudes or phases of the harmonic model are based on the uncorrelated noise model of NS-TIDE (Matte and Jay, et al. 2013). The uncorrelated noise is used to calculate a distribution realisation for each model coefficient. Subsequently, for each replicate, the resulting amplitude and phase are calculated based on Eqs. C.11−C.12, and used to compute the time varying confidence bounds for each tidal constituent. In NS-TIDE, the significance of each constituent is estimated using the squared ratio of the resulting amplitude and amplitude error. The drawback of this approach is that only the contribution of the overall resulting amplitude is evaluated, while the contribution of the amplitudes related to individual mechanisms, based on Eq. C.7˜C.8, may be insignificant. Therefore, first, the significance of each tidal constituent based on the overall resulting amplitude is tested, adopting a signal-to-noise ratio (SNR) bound of 4. Hereafter, it is tested whether the amplitudes related to the individual mechanisms are actually significant, adopting the same SNR bound. If not, the terms related to the individual mechanisms are removed from the model structure for that specific tidal constituent.

C.2 Alternative base-function for the harmonic regression model

In this paper, we have chosen to use the analytical model for steady-state salinity distribution derived by Savenije (1986). However, an analogous set of equations to Eq. 6.9–6.12 can also be derived using the more theoretically substantiated model proposed by Gay and O'Donnell (2007). Equation 6.18 can be extended to account for tidal and storm surge variations in a similar manner as described in Section 6.3.1. The harmonic regression including tidal variations is expressed as:

$$\left(\frac{S_s - S_r}{S_0 - S_r}\right)^{\left(\gamma \frac{D_0}{Q_r}\right)} = 1 - c_0 + \sum_{k=1}^{n} \left[c^c_{2,k} \cos(\omega_k t) + c^s_{2,k} \sin(\omega_k t)\right], \tag{C.14}$$

and the extension with storm surge variations is given by:

$$\left(\frac{S_s - S_r}{S_0 - S_r}\right)^{\left(\gamma \frac{D_0}{Q_r}\right)} = 1 - \underbrace{c_0}_{\text{TA}} + \underbrace{c_1 \delta_w}_{\text{SURGE}} + \underbrace{\sum_{k=1}^{n} \left[\left(c^c_{2,k} + c^c_{3,k}\delta_w\right) \cos(\omega_k t) + \left(c^s_{2,k} + a^s_{3,k}\delta_w\right) \sin(\omega_k t)\right]}_{\text{TIDAL}}. \tag{C.15}$$

Eq. C.14 and C.15 include two power coefficients that need to be optimized: P associated with D_0, and γ, which scales the power ($\gamma \frac{D_0}{Q_r}$). To obtain the best-fit values for these parameters, the same optimization procedure described in C.1 is applied. The results for the experiments performed in Section 6.4.3 using Eq. C.14 and C.15 are tabulated in Table C.1 and C.2 and provide comparable results.

Table C.1: Overview of the model experiments performed for the Ems Estuary and results discussed in Sections 6.4.3. The missing percentage refers to the total percentage of missing and rejected data points.
[1]: Fortnightly averaged salinity at Knock station for the seaward boundary condition.
[2]: Total of the fitted proportionality coefficients.

Regression model:	Boundary:	Calibration:	Prediction:	Station:	Missing	Pars[2]	P/γ	Calibration		Predictions	
								rmse	Un. var.	rmse	Un. var.
				(-)	(%)	(-)	(-)	(psu)	(%)	(psu)	(%)
Tides (Eq. C.14)	Obs[1]	17 months	7 months	Emspier	13	31	$0.37/8.7{\cdot}10^{-5}$	1.9	7.8	2.2	8.9
				Pogum	4	31	$0.35/7.4{\cdot}10^{-5}$	1.9	7.2	2.0	7.6
				Gandersum	8	31	$0.39/1.2{\cdot}10^{-4}$	1.7	7.7	2.1	9.2
				Terborg	37	31	$0.44/2.1{\cdot}10^{-4}$	1.2	11.7	1.6	16.3
Tides + surges (Eq. C.15)	Obs[1]	17 months	7 months	Emspier	13	44	$0.39/9.4{\cdot}10^{-5}$	1.8	7.2	2.1	7.6
				Pogum	4	48	$0.36/8.5{\cdot}10^{-5}$	1.8	6.6	1.9	6.3
				Gandersum	8	48	$0.41/1.4{\cdot}10^{-4}$	1.6	7.1	1.9	7.5
				Terborg	37	48	$0.42/2.1{\cdot}10^{-4}$	1.1	11.4	1.5	14.8

Table C.2: Overview of the model experiments performed for the Scheldt Estuary and results discussed in Section 6.4.3. The missing percentage refers to the total percentage of missing and rejected data points.
[1]: Fortnightly averaged salinity at Prosperpolder for the seaward boundary condition.
[2]: Total of the fitted proportionality coefficients

Regression model:	Boundary:	calibration:	Prediction:	Station:	Missing	Pars[2]	P/γ	calibration		Predictions	
								rmse	Un. var.	rmse	Un. var.
				(-)	(%)	(-)	(-)	(psu)	(%)	(psu)	(%)
Tides + surges (Eq. C.14)	Obs[1]	2.5 years	1 year	Lillo Meetpaal	13	27	$0.75/7.5{\cdot}10^{-4}$	0.5	1.5	0.64	3.9
				Oosterweel	25	29	$0.57/4.0{\cdot}10^{-4}$	1.2	7.5	1.3	10.5
				Hemiksem	19	25	$0.55/4.2{\cdot}10^{-4}$	0.6	11.8	0.56	13.0
Tides + surges (Eq. C.15)	Obs[1]	2.5 years	1 year	Lillo Meetpaal	13	36	$0.75/7.2{\cdot}10^{-4}$	1.3	10.8	1.4	3.8
				Oosterweel	25	28	$0.57/4.2{\cdot}10^{-4}$	1.4	11.1	1.6	9.8
				Hemiksem	19	34	$0.56/4.3{\cdot}10^{-4}$	0.6	11.0	0.54	12.0

Bibliography

K. A. Abood (1974). "Circulation in the Hudson estuary". In: *Annals of the New York Academy of Sciences* 250.1, pp. 39–111.

G. Abraham and P. de Jong and F. Van Kruiningen (1986). "Large-scale Mixing Processes in a Partly Mixed Estuary". In: *Physics of Shallow Estuaries and Bays* 16, pp. 5–21.

H. M. van Aken (1986). "The onset of seasonal stratification in shelf seas due to differential advection in the presence of a salinity gradient". In: *Continental Shelf Research* 5.4, pp. 475–485.

N. Alebregtse and H. de Swart (2016). "Effect of river discharge and geometry on tides and net water transport in an estuarine network, an idealized model applied to the Yangtze Estuary". In: *Continental Shelf Research* 123, pp. 29–49.

S. Andrews and E. Gross and P. Hutton (2017). "Modeling salt intrusion in the San Francisco Estuary prior to anthropogenic influence". In: *Continental Shelf Research* 146, pp. 58–81.

R. Aris (1956). "On the dispersion of a solute in a fluid flowing through a tube". In: *Proceedings of the Royal Society of London. Series A. Mathematical and Physical Sciences* 235.1200, pp. 67–77.

L. Armi (1986). "The hydraulics of two flowing layers with different densities". In: *Journal of Fluid Mechanics* 163, pp. 27–58.

L. Armi and D. M. Farmer (1986). "Maximal two-layer exchange through a contraction with barotropic net flow". In: *Journal of Fluid Mechanics* 164, pp. 27–51.

P. G. Baines (2022). *Topographic effects in stratified flows*. Cambridge university press.

N. Banas et al. (2004). "Dynamics of Willapa Bay, Washington: A highly unsteady, partially mixed estuary". In: *Journal of Physical Oceanography* 34.11, pp. 2413–2427.

T. B. Benjamin (1968). "Gravity currents and related phenomena". In: *Journal of fluid mechanics* 31.2, pp. 209–248.

B. Biemond et al. (2025). "Dynamics of salt intrusion in complex estuarine networks: an idealised model applied to the Rhine–Meuse Delta". In: *Ocean Science* 21.1, pp. 261–281.

T. Bo and D. K. Ralston (2020). "Flow separation and increased drag coefficient in estuarine channels with curvature". In: *Journal of Geophysical Research: Oceans* 125.10, e2020JC016267.

— (2022). "Frontogenesis, mixing, and stratification in estuarine channels with curvature". In: *Journal of Physical Oceanography* 52.7, pp. 1333–1350.

T. Bo and D. K. Ralston, et al. (2024). "Tidal intrusion fronts, surface convergence, and mixing in an estuary with complex topography". In: *Journal of Physical Oceanography* 54.3, pp. 653–677.

R. Brockway et al. (2006). “A note on salt intrusion in funnel-shaped estuaries: Application to the Incomati estuary, Mozambique”. In: *Estuarine, Coastal and Shelf Science* 66.1-2, pp. 1–5.

H. Burchard and K. Bolding, et al. (2018). “The Knudsen theorem and the Total Exchange Flow analysis framework applied to the Baltic Sea”. In: *Progress in oceanography* 165, pp. 268–286.

H. Burchard and R. D. Hetland (2010). “Quantifying the contributions of tidal straining and gravitational circulation to residual circulation in periodically stratified tidal estuaries”. In: *Journal of Physical Oceanography* 40.6, pp. 1243–1262.

H. Burchard and R. D. Hetland, et al. (2011). “Drivers of residual estuarine circulation in tidally energetic estuaries: Straight and irrotational channels with parabolic cross section”. In: *Journal of Physical Oceanography* 41.3, pp. 548–570.

H. Burchard and H. Rennau (2008). “Comparative quantification of physically and numerically induced mixing in ocean models”. In: *Ocean modelling* 20.3, pp. 293–311.

H. Cai et al. (2015). “A predictive model for salt intrusion in estuaries applied to the Yangtze estuary”. In: *Journal of Hydrology* 529, pp. 1336–1349.

R. J. Chant and C. K. Sommerfield and S. A. Talke (2018). “Impact of channel deepening on tidal and gravitational circulation in a highly engineered estuarine basin”. In: *Estuaries and Coasts* 41.6, pp. 1587–1600.

P. Chatwin (1976). “Some remarks on the maintenance of the salinity distribution in estuaries”. In: *Estuarine and Coastal Marine Science* 4.5, pp. 555–566.

S.-N. Chen and W. R. Geyer, et al. (2012). “Estuarine exchange flow quantified with isohaline coordinates: Contrasting long and short estuaries”. In: *Journal of Physical Oceanography* 42.5, pp. 748–763.

S.-N. Chen and L. P. Sanford (2009). “Axial wind effects on stratification and longitudinal salt transport in an idealized, partially mixed estuary”. In: *Journal of Physical Oceanography* 39.8, pp. 1905–1920.

P. Cheng and A. Valle-Levinson and H. E. De Swart (2010). “Residual currents induced by asymmetric tidal mixing in weakly stratified narrow estuaries”. In: *Journal of physical oceanography* 40.9, pp. 2135–2147.

K.-H. Cho et al. (2012). “A modeling study on the response of Chesapeake Bay to hurricane events of Floyd and Isabel”. In: *Ocean Modelling* 49, pp. 22–46.

D. L. Codiga (2011). “Unified tidal analysis and prediction using the UTide Matlab functions”. In.

W. B. Corlett and W. R. Geyer (2020). “Frontogenesis at estuarine junctions”. In: *Estuaries and Coasts* 43.4, pp. 722–738.

J. R. Cox et al. (2021). “Anthropogenic effects on the contemporary sediment budget of the lower Rhine-Meuse Delta channel network”. In: *Earth’s Future* 9.7, e2020EF001869.

C. Craft et al. (2009). “Forecasting the effects of accelerated sea-level rise on tidal marsh ecosystem services”. In: *Frontiers in Ecology and the Environment* 7.2, pp. 73–78.

M. A. De Nijs and J. C. Winterwerp and J. D. Pietrzak (2009). “On harbour siltation in the fresh-salt water mixing region”. In: *Continental Shelf Research* 29.1, pp. 175–193.

H. De Swart and V. De Jonge and M. Vosbeek (1997). “Application of the tidal random walk model to calculate water dispersion coefficients in the Ems estuary”. In: *Estuarine, Coastal and Shelf Science* 45.1, pp. 123–133.

Deltares (2021). *Delft3D-FLOW User Manual*. Version 3.15. Software manual. Deltares.

— (2023). *SOBEK-RE: River and Estuary modelling suite – User Manual*. Deltares. Delft, The Netherlands. URL: https://www.deltares.nl/en/software/sobek-suite/.

— (2025). *SOBEK Suite for Integral Water Solutions*. Version latest. Accessed: 2025-09-26. URL: https://www.deltares.nl/en/software-and-data/products/sobek-suite.

Y. M. Dijkstra and H. M. Schuttelaars (2021). "A unifying approach to subtidal salt intrusion modeling in tidal estuaries". In: *Journal of Physical Oceanography* 51.1, pp. 147–167.

Y. M. Dijkstra and H. M. Schuttelaars and H. Burchard (2017). "Generation of exchange flows in estuaries by tidal and gravitational eddy viscosity-shear covariance (ESCO)". In: *Journal of Geophysical Research: Oceans* 122.5, pp. 4217–4237.

Y. M. Dijkstra and H. M. Schuttelaars and W. M. Kranenburg (2022). "Salt transport regimes caused by tidal and subtidal processes in narrow estuaries". In: *Journal of Geophysical Research: Oceans* 127.12, e2021JC018391.

J. Dronkers (1978). "Longitudinal dispersion in shallow well-mixed estuaries". In: *Proceedings of the 16th Coastal Engineering Conference*. Vol. 3. Hamburg, Germany: American Society of Civil Engineers (ASCE), pp. 2761–2776.

J. Dronkers and J. Van de Kreeke (1986). "Experimental determination of salt intrusion mechanisms in the Volkerak estuary". In: *Netherlands Journal of Sea Research* 20.1, pp. 1–19.

J. J. Dronkers (1964). "Tidal computations in rivers and coastal waters". In.

S. L. Dykstra et al. (2024). "Reflection of storm surge and tides in convergent estuaries with dams, the case of Charleston, USA". In: *Journal of Geophysical Research: Oceans* 129.9, e2023JC020498.

E. Eidam and D. Sutherland and D. Ralston and T. Conroy, et al. (2021). "Shifting sediment dynamics in the Coos Bay Estuary in response to 150 years of modification". In: *Journal of Geophysical Research: Oceans* 126.1, e2020JC016771.

E. Eidam and D. Sutherland and D. Ralston and B. Dye, et al. (2022). "Impacts of 150 years of shoreline and bathymetric change in the Coos Estuary, Oregon, USA". In: *Estuaries and Coasts* 45.4, pp. 1170–1188.

J. Evans and D. Pugh (1982). "Analysing clipped sea-level records for harmonic tidal constituents". In: *The International Hydrographic Review*.

W. Eysink (1989). "Sedimentation in harbour basins. Small density differences may cause serious effects". In: *International Harbour Congress, 9th*.

R. Familkhalili and S. A. Talke (2016). "The effect of channel deepening on tides and storm surge: A case study of Wilmington, NC". In: *Geophysical research letters* 43.17, pp. 9138–9147.

R. Familkhalili and S. A. Talke and D. A. Jay (2020). "Tide-storm surge interactions in highly altered estuaries: How channel deepening increases surge vulnerability". In: *Journal of Geophysical Research: Oceans* 125.4, e2019JC015286.

S. M. Figueroa and M. Son and G.-h. Lee (2022). "Effect of estuarine dam location and discharge interval on estuarine hydrodynamics, sediment dynamics, and morphodynamics". In: *Frontiers in Marine Science* 9, p. 1035501.

H. Fischer (1972). "Mass transport mechanisms in partially stratified estuaries". In: *Journal of fluid mechanics* 53.4, pp. 671–687.

H. B. Fischer (1976). "Mixing and dispersion in estuaries". In: *Annual review of fluid mechanics* 8.1, pp. 107–133.

H. B. Fischer et al. (1979). *Mixing in inland and coastal waters*. Academic press.

M. G. Foreman and J. Y. Cherniawsky and V. Ballantyne (2009). "Versatile harmonic tidal analysis: Improvements and applications". In: *Journal of Atmospheric and Oceanic technology* 26.4, pp. 806–817.

C. T. Friedrichs (2010). "Barotropic tides in channelized estuaries". In: *Contemporary issues in estuarine physics* 27, p. 61.

J. Garcés-Vargas et al. (2020). "Tidally forced saltwater intrusions might impact the quality of drinking water, the Valdivia River (40 S), Chile Estuary Case". In: *Water* 12.9, p. 2387.

A. M. P. Garcia and T. Bo, et al. (2025). “Topographically induced dispersion in a salt marsh estuary”. In: *Journal of Physical Oceanography* 55.11, pp. 2209–2227.
A. M. P. Garcia and W. R. Geyer (2022). “Tidal dispersion in short estuaries”. In: *Journal of Geophysical Research: Oceans*, e2022JC018883.
A. M. P. Garcia and W. R. Geyer and N. Randall (2022). “Exchange Flows in Tributary Creeks Enhance Dispersion by Tidal Trapping”. In: *Estuaries and Coasts* 45.2, pp. 363–381.
P. S. Gay and J. O’Donnell (2007). “A simple advection-dispersion model for the salt distribution in linearly tapered estuaries”. In: *Journal of Geophysical Research: Oceans* 112.C7.
Gemeente Rotterdam (2024). *Getijdenpark*. URL: https://www.rotterdam.nl/getijdenpark (visited on 04/24/2026).
A. Gerritsma et al. (2025). “The effects of a storm surge event on salt intrusion: Insights from the Rhine-Meuse Delta”. In: *Journal of Geophysical Research: Oceans* 130.4, e2024JC021520.
W. R. Geyer and P. MacCready (2014). “The estuarine circulation”. In: *Annual review of fluid mechanics* 46, pp. 175–197.
W. R. Geyer and D. K. Ralston (2015). “Estuarine frontogenesis”. In: *Journal of Physical Oceanography* 45.2, pp. 546–561.
W. R. Geyer and R. P. Signell (1992). “A reassessment of the role of tidal dispersion in estuaries and bays”. In: *Estuaries* 15.2, pp. 97–108.
W. R. Geyer and J. H. Trowbridge and M. M. Bowen (2000). “The dynamics of a partially mixed estuary”. In: *Journal of Physical oceanography* 30.8, pp. 2035–2048.
W. Geyer and D. Ralston, et al. (2024). “The structure and dynamics of an estuarine tidal intrusion front”. In: *Journal of Geophysical Research: Oceans* 129.2, e2023JC020371.
S. N. Giddings et al. (2012). “Frontogenesis and frontal progression of a trapping-generated estuarine convergence front and its influence on mixing and stratification”. In: *Estuaries and Coasts* 35.2, pp. 665–681.
J. I. A. Gisen and H. H. Savenije (2015). “Estimating bankfull discharge and depth in ungauged estuaries”. In: *Water Resources Research* 51.4, pp. 2298–2316.
J. Gisen and H. H. Savenije, et al. (2015). “Testing a 1-D analytical salt intrusion model and its predictive equations in Malaysian estuaries”. In: *Hydrological Sciences Journal* 60.1, pp. 156–172.
W. Gong et al. (2018). “Effects of wave–current interaction on salt intrusion during a typhoon event in a highly stratified estuary”. In: *Estuaries and Coasts* 41.7, pp. 1904–1923.
G. Green et al. (1838). “On the motion of waves in a variable canal of small depth and width”. In: *Transactions of the Cambridge Philosophical Society* 6, p. 457.
G. E. Guerra-Chanis et al. (2019). “Saltwater intrusion in a subtropical estuary”. In: *Estuarine, Coastal and Shelf Science* 217, pp. 28–36.
R. L. Haney (1991). “On the pressure gradient force over steep topography in sigma coordinate ocean models”. In.
D. V. Hansen and M. Rattray (1965). “Gravitational circulation in straits and estuaries”. In: *Journal of Marine Research* 23, pp. 104–122.
D. V. Hansen and M. Rattray Jr (1966a). *Gravitational circulation in straits and estuaries*.
— (1966b). “New dimensions in estuary classification 1”. In: *Limnology and oceanography* 11.3, pp. 319–326.
W. Helder and P. Ruardij (1982). “A one-dimensional mixing and flushing model of the Ems-Dollard estuary: calculation of time scales at different river discharges”. In: *Netherlands Journal of Sea Research* 15.3-4, pp. 293–312.
G. G. Hendrickx and S. G. Pearson (2024). “On the effects of intertidal area on estuarine salt intrusion”. In: *Journal of Geophysical Research: Oceans* 129.9, e2023JC020750.

E. R. Herbert et al. (2015). “A global perspective on wetland salinization: ecological consequences of a growing threat to freshwater wetlands”. In: *Ecosphere* 6.10, pp. 1–43.
R. D. Hetland and W. R. Geyer (2004). “An idealized study of the structure of long, partially mixed estuaries”. In: *Journal of Physical Oceanography* 34.12, pp. 2677–2691.
A. Hill and A. Souza (2006). “Tidal dynamics in channels: 2. Complex channel networks”. In: *Journal of Geophysical Research: Oceans* 111.C11.
A. Hoitink et al. (2017). “Tidal controls on river delta morphology”. In: *Nature Geoscience* 10.9, pp. 637–645.
A. R. Horner-Devine and R. D. Hetland and D. G. MacDonald (2015). “Mixing and transport in coastal river plumes”. In: *Annual Review of Fluid Mechanics* 47.1, pp. 569–594.
A. T. Ippen and D. R. Harleman (1961). *One-dimensional analysis of salinity intrusion in estuaries.* Tech. rep. ARMY ENGINEER WATERWAYS EXPERIMENT STATION VICKSBURG MS.
A. D. Jassby et al. (1995). “Isohaline position as a habitat indicator for estuarine populations”. In: *Ecological applications* 5.1, pp. 272–289.
D. A. Jay (1991). “Green’s law revisited: Tidal long-wave propagation in channels with strong topography”. In: *Journal of Geophysical Research: Oceans* 96.C11, pp. 20585–20598.
D. A. Jay and J. D. Musiak (1994). “Particle trapping in estuarine tidal flows”. In: *Journal of Geophysical Research: Oceans* 99.C10, pp. 20445–20461.
— (1996). “Internal tidal asymmetry in channel flows: Origins and consequences”. In: *Coastal and Estuarine Studies*, pp. 211–249.
D. A. Jay and J. D. Smith (1990). “Circulation, density distribution and neap-spring transitions in the Columbia River Estuary”. In: *Progress in Oceanography* 25.1-4, pp. 81–112.
H. Jongbloed and B. Vermeulen and A. Hoitink (2023). *Physics-informed estimation of open channel flow fields from acoustic Doppler current profiler transect data.*
H. Jongbloed and H. M. Schuttelaars, et al. (2022). “Influence of wind on subtidal salt intrusion and stratification in well-mixed and partially stratified estuaries”. In: *Journal of Physical Oceanography* 52.12, pp. 3139–3158.
K. Kästner et al. (2019). “Propagation of tides along a river with a sloping bed”. In: *Journal of Fluid Mechanics* 872, pp. 39–73.
M. Knudsen (1900). “Ein hydrographischer lehrsatz”. In: *Annalen der Hydrographie und Maritimen Meteorologie* 28.7, pp. 316–320.
C. Kranenburg (1986). “A time scale for long-term salt intrusion in well-mixed estuaries”. In: *Journal of Physical Oceanography* 16.7, pp. 1329–1331.
— (1996). “Density currents”. In: *Reader lecture b81, Delft Technical University (in Dutch).*
W. Kranenburg et al. (2022). “Salt intrusion in the Rhine Meuse Delta: Estuarine circulation, tidal dispersion or surge effect”. In: *Proceedings of the 39th iahr world congress*, pp. 19–24.
K. Kuijper and L. C. Van Rijn (2011). “Analytical and numerical analysis of tides and salinities in estuaries; part II: salinity distributions in prismatic and convergent tidal channels”. In: *Ocean Dynamics* 61.11, pp. 1743–1765.
S. Lanzoni and G. Seminara (1998). “On tide propagation in convergent estuaries”. In: *Journal of Geophysical Research: Oceans* 103.C13, pp. 30793–30812.
J. L. Largier (1992). “Tidal intrusion fronts”. In: *Estuaries* 15.1, pp. 26–39.
J. Lee et al. (2025). “Global increases of salt intrusion in estuaries under future environmental conditions”. In: *Nature Communications* 16.1, p. 3444.
J. A. Lerczak and W. R. Geyer and R. J. Chant (2006). “Mechanisms driving the time-dependent salt flux in a partially stratified estuary”. In: *Journal of Physical Oceanography* 36.12, pp. 2296–2311.

J. A. Lerczak and W. R. Geyer and D. K. Ralston (2009). “The temporal response of the length of a partially stratified estuary to changes in river flow and tidal amplitude”. In: *Journal of Physical Oceanography* 39.4, pp. 915–933.
J. A. Lerczak and W. Rockwell Geyer (2004). “Modeling the lateral circulation in straight, stratified estuaries”. In: *Journal of Physical Oceanography* 34.6, pp. 1410–1428.
J. R. Leuven et al. (2023). “Peak Water Levels Rise Less Than Mean Sea Level in Tidal Channels Subject to Depth Convergence by Deepening”. In: *Journal of Geophysical Research: Oceans* 128.4, e2022JC019578.
R. E. Lewis and R. J. Uncles (2003). “Factors affecting longitudinal dispersion in estuaries of different scale”. In: *Ocean Dynamics* 53.3, pp. 197–207.
C. Li and E. Weeks and B. W. Blanchard (2010). “Storm surge induced flux through multiple tidal passes of Lake Pontchartrain estuary during Hurricanes Gustav and Ike”. In: *Estuarine, Coastal and Shelf Science* 87.4, pp. 517–525.
M. Li and L. Zhong, et al. (2006). “Hurricane-induced storm surges, currents and destratification in a semi-enclosed bay”. In: *Geophysical Research Letters* 33.2.
— (2007). “Hurricane-induced destratification and restratification in a partially-mixed estuary”. In: *Journal of Marine Research* 65.2, pp. 169–192.
X. Li and W. R. Geyer, et al. (2018). “The transformation of salinity variance: A new approach to quantifying the influence of straining and mixing on estuarine stratification”. In: *Journal of Physical Oceanography* 48.3, pp. 607–623.
P. MacCready (1999). “Estuarine adjustment to changes in river flow and tidal mixing”. In: *Journal of Physical Oceanography* 29.4, pp. 708–726.
— (2004). “Toward a unified theory of tidally-averaged estuarine salinity structure”. In: *Estuaries* 27, pp. 561–570.
— (2007). “Estuarine adjustment”. In: *Journal of Physical Oceanography* 37.8, pp. 2133–2145.
P. MacCready and W. R. Geyer (2010). “Advances in estuarine physics”. In: *Annual Review of Marine Science* 2, pp. 35–58.
D. G. MacDonald and W. R. Geyer (2005). “Hydraulic control of a highly stratified estuarine front”. In: *Journal of Physical Oceanography* 35.3, pp. 374–387.
L. J. MacVean and M. T. Stacey (2011). “Estuarine dispersion from tidal trapping: a new analytical framework”. In: *Estuaries and Coasts* 34.1, pp. 45–59.
D. S. van Maren et al. (2009). “The effect of dock length on harbour siltation”. In: *Continental Shelf Research* 29.11-12, pp. 1410–1425.
P. Matte and D. A. Jay and E. D. Zaron (2013). “Adaptation of classical tidal harmonic analysis to nonstationary tides, with application to river tides”. In: *Journal of Atmospheric and Oceanic Technology* 30.3, pp. 569–589.
P. Matte and Y. Secretan and J. Morin (2014). “Temporal and spatial variability of tidal-fluvial dynamics in the St. Lawrence fluvial estuary: An application of nonstationary tidal harmonic analysis”. In: *Journal of Geophysical Research: Oceans* 119.9, pp. 5724–5744.
S. G. Monismith et al. (2002). “Structure and flow-induced variability of the subtidal salinity field in northern San Francisco Bay”. In: *Journal of physical Oceanography* 32.11, pp. 3003–3019.
W. Mueller et al. (2024). “Saltwater intrusion and human health risks for coastal populations under 2050 climate scenarios”. In: *Scientific Reports* 14.1, p. 15881.
A. Nguyen and H. Savenije (2006). “Salt intrusion in multi-channel estuaries: a case study in the Mekong Delta, Vietnam”. In: *Hydrology and Earth System Sciences* 10.5, pp. 743–754.
A. D. Nguyen and H. H. Savenije, et al. (2008). “New analytical equation for dispersion in estuaries with a distinct ebb-flood channel system”. In: *Estuarine, coastal and shelf science* 79.1, pp. 7–16.
I. Niesten and Y. Huismans and A. Hoitink (2024). “Ebb-Dominant Mixing Increases the Seaward Sediment Flux in a Stratified Estuary”. In: *Journal of Geophysical Research: Oceans* 129.12, e2024JC021201.

M. A. de Nijs and J. D. Pietrzak and J. C. Winterwerp (2011). "Advection of the salt wedge and evolution of the internal flow structure in the Rotterdam Waterway". In: *Journal of Physical Oceanography* 41.1, pp. 3–27.
R. Nunes and J. Simpson (1985). "Axial convergence in a well-mixed estuary". In: *Estuarine, Coastal and Shelf Science* 20.5, pp. 637–649.
A. Okubo (1973). "Effect of shoreline irregularities on streamwise dispersion in estuaries and other embayments". In: *Netherlands Journal of Sea Research* 6.1-2, pp. 213–224.
R. Pawlowicz and B. Beardsley and S. Lentz (2002). "Classical tidal harmonic analysis including error estimates in MATLAB using T_TIDE". In: *Computers & Geosciences* 28.8, pp. 929–937.
D. Prandle (1981). "Salinity intrusion in estuaries". In: *Journal of Physical Oceanography* 11.10, pp. 1311–1324.
D. W. Pritchard (1952). "Estuarine hydrography". In: *Advances in geophysics*. Vol. 1. Elsevier, pp. 243–280.
D. T. Pugh (1987). "Tides, surges and mean sea level". In.
D. K. Ralston and W. R. Geyer (2019). "Response to channel deepening of the salinity intrusion, estuarine circulation, and stratification in an urbanized estuary". In: *Journal of Geophysical Research: Oceans* 124.7, pp. 4784–4802.
D. K. Ralston and W. R. Geyer and J. A. Lerczak (2008). "Subtidal salinity and velocity in the Hudson River estuary: Observations and modeling". In: *Journal of Physical Oceanography* 38.4, pp. 753–770.
D. K. Ralston and M. T. Stacey (2005). "Longitudinal dispersion and lateral circulation in the intertidal zone". In: *Journal of Geophysical Research: Oceans* 110.C7.
D. K. Ralston and S. Talke, et al. (2019). "Bigger tides, less flooding: Effects of dredging on barotropic dynamics in a highly modified estuary". In: *Journal of Geophysical Research: Oceans* 124.1, pp. 196–211.
J. S. Rath et al. (2017). "A hybrid empirical-Bayesian artificial neural network model of salinity in the San Francisco Bay-Delta estuary". In: *Environmental Modelling & Software* 93, pp. 193–208.
M. Á. Reyes-Merlo et al. (2013). "On the relative influence of climate forcing agents on the saline intrusion in a well-mixed estuary: Medium-term Monte Carlo predictions". In: *Journal of Coastal Research* 65, pp. 1200–1205.
L. C. van Rijn (2011). "Analytical and numerical analysis of tides and salinities in estuaries; part I: tidal wave propagation in convergent estuaries". In: *Ocean dynamics* 61.11, pp. 1719–1741.
W. Rodi (2017). *Turbulence models and their application in hydraulics*. Routledge.
A. Roelfzema and A. Van Os (1978). "Effect of harbours on salt intrusion in estuaries". In: *Coastal Engineering 1978*, pp. 2810–2826.
J. Rohmer and N. Brisset (2017). "Short-term forecasting of saltwater occurrence at La Comté River (French Guiana) using a kernel-based support vector machine". In: *Environmental Earth Sciences* 76.6, p. 246.
K. Rummel et al. (2025). "Spatially resolved salt intrusion mechanisms in a tidal estuary and the impact of channel deepening". In: *Journal of Geophysical Research: Oceans* 130.6, e2024JC022073.
E. Saccon et al. (2025). "Wetland topography drives salinity resilience in freshwater tidal ecosystems". In: *Ecological engineering* 217, p. 107650.
H. Savenije (1986). "A one-dimensional model for salinity intrusion in alluvial estuaries". In: *Journal of Hydrology* 85.1-2, pp. 87–109.
H. H. G. Savenije (2015). "Prediction in ungauged estuaries: An integrated theory". In: *Water Resources Research* 51.4, pp. 2464–2476.
— (1989). "Salt intrusion model for high-water slack, low-water slack, and mean tide on spread sheet". In: *Journal of Hydrology* 107.1-4, pp. 9–18.

H. H. Savenije (1993). “Predictive model for salt intrusion in estuaries”. In: *Journal of Hydrology* 148.1-4, pp. 203–218.
— (2006). *Salinity and tides in alluvial estuaries*. Elsevier.
H. H. Savenije et al. (2008). “Analytical description of tidal dynamics in convergent estuaries”. In: *Journal of Geophysical Research: Oceans* 113.C10.
J. Schijf and J. Schönfled (1953). “Theoretical considerations on the motion of salt and fresh water”. In.
E. Schulz et al. (2015). “Impact of the depth-to-width ratio of periodically stratified tidal channels on the estuarine circulation”. In: *Journal of Physical Oceanography* 45.8, pp. 2048–2069.
M. E. Scully and C. Friedrichs and J. Brubaker (2005). “Control of estuarine stratification and mixing by wind-induced straining of the estuarine density field”. In: *Estuaries* 28.3, pp. 321–326.
D. Shaha and Y.-K. Cho (2009). “Comparison of empirical models with intensively observed data for prediction of salt intrusion in the Sumjin River estuary, Korea”. In: *Hydrology and Earth System Sciences* 13.6, pp. 923–933.
M. Shammi et al. (2019). “Impacts of salinity intrusion in community health: a review of experiences on drinking water sodium from coastal areas of Bangladesh”. In: *Healthcare*. Vol. 7. 1. MDPI, p. 50.
R. W. Siemes et al. (2025). “Salt intrusion affected by large-scale human interventions and sea level rise: A 3D modeling study of an engineered estuary”. In: *Journal of Geophysical Research: Oceans* 130.6, e2025JC022504.
J. Simpson and P. Linden (1989). “Frontogenesis in a fluid with horizontal density gradients”. In: *Journal of Fluid Mechanics* 202, pp. 1–16.
J. H. Simpson and J. Brown, et al. (1990). “Tidal straining, density currents, and stirring in the control of estuarine stratification”. In: *Estuaries* 13.2, pp. 125–132.
M. T. Stacey and M. L. Brennan, et al. (2010). “The tidally averaged momentum balance in a partially and periodically stratified estuary”. In: *Journal of Physical Oceanography* 40.11, pp. 2418–2434.
M. T. Stacey and J. R. Burau and S. G. Monismith (2001). “Creation of residual flows in a partially stratified estuary”. In: *Journal of Geophysical Research: Oceans* 106.C8, pp. 17013–17037.
M. T. Stacey and D. K. Ralston (2005). “The scaling and structure of the estuarine bottom boundary layer”. In: *Journal of Physical Oceanography* 35.1, pp. 55–71.
G. S. Stelling and J. A. T. M. Van Kester (1994). “On the approximation of horizontal gradients in sigma co-ordinates for bathymetry with steep bottom slopes”. In: *International journal for numerical methods in fluids* 18.10, pp. 915–935.
H. Stommel and H. G. Farmer (1952). *On the nature of estuarine circulation: part I (chapters 3 and 4)*. Woods Hole Oceanographic Institution.
E. Struyf and S. Van Damme and P. Meire (2004). “Possible effects of climate change on estuarine nutrient fluxes: a case study in the highly nutrified Schelde estuary (Belgium, The Netherlands)”. In: *Estuarine, Coastal and Shelf Science* 60.4, pp. 649–661.
S. A. Talke and R. Familkhalili and D. A. Jay (2021). “The influence of channel deepening on tides, river discharge effects, and storm surge”. In: *Journal of Geophysical Research: Oceans* 126.5, e2020JC016328.
G. I. Taylor (1953). “Dispersion of soluble matter in solvent flowing slowly through a tube”. In: *Proceedings of the Royal Society of London. Series A. Mathematical and Physical Sciences* 219.1137, pp. 186–203.
M. Toffolon and G. Vignoli and M. Tubino (2006). “Relevant parameters and finite amplitude effects in estuarine hydrodynamics”. In: *Journal of Geophysical Research: Oceans* 111.C10.
R. E. Uittenbogaard and J. T. M. Van Kester and G. S. Stelling (1992). *Implementation of Three Turbulence Models in TRISULA for Rectangular Horizontal Grids: Including 2DV-testcases*. Delft Hydraulics.

Unesco (1981). *Tenth Report of the Joint Panel on Oceanographic Tables and Standards-Sidney, BC, Canada, 1-5 September 1980, Sponsored by Unesco, Ices, Scor, Iapso*.

A. Valle-Levinson (2010). *Contemporary issues in estuarine physics*. Cambridge University Press.

A. Valle-Levinson and K.-C. Wong and K. M. Lwiza (2000). "Fortnightly variability in the transverse dynamics of a coastal plain estuary". In: *Journal of Geophysical Research: Oceans* 105.C2, pp. 3413–3424.

L. Van Rijn et al. (2010). "Tidal phenomena in the Scheldt Estuary". In: *Report, Deltares* 105, p. 99.

P. Vd Burgh (1972). "Ontwikkeling van een methode voor het voorspellen van zoutverdelingen in estuaria, kanalen en zeeen". In.

N. Vellinga et al. (2014). "Human impacts on tides overwhelm the effect of sea level rise on extreme water levels in the Rhine–Meuse delta". In: *Coastal engineering* 90, pp. 40–50.

B. Vermeulen and M. Sassi and A. Hoitink (2014). "Improved flow velocity estimates from moving-boat ADCP measurements". In: *Water resources research* 50.5, pp. 4186–4196.

J. Wang and H. E. de Swart and Y. M. Dijkstra (2021). "Dependence of tides and river water transport in an estuarine network on river discharge, tidal forcing, geometry and sea level rise". In: *Continental Shelf Research* 225, p. 104476.

J. Warner et al. (2002). "Effects of tidal current phase at the junction of two straits". In: *Continental Shelf Research* 22.11-13, pp. 1629–1642.

T. M. Wegman et al. (2025). "Observations of estuarine salt intrusion dynamics during a prolonged drought event in the Rhine-Meuse Delta". In: *Journal of Geophysical Research: Oceans* 130.1, e2024JC021655.

X. Wei and G. P. Schramkowski and H. M. Schuttelaars (2016). "Salt dynamics in well-mixed estuaries: Importance of advection by tides". In: *Journal of Physical Oceanography* 46.5, pp. 1457–1475.

X. Wei and M. E. Williams, et al. (2022). "Salt intrusion as a function of estuary length in periodically weakly stratified estuaries". In: *Geophysical Research Letters* 49.15, e2022GL099082.

J. C. Winterwerp and J. Vroom, et al. (2017). "SPM response to tide and river flow in the hyper-turbid Ems River". In: *Ocean Dynamics* 67.5, pp. 559–583.

J. C. Winterwerp and Z. B. Wang, et al. (2013). "Man-induced regime shifts in small estuaries—II: a comparison of rivers". In: *Ocean Dynamics* 63.11, pp. 1293–1306.

E. Wolanski and P. Ridd (1986). "Tidal mixing and trapping in mangrove swamps". In: *Estuarine, Coastal and Shelf Science* 23.6, pp. 759–771.

B. J. Wullems et al. (2023). "Forecasting estuarine salt intrusion in the Rhine–Meuse delta using an LSTM model". In: *Hydrology and Earth System Sciences* 27.20, pp. 3823–3850.

Y. Xu et al. (2019). "Analytical model captures intratidal variation in salinity in a convergent, well-mixed estuary". In: *Hydrology and Earth System Sciences* 23.10, pp. 4309–4322.

E. Zhang and H. H. Savenije, et al. (2011). "Analytical solution for salt intrusion in the Yangtze Estuary, China". In: *Estuarine, coastal and shelf science* 91.4, pp. 492–501.

Z. Zhang and H. Savenije (2019). "Maximum power of saline and fresh water mixing in estuaries". In: *Earth System Dynamics* 10.4, pp. 667–684.

F. Zhou and B. Liu and K. Duan (2020). "Coupling wavelet transform and artificial neural network for forecasting estuarine salinity". In: *Journal of Hydrology* 588, p. 125127.

X. Zhou and T. Yang, et al. (2017). "Prospective scenarios of the saltwater intrusion in an estuary under climate change context using Bayesian neural networks". In: *Stochastic Environmental Research and Risk Assessment* 31.4, pp. 981–991.

DANKWOORD

De afgelopen jaren, waarin ik aan dit proefschrift heb gewerkt, heb ik de vrijheid gekregen om mij te verdiepen in estuariene dynamica, iets waarvan ik enorm genoten heb en veel van heb geleerd. Daarnaast heb ik in deze periode veel hulp gekregen, en daarom wil ik graag de volgende personen bedanken.

Ten eerste mijn (co)promotoren Prof. Ton Hoitink en Dr. Wouter Kranenburg. Om meerdere jaren intensief samenwerken volledig te beschrijven is onmogelijk; daarom hou ik het kort. Beste Ton, ik wil je ontzettend bedanken voor de vrijheid die ik heb gekregen in het vormgeven van mijn onderzoek, voor de hulp en bijsturing op cruciale momenten, en voor de kansen die je mij daarbuiten hebt gegeven. Wouter, jou wil ik in het bijzonder bedanken voor de vele interessante discussies die hebben bijgedragen aan dit proefschrift, voor het helpen bij de verbinding met Deltares, en voor het op sleeptouw nemen in het werkveld en tijdens conferenties. Naast mijn directe begeleiding wil ik Paul Torfs bedanken voor het meedenken en de discussies die we hebben gehad, evenals voor de hulp bij de numerieke aspecten. Deze support is essentieel geweest voor de betreffende onderdelen. Daarnaast dank aan Henk Jongbloed voor de discussies over zoutdynamica en Joris Beemster voor de inhoudelijke gesprekken over getijdynamica; deze gesprekken hebben bijgedragen aan dit proefschrift. Voor de hulp bij de meetcampagne van 2022 wil ik specifiek Gerrit van Santen en het volledige surveyteam van de Port of Rotterdam bedanken voor hun support bij de vier 13-uursmetingen. Daarnaast Lamber Hulsen voor het meedenken bij de opzet, Tess Wegman voor het trekken van de grote meetcampagne waarvan deze metingen onderdeel waren, en Jan-Willem Mol voor het mogelijk maken en ondersteunen van de vaste metingen vanuit de CIV (RWS). Tijdens het schrijven van dit proefschrift heb ik vaak mogen overnachten bij vrienden en familie. Bedankt voor het aanbieden van bed, bad en brood in deze periode en jullie overall support. Tot slot wil ik graag woorden wijden aan de persoon die niet bedankt wil worden, maar vooral beloond wil worden voor het fungeren als spelling-checker, voor de support en voor het bijstaan gedurende deze leuke maar ook intensieve periode.

PUBLICATIONS

Van Keulen, D., W. M. Kranenburg, and A. J. F. Hoitink. "Harbor-induced tidal salinity dispersion in partially stratified estuaries." Journal of Geophysical Research: Oceans 131.4 (2026): e2025JC023208.

van Keulen, Daan, Wouter M. Kranenburg, and Antonius J.F. Hoitink. (2025). Tidal Trapping and Its Effect on Salinity Dispersion in Well-Mixed Estuaries Revisited. Estuaries and Coasts, 48(6), 153.

van Keulen, D., Kranenburg, W. M., & Hoitink, A. J. F. (2025). A new harmonic regression approach to interpret and predict estuarine salinity variation. Journal of Geophysical Research: Oceans, 130(5), e2024JC022185.

Lee, J., Biemond, B., van Keulen, D., Huismans, Y., van Westen, R. M., de Swart, H. E., ...& Kranenburg, W. M. (2025). Global increases of salt intrusion in estuaries under future environmental conditions. Nature Communications, 16(1), 3444.

Leuven, J. R. F. W., van Keulen, D., Nienhuis, J. H., Canestrelli, A., & Hoitink, A. J. F. (2021). Large-scale scour in response to tidal dominance in estuaries. Journal of Geophysical Research: Earth Surface, 126(5), e2020JF006048.

Graduate School Diploma

Netherlands Research School for the
Socio-Economic and Natural Sciences of the Environment

D I P L O M A

for specialised PhD training

The Netherlands research school for the
Socio-Economic and Natural Sciences of the Environment
(SENSE) declares that

Daan van Keulen

born on 1993-06-18 in Heemstede, the Netherlands

has successfully fulfilled all requirements of the
educational PhD programme of SENSE.

Wageningen, 14 October 2026

SENSE coordinator PhD education

Dr Ir Peter Vermeulen

The SENSE Director

Dr Jampel Dell'Angelo



The SENSE Research School declares that **Daan van Keulen** has successfully fulfilled all requirements of the educational PhD programme of SENSE with a work load of **41.5**, including the following activities:

Academic knowledge and skills	
o PhD research proposal (2021)	WIMEK
o Reviewing two scientific manuscripts (2024, 2026)	
Oral presentations	
o A new harmonic regression approach for predicting estuarine salinity variation subject to storm surge effects, (2022)	OSM
o A new harmonic regression approach to predict estuarine salinity variation subject to storm surge effects (2022)	Ems Scheldt Symposium 2022
o Tidal trapping and its effect on salinity dispersion in well-mixed estuaries (2025)	Ems Scheldt Symposium 2025
o Channel-harbour exchange and its influence on salinity dispersion in a partially stratified branch of the Rhine-Meuse estuary by Daan van Keulen et al. (2025)	EGU25
Transferable Professional Skills	
o A1 reflection report (2026)	SENSE
o Intense writing weeks (2024)	Wageningen into lanquages
o Organiser of the HWM -Science Cafe (2021)	
o Member of HWM PhD Committee (2021)	
Societal impact	
o A2 impact incubator: "Sediment relocation pilot (2026)	Sense
o Attending two Hackathons with other stakeholder on verziltingsmaatregelen RMM (2025)	HVK & RWS
o Attending expertsessie sturen op afvoer (2026)	RWS
o Teaching in the practical of Coastal Oceanography and Delta Geology (2021-2023)	Wageningen University
o Writing two chapters in the reader of the course 'Morphodynamics of Rivers, Estuaries and Deltas' (2026)	Wageningen University
Career perspectives	
o NCK Days 2025 (2025)	Netherlands Centre for Coastal Research

Authorship statement

Chapter 1: Introduction
I wrote the initial draft of the Introduction, on which both supervisors provided comments.

Chapter 2: Tidal trapping and its effect on salinity dispersion in well-mixed estuaries revisited
The idea to examine how geometric complexity affects salt dispersion originated from the project proposal. The initial goal was to apply or extend the framework of MacVean (2011). I found that the model did not produce the physically correct response; instead, its behaviour contrasted with my own analysis, which I later found to be consistent with Dronkers (1978). This insight initiated Chapter 2, for which I designed and performed the analysis and wrote the initial manuscript. Both supervisors contributed by helping to improve the manuscript and by shaping this chapter through various discussions.

Chapter 3: Critical Examination of the MacVean and Stacey (2011) formulations
This chapter emerged from the discussion surrounding the manuscript presented in Chapter 2. The reviewers highlighted methodological differences that could explain the discrepancies between the frameworks. This chapter was developed to reject that suggestion and to demonstrate the implications of the alternative approach. I designed the study and performed the analysis myself. Both supervisors contributed to the scientific discussion and provided suggestions on the manuscript.

Chapter 4: Harbor-induced tidal salinity dispersion in partially stratified estuaries
The central idea for this chapter arose from my own observation of substantial differences in exchange processes between harbour basins. I developed the conceptual interpretation, performed the analyses, and wrote the initial manuscript. Both supervisors contributed to shaping the manuscript and provided suggestions and support during the writing of the final version.

Chapter 5: Salinity Dynamics in Partially Deepened Estuaries With stepwise Bathymetry
This chapter originated from insights gained while writing Chapter 4, specifically the recognition that abrupt depth transitions exert a significant influence on salt dynamics. The initial idea and the analytical framework were developed by me. Both supervisors contributed by discussing how to structure the manuscript. I wrote the initial manuscript, after which both supervisors provided feedback and suggestions for improvement.

Chapter 6: A new harmonic regression approach to interpret and predict estuarine salinity variation

The general research objective to reformulate the harmonic regression model was proposed in the original project plan and originated from my supervisors. I developed the resulting model and wrote the initial manuscript. For this chapter, I received substantial support during the publication process in terms of written manuscript, on which the present chapter is based.

Chapter 7: Synthesis
I wrote the initial draft of the synthesis, on which both supervisors provided comments.

The research described in this thesis is part of the SALTISolutions Perspective Programme (2022/TTW/01344701P18-32 project 4) and was financially supported by the Dutch Research Council NWO, Rijkswaterstaat, Deltares, Port of Rotterdam, Hydrologic, Hoogheemraadschap van Schieland en de Krimpenerwaard, Hoogheemraadschap Rijnland, and Royal BAM.

Financial support from Wageningen University for printing this thesis is gratefully acknowledged.

Cover design by Daan van Keulen, based on aerial pictures of the Rhine–Meuse estuary, adjusted using Gemini.
Printed by ProefschriftMaken.

